Development of methods for Electrical Impedance Tomography of epileptic seizures

Lorenzo Fabrizi

Submitted for the degree of Doctor of Philosophy

Department of Medical Physics

University College London

2008

ProQuest LLC
789 East Eisenhower Parkway
P.O. Box 1346
Ann Arbor, MI 48106-1346

Declaration of authorship

I, Lorenzo Fabrizi, confirm that the work presented in this thesis is my own. Where information has been derived from other sources, I confirm that this has been indicated in the thesis.

Lorenzo Fabrizi

Table of Content

List of figures

List of table

Chapter 1 – Introduction

1.1 Overview

For over 15 years our group at University College London has been climbing the steep ladder of Electrical Impedance Tomography (EIT), trying to reach its last step - the use of EIT as a functional and structural imaging technique for pathophysiological conditions of the brain.

Each tissue that constitutes our body has a specific conductivity that distinguishes it from the others. Therefore, in principle, by knowing each tissue conductivity, we should be able to provide an anatomical map of a structure, in the same way that knowing its X-ray absorption allows us to obtain its CT image. EIT is a non-invasive, portable and inexpensive medical imaging technique that allows the reconstruction of the internal conductivity distribution of an object via impedance measurement from its surface. The success of EIT would be a revolutionary breakthrough, since it would make the diagnosis of neurological conditions of the brain possible in cases where the use of the traditional CT and MRI scanners is not feasible or affordable.

The conductivity of each tissue is influenced by its functions. For example, activity in the brain can change the regional blood volume and thus the conductivity of the involved region, since blood and brain have different electrical characteristics. This property and others can be exploited to deliver functional images of the brain and in particular of the epileptic foci.

Epilepsy can sometimes be treated with Neurosurgery: the part of the brain considered responsible for the epileptic onset is surgically removed. The aim of this work was to set a solid basis for using EIT as functional imaging technique for bedside monitoring of seizures in concurrence with EEG, during presurgical assessment. The background and engineering work to produce an optimised EIT system ready for clinical studies is presented. The first chapter provides an introduction to the impedance properties of the tissues of the head, to epilepsy and related conditions, how bioimpedance changes with these and to function and applications of EIT. The subsequent chapters address the problems in simultaneous recording of EIT and EEG; the definition of an optimal trial set-up and data analysis based on data previously collected at King's College Hospital, London; the size of the expected changes in the boundary voltages due to epileptic conductivity changes, based on a realistic FEM model of the head and literature review; the noise level of 3 EIT systems (UCH Mark1b, UCH Mark2.5 and KHU Mark1 16-channel system) to decide upon the most feasible for clinical trials; the design of a

16 channel protocol for the KHU Mk1 for brain imaging; and a final comparison between the UCH Mk2.5 and the KHU Mk1 in reconstructing impedance changes of the size of those expected in epilepsy in a head-shaped saline tank containing a real human skull.

1.2 Background

1.2.1 Introduction to bioimpedance

Bioimpedance represents the electrical properties of tissue measured when an external current (or voltage) is applied to it. Tissue can be characterised as a dielectric or an electrolytic, since it has features of both, and can be modelled in different ways, depending on the properties one wants to investigate. According to this, bioimpedance bulk and specific properties can be expressed in diverse, but related forms. The bulk properties can be expressed as impedance Z (Ohm, Ω), or admittance Y=1/Z (Siemens, S), while the specific properties as complex permittivity ε^* (Farad/m), or complex conductivity σ^* (S/m). A tissue's electrical property is strongly related to its physiological state and therefore its measurement can be used to monitor variations in its conditions, i.e. from normal to pathological.

1.2.1.1 Principle of bioimpedance

Bioimpedance depends on the measuring frequency and on the underlying histology of the tissue. Biomaterials are generally approximated as cells with an insulating membrane enclosing a highly conductive intracellular fluid (1 S/m), suspended in an extracellular fluid with similar properties (Grimnes and Martinsen 2000). Intra- and extra-cellular fluids are essentially *electrolytic* suspensions rich of ions free to migrate and therefore able to conduce ionic DC. The cell membrane, instead, mainly comprised by a double layer of polar lipids, which is the basis of the capacitive nature of cells and tissue, has a low intrinsic conductance of 10^{-6} S/m and capacitance of the order of 0.81-20 $\mu F/cm^2$ and typical thickness of 7-9 nm (Fricke 1925; Pethig 1987; Grimnes and Martinsen 2000).

Mostly because of this reason, tissue electrical properties have a dual nature. In the lower frequency range (< 1 MHz), the behaviour is predominantly *electrolytic*, being the extracellular space the primary conductor. At higher frequencies the capacitance of the tissue becomes relevant and its *dielectric* properties may dominate. In this case the current is not carried by free ions, but it is a result of local charge displacement and dipole polarization.

Such tissue composition can be modelled in a simple and intuitive way employing just four ideal (frequency independent and linear) electronic components (Figure 1-1). The extracellular space is represented as a resistor (Re), while the characteristics of the cells are summarized in a capacitor and resistor for the membrane (Cm, Rm) and a resistor for the intracellular space (Ri) (Holder 2005). At lower frequencies, almost all the current flows through the extracellular space only because the equivalent impedance of Rm and Cm is high in this range, so the total impedance is largely resistive and equivalent to Re. As the volume fraction of the extracellular space with respect to brain volume ranges between 5 to 20% (Lux et al. 1986), the resulting impedance is high respect to a situation in which the current is free to flow in the all brain. At higher frequencies, the current can cross the membrane capacitance, gaining access to the conductive ions of the intracellular space, causing the overall impedance to decrease.

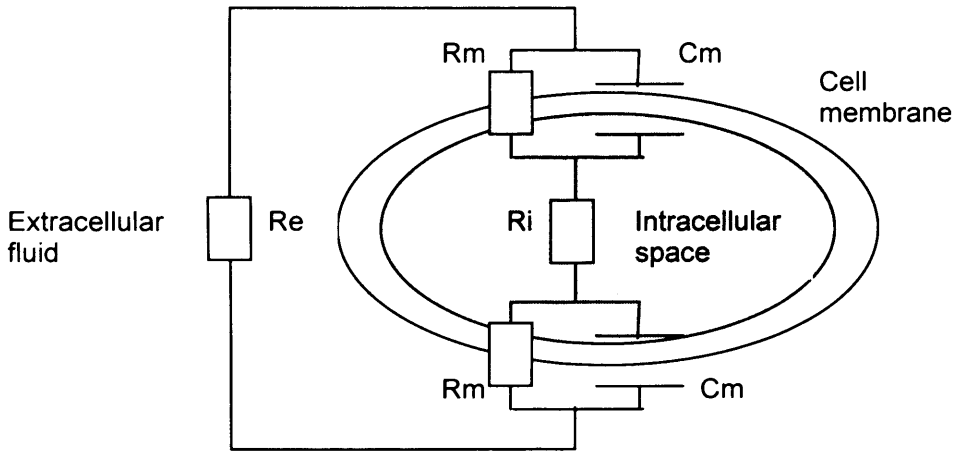

Figure 1-1 A simple electrical model of a living tissue. The electrolytic extra- and intra-cellular fluid are represented by two resistors (Re, Ri), while the characteristics of the insulating cell membranes are summarized in a capacitor and a resistor (Cm, Rm) (Rabbat 1990).

1.2.1.2 Dielectric AC polarization and relaxation

Biomaterials have dual nature of conductor and dielectric. Therefore according to the way in which they are considered, they may be described as non-ideal dielectrics or non-ideal conductors. A biomaterial behaves as a *non ideal dielectric* at high frequencies: the in-phase current is not null, but the capacitative current is more relevant (Grimnes and Martinsen 2000). In a dielectric, there are no free charges, only bound ions. These can only move (translate or rotate) locally under strong confinement. A typical example is the *dipole,* formed by two equal charges of opposite sign kept at a small distance. Under an external electric field, dipoles can

be oriented and bound charges displaced, *polarising* the tissue. The permittivity and then the capacitance of a tissue depend on the extent to which the tissue is polarized. The higher the polarization, the higher is the permittivity. However, polarisation and charge displacement do not occur instantaneously; for example, a dipole will take some time to rotate and align with the electric field and the process will be slower the larger the dipole and the more viscous is the medium. Therefore polarisation and permittivity will be maximal only if the measuring frequency will be low enough to allow all the charges to change their position and the dipole to change their orientation, otherwise, for higher frequency, polarisation and permittivity will decrease.

Polarization is characterised by its *relaxation time*, which depends on the underlying mechanism. This is the time in which a dielectric system reaches a new polarisation equilibrium after it has been disturbed with a step change of the electric field applied to it. The corresponding frequency domain concept of relaxation is the *dispersion.*

This can be modelled by the *Debye single dispersion equation* (1-1). In the simple case of a single dispersion there will be one frequency-independent permittivity level at low frequencies and a lower one at higher frequencies, divided by a transition zone.

$$\varepsilon^*(\omega) = \varepsilon'_\infty + \Delta\varepsilon' / (1 + j\omega\tau) \text{ where } \Delta\varepsilon' = \varepsilon'_s - \varepsilon'_\infty \qquad (1\text{-}1)$$

Where the apex refers to the *real* or *in-phase part* of ε^*, ε'_s is the *static* value of the permittivity (when the polarisation is maximal); ε'_∞ is the permittivity at high frequencies, when the charge displacement can not respond; ω is the angular frequency of the injected current (rad/sec), τ is the relaxation time and $j = \sqrt{-1}$. The transition is characterized by the *relaxation frequency or centre frequency* ω_c, corresponding to $\omega\tau = 1$, for which the real part of ε^* is at half of its transition and the imaginary part is at its maximum.

However, diverse relaxation mechanisms occur at different frequencies, and usually biological materials exhibit a combination of them, called *distribution of relaxation time* (Schwan 1957). The fastest one is called γ-dispersion and is the relaxation of permanent dipoles (MHz-GHz region), for example of proteins in water. Permanent dipoles experience a torque due to an applied electric field, which determines their orientation. In the region of the MHz there is the β-dispersion due to the Maxwell-Wagner effects (Fricke 1953). They deal with the polarization of interfaces in

inhomogeneous dielectric, due to bound or free charges, and with the membrane passive charging effect. At lower frequencies (Hz-kHz) the dispersion due to double layer formations in wet systems dominates and is called α-dispersion. These are areas of interface, usually between a solid and a liquid, where ions concentrate to exchange electrons, creating a 'molecular capacitor'. Later a δ-dispersion was added in the lower GHz range (Figure 1-2).

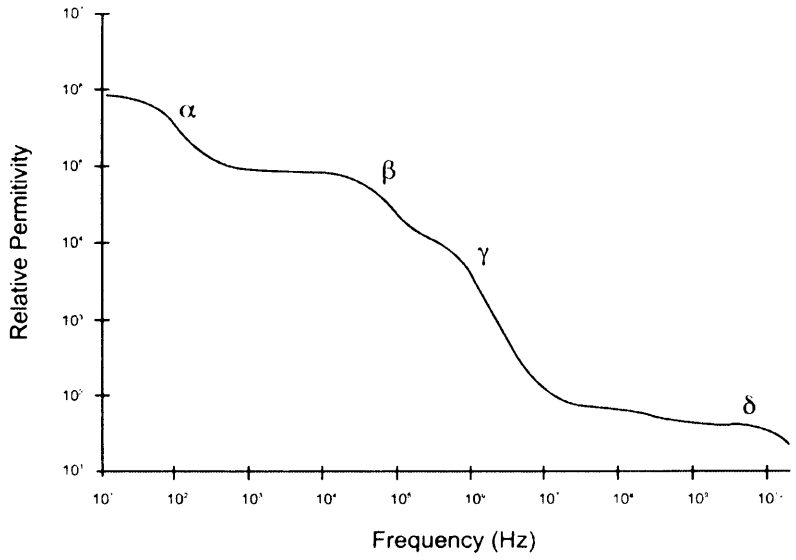

Figure 1-2 Distribution of relaxation time of the muscle (Hurt 1985).

The distribution of relaxation time can be modelled as a summation of more Debye dispersion with different central frequencies in addition to a conductivity term in which σ_s is the static ionic conductivity:

$$\varepsilon^*(\omega) = \varepsilon_\infty + \sum_n \frac{\Delta\varepsilon_n}{1+(j\omega\tau_n)} + \frac{\sigma_s}{j\omega\varepsilon_0} \tag{1-2}$$

In reality, the dispersion regions are usually broadened by several contributions to it, because of the complexity of both the structure and composition of biological material. An empirical version of the Debye model (Cole and Cole 1941) accounts for this by introducing a distribution parameter *a* and is known as the *Cole-Cole equation*:

$$\varepsilon^*(\omega) = \varepsilon_\infty + \frac{\Delta\varepsilon}{1+(j\omega\tau)^{1-a}} \tag{1-3}$$

The distribution of relaxation time may then be appropriately described replacing the Debye dispersion model in (1-2) with the Cole-Cole equation. The parameters are

chosen empirically in a way that the description will fit real measurements over the desired frequency range (Hurt 1985).

1.2.1.3 Different ways to describe bioimpedance

The *admittance* Y (considering sinusoidal AC) of a tissue sample, with non-ideal dielectric characteristics, of sectional area A and thickness d, is (Grimnes and Martinsen 2000):

$$Y = G + j\omega C = (A/d)(\sigma' + j\omega\varepsilon') \tag{1-4}$$

where G and C are the *conductance* and *capacitance* of the sample, ω the angular frequency and σ' and ε' $(=\varepsilon_0\varepsilon_r')$ the real part of the *conductivity* and of the *permittivity* of the tissue.

Two other ways to express the admittance are through complex conductivity $(\sigma^* \equiv \sigma' + j\sigma'')$ and complex permittivity $(\varepsilon^* \equiv \varepsilon' - j\varepsilon'' \equiv (\varepsilon'_r - j\varepsilon''_r)\varepsilon_0)$, depending if the material is considered as a conductor with some capacitive properties or as a capacitor with losses. Therefore Y can be also written as:

$$Y = (A/d)(\sigma' + j\omega\varepsilon') = j\omega C^* = j\omega(A/d)\varepsilon^* = j\omega(A/d)(\varepsilon' - j\varepsilon'') = (A/d)(\omega\varepsilon'' + j\omega\varepsilon') \tag{1-5}$$

Or

$$Y = (A/d)(\sigma' + j\omega\varepsilon') = G^* = (A/d)\sigma^* = (A/d)(\sigma' + j\sigma'') \tag{1-6}$$

It is clear that all the three forms give exactly the same information. Bioimpedance can also be written as *impedance*:

$$Z = \frac{1}{Y} = R + jX = \frac{d}{A}\rho^* \tag{1-7}$$

where R and X are the *resistance* and *reactance* of the sample. The complex *resistivity* is defined as:

$$\rho^* = \rho' - j\rho'' = 1/\sigma^* = (\sigma' - j\sigma'')/|\sigma^*|^2 \tag{1-8}$$

All the different quantities with their measurement units are summarized in Table 1-1 while relevant relationships within them are reported in Table 1-2.

Table 1-1 Quantities that characterise the bioimpedance.

Name	Symbol/Definition	Units
Conductance	G	Siemens (S)
Capacitance	C	Farad (F)
Admittance	$Y=G+j\omega C$	S
Permittivity of vacuum	$\varepsilon_0=8.85*10^{-12}$	F/m
Complex permittivity	$\varepsilon^*=\varepsilon'-j\,\varepsilon''$	F/m
Complex conductivity	$\sigma^*=\sigma'+j\,\sigma''=j\omega\varepsilon^*$	S/m
Resistance	R	Ω
Reactance	X	Ω
Impedance	$Z=R+jX$	Ω
Complex resistivity	$\rho^*=\rho'-j\,\rho''$	Ωm

Table 1-2 Relevant relationships within bioimpedance characterising quantities.

In-phase components	Out-of-phase components
$\sigma' = \omega\varepsilon'' = G(d/A)$	$\sigma'' = \omega\varepsilon' = \omega\, C(d/A)$
$\varepsilon' = \sigma''/\omega = C(d/A)$	$\varepsilon'' = \sigma'/\omega = (\,G\,/\omega)(d/A)$
$\rho' = \sigma'/\lvert\sigma^*\rvert^2$	$\rho'' = \sigma''/\lvert\sigma^*\rvert^2$

A useful way to display these complex quantities is the *Wessel diagram*. This represents in a complex plane the values of the in-phase and quadrature components of a chosen bioimpedance representation at different frequencies. In particular the Wessel diagram of the complex permittivity ε^* is called *Cole-Cole plot* (Holder 2005). Considering for example a simplified version of the model in Figure 1-1 (Figure 1-3a), the impedance locus in the Wessel diagram is a complete semicircle with the centre on the real axis (Figure 1-3b). At low frequencies no current crosses the cell membrane, therefore the impedance is only resistive and equivalent to Re. Increasing the applied frequency, the quadrature component of the impedance increases as more current passes through the cell membrane capacitance. At high frequencies, the membrane capacitance becomes negligible, so the impedance is again only resistive and equivalent to the parallel of Re and Ri. The frequency for which the quadrature component is maximal is the centre frequency ω_c.

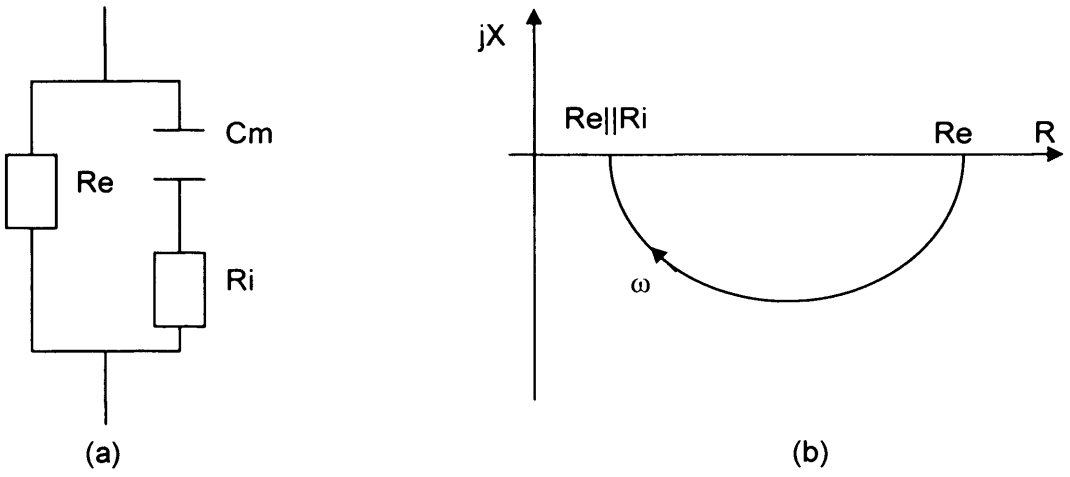

Figure 1-3 (a) Tissue model. Ri and Re are the resistance of the intra- and extra-cellular space, and Cm is the membrane capacitance. (b) Wessel diagram of this model, where ω is the angular frequency of the injected current (Grimnes and Martinsen 2000; Holder 2005).

1.2.1.4 Impedance measurement

Bioimpedance measurements are usually conducted *in-vitro* for practical reason. A constant alternating current I is injected in a sample of the tissue through a pair of electrodes and the resulting voltage V is measured with a differential amplifier through the same pair of electrode (bipolar measurement; Figure 1-4a) or through another pair (tetrapolar measurement; Figure 1-5a) (Holder 2005). The impedance is then calculated with Ohm's law:

$$Z = V/I \tag{1-9}$$

When the dimension of the sample is known, (this may be difficult *in-vivo),* it is possible to recover the specific property of the tissue, such as conductivity or permittivity.

Bipolar measurements are simpler, but the impedance reading will include the electrodes impedance Z_{el} in series with that of the tissue Z_{ti} (Figure 1-4b). The problem might be overcome performing a calibration before the experiment to determine the electrode impedance that should be subtracted from the overall recording. This technique is more likely to fail at lower frequencies where the electrode and tissue impedance are at similar level.

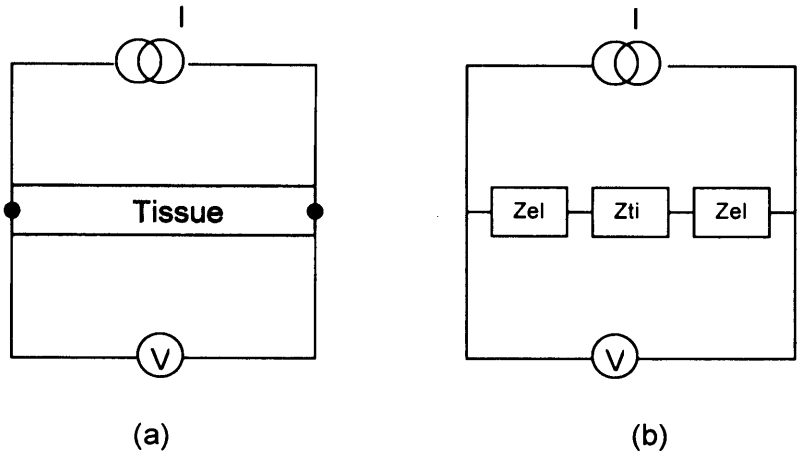

Figure 1-4 (a) Two-electrode (black dots) measurement set-up, with constant current *I* injection and voltage measurement *V*; (b) series of the tissue (Z_{ti}) and of the electrodes impedance (Z_{el}) in the electrical model, measured in biopolar mode (Holder 2005).

In tetrapolar measurements two electrodes are driven by an ideal constant current source, independent from the load, and the other two electrodes record the voltage with high input impedance differential amplifiers, so that all the current I flows through the tissue impedance Z_{ti} (Figure 1-5b). As a result, the impedance measurement is relatively insensitive to the electrode impedance Z_{el}.

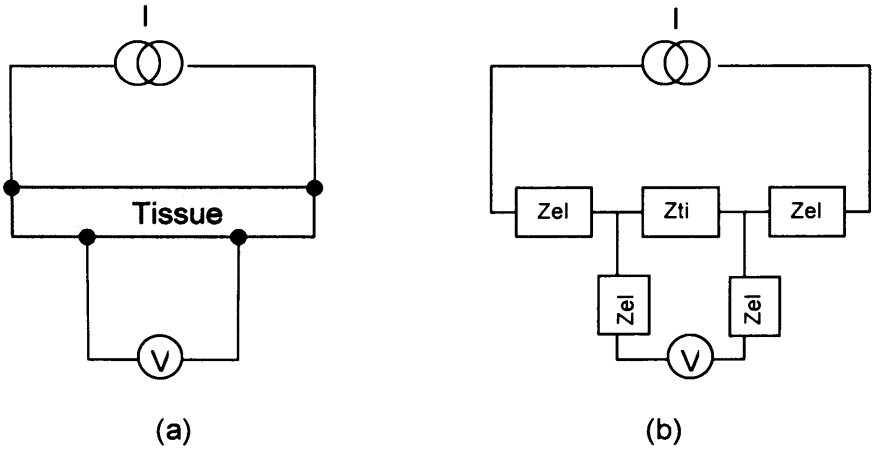

Figure 1-5 (a) Four-electrode measurement set-up (black dots), with constant current *I* injection and voltage measurement *V*; (b) tissue (Z_{ti}) and of the electrodes impedance (Z_{el}) in electrical model, measured in tetrapolar mode (Holder 2005).

1.2.1.5 Factors affecting tissue impedance

Bioimpedance is related to tissue composition, but it is also dependent on other factors not related to the tissue histology, such as: measurement frequency, temperature, measurement direction and whether the tissue is in situ or in vitro.

Frequency dependence (as explained above). The cell membranes have a high capacitance and a low conductivity, while the intra- and extra-cellular fluids are highly conductive. At DC and low frequencies current passes around the cells, and the cell interior does not contribute significantly to the current flow. At higher frequencies, the current can cross the membrane capacitance and so can employ the intracellular ions as well, which reduces the overall impedance.

Temperature dependence. The biological conductivity (σ') increases with the temperature because of the enhanced ions mobility. This increase is constant up to the GHz region and approximately corresponds to the one of a simple electrolyte (since most of the current is extracellular), of about +2%/°C (Foster et al. 1979). The quadrature ε' component has instead a smaller temperature coefficient of about -0.5%/°C (Grimnes and Martinsen 2000).

Anisotropy dependence. Tissue can be an anisotropic medium because of the orientation of cells, macromembranes and organs; therefore the impedance value depends on the direction in which the current crosses it. This property is evident in white matter, scalp muscle and skull. For example, in muscle the impedance measured transversely is 10 times as large as that measured longitudinally (Grimnes and Martinsen 2000). Such anisotropy is a low-frequency phenomenon if it is due to membranes and it depends on the section of extracellular fluid the current has available to travel.

In situ or in vitro dependence. Tissue metabolism decreases after it has been excised or removed from its natural physiological surrounding and perfusion, affecting the impedance measurement. The temperature can drop and if the tissue is not supported, irreversible changes will occur, followed by cell and tissue death (in brain tissue within 5 minutes at 37°C). Without blood the metabolism proceeds, but anaerobically, causing ionic unbalance and osmosis. This causes cell swelling and therefore a narrowing of the extracellular space which typically gives an increase in the low frequency impedance. For example, most of the α-dispersion disappeared after a few hours after excision of haddock muscle (Martinsen et al. 2000). The low-frequency resistance of the β-dispersion increased initially for 5 hours, and then decreased as cells deconstructed.

1.2.2 Overview of Electrical Impedance Tomography

Electrical Impedance Tomography (EIT) is an imaging technique that uses the difference in the bioimpedance of the tissues of the body to generate a tomographic

image of its passive electrical properties (Barber and Brown 1989). In medicine it could be used with a structural connotation, like CT or MRI, by reconstructing maps of the bioimpedance or with a functional connotation, like PET or fMRI, by reconstructing bioimpedance changes related to the structure activity. The advantages of such a method over its counterparts are that it is less expensive, portable, non-invasive and suitable for long term monitoring. On the other hand it is limited by a poor spatial resolution, which depends on the ability to model current paths accurately and is proportional to the number of independent impedance measurements that can be taken for one image (Seagar et al. 1987; Seagar and Brown 1987). These depend on the number of electrodes applied to the body, which is clearly limited, but are also constrained by dynamic range of the recording system and the computational complications in processing large amount of data. Because of this most of EIT systems include 16-32 electrodes which results in a resolution of about 12% of the image diameter (Sinton et al. 1992).

1.2.2.1 Imaging principle

EIT attempts to produce an internal conductivity map of the body from electrical measurements made at its surface. Every image data set is usually obtained by a series of many tetrapolar impedance measurements v (section 1.2.1.4) sampled at the boundary of the object. Each of those is related to the internal conductivity (σ) by a non-linear forward transformation (A) as (Holder 2005):

$$v = A(\sigma) \tag{1-10}$$

which can be seen as a system of equations $\mathbf{A}(\sigma)$ when a vector of external measurements $\mathbf{v}$ is considered:

$$\mathbf{v} = \mathbf{A}(\sigma) \tag{1-11}$$

Finding the solution to (1-11) leads to *structural or 'absolute' images*, which take into account the non-linearity of the relation and show the absolute conductivity distribution (Brown et al. 1985). Unfortunately this approach is very susceptible to measurement noise and requires an accurate knowledge of the geometry of the object and of the electrodes.

A linearized approximation of (1-11) which links small changes in conductivity to small changes in external measurements leads instead to *functional or 'differential' images*, which represent the changes in conductivity between a reference

distribution and a perturbed one. This approach is more robust since errors in the geometry and measurement noise are similar in the two conditions and therefore are reduced when the latter is referred to the former (Brown et al. 1985).

1.2.2.2 Image reconstruction

The nature of (1-10) is understood considering the body as an ohmic conductor and the interaction between current, electric field, potential field and conductivity in it. In this section bold letters will represent vectors or matrices.

When a current **I** is injected into the body a *scalar potential field* ϕ is generated. The gradient of this field is the opposite of the *electric field* $\mathbf{E} = -\nabla\phi$ and is related to the density of the injected current **J** by the conductivity σ:

$$\mathbf{J} = \sigma\mathbf{E} = -\sigma\nabla\phi \tag{1-12}$$

which is the continuum Ohm's law. In absence of current sources inside the body, there is no net flux of charge out of the boundary, which means that the divergence of the current density is null:

$$\nabla\cdot(\sigma\nabla\phi) = 0 \tag{1-13}$$

which is the continuum Kirchoff's law. Its expansion leads to the Poisson's equation:

$$\nabla^2\phi = -\frac{\nabla\sigma\cdot\nabla\phi}{\sigma} \tag{1-14}$$

The solution of this non-linear equation for a given distribution of σ is known as the *forward problem* (Metherall 1998) and provides the distribution of ϕ throughout the domain. This depends on the conductivity distribution, the shape of the object, the current injected and the position of the electrodes. An analytical solution of (1-14) is only possible for simple geometries, therefore, usually, numerical solutions such as Finite Element Modelling are adopted. The object is divided into a number of discrete elements of uniform conductivity and the forward problem is solved for each of them, ensuring continuity of voltage and current.

The solution of the forward problem is the first necessary step for image reconstruction of bioimpedance. When performing EIT we only have a limited knowledge of the potential distribution ϕ inside the body, because we can only measure the voltages at the surface *v* (1-10). These are usually called *boundary*

voltages because they are measured by the EIT systems on the boundary of the body under investigation and should not be confused with voltage at the boundary of the conditions. Therefore iterative algorithms, for example, repeatedly solve the forward problem as the conductivity distribution is modified at each iteration until the boundary voltages picked from the computed ϕ converge with those observed. Solution of the forward problem is also required for the computation of the transformation *A* called the *sensitivity relationship* in (1-10). This describes the link between the measured boundary voltages *v* and the conductivity distribution σ, and is based on the *reciprocity theorem* (Figure 1-6):

$$v = \Phi_{ab} = \Psi_{cd} = \int_{\Omega} \sigma \nabla\Phi \cdot \nabla\Psi d\Omega \qquad (1\text{-}15)$$

where Φ is the scalar potential field ϕ generated injecting a unitary current *I* though the electrodes c-d into the body Ω and Ψ is the scalar potential field ϕ generated injecting a unitary current though the electrodes a-b. The subscript *ab* and *cd* indicate that the fields have been sampled on the surface between these electrodes. Equation (1-15) means that if we inject a unitary current through a-b the measured voltage *v* between c-d is the same as that measured between a-b injecting unitary current through c-d.

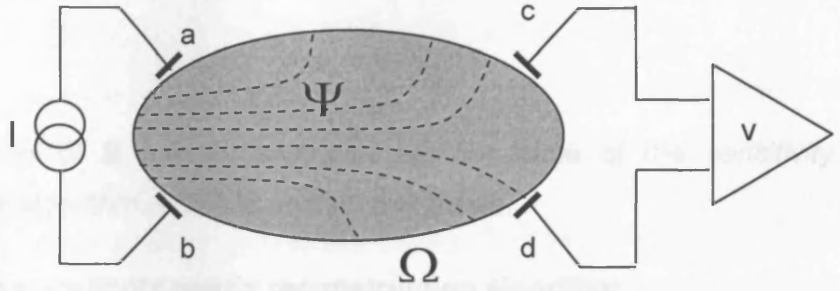

Figure 1-6 Unitary current *I* is driven into Ω through electrodes a-b, generating a potential field Ψ. This is sampled on the surface through c-d and is equal to the boundary voltage *v*, which would be measured if injecting *I* from c-d and measuring voltage from a-b. The conductivity of Ω is σ (Metherall 1998).

(1-15) is a non-linear relationship as Φ and Ψ are function of σ and correspond with the transformation *A* of (1-10). However this relationship can be linearized when considering small variation in the conductivity distribution $\Delta\sigma$:

$$\Delta v = S\Delta\sigma \qquad (1\text{-}16)$$

Where S is the *linearized sensitivity relationship* and Δv is the boundary voltage change resulting from the conductivity variation. Hereinafter the symbol Δ will be substituted with subscript p (perturbation) for ease of reading, and the initial condition will be indicated with the subscript *in*.

If we split Ω into discrete elements of uniform conductivity, (1-16) becomes a set of linear equations:

$$\mathbf{v_p} = \mathbf{S}\mathbf{c_p} \tag{1-17}$$

Where $\mathbf{v_p}$ is the vector of the changes in the boundary voltages, $\mathbf{c_p}$ the *discretized conductivity vector* and **S** the *linearized sensitivity matrix*, whose elements are:

$$S_{ij} = -\int_{j^{th}element} \nabla\Phi_{in} \cdot \nabla\Psi_{in} d\Omega \tag{1-18}$$

Where i refers to the i^{th} tetrapolar electrode combination and j to the j^{th} element and the integration is only on the volume of the element. S_{ij} represents the influence of a variation of the conductivity of the element j on the measurement of the i electrode combination. This means that in each row of **S** there is the contribution of a variation in each element to a certain tetrapolar measure.

In the linear limit $\mathbf{c_p}$ can be recovered inverting the sensitivity matrix:

$$\mathbf{c_p} = \mathbf{S}^{-1}\mathbf{v_p} \tag{1-19}$$

The formulation of **S** and its inversion are the base of the *sensitivity matrix reconstruction algorithm*, which is used in this thesis.

1.2.2.2.1 The sensitivity matrix reconstruction algorithm

$\nabla\Phi_{in}$ and $\nabla\Psi_{in}$ in (1-18) are obviously not known, so they have to be somehow calculated in order to build the linearized sensitivity matrix **S**. This is done solving the forward problem for a *model* of the body under examination for each drive and receive pair included in the measuring protocol in order to provide an estimation of the potential fields Φ_{in} and Ψ_{in}. For complex geometries this is usually a Finite Element Model, which includes a mesh and a *guess* of the conductivity distribution σ of the object. In practice this is a vector of discrete conductivity values $\mathbf{c}_{in}$ assigned to the elements of the mesh and is educated by studies which invasively measured the bioimpedance of the tissues. The closer is the model to the real object in terms

of geometry and conductivity distribution, the closer $\nabla\Phi_{in}$ and $\nabla\Psi_{in}$ will be to their real value. The computation of **S** is therefore performed in 3 steps (Metherall 1998):

1. *Mesh definition.* The object is split into discrete elements (triangles in 2D, tetrahedra in 3D), whose vertexes are called nodes. The sensitivity is larger near the electrodes, because of the higher current density. For this reason the central sensitivity coefficients S_{ij} are smaller than the peripheral. To compensate for this the central elements of the mesh are larger, as increasing their size tends to increase their corresponding sensitivity. The electrodes are then placed on the surface of the mesh in the required positions and the guessed conductivity values assigned to each element.
2. *Voltage gradient calculation.* In order to calculate $\nabla\Phi_{in}$ and $\nabla\Psi_{in}$ the potential fields Φ_{in} and Ψ_{in} generated by a unitary current injected in all the drive-receive pairs have to be calculated in all the nodes of the mesh. This means to solve the forward problem for each drive-receive pair. $\nabla\Phi_{in}$ and $\nabla\Psi_{in}$ are then calculated using the nodal voltages and finding the constant gradient within each element.
3. *Construction of the sensitivity matrix.* Each element defined in (1-18) is calculated evaluating the scalar product of the elemental voltage gradients. Since those are constant in each elements they can be taken out of the integral, which then becomes the volume of the j^{th} element.

Unfortunately to have good image reconstruction the sensitivity matrix must be calculated with exactly the same geometry as the body under inspection, and for example a small electrode misplacement in the model can lead to large error in the reconstructed image (Barber and Brown 1988). This may be feasible in industrial application with rigid geometries, but it is difficult to achieve on the human body. Nevertheless the influence of the deviation from the expected geometry on the reconstruction can be reduced with *normalizing* equation (1-17) by the boundary voltages measured before the conductivity perturbation occurs. In this way the errors are reduced since they are similar in the 2 conditions. The data used to reconstruct are then the normalized perturbed voltages $\mathbf{v}_n$:

$$\mathbf{v}_n = \left[\frac{\mathbf{v}_p^1}{\mathbf{v}_{in}^1} \quad \frac{\mathbf{v}_p^2}{\mathbf{v}_{in}^2} \quad \cdots \quad \frac{\mathbf{v}_p^m}{\mathbf{v}_{in}^m} \right] = \frac{\mathbf{v}_p}{\mathbf{v}_{in}} \tag{1-20}$$

Where $\mathbf{v}_{in}$ can be:

1. derived solving the forward problem for each driven pair and taking the difference between electrodes which constitute a measuring pair;
2. calculated using the sensitivity matrix considering that each boundary voltage is:

$$v_{in} = \int_{\Omega} c_{in} \nabla \Phi_{in} \cdot \nabla \Psi_{in} d\Omega \tag{1-21}$$

   Where the integration is over the entire volume Ω, and therefore corresponds to the row summation of the sensitivity matrix multiplied by the discrete conductivity vector initial guess $\mathbf{c}_{in}$;
3. measured rather than calculated.

Combining (1-20) and (1-21), $\mathbf{v_n}$ can be rewritten as:

$$\mathbf{v}_n = \mathbf{G}^{-1}\mathbf{v}_p \tag{1-22}$$

Where **G** is a diagonal matrix with:

$$G_{ii} = \int_{\Omega} c_{in} \nabla \Phi_{in} \cdot \nabla \Psi_{in} d\Omega \tag{1-23}$$

and *i* refers to a particular drive-receive combination, which generates the voltage distributions Φ_{in} and Ψ_{in}.

c_{in} can be taken out from the integral so that:

$$\mathbf{v}_n = \frac{\mathbf{G}^{-1}\mathbf{v}_p}{\mathbf{C}_{in}} \tag{1-24}$$

Where **G** and $\mathbf{C_{in}}$ are diagonal matrices whose non-zero elements are:

$$\begin{aligned} G_{ii} &= \int_{\Omega} \nabla \Phi_{in} \cdot \nabla \Psi_{in} d\Omega \\ C_{ii} &= \begin{bmatrix} c_{in}^1 & c_{in}^2 & \cdots & c_{in}^n \end{bmatrix} \end{aligned} \tag{1-25}$$

Where $\mathbf{c_{in}} = \begin{bmatrix} c_{in}^1 & c_{in}^2 & \cdots & c_{in}^n \end{bmatrix}$ are the initial conductivities of each voxel.

Considering (1-17):

$$\mathbf{v}_n = \frac{\mathbf{G}^{-1}\mathbf{S}\mathbf{c}_p}{\mathbf{c}_{in}} = \mathbf{F}\mathbf{c}_n \tag{1-26}$$

Where $\mathbf{F} = \mathbf{G}^{-1}\mathbf{S}$ and $\mathbf{c_n} = \mathbf{c_p}/\mathbf{c_{in}}$, describing the relationship between normalized changes in the boundary voltages and normalized changes in conductivity. This is called *row normalization* as the elements of **G** are the integrals of the row of **S**.

F has then to be inverted to find $\mathbf{c_n}$, according to (1-19). Consider a system of linear equation similar to (1-17):

$$\mathbf{A}\mathbf{x} = \mathbf{b} \tag{1-27}$$

where **x** is the vector of *n* unknown, **b** the vector of *m* data and **A** the linear transformation which maps one into the other (Metherall 1998). If **A** is *well-conditioned* then there exists a unique vector **x** which is solution to (1-27) in the least square sense and thus minimize:

$$\|\mathbf{b} - \mathbf{A}\mathbf{x}\|^2 \tag{1-28}$$

and **A** can be inverted. If **A** is instead *ill-conditioned*, as are **S** and **F**, then there will be infinitely many vector **x** which nearly minimize (1-28), as large variation in **x** will only cause small variation in **b**. This means that large conductivity changes in some part of the object can cause very small changes in the boundary voltages, which seen in the other way implies that measurement noise at the boundary translates in large artefacts in the image in those parts when multiplied by the inverse of **F**. To avoid this problem **F** has to be *regularized* to obtain a stable inversion. This can be achieved with the *Singular Value Decomposition* (SVD) method. The SVD provides a pseudo inversion of **F** to find the unique solution $\mathbf{c_n}$ that minimizes $\|\mathbf{v_n} - \mathbf{F}\mathbf{c_n}\|^2$. To obtain it, **F** is firstly decomposed as:

$$\mathbf{F} = \mathbf{U}\mathbf{W}\mathbf{V}^T \tag{1-29}$$

Where **U** and **V** are orthogonal matrices and **W** is a diagonal matrix whose elements w_{ii} are the *singular values* (SV), arranged in order of decreasing magnitude and whose meaning will be clear later. The inverse of an orthogonal matrix is its transpose and that of a diagonal matrix is simply another diagonal matrix whose diagonal elements are $(1/ w_{ii})$ so that:

$$\mathbf{F}^\dagger = \mathbf{V}\mathbf{W}^{-1}\mathbf{U}^T \tag{1-30}$$

And therefore:

$$\mathbf{c}_n = \mathbf{F}^{\dagger}\mathbf{v}_n \tag{1-31}$$

The meaning of (1-29), (1-30) and (1-31) and the need to regularize **F** is clarified considering the *spectral expansion* of the solution $\mathbf{c}_n$ (Zadehkoochak et al. 1990; Zadehkoochak et al. 1991; Meeson et al. 1995). This can be regarded as a decomposition of $\mathbf{c}_n$ in *m* orthogonal *basis images* ($\mathbf{x}_1,\ldots,\mathbf{x}_m$), where *m* is the number of independent measurements:

$$\mathbf{c}_n = \sum_{i=1}^{m} a_i \mathbf{x}_i = \mathbf{XA} \tag{1-32}$$

Where **X** is a matrix whose columns are the basis images $\mathbf{x}_i$ and **A** is the diagonal matrix of the associated coefficients a_i, which are derived from the measured data and are characterized by an uncertainty due to the data noise. In this respect, the SVs are an index of how well the basis image amplitudes a_i are defined by the data. The concept can be simplified considering $\mathbf{c}_n$ as a point in space, the basis images as the Cartesian axis x y and z and the coefficient a_1, a_2 and a_3 as the coordinates of $\mathbf{c}_n$, defined by the data $\mathbf{v}_n$ (Figure 1-7).

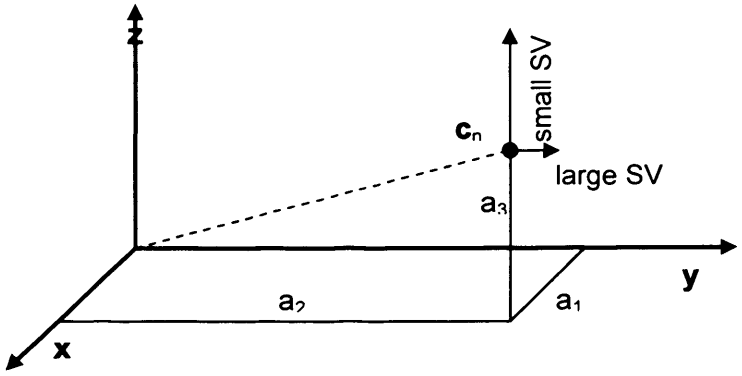

Figure 1-7 Concept of the basis images expressed as space coordinates. Refer to the text for details.

In this case if the SV associated with for example a_2 is large, then the y component of $\mathbf{c}_n$ will not be influenced by the noise. On the other hand if the SV associated to a_3 is small, than a small variation in the data will cause a large swing of $\mathbf{c}_n$ in the z direction.

Comparing (1-32) with (1-30) and (1-31) **V** defines the basis images and correspond to **X**, while **U** describes how boundary voltages are combined to produce the coefficient matrix **A** which is then $\mathbf{W}^{-1}\mathbf{U}^{T}\mathbf{v}_n$. It is clear that the smallest singular values when inverted will amplify the coefficient for the corresponding basis images,

whose amplitudes are not well defined by the data. For this reason a regularization filter has to be applied. In the case of the *truncated SVD* (*tSVD*) regularization, this simply consists of setting to 0 all the singular values below a predetermined threshold, excluding the influence of their basis images. This operation increases the signal-to-noise ratio in the image, but reduces the resolution especially towards the centre of the image. This is because the basis images best defined by the data have predominant features where the current density is more intense, meaning higher sensitivity, therefore near the electrodes. As a result the regularization filter has to be chosen as a trade off between signal-to-noise ratio and resolution.

1.2.2.3 Instrumentation

The aim of any EIT system is to provide the broadest and most accurate set of impedance measurements to feed into the reconstruction algorithm, in the shortest amount of time. In the most simple form each of this measurement is usually carried out with a constant current source and a voltmeter attached to the subject through EEG or ECG-type electrodes in a tetrapolar fashion (Figure 1-5; Figure 1-6) (Boone and Holder 1996). Some systems use instead constant voltage sources or two-terminal measurement, in particular when the recording frequencies are so high that the electrode impedance is negligible (Halter et al. 2004; Saulnier et al. 2006).

The tretrapolar configuration is commonly chosen because errors due to the unknown electrode-skin interface are reduced (section 1.2.1.4). With an ideal constant current source, the injected boundary current is essentially independent from the body's transfer impedance and the high contact impedance. In the same way if the voltage amplifiers have good input impedance, the potential measurement will be fundamentally unaffected by these factors.

Nevertheless, even with this arrangement, hardware design has to take into account of special problems produced by the electrode-skin interface and stray capacitances, which are unwanted capacitance to ground or between channels caused by the use of cables and multiplexers (McEwan et al. 2007). In reality, the current source has a finite output impedance (R_0, C_0), which will divide the current output of I_s by an amount that depends on the ratio of $R_0//C_0$ to the unknown contact impedance of the drive electrodes $R_{ed}//C_{ed}$ (Figure 1-8). The situation worsens for higher frequency because the stray capacitance adds in parallel to C_0, shunting the current source output impedance. In this condition the current becomes load dependent. Moreover the current source has to be balanced as any injected offset

current that flows to ground through a finite impedance will cause a common-mode voltage at the measuring side.

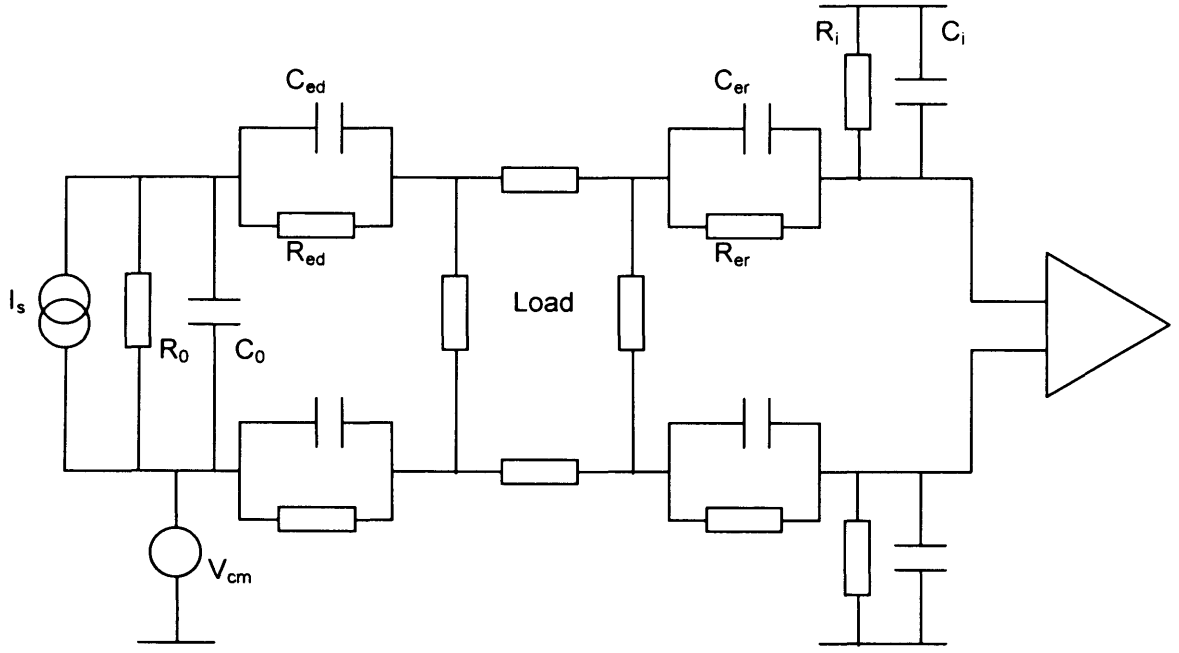

Figure 1-8 Equivalent circuit of the EIT measurement (Boone and Holder 1996).

The instrumentation amplifier has also a finite input impedance (R_i, C_i), which will create a voltage divider between $R_i//C_i$ and the contact impedance ($R_{er}//C_{er}$), whose effect will worsen at higher frequencies too. A low input impedance sinks the current through the amplifier, which would cause a common-mode to differential-mode conversion in case of unbalanced contact impedances.

Measurement errors are mostly due to system-based phase delays and stray capacitance and influence the component in quadrature with the applied current. Therefore most EIT systems apply a synchronous demodulation, which reduces the system-based delays, and recover only the resistive part of the impedance, corresponding to the voltage in phase with the injected current (Fitzgerald et al. 2002). This technique is based on the assumption that the reactive component at the applied frequencies is a small proportion of the total impedance. Besides the measured differential voltages have a large dynamic range, depending on the used electrode combination at a time, therefore adjustable gain and automatic gain control systems are preferable to take advantage of the full voltage range of the amplifier and of the full scale of the following analog-to-digital converter (ADC).

EIT systems can be classified according to the protocol used to collect voltage measurement in: serial, semi-parallel and, in a lesser extent, fully-parallel (Frangi et al. 2002). These arise from a trade-off between speed and complexity. In the serial

systems current is injected serially through user-defined electrode pairs (Figure 1-9). For each of these, the voltages between other user-defined pairs are recorded serially by time-multiplexing a unique differential amplifier and ADC. These systems are more practical, flexible and easier to build, but use multiplexers, which introduce parasitic capacitance, and have a lower frame rate.

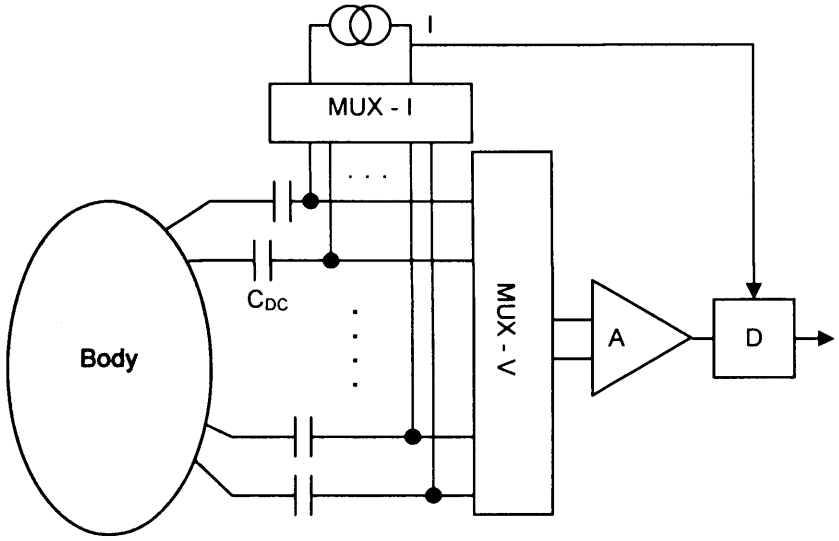

Figure 1-9 Serial acquisition system diagram modified from (Frangi et al. 2002). A single 4-terminal impedance measurement circuit is time multiplexed between user-defined electrode combinations. Usually current injection and voltage measurement are multiplexed with the same switch, here they are presented separated for clarity (MUX-I and MUX-V). Each electrodes is provided with a DC blocking capacitor C_{DC} and the voltage is measured with an amplifier A and then demodulated (D) using the injected current I as reference.

The semi-parallel approach (Oh et al. 2007) allows faster acquisition as the current is driven in the same way as in the serial systems, but simultaneous recording are performed with a differential amplifier for each electrode pair (Figure 1-10). On the other hand this poses a limit in the design of the measurement pattern, since the recording couples are hardwired together and are not arbitrarily addressable. This approach is also more technically demanding since it requires extensive calibration and accurate symmetry of the recording channels. Fully-parallel systems instead employ also multiple current sources.

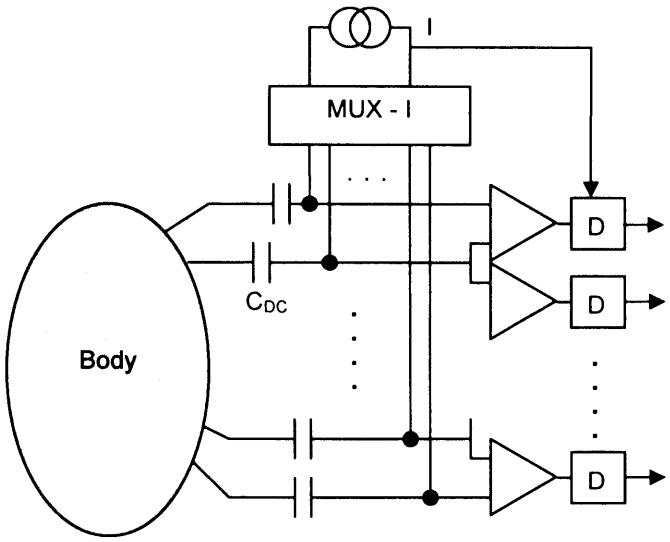

Figure 1-10 Semi-parallel acquisition system diagram modified from (Frangi et al. 2002). The current is still injected serially, but the acquisition is performed simultaneously between usually adjacent pairs.

Some MFEIT systems reduce the measurement time by measuring at more than one frequency at a time. For example, the signal used in the UCH Mk2.5 is a summation of sine waves at 10 frequencies (McEwan et al. 2006). Unfortunately the peak amplitude of the composite signal is 3-4 times greater than that of each frequency, and since this is restricted by safety limit and neurons excitation, the amplitude is reduced for each component (McEwan et al. 2007). In the same way the dynamic range of the current source and of the measuring amplifier has to be shared between all the used frequencies. Lastly, Negative Impedance Converters and General Impedance Converters, used to reduce stray capacitance, can not be easily employed with composite waveforms.

1.2.2.4 Biomedical application of EIT

1.2.2.4.1 Gastrointestinal function

EIT has been shown to be successful in measuring gastric function, mostly because of the lack of highly resistive bones between the electrodes and the region of interest and of the presence of large movements of conducting fluids within the stomach. Moreover the poor spatial resolution of EIT and inaccuracy in absolute impedance measurement are not relevant since the quantity of interest is the timing of activity. A significant linear correlation was found in measuring the time of half gastric emptying with that measured with radioisotope scintigraphy or dye dilution with acid suppression, and it was usually possible to identify a region of decreased impedance in the image (Mangnall et al. 1987). This test could be used to diagnose

pyloric stenosis (Lamont et al. 1988), but it was not accurate in measuring quantitatively the gastric volume (Nour et al. 1995) or the half time without acid suppression (Giouvanoudi et al. 2003). EIT has been also somewhat successful in measuring gastric motility, such as gastric contraction (Smallwood et al. 1994) and could also be used to monitor acid production for screening gastrinomas or achlorhydria (Baxter et al. 1988). EIT has the advantage of being non-invasive compared to the traditional tests which involve for example use of radiation, gastric intubation or blood sampling, and are therefore not suitable for paediatric use or long term monitoring.

1.2.2.4.2 Pulmonary function

Air has far larger resistivity than the pulmonary tissue: inhalation is therefore expected to be detected by EIT as an increase in lung impedance. However measurements are impaired by the presence of the ribs and of the movement of the ribcage and thoracic tissues during respiration, which may corrupt the image. Nevertheless early validation studies have shown that overall ventilation can be measured with EIT in concurrence with the respiratory inductance plethysmograph during normal breathing (Harris et al. 1988), and that the resolution was sufficient to image differences in ventilation between the right and left lung with breath holding at specific intervals using fully deflated lungs as reference (Harris et al. 1987). Therefore EIT was suggested as a non-invasive bedside technique to monitor ventilation changes during procedures as pleura aspiration or drainage of pneumothorax, or as a tool for detecting lung abnormalities. More recently EIT has been shown to be able to detect local changes in pulmonary air content (Frerichs et al. 2002), which together with fastest acquisition speed suggests the use of EIT in defining adequate lung-protective strategies in artificial ventilation (Frerichs et al. 2003). The increase of impedance in certain parts of the lungs would mean that the corresponding alveoli have been open, indicating the right pressure for their recruitment (Kunst et al. 1999). Differences in the impedance across frequency between neonatal and adult lungs can also be exploited as method to track developmental changes in the lung (Smallwood et al. 1999).

1.2.2.4.3 Cardiac function

The impedance of the blood is lower than that of other intrathoracic tissues, it therefore seems possible to image blood movement related to cardiac function with EIT. On the other hand the small dimensions of the heart compartments and proximity make it difficult to distinguish them for this low resolution method. Beside,

as in lung imaging, problems related to movement of the chest and thoracic tissues are present and affect the images. Impedance data is synchronized with the ECG; this permits averaging with respect to the cardiac cycles and separation of cardiac from the respiratory changes. In this way, it is possible to observe movement of blood from the ventricles to the lungs and back to the atria as impedance changes of 0.8-2.7% (Eyuboglu et al. 1987; Eyuboglu et al. 1989). However the spatial resolution, although improved with optimal electrodes placement (Vonk Noordegraaf A. et al. 1996), is not good enough to allow quantitative measurement of the cardiac stroke volume (Vonk-Noordegraaf et al. 2000). Even so EIT may be used in a more qualitative way to monitor non-invasively right ventricular diastolic functions in patients with chronic obstructive pulmonary disease (Vonk Noordegraaf A. et al. 1997) or lung perfusion for diagnosis of pulmonary embolism (McArdle et al. 1988) and pathological changes of the vascular bed (Vonk Noordegraaf A. et al. 1998; Smit et al. 2004).

1.2.2.4.4 Breast cancer screening

Cancerous tissue has lower impedance than normal breast tissue which includes fat and connective tissue (Jossinet 1996). Breast impedance can be measured between a flat array of electrodes, which presses the breast against the rib cage, and a common electrode usually held in the hand and displayed as relative impedance as sensed across the array in the corresponding positions. This technique gave better results than other diagnostic techniques in an early study (Piperno et al. 1990), and later on showed good specifity and sensitivity in a series of clinical studies (Malich et al. 2000; Martin et al. 2002), and the potential of distinguishing between malignant and benign abnormalities with improved data analysis algorithms (Glickman et al. 2002). Another way of monitoring breast impedance is with more complicated tomographic systems, which use sets of electrodes surrounding the breast, and request the solving of the forward and inverse problem. This technique showed the potential of discriminating abnormalities in the permittivity images, but no clinical studies worked yet (Osterman et al. 2000).

1.2.2.4.5 Other applications

There are other medical applications of EIT, which for one reason or another have been abandoned.

The resistivity of ionic solution linearly decreases with temperature increase by 2% per °C (Griffiths and Ahmed 1987). For this reason EIT could be adopted to monitor

the heating of tumours treated with microwave or laser, which have to reach temperature of about 43° without damaging the surrounding normal tissue. Unfortunately boundary voltages may vary as for temperature changes of few degrees without warming. For these reasons it seems unlikely that EIT could be an accurate technique for temperature monitoring.

EIT could also be used to image pooling and congestion of blood in the female pelvis by placing the subject in horizontal and vertical position, with the idea that this would cause fluid shifts in the pelvis. A significant difference in the peak impedance changes but not in the mean amplitude was observed with this method (Thomas et al. 1991).

1.2.3 EIT of brain function

The impedance of the brain in its normal state and during epilepsy and related conditions are treated separately and looked at more extensively in this thesis. In this section, only impedance changes due to normal activity, stroke and neuronal depolarization are considered.

1.2.3.1 Summary of impedance of the head

The brain is composed of grey and white matter and floats in the cerebrospinal fluid (CSF) inside the skull, which is covered by the scalp, a layer of muscle and connective tissue just below the skin. Each of these tissues has a different impedance which generally decreases with frequency increase because of the presence of the capacitive and highly resistive membrane of cells, through which current flows at high frequencies. The conductivity values presented below have been estimated as discussed in Chapter 4. When current is injected for EIT measurements, the first tissue it passes through after the skin is the scalp, which can be approximated as a layer of flat muscle as the highly resistive stratum corneum of the skin is largely removed by abrasion during EIT recordings. Its conductivity may be estimated as 0.235 S/m at 5 Hz rising to 0.653 S/m at 4MHz (Gabriel et al. 1996a). Below the scalp, there is the highly resistive barrier of the skull. This is a flat bone constituted by a layer of marrow sandwiched between 2 layers of cortical bone. If approximated as homogeneous, its conductivity is about 0.04 S/m and almost frequency independent (Kosterich et al. 1983; Sierpowska et al. 2003; Sierpowska et al. 2005). The CSF is a ionic solution with high, frequency-independent, conductivity of 1.8 S/m (Baumann et al. 1997). The grey and white matter have similar conductivity with the grey matter slightly more resistive than the

white at 5 Hz (0.18 and 0.24 S/m respectively), but less at 4 MHz (0.39 and 0.36 S/m respectively) (Ranck, Jr. 1963b; Ranck, Jr. and BEMENT 1965; Gabriel et al. 1996a; Latikka et al. 2001). It is clear that the proportion of current which reaches the brain when injected from scalp electrodes is low as it may be shunted through the scalp which has a lower resistivity than the skull and before reaching the brain it may be shunted also through the CSF. Finally, the other tissue which plays an important role in EIT of brain functions is the blood. This is composed of plasma and cells and its conductivity depends on its haematocrit, which is the ratio between these two components. Its conductivity is about 0.7 S/m up to about 100 kHz and mostly frequency-independent (Zhao et al. 1993), while for higher frequencies it may increase up to 1 S/m (Jaspard et al. 2003) and is therefore less resistive than the brain tissue.

1.2.3.2 Impedance properties of the brain

Simply stated, because of the highly resistive membrane of the neurons, current at relatively low frequencies travels in the brain through the very conductive extracellular fluid, blood volume and the bulky glial cells, which are permeable to potassium and chloride ions. For this reason impedance changes on the macroscopic scale are measured when the membrane of the neurons or the relative volume of the brain compartments alter their characteristics.

In ischemic stroke, the blockage of arteries leads to a reduced blood supply to the affected brain region. The neurons of this area outrun their energy and a substantial movement of sodium and water inside the cells follows as they are incapable of maintaining the ionic homeostasis. As a result, the neurons swell, decreasing the extracellular space and therefore increasing the impedance of, for example, 15-60% at 50kHz in rats (Holder 1992a).

During physiological stimulation and functional brain activity, blood volume and flow alter, peaking at 5-6 seconds after stimulation onset and decaying to baseline within 6 seconds of stimulus cessation (Malonek et al. 1997). Increases in blood volume may change the tissue impedance or by replacing a fluid of different impedance or by offering lower impedance to the current in parallel to the extracellular fluid. This is probably the cause of the slow impedance decreases of about 2% measured with implanted electrodes in the cat brain during physiological stimuli (Adey et al. 1962).

Neuronal depolarization during brain activity leads also to fast impedance decreases because of the opening of the ion channels as measured directly on squid axon (Cole and Curtis 1939). The same effect may be present in human for the action

potential in white matter, or to summated effects of synaptic activity in grey matter and EIT could potentially image these fast changes because of its high time resolution.

Other factors which may influence the brain impedance are: (i) the rise in temperature of few tenths degree centigrade linked with the increased metabolic activity of recruited neurons, which however occurs over minutes, rather than seconds (LaManna et al. 1989; Freund et al. 1989) and (ii) the displacement of small amounts of CSF from areas with increased blood volume to areas with lower volume (Vollmer-Haase et al. 1998).

1.2.3.3 EIT of stroke

In the case of ischemic stroke, treatment with thrombolytic drugs is effective, but only if these are administered within 3 hours of the onset of the symptoms. A brain scan is needed prior treatment to discriminate ischemic from haemorrhagic stroke, because in the latter case thrombolytic use may extend it. Unfortunately it is difficult to access CT or MRI scanning facility and obtain a report within that time. EIT instead could be placed in the ambulance or in the casualty department, providing a fast and easily available brain scanner.

Even though impedance changes from normal conditions due to stroke are the largest in the brain, time difference imaging is not possible because data can only be collected when the stroke has already occurred. Static imaging of the conductivity values is therefore needed, but this requires the solution of the nonlinear problem (1-10), which involves accurate knowledge of electrode position, initial impedance and anatomy of the head. However the impedance spectrum of the blood and of ischemic brain is different from that of the normal brain. This property could be exploited producing frequency difference images by referencing one frequency against another (Brown et al. 1994). Measurements over a wide frequency range – 20Hz-1MHz, are therefore important, being this difference more evident between frequencies far apart in the spectrum (Horesh et al. 2005).

In patients with known lesions that happen to have impedance properties similar to stroke, such as tumour, arteriovenous malformation or chronic stroke, there was no significant difference between the background brain and the lesion in linear frequency difference imaging or in non-linear reconstruction of the conductivity (Romsauerova et al. 2006b). This was probably due to the restricted frequency range of the employed system and the large variability over load and frequencies. Nevertheless time difference images of 10% impedance increases during reversible

model of cerebral ischemia in rat were obtained with scalp electrodes and a 2D reconstruction algorithm (Holder 1992c). Even though the accuracy of the image was not clear, the result were encouraging and supported the possibility of the stroke imaging application of EIT.

1.2.3.4 EIT of functional activity

If successful in imaging blood volume increases during brain physiological activity, EIT could provide a low-cost and portable alternative to fMRI or PET in cognitive neuroscience studies of healthy and neurological or psychiatric subjects.

Time difference images could be obtained at any frequency which can discriminate brain tissue, CSF and blood. The difference between these compartments is higher at low frequencies, since the current is confined in the extracellular space in the brain tissue, which has therefore a more markedly higher resistance than the conductive blood. Nevertheless contact impedance is higher at low frequencies, increasing the risk of saturation of the current source and of unbalanced measuring electrode impedances with consequent lower common mode rejection ratio (McEwan et al. 2007). For this reason measurements have been conducted at tens of kHz.

At these frequencies, reproducible impedance decreases of 2.7±0.8% and 4.5±0.9% (mean±SE) during visual and somatosensory stimulation were reconstructed in the appropriate area of the brain in 8 rabbits, using a ring of 16 electrodes placed on the exposed surface of the cortex and a 2D reconstruction algorithm (Holder et al. 1996b).

The attempt of extending these findings to human recording with scalp electrodes, new hardware and 3D reconstruction algorithm, was successful to the extent that boundary voltage measurements showed significant impedance changes of about 0.5% in concurrence with the experiment paradigm (Tidswell et al. 2001b). Unfortunately, the reconstructed images were noisy and did not show consistent and properly localized impedance changes. These have then been subsequently improved considering a finite element model of the realistic anatomy of the head in the reconstruction algorithm (Bagshaw et al. 2003), and showed correctly localized impedance changes with the same time course as the stimulus in 38/51 images (Tidswell 2004). However the EIT images were still noisy and contained multi-focal impedance changes. The bottleneck of the image quality is not clear, but it is possibly related to the low signal-to-noise ratio in the measured data and the

imprecision in the geometry of the models used in the reconstruction, which may need to be customized to each patient.

1.2.3.5 EIT of neuronal depolarization

EIT has in principle the unique potential of detecting fast impedance changes over milliseconds. In this way it would be possible to image neuronal activity in any selected pathway during evoked responses, using repeated stimuli and averaging technique similar to those employed in EEG.

Successively refined modelling study employing cable theory (Boone and Holder 1995; Liston 2004) showed that the recorded impedance change would depend on the recording frequency, being a decrease of 2.8% at DC the highest variation. This was confirmed by recordings resistance decreases of 1.1±0.1% on crab nerves (Liston 2004; Gilad et al. 2005b). The same kind of modelling extended to the cerebral cortex showed that the size of the change was dependent on the amount of recruited neurons during activity. Assuming that this was 10%, a local conductivity change of 0.6% was predicted, which translated into peak scalp boundary voltage changes of 0.06% for a physiologically sensible volume of cortex near the surface. Supporting this guess were preliminary recordings of 0.01-0.03% decreases in the cortex of anaesthetized rabbits during visual evoked responses (Boone 1995). The possibility of obtaining more sensitive measurement using magnetoencephalography was also explored (Liston 2004; Ahadzi et al. 2004), but the conclusion was that the signal-to-noise ratio would have been similar to that of electrical measurement. The signal-to-noise ratio can be improved by long averaging allowing detection of 0.01% changes, which is the order of magnitude of depolarization of large volumes of cortex near the surface. However the possibility of detecting changes with shorter experiment paradigms or of deeper and smaller regions is still not clear.

1.2.4 Introduction to epilepsy

1.2.4.1 Clinical introduction

The word "epilepsy" owes its origin to the Greek expression *epilamvanein*, that literally means "to be seized" (Engel, Jr. and Pedley 1998), going back to the old belief that epileptic patients were people possessed by demons or by the devil ("to seize" means actually "to take possession of"). Today, textbooks define *epilepsy* as a neurological disorder characterized by repeated unprovoked seizures where

"unprovoked" means not generated from conditions that would cause seizures in brains that might be perfectly normal (e.g. electrical stimulation). *Epileptiform seizures* are identified as episodic, uncontrolled, excessive, synchronous discharges of groups of central neurons, that can generated from excessive synaptic excitation, decrease inhibition, or increased activity of both excitatory and inhibitory synapses (Somjen 2004). The word "synchronous" has to be interpreted here as synchronization in time rather than in frequency and phase. In other words it means that many neurons have to be excited together to make a seizure, but they do not have to fire in phase and at the same frequency. This condition actually characterizes a particular type of discharge, known as *clonic*, in opposition to the *tonic* discharge, where neurons are firing incoherently and randomly.

Seizures can be classified according to their symptoms in patients and the portion of the brain involved in the discharge. A general distinction divides them into *convulsive* if there is twitching or cramping of muscles or *nonconvulsive* in their absence. Seizures can be *partial* if only a limited part of the brain is involved or *generalized* if a major area is implicated. Partial seizures can also be classified in *simple* and *complex*: simple if consciousness is retained and complex if it is lost or at least impaired (Engel, Jr. and Pedley 1998). Partial seizures can also evolve into *secondary generalized seizures*, spreading in larger brain areas. This kind of condition may be known as *temporal lobe epilepsy*, if they originate in structures of the temporal lobe, which is the most common type. Generalized seizures on the other hand always imply the patient's unconsciousness. A minor generalized seizure can cause *absence*, without major convulsion.

Epileptic EEGs are also characterized by *interictal* discharges, brief abnormalities that occur between seizures (*ictus* or *ictal activity*), usually without noticeable effect on the patient. Other things are the *auras*, various sensations that forecast impending attacks. They consist of optical or olfactory hallucinations or peculiar feelings in the viscera.

Structural imaging of the brain allows the possibility of distinguishing epilepsies into *symptomatic* and *essential*. Symptomatic epilepsy is the manifestation of an identifiable brain lesion or disease, while essential epilepsy does not have clear origin.

Epilepsy is the most common serious neurological disorder; it affects people of all ages and more than 5% of all people have experienced at least one epileptiform seizure during their lives (Somjen 2004). Keeping seizures under control occupies a

major fraction of neurological practice. According to the National Society for Epilepsy (NSE, www.epilepsynse.org.uk) 1 in every 200 adults in the UK has epilepsy and 1 in every 100 children. This means that there are at least 300,000 people with epilepsy in this country. Although epilepsy can be controlled by the appropriate drug treatment in up to 75% of the patients, some continue to have seizures despite these treatments. A small percentage of the remainder may be eligible for Neurosurgery (approx 3%), during which the part of the brain that is considered the cause of the seizures is removed with a surgical operation (Engel, Jr. 1993).

1.2.4.2 Presurgical evaluation of epilepsy

The objective of the neurosurgical practice in epilepsy, also known as *resective epilepsy surgery*, is to remove or disconnect the epileptogenic zone completely, which is the area of the cortex responsible for seizure generation (Lee et al. 2003; Quarato et al. 2005). Depending on the kind of epilepsy and on the ability to localize and remove completely the epileptogenic zone, neurosurgery is helpful in 30-85% of the patients operated, rendering them seizure free (Engel, Jr. 1993; Rosenow and Luders 2001). It is obviously important to leave undamaged the largest possible part of the brain during resection and particular attention has to be given to the motor and language centres of the cortex. Therefore it is important to define precisely the location and the boundaries of the epileptogenic zone before undergoing resection. This presurgical diagnosis is performed using techniques such as analysis of seizure semiology, electrophysiological recordings, functional testing and neuroimaging methods. These are aimed at identifying functional and structural zones of the cortex, which are related to the seizures (Rosenow and Luders 2001). The former are the irritative zones and the seizure onset zones, while the latter are the epileptogenic lesions. The irritative zone is the cortical area that generates interictal electroencephalographic spikes, the onset zone instead is the area from which the clinical seizures are generated. The epileptogenic lesions are abnormalities in the brain structure, which are considered to be the cause of the epileptic activity. The irritative zone is identified with EEG (scalp or invasive) and video-EEG, magnetoencephalography (MEG) (Wheless et al. 2004), functional MRI (fMRI) triggered by interictal spikes (Ives et al. 1993; Seeck et al. 1998), Single Photon Emission Computed Tomography (SPECT) (Kuzniecky and Knowlton 2002) or Positron Emission Tomography (PET) (Kuzniecky and Knowlton 2002). The onset zone is routinely evaluated with prolonged EEG (scalp or invasive) and video-EEG (Porter and Sato 1993; Rosenow and Luders 2001) and if necessary with ictal

Single Photon Emission Computed Tomography (SPECT) (Van Paesschen 2004). The epileptogenic lesions were identified in the past with Computer Tomography (CT), but today Magnetic Resonance Imaging (MRI) is more commonly used (Rosenow and Luders 2001; Kuzniecky and Knowlton 2002).

As mentioned, in presurgical assessment, the epileptic onset zone is routinely localized with prolonged video-EEG monitoring. Epileptic patients are admitted to a Telemetry ward (a specialized monitoring unit equipped with instrumentations for automatic measurement and transmission of 24 hour video-EEG) for several days, and video-EEG recordings are made until some seizures are detected. The integration of EEG and seizures semiology, recorded by the video, helps the doctors to formulate a diagnosis on the patient's condition and to elaborate a hypothesis on the location of the epileptic onset zone. Sometimes the information given by the surface EEG is inconclusive, since the signal is attenuated and distorted by the conductive volume between the signal font and the scalp, especially in deep epileptic sources. In this case an invasive implantation of subdural or depth electrodes may be needed (Seeck et al. 1998; Jayakar 1999). This implies significant risk related to the implant and high costs. Beside, since these electrodes sample confined cortical areas, its use is limited to condition where the hypothetical onset zone is strictly circumscribed by non-invasive studies. Ictal SPECT is also used for presurgical evaluation. This is performed with cerebral perfusion imaging agents which trace the focal increase in cerebral blood flow subsequent to the metabolic demand of the enhanced ictal neuronal activity (Van Paesschen 2004). With this technique, a sequence of perfusion changes of the brain during complex partial seizures in temporal lobe epilepsy has been obtained. At the onset it starts with hyperperfusion of the whole temporal lobe, which postictally shifts to the mesial temporal structures with hypoperfusion of the lateral structures and ends with hypoperfusion of the whole temporal lobe (Newton et al. 1994; Newton et al. 1995). Ictal SPECT requires the availability of a gamma camera and carries various technical difficulties, such as that the radioisotope has to be available for immediate injection at the aura or seizure onset and that the personnel of the telemetry ward if not the patient himself has to be trained to use and inject radioactive substances (Van Paesschen et al. 2000). It is crucial that the tracer is injected as soon as possible since it takes at least 30 sec to reach the brain and needs 30 seconds to provide an image, which determines the low time resolution of SPECT (Van Paesschen 2004).

1.2.5 Bioimpedance in epilepsy and related conditions

1.2.5.1 Pathophysiology

1.2.5.1.1 Epilepsy

Increased brain neuronal activity alters the ionic distribution between intra- and extra-cellular space and so changes the dimensions of the two compartments (Somjen 2004). During epilepsy, extracellular potassium concentration ($[K^+]_o$) increases together with chloride ($[Cl^-]_o$), while extracellular sodium ($[Na^+]_o$) and calcium ($[Ca^{2+}]_o$) concentrations tend to decrease. K^+ is released by the neurons in the extracellular space when they are activated, therefore $[K^+]_o$ is high where neuronal activity is increased. K^+ is partially removed from the extracellular space by the glial cells through KCl uptake and spatial glial buffering. This mechanism is associated with water flux from the extracellular space into the cells, causing an osmotic swelling of the cells and shrinkage of the extracellular space in area of enhanced neuronal activity.

$[Na^+]_o$ decreases by about 10% mainly because of the inward Na^+ current that generates action potentials. Even if this influx is mitigated by active $3Na^+/2K^+$ pumps, it creates an ionic unbalance across the neuronal membrane that causes water to move into neurons, which then swell, shrinking again the extracellular space.

As a consequence, the size of the extracellular space decreases by about 30% where the neuronal activity is maximal. Moreover, the ions are trapped inside the highly resistive cell membrane, which prevents them from freely participating in the extracellular current, which is the dominant component of tissue conductivity.

This is going to be the leading mechanism generating impedance change during epilepsy, but also other factors are involved. (i) Tissue activation causes vasodilatation and blood volume increase, which can be expected to decrease tissue impedance (Holder et al. 1996b) and (ii) the opening of ion channels during excitation increase the permeability of cell membranes, decreasing their electrical resistance (Boone and Holder 1995; Liston 2004).

1.2.5.1.2 Spreading depression

Spreading depression (SD) is a neurological phenomenon related to epilepsy, possibly generated by the same cellular processes, as it was observed during experimental epilepsy in anaesthetized rabbits (Leao 1944). SD may be triggered by

the same stimulation that trigger a seizure and starts as a nearly complete depolarisation of a considerable area of the brain, accompanied by a significant alteration of the ionic distribution between intracellular and extracellular space (Somjen 2001). This lasts for about 1 min, and then it propagates as a wave in the grey matter at a velocity of 2.5-7 mm/min. SD appears in the ECoG as a silencing of the ongoing normal electrical activity, which spreads slowly over the cortex.

During SD, K^+ flows out of the cells while Na^+, Ca^{2+} and Cl^- flow into neurons. K^+ inside is replaced by Na^+, but the exchange ratio is not 1-to-1 and the decrease of $[Na^+]_o$ is higher than the increase of $[K^+]_o$. Moreover $[Cl^-]_o$ decreases because accompanies some of Na^+ entering the neurons and K^+ picked up by the glial cells. The consequence is a even more evident extracellular space decrease than epilepsy.

1.2.5.2 Impedance changes

1.2.5.2.1 Epilepsy

Van Harreveld and Schade' (VAN HARREVELD and Shade 1962) measured cortical impedance changes with an AC bridge at 1 kHz using two terminals (silver electrodes resting on the cortex) in rabbits and cats with *encephale isole'*. The magnitude of the changes depended on the way the convulsion was induced (with Metrazol or with electrical stimulation) and whether it was developing in SD or not. The conductivity fell during convulsions by up to 5% and by 10% if convulsions triggered SD.

In the same year, Adey et al. (Adey et al. 1962) induced hippocampal seizures with electrical stimulation in cats and measured local resistance changes with a coaxial electrode (two terminals) and a Wheatstone bridge. They observed slow progressive impedance increases of 2.5-33% at 1kHz.

Porter et al. (PORTER et al. 1964) conducted preliminary observations on 3 human patients with temporal lobe epilepsy using implanted manufactured coaxial electrodes (two terminals) in the hippocampus and hippocampal gyrus. A Wheatstone bridge with provision for balancing parallel capacitance and resistance at 1 kHz was used to measure in-phase and quadrature components. No changes were present during spontaneous and electrically induced seizures, while resistance drops between 2-14% and capacitance increases of almost 1% were recorded in Metrazol induced seizures.

Shalit (SHALIT 1965), in assessing the influence of Metrazol on cerebral blood flow, measured cortical impedance variations in the cat with two terminals and a Wheatstone bridge at 10 kHz. Although blood flow increased during convulsions, impedance increases of up to 100% were found in 85% of the cases, decreases in 9% and a combination of the two phenomena in the remaining 6%. The magnitude of the changes was really variable: from few ohms to several hundreds ohms.

Elazar et al. (Elazar et al. 1966) induced spontaneous seizures with tungstic acid in a chronic epilepsy preparation in cats. They measured separately local resistive and capacitive components at 1 kHz with a coaxial stainless steel electrode (two terminals). The resistance changes started within 10 sec after the beginning of the electrical seizures and increased to 10-12% for long attacks (>150 sec), while the capacitance changed in the opposite direction. The region of maximal variation correlated with the maximal EEG activity. During interictal periods baseline fluctuations between 1-3% were observed.

Rao (Rao 2000) measured local cortical impedance changes associated with electrically-induced focal and generalized seizures with four terminals in rabbits at 47 kHz. During focal activity consistent increases of 9.5±1.4% were found close to the stimulation site together with an increase of 1.7±0.5% 8 mm away. During generalized activity, instead, an increase of 14.3±0.5% followed by a second increase of 15.6±1.5% was detected close to the stimulation site together with an increase of 11.9±2.0% 8 mm apart after 2 minutes delay.

Fox et al. (Fox et al. 2004) measured resistivity increases of 22±3% in the pyramidal cell layer of rats transverse hippocampal slices bathed in a "low-Ca^{2+}" artificial CSF (ACSF), which induces spontaneous seizures and does not allow synaptic connections. A three-terminal system with high spatial resolution using square pulses of 200 ms was employed.

Porter et al. (PORTER et al. 1964) hypothesized that the resistance fall was due to the hyperventilation associated with the seizure, which they found causing resistance decreases also in normal conditions. This would be not present in other studies because they were conducted under anaesthesia, but may be present in spontaneous seizures. It may also be possible that the resistance decrease was caused by the increase in systemic blood pressure due to Metrazol and therefore not associated with the seizure event itself. However, overall, the impedance appears to increase and this is probably due to the dominance of the extracellular space decrease over the increase in blood volume, rise in temperature and ion

channel opening which produce a change in the opposite direction but probably to a lesser extent. This is also confirmed in that the change is greater at lower frequency: 9.5% at 47 kHz (Rao 2000), 10-12% at 1kHz (Elazar et al. 1966), up to 22% with square pulses of 200 ms (Fox et al. 2004). This happens because the lower is the frequency of the current the more it is confined to the extracellular space and therefore the more is influenced by the cell swelling.

1.2.5.2.2 Spreading depression

Freygang and Landau (FREYGANG, Jr. and LANDAU 1955) found resistivity increases across cat cerebral cortex of 10-20% most markedly in the superficial layer. They used a four-terminal measurement, injecting constant current pulses. The current was injected between a platinum-platinum coil placed in a flowing pool of modified Tyrode's solution above the cortex and a deep electrode in the pharynx, while the voltage was measured between two pipettes filled with Tyrode's solution. To make the cortex more susceptible to SD, experiments were conducted under Tyrode's solution with increased [K^+], replacing [Na^+], which may affect impedance measurement. The resistivity was calculated by comparing the amplitude of the recorded voltages with the one measured across a known portion of the Tyrode's pool of know resistivity.

Van Harreveld and Ochs (VAN HARREVELD and Ochs 1957) measured cortical conductance changes during SD in rabbits and cats at 1 kHz, using a Wheatstone bridge. They found a mean of 17±2% conductance decrease (i.e.impedance increase) in rabbits and 10% in cats. This started at the same time as the typical slow potential change of the SD and it was accompanied by a vasodilatation over a considerable area of the cortex, which was not significantly affecting the conductance decrease.

Ranck (Ranck Jr 1964) measured complex impedance changes in rabbits using four terminal at 5 frequencies (from 5 to 50000 Hz). He considered results to be uninfluenced by interelectrode capacitance and checked the system response at the end of every day. He measured separately real and imaginary part of specific impedance across time. The changes ranged between: 15 to 75 % for the real and from 0 to 275 % for the imaginary component, depending on the measuring frequency and time from SD initiation. The results were interpreted according to three processes occurring at different times: (i) decrease in the size of interstitial space; (ii) decrease in neurons membrane resistance; (iii) increase in neuroglia membrane resistance.

Later Hoffman et al. (Hoffman et al. 1973) measured local complex specific impedance (ρ^*) changes at various depths (between 100 μm and 2000 μm) in rat cerebral cortex mainly at 1600 Hz (current of 20 nA) with a custom made microelectrode in a three terminal configuration. Each electrode was calibrated against solutions of known resistivity throughout the experiment. At rest $|\rho^*|$ was between 200-700 Ωcm, values clustered around 250 Ωcm, in agreement with (Ranck Jr 1964) and 550 Ωcm. $|\rho^*|$ changes during SD were large with peak of 2-3 times resting level. These large changes may be due to the small sample volume involved, which is likely to be completely occupied by the SD at the same time, in contrast to surface electrodes that may drive current trough inactive tissue. The resting and change values were not significantly different at different depths (between 300 and 1200 μ). An experiment at 4 different frequencies (400, 800, 1600, 3200 Hz) confirmed previous findings with maximum impedance change in the lower band and phase angle in the higher.

Holder (Holder 1992b) measured maximal cortical resistance increases of 40% using four terminals at 50 kHz. He also measured decreases of about 0.8% using scalp electrodes, these changes were attributed to temperature increases in the scalp, due to increased blood flow and metabolism.

Yoon (Yoon et al. 1999) measured complex cortical conductivity percentage changes in spreading depression in the RF range (from 300 kHz to 100 MHz) in 8 rats. They recorded the reflection coefficient of a coaxial copper transmission line and converted it in impedance. The conversion equations were correct for a homogeneous media, so they were only an approximation for the cortex. Calibration measurements and prediction of the sensitivity depth of probe with a FEM simulation were conducted. The conductivity measurements revealed a change with short latency (30-60 s) followed by a change with a longer latency (200-300 s), ranging the first from 1.5% to 5% and the second from 3% to 34%, depending on the frequency and animal. The probe was abutting the cortex, so these changes may be larger locally due to the limited depth probe sensitivity. This was the first study where short latency changes were detected. The values reported were σ and ε_r', where σ is the real part of the conductivity. The imaginary part could be computed, but the baseline conductivity values were not reported.

1.2.5.3 Time course of impedance changes

Some of the studies mentioned above (Elazar et al. 1966; Rao 2000; Fox et al. 2004) showed that changes in cerebral impedance during epilepsy commenced

within 10 sec after the onset of the seizure detected with implanted or cortical electrodes and recover within 300 sec after discharge cessation. Regarding the time constant with which the impedance changes build up, Elezar et al. measured changes between DC and 2 Hz, and Fox et al. showed a gradual increase in tissue resistance with $\tau \sim 5$ sec and a slow decay with $\tau \sim 10$ sec after burst cessation. Since there is no previous study considering impedance changes measured from scalp electrodes during epilepsy, the time course of the change in the boundary voltages recorded in this configuration can only be estimated. It has to be considered now that the scalp EEG is only an attenuated and blurred representation of direct intracranial recording because of the distance between the brain and the scalp and the presence of the skull in the middle. Thus we do not expect the time course of the boundary voltage changes to be the same respect to the EEG seizure onset measured from the scalp as in the case of intracranial recording. Epileptic onset detected with intracranial electrodes may precede that detected with scalp electrodes by up to 40 seconds, depending on the depth of the seizure focus (Alarcon et al. 2001; Tao et al. 2007). This is probably because substantial area of the cortex must be recruited and synchrony obtained before significant signals can be seen on the scalp. Moreover subtle early changes, difficult to identify by eye, could be recognised as variation in the frequency content of intracranial recording several second before onset (Alarcon et al. 1995). All these considerations lead to a possible anticipation of boundary voltage changes of up to 1 minute over the EEG onset detected by ordinary scalp EEG recordings.

1.3 Purpose

1.3.1 Rationale for use of EIT in imaging during epileptic seizures

Local impedance measurements in the brain, during experimental epilepsy in animals, clearly showed that seizures are accompanied by focal conductivity changes of a few percent. This is possibly due to cell swelling, and subsequent extracellular space shrinkage, following the ionic unbalance and water movement occurring during seizures. Images of these conductivity alterations have been obtained with EIT, placing electrodes on the exposed cortex of rabbits, and boundary voltage variations have been observed in scalp measurement during seizures. Therefore EIT has the potential of measuring voltage changes associated with epilepsy and reconstructing them into images of internal conductivity. In

principle, this would provide information in much the same way as if a patient were to have a seizure while in a functional Magnetic Resonance Imaging or Positron Emission Tomography scanner. However, seizures arise unpredictably – usually occurring once or so each day; so it is not practicable to perform this in one of these large immobile scanners. EIT instead could be used on the bedside during presurgical assessment of intractable epilepsy in the Telemetry ward. Impedance data could be collected continuously over several days and, uniquely, be analyzed retrospectively at the time of a seizure, when these are identified by the use of video or EEG. The limited success of resective surgery is due in part to an inability to image the seizure source directly. If successful, EIT would provide a vital additional method for presurgical evaluation in intractable epilepsy and, if spike-triggered, it could give an out-patient guide to the seizure onset area with averaging.

1.3.2 Statement of purpose

The overall purpose of the work undertaken for this thesis was to develop a method for EIT imaging during epileptic seizures. Specific issues which were addressed were:

1) To develop a method for simultaneous recording of EIT and EEG (as the latter may be corrupted by the current injected by the former) to permit clinical reporting and correlation between the two methods.

2) To analyze fully a pilot clinical study with EIT during seizures, to see if any significant changes could be measured.

3) In the event, this analysis proved negative, so the next step was to re-examine the engineering aspects of the problem and specify an improved system. The next aim was to examine the feasibility of undertaking EIT during seizures with scalp electrodes. A detailed finite element model of the head was used in order to estimate the likely amplitude of scalp potentials. These were then considered in relation to the baseline noise of three available EIT systems. The purpose of this was to determine if EIT appeared feasible, suggest optimal recording conditions (such as optimal applied frequency), and choose the best available system for a clinical study.

4) Finally, a study was undertaken in saline filled tanks to determine if indeed the performance of the two best systems appeared sufficient for a clinical study.

It was originally my intention to undertake a final clinical study with the optimal system thus designed, but there was not sufficient time left; this study is planned and will take place with other researchers in the near future.

1.4 Design and outline of the thesis

This work contains seven main sections, related to this goal :

1) Filtration of artefact introduced in EEG by concurrent EIT recording (Ch. 2). EEG is required to be recorded in parallel with EIT for 2 main reasons: (i) to allow the routine clinical work of the telemetry ward, where video-EEG is needed for the diagnosis of the epileptic condition and (ii) to give a reference to the EIT recording for seizures occurrence timing and localization. Unfortunately, simultaneous EEG/EIT recording makes EEG unusable because it gets corrupted by the current injection of EIT. So the first purpose of this thesis was to investigate a method to recover the underlying EEG signal eliminating the artefacts introduced by EIT.

The EIT artefact introduced in EEG during concurrent recordings was firstly reduced with a set of hardware filters and then eliminated with a further off-line software filtering. In order to design the software filtering, the EIT artefact was characterized looking at simultaneous EEG recordings and four algorithm permutations were tested. The clinical acceptability of the resulting traces was assessed by experienced EEG readers.

2) Re-analysis of clinical EIT study collected with scalp electrodes during seizures (Ch. 3). An attempt at designing an optimal method for clinical recording as a support for further experiments was then conducted, employing clinical data collected during ictal periods on 7 patients undergoing presurgical assessment at King's College Hospital London. The question was whether changes in internal conductivity related to seizures could be seen in potential measurements from scalp electrodes on human subjects. If these were present, the possibility of localising the epileptic onset area, concurring with seizure semiology, EEG and MRI, was considered. The quality of the scalp measurements during the pre-ictal period was assessed together with the plausibility of the voltage changes recorded during seizures and of the related reconstructed conductivity changes. The boundary voltage changes were normalized respect to the period preceding the seizure which represents their values during normal brain activity and their deviation from this level was considered. The results were compared against a set of EIT segment recorded during non-ictal periods, to assess whether the seen changes were genuinely due to

epileptic conductivity variations. Time-difference conductivity images were reconstructed, visually inspected and compared with the EEG and MRI findings.

3) Estimation of expected signal changes recorded with scalp electrodes using a computer model (Ch. 4). Since the results of the previous study were negative, I examined the size of the expected boundary voltage changes associated with epilepsy in order to estimate the expected signal size and so set the specifications for an improved EIT system. This part of the work was intended to assess the feasibility of this application of EIT, and, if practicable, to optimise the recording system so as to reduce baseline noise in order to enable imaging of the conductivity changes. The complex boundary voltages on the scalp were calculated by solving the forward problem for a realistic 3D Finite Element Model (FEM) of the human head under normal conditions and during focal epilepsy for 7 frequencies between 5Hz and 4MHz. To assess whether the voltage changes obtained in the simulation were large enough to provide clinically useful EIT images, epileptic admittivity changes starting from boundary voltages corrupted with white noise were reconstructed into images.

4) Analysis of noise produced by three different EIT systems, with a view to optimising recording and selection of the best system (Ch. 5). Once the prediction of the signal was completed, the size of the noise delivered by 3 available EIT systems was investigated in order to select the system which was the most feasible for conducting clinical experiments. The purpose was to investigate the possible sources of noise in the UCH Mark1b, UCH Mark2.5 and KHU Mk1 16 channel systems and select the most likely to give the highest signal-to-noise ratio. An attempt was made to divide the noise into its components due to electronic and thermal noise, to metal-ion interaction and environment and to ion-skin interaction and physiological processes. The noise dependence on measuring frequency and on load impedance and the difference between 4-terminal and multiplexed measurements was also explored. In order to divide the sources of noise, experiments of increasing complexity, trying to add the possible causes of noise one at a time, were performed. The full operational frequency range was investigated and the highest current level for each system used. A comparison of the noise spectra delivered was conducted to decide upon the most feasible system for clinical measurements.

5) Design of a protocol for 3D imaging of the human head for a 16 channel system with adjacent recording (Ch. 6) The 16 channel KHU Mk1 system is a semi-parallel system with adjacent voltage measurements and flexible current injection. No

protocol for 3D imaging of the human head was available for such system. In this chapter, I devised a system for recording impedance from scalp electrodes with these limitations. Twelve protocols were tested, based on three different electrode placements and different combinations of current injections from electrode at 180°, 120° and 60°. These protocols were compared by assessing the reconstruction quality of a simulated perturbation in 5 positions in a saline head-shaped tank model and in focal epilepsy in an anatomically realistic head model. This was done in terms of localization error, resolution, image distortion and sensitivity in the region of interest.

6) Comparison of the imaging performance of two EIT systems suitable for long term epilepsy recording (Ch. 7). This chapter compares the performance of the UCH Mk2.5 and of the KHU Mk1 in reconstructing 3D time difference images after implementing modifications to optimise the signal-to-noise ratio and to practically allow long term impedance monitoring. The image reconstruction of a 30% conductivity perturbation in 3 positions in a homogeneous head-shaped saline tank and with a real human skull were compared for two optimal protocols in terms of localization error, resolution, image distortion and sensitivity in the region of interest.

7) Discussion and future work (Ch. 8). In this chapter, I summarize the finding of the work in this thesis, discuss their overall significance and propose future work required for EIT in epilepsy.

At the end of the thesis three additional appendices are presented:

1) Derivation and physiological explanation of the conductivity change due to epilepsy (Appendix A). This appendix provides a description of the phenomena underlying the impedance spectra of the head tissue based on the literature.

2) Graphical User Interface for UCH Mk2.5 data collection (Appendix B). This appendix describes the design and implementation of a graphical user interface for data collection with UCH Mk2.5 in a clinical environment by technicians or physicians with no previous knowledge about programming or impedance data collection.

3) Technical modifications to the UCH Mk2.5 for optimal epilepsy imaging (Appendix C). In this appendix the technical modifications on the hardware and controlling software of the UCH Mk2.5 to optimize it for epilepsy recording are reported.

1.5 Personal statement

Much of the work in this thesis was undertaken in collaboration with other members of the research group. This describes my personal contribution. The hardware filter in Chapter 2 was originally designed and developed by Dr Rebecca Yerworth. However, I designed the software filter described in Chapter 2, and I undertook all the work on its refinement and testing. The EIT seizure recordings of Chapter 3 were collected previously at King's College Hospital by Matthew Sparkes. However, I undertook all the analysis and image reconstruction described, using the forward and inverse solver provided by Lior Horesh and based on EIDORS. The model developed in Chapter 4 was based on the same forward solver, modified for my purpose. The choice of the conductivity values was educated by a broad literature review conducted by Lior Horesh and Andrea Romsauerova; while the choice for the conductivity change during epilepsy was based on a review conducted by me. I implemented these values into the forward solver, and undertook all the modelling and its analysis. All remaining and other studies were performed solely by myself, though with technical advice from the post-doctoral fellows in the group, Alistair McEwan and DongIn Oh.

1.6 Acknowledgement

This work would have not been possible without the help of the people which I have met during the past 4 years and advised and supported me in a way or another.

Firstly I would like to thank David Holder, my first supervisor, who has been not only a wise and patient guide throughout this work, but also an understanding and supportive friend and helped me grow as a person and as a researcher. Alistair McEwan took up the hard role of second supervisor, taught me about instrumentation and a lot of other things and spent so much time listening to my complaints and cheering me up.

Juan Felipe Perez-Justed Abascal has been a great friend and flatmate and helped me with the linear solver and principal component analysis even after he went to Paris. Lior Horesh and Ori Gilad have been my judicious older "brothers". They gave me precious advice on science and life and helped me with the forward modelling and signal analysis. Andrea Romsauerova has been my cheerful desk mate, helped me to collect tank data and most importantly to smile. DongIn Oh has always been available for support, from Korea first, and now from here with his KHU Mk1. Juan

Fritschy always had a wise word in difficult situations and has been an example of strategy and organization.

Thanks also to my flatmate Daniele Savi, which, with Juan, has been my family here in London and made my everyday life more enjoyable and secure.

Voglio anche ringraziare Andrea Del Duce, Giancarlo Gavioli e Marzia de Lucia per gli innumerevoli pranzi e caffe' insieme, per avermi ascoltato e tollerato, per aver condiviso le nostre passioni e anche per quei due suggerimenti che mi hanno dato sull'analisi di segnale.

Thanks to Riccardo Savi for helping in formatting this document and Russell Bradley-Cook for correcting the English of part of this thesis.

Thanks to Dimitra Laskou, which has always been there for me, even coming to the laboratory on Saturdays, never spared a hug especially in the last stressful period of completing this thesis and helped me with some of the graphics in this work.

This thesis is dedicated to my family. Questa tesi e' dedicata a mamma, papa' e Andrea che hanno sempre creduto nelle mie capacita' anche quando ero giu' e non mi hanno mai lasciato da solo, spingendomi con il loro affetto fino alla fine.

1.7 List of publications resulting from this work

1.7.1 In peer reviewed journals

Factors limiting the application of Electrical Impedance Tomography for identification of regional conductivity changes using scalp electrodes during epileptic seizures in humans. (2006) L Fabrizi, M Sparkes, L Horesh, J F Perez-Juste Abascal, A McEwan, R H Bayford, R Elwes, C D Binnie, D S Holder. *Physiol. Meas.* **27** S163-S174.

Review of the dielectric properties of human head pathophysiology for Multi-Frequency Electrical Impedance Tomography. L Horesh, A Romsauerova, L Fabrizi, A McEwan, S Arridge, D S Holder. Article submitted to Medical & Biological Engineering & Computing.

Analysis of resting noise characteristics of three EIT systems in order to compare suitability for time difference imaging with scalp electrodes during epileptic seizures. (2007) L Fabrizi, A McEwan, E Woo, D S Holder. *Physiol. Meas.* **28** S217-S236.

1.7.2 Peer reviewed conference proceedings

EIT during epileptic seizures: preliminary clinical studies. (2004) L Fabrizi, M Sparkes, R Yerworth, C Binnie, R H Bayford, D S Holder. *5th Electrical Impedance Tomography Conference*, Gdansk, Poland.

EIT in epilepsy: not an easy task. (2005) L Fabrizi, M Sparkes, J F Perez-Juste Abascal, L Horesh, D S Holder. *6th Electrical Impedance Tomography Conference*, London, UK.

A feasibility study for imaging of epileptic seizures by EIT using a realistic FEM of the head. (2006) L Fabrizi, L Horesh, A McEwan, D S Holder. *7th Electrical Impedance Tomography Conference*, Seoul, Korea.

Analysis of resting noise characteristics of three EIT systems in order to compare suitability for time difference imaging with scalp electrodes during epilepsy (2007) L Fabrizi, A McEwan, D Oh, D S Holder. *8th Electrical Impedance Tomography Conference*, Gradz, Austria.

1.7.3 Posters

Non-invasive imaging of the sources of epileptic seizures using Electrical Impedance Tomography (EIT) (2005) L Fabrizi, R Yerworth, R Bayford, and D S Holder. *Medical Physics and bioengineering departmental poster competition.* 1st prize winner.

Can Electrical Impedance Tomography be used to image epileptic foci?: A FEM feasibility study (2006) L Fabrizi, L Horesh, A McEwan, D S Holder. *Medical Physics and bioengineering departmental poster competition.*

Chapter 2 – Removal of the artefact induced in the EEG by concurrent EIT

2.1 Introduction

In the proposed application EIT could be used in presurgical assessment simultaneously with EEG and video recording and produce fMRI like images continuously, while patients were monitored on the telemetry ward. Unfortunately, the use of injected current generates artefacts in the scalp EEG, in a fashion somewhat similar to the fMRI artefacts encountered in spike triggered fMRI recording. In this chapter is presented a signal processing method and some preliminary results for removal of this artefact so that EIT and the EEG can be acquired simultaneously.

2.1.1 Artefact problem

At first sight, it would appear that the two signals would not interfere with each other, as EIT current is injected at tens of kHz, which is well above the EEG band. Unfortunately, in practice, the EIT significantly corrupts the EEG signal, even when separated electrodes are used for EIT and EEG recording. Without the hardware filtering outlined below, the EEG was completely obscured by artefact which was orders of magnitude greater; but even with hardware correction, an artefact about one order of magnitude greater than the EEG, with a period of about the period of one complete EIT image data set – typically 420 ms – may be seen. The complete explanation is not entirely clear. It is probably due in part to saturation of the EEG amplifiers by the injected currents near to EEG electrodes, and to switching effects as different electrodes are selected for transimpedance measurement in EIT, coupled to irregular discharge of electrodes which have just been used to drive current.

2.1.2 A similar problem in fMRI

The problem of the EIT artefact generation in the EEG recordings is analogous to that met during simultaneous EEG and fMRI in interictal spike triggered fMRI which was due to a ballistocardiographic effect (Allen et al. 1998) and current induction in electrodes due to alterations in the magnetic field gradient (Allen et al. 2000; Garreffa et al. 2003). The artefacts were removed through the calculation of the averaged artefact shape and consecutive subtraction from the EEG signal. This is achieved by detecting the occurrence of the artefact cause and time-locking sections of EEG to it. For example, the fMRI pulse artefact, related to blood flow changes in the head, is removed by time-locking sections of EEG to the QRS

complex occurrence in the ECG (Allen et al. 1998). ECG peaks were detected and then sections of EEG signal, as long as the mean R-R interval and centred on the ECG peaks, were averaged and subtracted. The resulting template was in some approaches adapted to each current section of the EEG before subtracting, by minimizing the difference between the frequency spectrum of the two (Sijbers et al. 1999).

2.1.3 Purpose

The purpose of the present study was to develop and test, for the first time, a method to recover a readable and clinically usable EEG, which has been contaminated by concurrent EIT image collection. This led to the necessity of characterizing the artefacts introduced by EIT, especially in terms of variation along time, and of designing a reliable method to remove them, leaving the underlying EEG unchanged. Different solutions have been considered and evaluated accordingly to the quality and clinical acceptability of the EEG recordings they were capable to recover.

2.1.4 Design

2.1.4.1 Principle of the proposed technique

2.1.4.1.1 Hardware filter

The high frequency components above 43 Hz introduced by the EIT system were reduced with a 2nd order hardware low pass filter placed between the subject and the EEG system, which brought the EEG amplifiers out of saturation. The low frequency components of the artefact, below 72 Hz, with the same timing as EIT frame collection, contained no useful information for EIT and were filtered out between the EIT system and the subject by the insertion of high-pass filters.

2.1.4.1.2 Software filter

Unfortunately, a residual although non-saturating artefact, with the same period as the EIT image collection rate, remained in the EEG traces. A procedure to calculate the artefact template, synchronize it with the occurrence of the artefact in the EEG raw data, and subtract it, similar to that employed in the removal of artefacts in spike triggered fMRI (Garreffa et al. 2003), was utilized.

Two main assumptions were employed in processing the raw continuous signal *a(t)* acquired by the EEG amplifiers after hardware filtering. The first one considered *a(t)* as a linear composition of three uncorrelated signals: the EEG normal activity *eeg(t)*, the instrumentation noise *i(t)* and the EIT artefact *eit(t)*.

$$a(t) = eeg(t) + i(t) + eit(t) \tag{2-1}$$

The second assumption was that *eeg(t)* and *i(t)* are not related in time with the EIT artefact. Therefore averaging EEG epochs time-locked to the EIT artefact, *eeg(t)* and *i(t)* will be reduced, isolating the EIT artefact in a way similar to that employed to isolate evoked potentials. To calculate the artefact template, an EEG trace segment containing *N* EIT frames, and eventually *N* EIT artefacts, was considered. The *N* artefacts (*S* samples long) were aligned and averaged together to get an EIT artefact estimation.

$$\begin{gathered} a_k(t) = \left[a_{k,1}(t), a_{k,2}(t), \ldots, a_{k,S}(t) \right] = eeg_k(t) + n_k(t) + eit_k(t) \\ \text{with } k = 1, 2, \ldots, N \end{gathered} \tag{2-2}$$

$$a_{avg}(t) = \frac{1}{N}\sum_{k=1}^{N} a_k(t) = \frac{1}{N}\left(\sum_{k=1}^{N} eeg_k(t) + \sum_{k=1}^{N} i_k(t) + \sum_{k=1}^{N} eit_k(t) \right) \tag{2-3}$$

$$a_{avg}(t) = eeg_{avg}(t) + i_{avg}(t) + eit_{avg}(t) \tag{2-4}$$

Using a suitable number of periods, the EEG basal activity and the instrumentation noise can be reduced to zero, isolating the EIT artefact that can then be subtracted from the EEG raw signal.

$$\begin{gathered} eeg_{avg} \to 0 \quad i_{avg} \to 0 \\ a_{avg}(t) \cong eit_{avg}(t) \end{gathered} \tag{2-5}$$

However, the EIT data collection was subjected to small timing fluctuations, probably due to unavoidable background processes of the operating system of the computer that controls the acquisition programme, and the digital electronics that generate the injected current in the EIT system. Thus for *k = 1,...,N* of (2-2) $a_k(t)$ had to be aligned before they could be added together, and the final artefact average has to be time locked to each artefact accordingly, before being subtracted. The time synchronization had to be done on the EEG traces themselves, without prior knowledge about the artefact. The alignment of the artefacts, before being

added, was achieved by calculation of the maximum correlation between an artefact running average created iteratively and consecutive EEG raw data sections of the same length. The final artefact template was then time-locked with the same process to each artefact period and subtracted.

Correction for the artefact required two steps : 1) Ascertainment of the timing of successive artefacts, in order to enable synchronization of averaging to produce the artefact template for subtraction and 2) Determination of the shape of the artefact template for subtraction. The latter was different for each EEG channel, but the timing could be synchronous between channels. Furthermore, it seemed possible that correction by a single template along one channel could produce errors if the amplitude of the artefact varied over the duration of the sampling section of the EEG; in this case, the template could be scaled in amplitude to give the best match to that period of EEG. This was termed "template scaling". It was uncertain which of these would have been optimal; so four possible versions of the algorithm were implemented and tested:

1. use of a single reference channel for timing without template scaling;
2. use of a single reference channel for timing with template scaling;
3. correction of timing on each channel individually without template scaling;
4. correction of timing on each channel individually with template scaling.

2.1.4.2 Artefact characterization

The EIT switching artefact which remained after hardware filtration was characterized by observing different examples of EEG recording obtained during EIT acquisition. The number of artefact waveforms necessary to obtain a reliable average estimation was investigated by considering the trend of the standard deviation. Then the possibility of decreasing its size and of simplifying its calculation was addressed. This would be an advantage in term of computational time, and in terms of the refresh rate. In addition, the period along which the artefact waveform did not change significantly, and therefore the necessary refreshing period for the artefact waveform average, was considered.

2.1.4.3 Clinical acceptance

The clinical feasibility of each software filtering version was tested by presenting blinded EEG files cleaned with the different algorithm variants to two experienced EEG readers (a consultant clinical neurophysiologist and a Senior Chief EEG

technologist in our department with over 20 years experience of recording and reading EEGs). They marked the corrected EEG traces following an evaluation scale similar to the one used in visual validation of compressed EEG files (Hinrichs 1991). Records were evaluated for the degree of artefact and if the lowest artefact yielded cleaned traces which were of a standard suitable for clinical diagnostic purposes.

2.2 Methods

2.2.1 Hardware filter

First order passive high pass filters with a 3dB point of 72Hz were inserted in series with each EIT electrode and second order passive low pass filters with 3dB point at 43Hz were inserted in series with each EEG electrode. Clinical testing was performed using thirty-eight cup electrodes applied to the head of a subject with conductive electrode paste (Ten20 Conductive, Weaver & Company), after skin preparation with abrasive gel (NuPrep Skin Prep, Weaver & Company). Thirty-two of these formed a complete set of electrodes for EIT imaging and were placed in a modified 10-20 format (Tidswell et al. 2001b). The remaining 6 were placed in the gaps (1 ground, 1 reference and 4 other electrodes) and used for EEG monitoring.

Initially, none of the above filters were inserted and EEG was recorded for 50 seconds without EIT. EEG was then collected during 50 seconds of EIT, under each of the following conditions: a) None of the additional filters present; b) Low pass filters in series with the EEG electrodes, only; c) High pass filters in series with the EIT electrodes, only; d) Both sets of filters present. The spectral components of the EEG were analyzed using FFT and the unprocessed EEG traces were observed qualitatively and any saturation of the EEG amplifiers noted. No digital filtering was applied to the data before the FFT.

2.2.2 Artefact characterization

The size of the sample of artefact waveforms necessary to have a reliable average estimation was assessed using EEG recordings collected with the hardware filter in place, but without software filtering. These were 15 minutes long segments, contaminated by EIT artefact, from 5 male subjects, between 20 and 39 years old, which were undergoing pre-surgical assessment for Neurosurgery at the King's College Hospital, London. Each subject gave informed consent for the study, which was approved by the local committee on the Ethics of Human Research (Ref.

089/92). A total of 6 channels were randomly selected from the full 10-20 montage available. The following analyses were performed:

(i) the artefact period T_r was calculated as in section 2.3;

(ii) the average waveform was then calculated as in section 2.3 using an increasing number of EEG segments T_r long, but excluding waveform outliers. *Outliers* were defined as segments where the artefact waveform: a) was obscured by other artefacts, such as due to movement, muscle contraction and eye blink or had a different shape than in the rest of the segment b) was not recognisable;

(iii) the standard deviation of each data point might be expected to vary with the number of measurements used to calculate the average and so eventually converge toward a stable value. The mean standard deviation value *sdm* of the data samples was calculated using increasing amount of measurements. A reliable estimation of the averaged artefact was obtained when the use of extra measurements did not change this value of more than 2% of a local mean, calculated on successive 100 *sdm*.

Three of these six artefact averages were compared with averages obtained using a reduced sample of waveforms (100, 200, 300, 400, and 500) from the same populations without outlier exclusion, in order to assess whether this may have made a significant difference in the artefact waveform template. A difference of more than 10 μV was considered significant.

One EEG raw channel of 7 hours was used to estimate the period over which artefact waveform did not change significantly. Averaged artefact periods were calculated every 15 minutes and compared with the first to assess whether the difference was increased over time. A difference of more than 10 μV was considered as significant.

2.2.3 Software filter

MATLAB (The Mathworks, MA) code was written to read EEG traces, remove the EIT artefact and output the cleaned traces in the same format as the original data. Before starting, the user visually inspected the EEG and roughly estimated the period length of the artefact ($T_g=1/f_g$), as this depended on the EIT recording settings. The averaged artefact waveform was then calculated over EEG segments, which were N times this period long. N was chosen on the results of the artefact characterisation study. These segments comprised EEG raw channels $x_k(t)$ as acquired by the EEG amplifiers:

$$X(t) = [x_1(t); x_2(t); ...; x_M(t)] \quad (2\text{-}6)$$

where M is the number of EEG amplifiers. These EEG segments were likely to include approximately N artefact waveforms.

2.2.3.1 Single EEG channel processing

The procedure to clean a single channel $x_k(t)$ of a corrupted EEG segment $X(t)$ was as follows (Figure 2-1).

Averaged artefact frequency and period length calculation. To create the artefact template, it is necessary to know its mean length so that segment of EEG of this size can be aligned and averaged together. This can be only approximately guessed by the user. The frequency, and therefore the length, of the artefact period were derived from the averaged spectrum of the corrupted EEG channels. Since the artefacts were periodic and of higher amplitude than the EEG components, their fundamental frequency and harmonics were recognisable in the spectrum of each channel. The averaging was used to increase the SNR of the artefacts frequency in respect to the underlying EEG. The EEG frequency content was higher at low frequencies; therefore harmonics of the EIT artefact other than the fundamental were easier to distinguish. The 4th harmonic of the EIT artefact frequency f_r was defined as the peak in a window (± 15% of f_g) centred around 4 f_g. The artefact period was then $T_r = 1/f_r$.

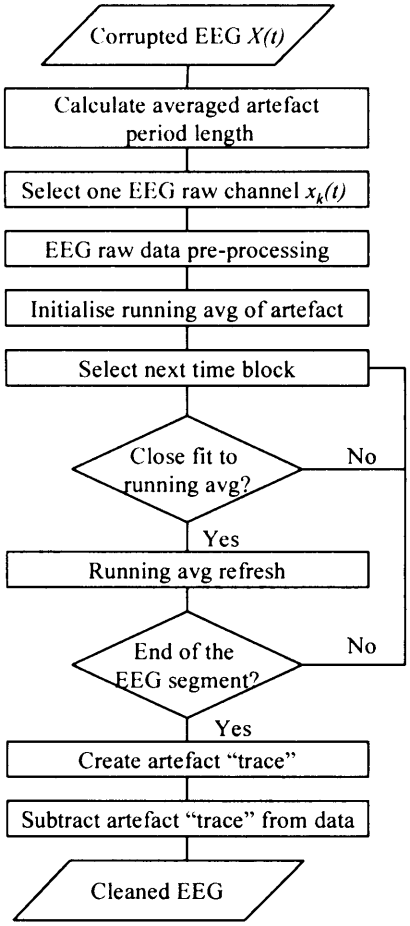

Figure 2-1 Flow chart describing the main body of the algorithm.

Single EEG channel pre-processing. (i) EEG is usually acquired at a sampling frequency between 200 and 500 Hz. $x_k(t)$ was interpolated up to 2000 data points per second in order to augment its temporal resolution and then the cross-correlation precision during the alignment of the artefact waveforms. (ii) A 50 Hz noise-free copy $x_{fk}(t)$ of the EEG raw channel $x_k(t)$ *was* created by application of a notch filter (symmetric FIR stop-band filter between 45 and 55 Hz). $x_{fk}(t)$ was used just for the artefact waveform alignment while the artefact template was created with $x_k(t)$ data.

Artefact template creation. A running artefact average $\hat{a}_{fk}(t)$ was obtained iteratively by summing linearly detrended sections of $x_{fk}(t)$, T_r long and time aligned by finding the best correlation between the current section and $\hat{a}_{fk}(t)$ itself (Figure 2-2). If $X(t)$ was the first segment of the EEG file, $\hat{a}_{fk}(t)$ was initialised as the first $x_{fk}(t)$ section that did not have any data point that exceeded a 200 μV threshold as these were

likely to be EEG distortions other than the EIT artefact. Otherwise $\hat{a}_{fk}(t)$ was initialised as the final artefact template of the previous segment.

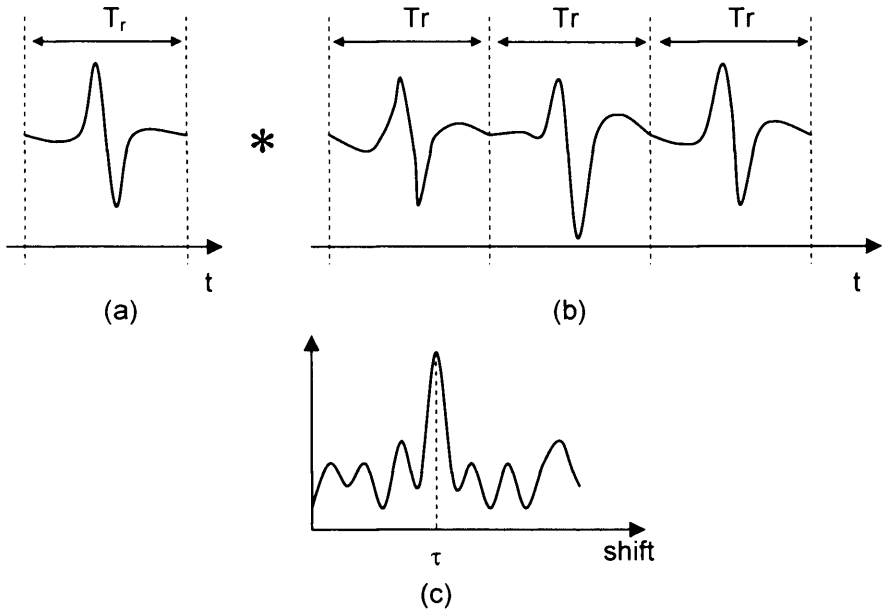

Figure 2-2 The artefact running average $\hat{a}_{fk}(t)$ (a) was cross-correlated with consecutive EEG sections of $x_{fk}(t)$ (b). The shift τ corresponding to the maximum correlation (c) was used to align the two waveforms.

The next section of $x_{fk}(t)$ was time shifted and added to $\hat{a}_{fk}(t)$ only if it had a "close fit" with the running average (Figure 2-3). The "fit" was considered close enough if:

- the absolute mean value of the current section did not exceed twice the maximum absolute value of $\hat{a}_{fk}(t)$;
- the maximum of the cross-correlation between $\hat{a}_{fk}(t)$ and the section did not occur for an absolute shift greater than $T_r/6$.

This operation was repeated for all the sections till the end of $x_{fk}(t)$. The average artefact $\hat{a}_k(t)$ that was used for the cleaning was obtained in parallel with $\hat{a}_{fk}(t)$, using data points from $x_k(t)$.

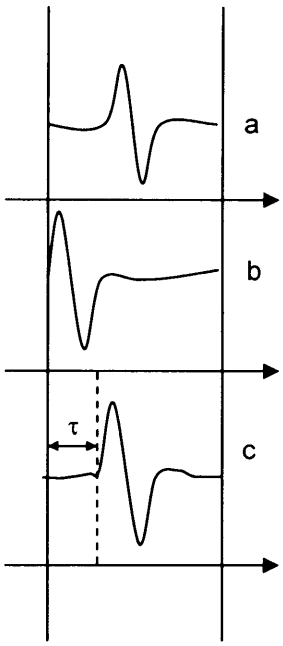

Figure 2-3 The best fit between $\hat{a}_{fk}(t)$ (a) and the current section of $x_{fk}(t)$ (b) was obtained for a τ shift. The current section was added after being aligned (c).

"EIT artefact trace" creation and subtraction. An "EIT artefact trace", which comprised a series of artefact templates $\hat{a}_k(t)$, was then created. Each artefact template was time locked to an EIT artefact in the EEG according to the time shifts calculated with the cross-correlation in the first part of the algorithm (Figure 2-4). If the maximum of the cross-correlation occurred for a positive shift of the averaged artefact then the gap from the previous template was zero padded, if it occurred for a negative shift instead, then the first part of the template was truncated.

The cleaned EEG raw trace was obtained by subtracting this "EIT artefact trace" from $x_k(t)$. If more than 30% of $x_{fk}(t)$ sections of the N^*T_g period were discarded while creating $\hat{a}_{fk}(t)$, the raw channel was substituted by a zero-line, the reason being that it was likely to be heavily corrupted. After all the channels had been cleaned the EEG segments were decimated to the original sampling rate and written out in a new file that had the same format as the original file.

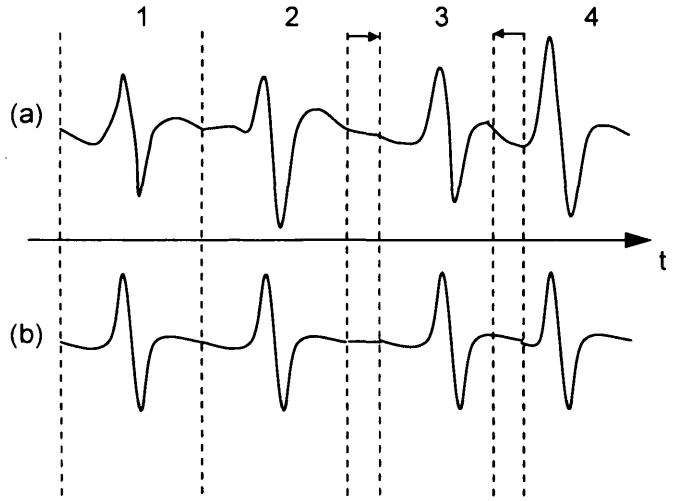

Figure 2-4 An EIT artefact trace was created with a series of artefact templates (b). Each template was time locked to a section of the EEG raw channel (a) according to the shifts τ for which the cross-correlation was maximum. In this diagram τ for section 1 and 2 was 0, for section 3 was negative (then the template had to be shifted forward and the gap between 2 and 3 zero-padded) and for section 4 was positive (then the template had to be shifted backward and the first part truncated).

2.2.3.2 Multiple EEG channel parallel processing

Instead of considering each EEG channel individually, the alignment between $\hat{a}_{fk}(t)$ and each EEG section T_r long could be achieved for one reference channel with the clearest EIT artefact and by time locking the artefact templates of the other channels accordingly.

Averaged artefact frequency and period length calculation. f_r and T_r were calculated as described in the previous section.

Reference channel selection. The reference channel was chosen from those that had a local peak in the frequency spectrum, in correspondence of $4f_r$. Among them the one with the highest SNR was chosen, defining:

$$SNR = \frac{P_p - P_b}{STE_b} \tag{2-7}$$

where P_p was the power at $4f_r$; P_b was the averaged power of the baseline, defined as the interval of the spectrum around $4f_r$ (±20% f_r) excluding a frequency interval around f_r of ±5% f_r; STE_b is the standard error of the baseline.

Reference EEG channel pre-processing. $x_k(t)$ was interpolated and a 50 Hz noise-free copy $x_{fk}(t)$ was generated as described in the previous section.

Multiple artefact template parallel creation. $\hat{a}_{fk}(t)$ and the time shifts to align each section of $x_{fk}(t)$ were calculated for the reference channel as described in the previous section. The same time shifts were used in parallel in all the other channels of $X(t)$ to create all the $\hat{a}_{fk}(t)$s. The "close fit" discrimination was performed independently in all the channels. If a section was not added to the reference channel $\hat{a}_{fk}(t)$, the corresponding sections were not added in the $\hat{a}_{fk}(t)$s of the other channels, the reason being that the alignment obtained was likely to not be accurate.

"EIT artefact trace" parallel creation and subtraction. An "EIT artefact trace" was created for each channel using the corresponding $\hat{a}_k(t)$ as described in the previous section, considering that the time shifts were all equal to the ones calculated for the reference channel. Each "EIT artefact trace" was then subtracted from the corresponding channel. If more than 30% of $x_{fk}(t)$ sections of the reference channel, over the N^*T_g period, were discarded while creating $\hat{a}_{fk}(t)$, then all the channels were substituted by zero-lines.

2.2.3.3 EIT artefact template scaling

The artefact template $\hat{a}_{fk}(t)$ could be adapted to each current section $s_{fk}(t)$ (T_r long) of $x_{fk}(t)$ by minimizing the difference (MSE) with respect to the parameter c as given by:

$$MSE = \int_{t=0}^{T_r} \left[s_{fk}(t) - c\hat{a}_{fk}(t) \right]^2 dt \tag{2-8}$$

If (2-8) was translated into the discrete domain by considering $\hat{a}_{fk}(t)$ and $s_{fk}(t)$ S samples long, then:

$$MSE = \sum_{i=1}^{S} \left[s_{fk}(i) - c\hat{a}_{fk}(i) \right]^2 \tag{2-9}$$

This minimization was done after the running average $\hat{a}_{fk}(t)$ and the current EEG section $s_{fk}(t)$ were aligned. Then each template $\hat{a}_k(t)$ was scaled using the optimised c-parameter before being subtracted from $x_k(t)$.

2.2.4 Clinical acceptability

Three male subjects, between 20 and 39 years old, undergoing pre-surgical assessment at King's College Hospital London, had 32 EIT electrodes (Ag/AgCl cup electrodes) attached to the head with Collodion, in a modified 10/20-placement system (Tidswell et al. 2001b). These were in addition to the normal 21 EEG electrodes placed using a modified Maudsley system (Binnie et al. 1982), which was employed in surgical planning. Each subject gave informed consent for the study, which was approved by the local committee on the Ethics of Human Research (Ref. 089/92). Where necessary, EIT electrodes were moved by up to 3mm to prevent shorting between EIT and EEG electrodes. Four EEG files of 15 minutes were acquired using the hardware filters. The four files were then processed using four software filter permutations:

1. *I+NoSc*: Individual sequential EEG channel timing processing;
2. *I+Sc*: Individual sequential EEG channel timing processing + EIT artefact template scaling;
3. *R+NoSc*: Single (Reference) EEG channel timing processing;
4. *R+Sc*: Single (Reference) EEG channel parallel processing + EIT artefact template scaling;

and submitted for evaluation to the two experienced EEG readers. They assessed the clinical reliability of each cleaned file with this evaluation scale (Hinrichs 1991):

1. Artefact obvious. EEG unreadable
2. Artefact recognisable. EEG significantly deteriorated in quality
3. Artefact recognisable. EEG still clinically usable
4. Sporadic and negligible small artefacts
5. EEG completely recovered

During the assessment, the files were presented in a random order and the readers were blinded to the software version and subject.

In clinical practice the EEG records should be available as soon as possible in order to give to the technicians a fast feedback on the state of the recording. The time taken for each software version to clean the files was also recorded.

2.3 Results

2.3.1 Hardware filter

Frequency components of up to 12 μV were present in the FFT of the unfiltered EIT artefact, which had peak-to-peak amplitude of about 2-3 mV (Figure 2-5a). Addition of the low pass filter reduced the number of the spikes (Figure 2-5b), whereas use of the high pass filter reduced the intensity of the spikes to ~<4 μV (Figure 2-5c). Using both filters reduced the spikes to <2 μV, except for mains interference at 50Hz (Figure
2-5d).

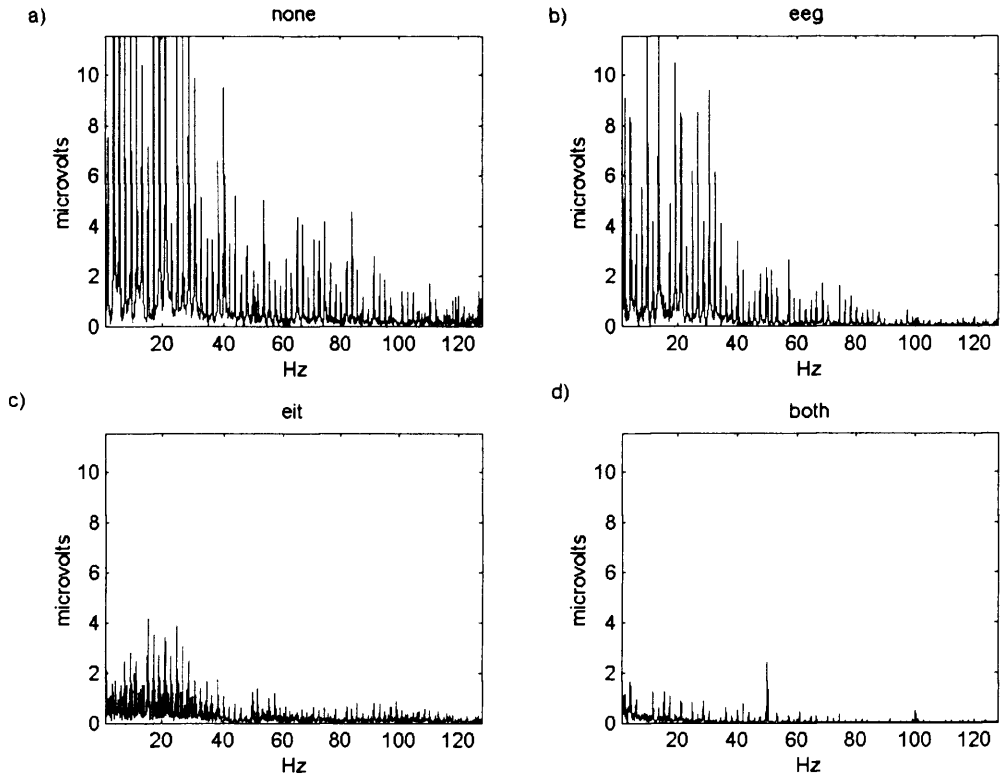

Figure 2-5 Example of FFT of 50 sec EEG traces: unfiltered (a); adding the low-pass filters in series with the EEG electrodes (b); adding the high-pass filters in series with the EIT electrodes (c) and adding both (d).

2.3.2 Artefact characterization

The size of the sample of artefact waveforms necessary to have a reliable average estimation was between 68 and 368 samples (Table 2-1), which was the number of artefact waveform need for the standard deviation to converge. The EEG recording of subject B was noisy and included large movement artefacts; therefore it was not

possible to obtain a standard deviation not influenced by outliers. In the worst cases (not considering subject B) 10% of the periods were removed as outliers.

Table 2-1 Artefact period length (Art_pr), number of artefact waveforms in 15 minutes (N_pr), total number of outliers removed (Outliers) and sample size to represent the artefact population (S) for each EEG channel recording and equivalent time.

Subject	EEG	Art_pr (s)	N_pr	Outliers	S	Time
A	a1	0.4145	2143	23	232	96 sec
	a2	0.4585	1946	6	68	31 sec
B	b1	0.415	2049	880	/	/
C	c1	0.4145	2167	10	368	152 sec
D	d1	0.415	2164	232	283	117 sec
F	f1	0.5865	1484	140	174	102 sec

Reducing the waveform sample size from 500 to 400, 200, 100 elements without outlier removal for EEG channel recording b1, c1, d1 did not significantly change the artefact template, with respect to the one calculated using 500 waveforms excluding outliers (Figure 2-6). The same figures illustrate that the peak-to-peak amplitude of these averaged artefacts could vary between 70 μV and 280 μV.

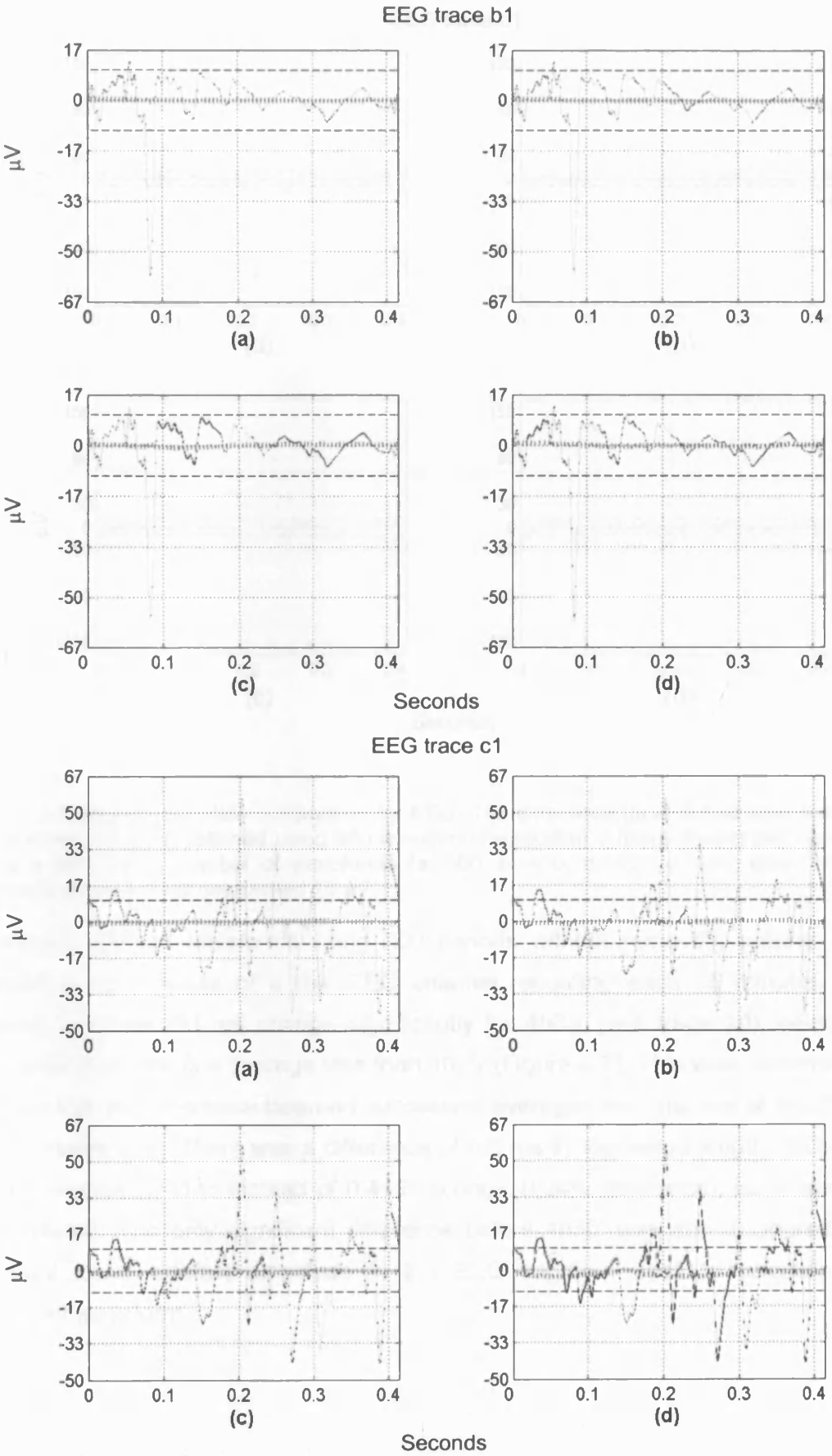
EEG trace b1
μV
17
0
-17
-33
-50
-67
0 0.1 0.2 0.3 0.4
(a)
(b)
(c)
(d)
Seconds
EEG trace c1
67
50
33
17
0
-17
-33
-50
Seconds

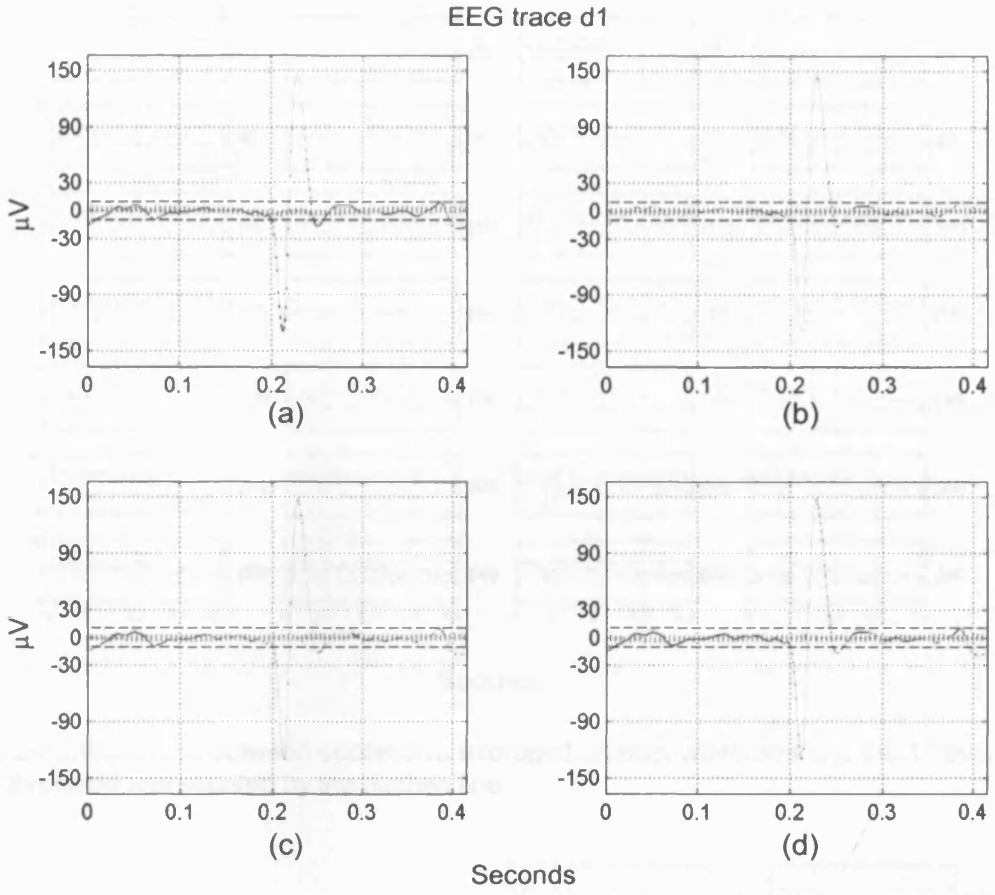

Figure 2-6 Artefact template comparison for EEG. The difference (bold dotted line) between the artefact template obtained using 500 waveforms excluding outliers (black) and obtained using a decreasing number of waveforms (a: 500; b: 400; c: 200; d: 100; grey) without removing outliers does not exceed 10 μV.

Averaged artefact waveforms using 500 periods without removing outliers were calculated for 7 hours of a raw EEG channel recording each 15 minutes. The artefact template did not change significantly for 4h30' (see trace 20), being the difference from the first average less than 10μV (Figure 2-7). This was confirmed by the fact that the difference between successive averages and the one at 4h30' was lower (Figure 2-8). There was a difference of 0.5 ms in the period length calculated for 4 averages (0.4145 instead of 0.415 seconds, 0.24% difference), but it was not time related. The only significant difference before 4h30' was due to unpredicted constant lower artefact amplitude in the EEG segment used to calculate the averaged waveform.

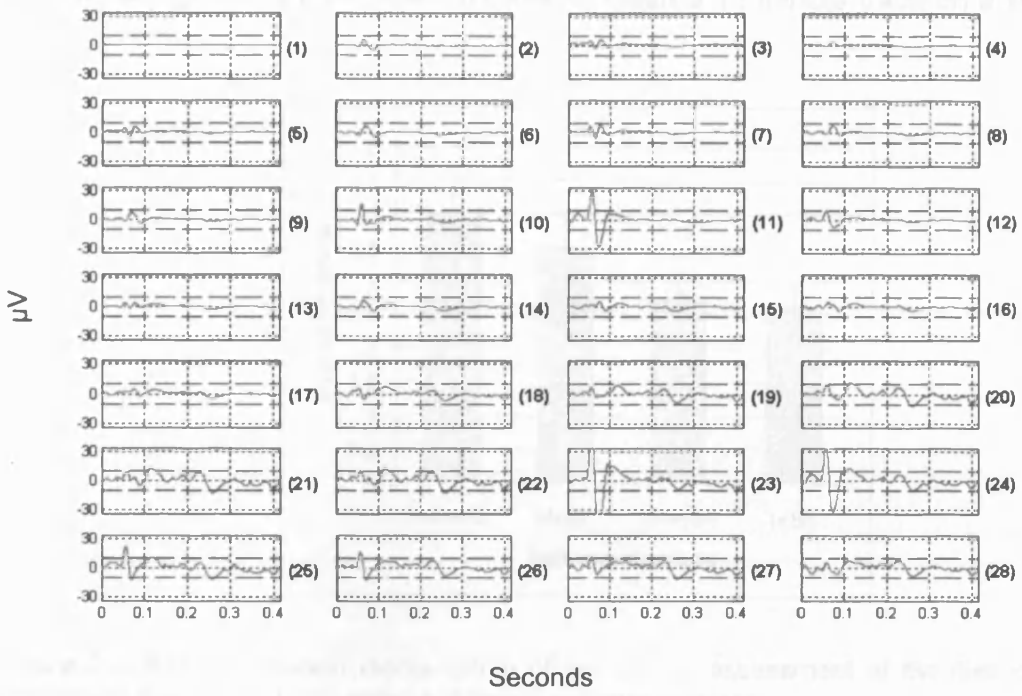

Figure 2-7 Differences between successive averaged artefact waveform and the 1st average. 10 μV threshold represented by the dashed line

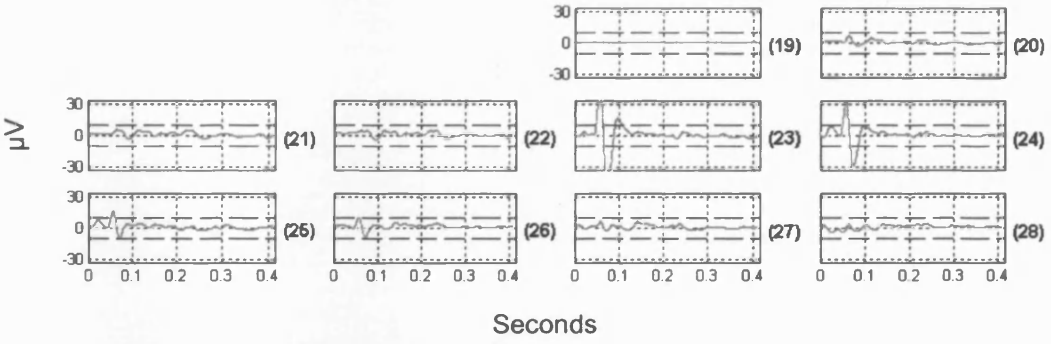

Figure 2-8 Difference between successive averaged artefact waveform and the 19th average. 10 μV threshold represented by the dashed line

In view of these findings, outlier exclusion was abandoned and further findings were obtained with inclusion of all segments. As it appeared empirically that using a larger number did not make a significant difference, 100 averages were utilised to generate artefact templates. These settings were employed in the clinical studies in the following section.

2.3.3 Software filter and clinical acceptability

The software version using single EEG channel timing processing without EIT artefact scaling gave the best performances (Figure 2-9, Figure 2-10) and it was the

fastest, taking 3'38'' ± 8.8'' (mean±SD, n=4) to clean a 15 minute trace on a standard PC.

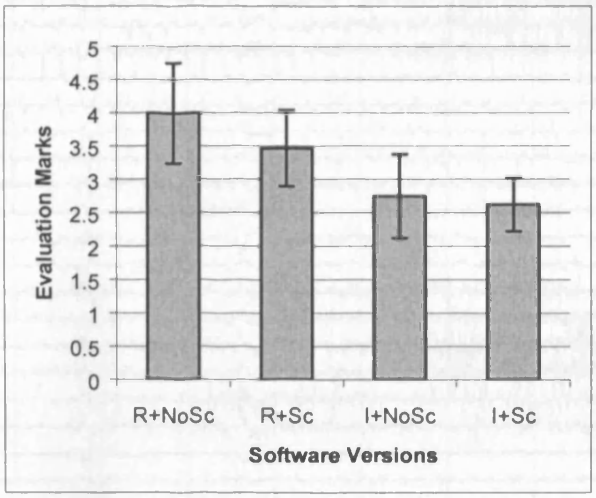

Figure 2-9 Mean evaluation marks (±SD) of the clinical assessment of the files obtained processing four 15min EEG, using 4 different software versions.

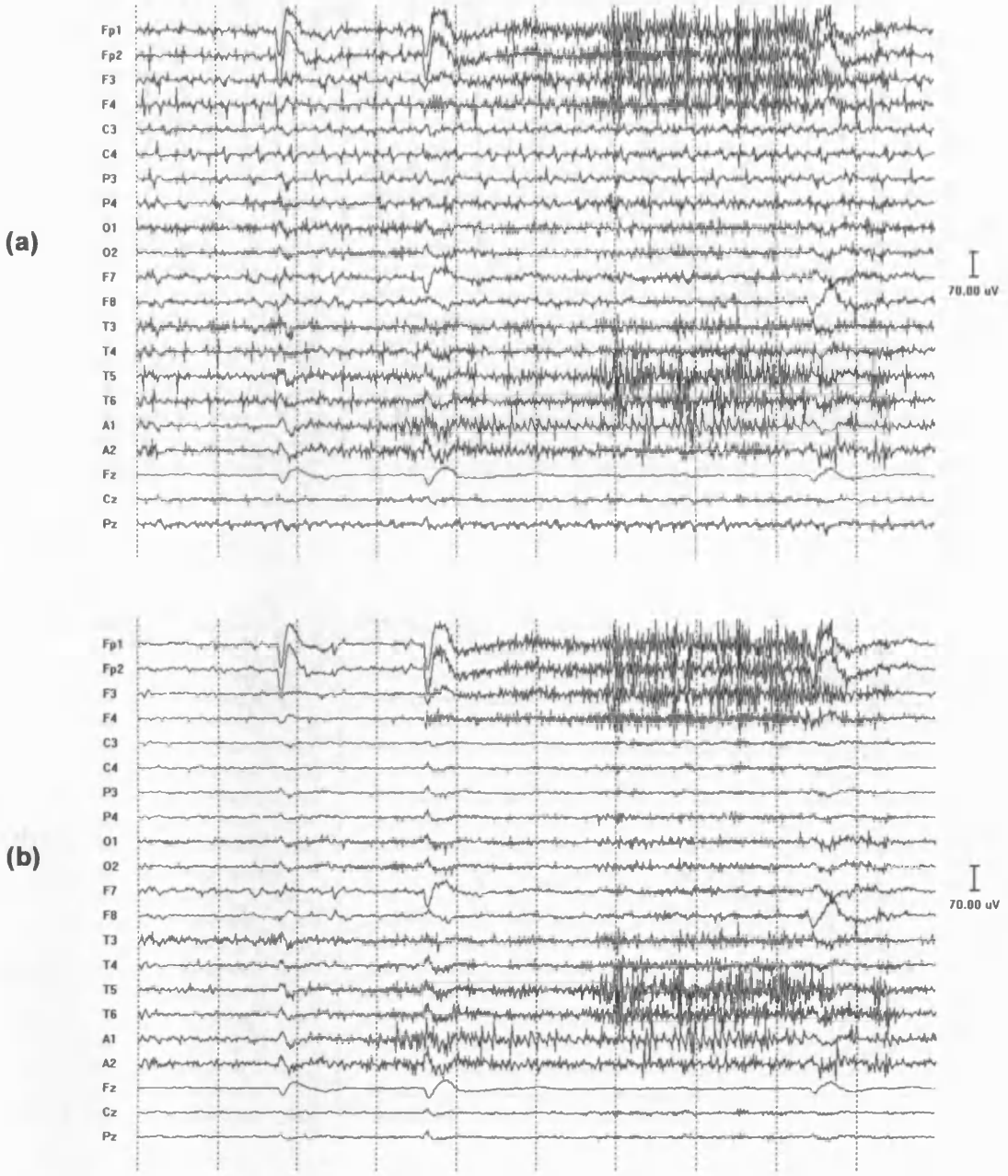
(a)
Fp1
Fp2
F3
F4
C3
C4
P3
P4
O1
O2
F7
F8
T3
T4
T5
T6
A1
A2
Fz
Cz
Pz
70.00 uV
(b)
Fp1
Fp2
F3
F4
C3
C4
P3
P4
O1
O2
F7
F8
T3
T4
T5
T6
A1
A2
Fz
Cz
Pz
70.00 uV

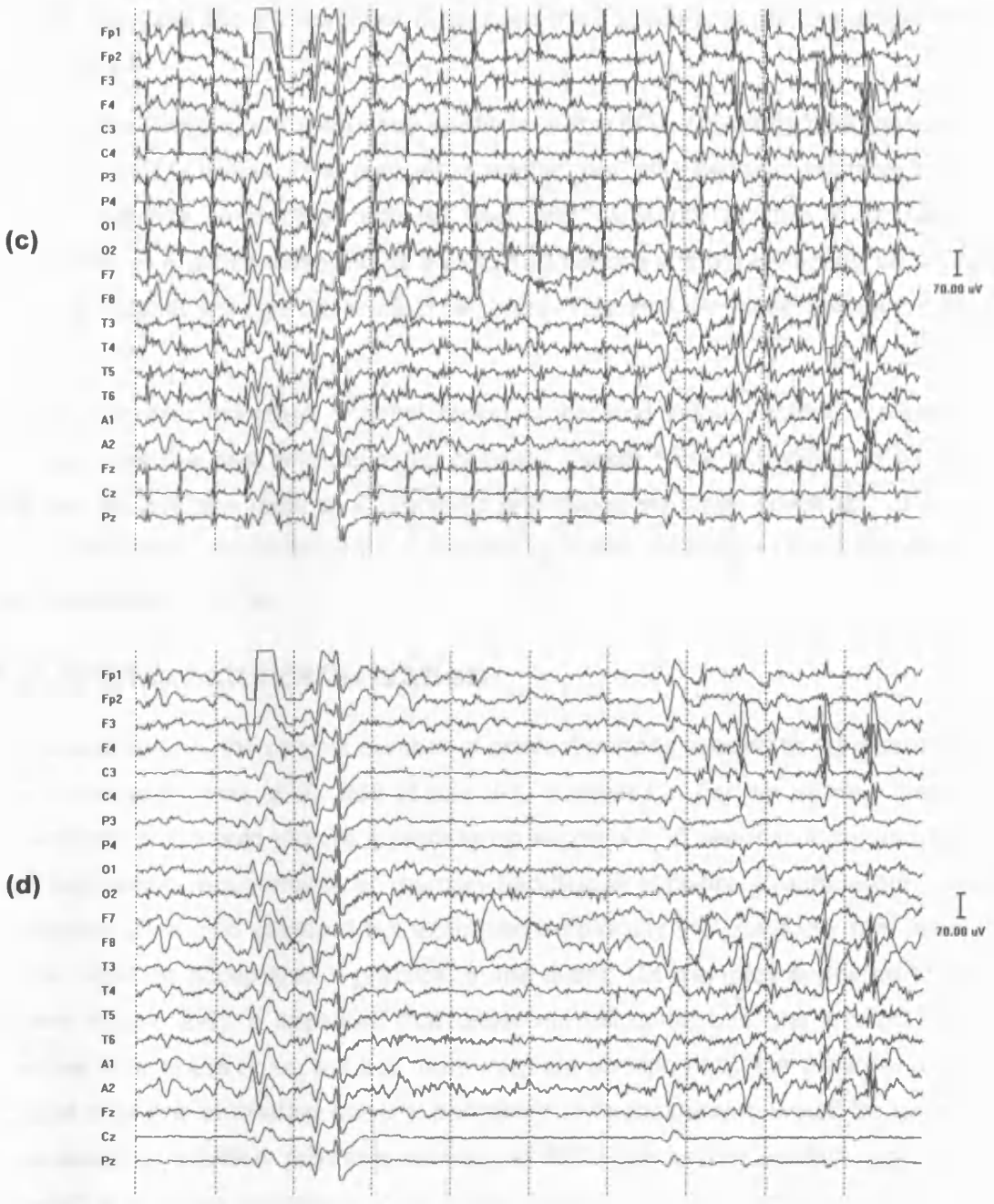

Figure 2-10 Examples of filtered EEG. These were acquired after hardware filtering for patient 3 (a) and 1 (c) and after software filtering (b, d) with individual channel timing correction without scaling. Each division represents 1 second.

2.4 Discussion

2.4.1 Summary of results

The spectral analysis showed the presence of frequency spikes in the EIT artefact of about 12 μV. The interposition of a low pass filter before the EEG amplifiers and of a

high pass filter after the EIT switches decreased the components and the amplitude of these spikes.

After hardware filtering, low frequency artefacts at the EIT acquisition rate were still present in the EEG traces. The number of artefact periods needed to represent the artefact accurately, excluding outliers, was 368 elements in the worst case. Nevertheless, in practice, reducing its size to 100 periods without excluding outliers, did not significantly change the artefact template. This also remained constant over 4h30'.

The approach with individual channel timing processing without outlier correction appeared to be the best and delivered clinically usable EEG recordings in all the cases with an average mark of 4 (sporadic and negligible small artefacts). It also gave the best performance in terms of processing speed, filtering an EEG file at four times the acquisition time.

2.4.2 Artefact characterisation

On statistical testing, the optimal number of artefact periods needed to represent the artefact accurately was about 368 (Table 2-1, Subject C). For an artefact lasting 0.42 seconds, this would require a processing segment 155 seconds long, and this placed substantial requirements on memory handling in software. We therefore took 500 samples as a gold standard but examined empirically the possibility that fewer samples might be acceptable in practice. In the event, 100 samples appeared to be sufficient (Figure 2-6). It appeared that under normal conditions, the artefact was stable over four hours or so, but this more frequent updating had the potential merit that rapid changes in artefact pattern, perhaps due to movement, would be rapidly compensated. In addition, providing sections of EEG with severe artefact had been eliminated, it was not necessary to eliminate outliers, and this further speeded up processing.

Our compromise was to use 100 periods to calculate the averaged artefact with simple global artefact and to refresh the template every time.

2.4.3 Software filter: best method

Single channel (Reference) EEG channel timing processing produced the simplest and fastest software version and gave the best performances in terms of clinical acceptability. The superiority in respect to the other versions is probably because the EIT artefact can have low amplitude in reference to the background EEG. In the

case of individual sequential EEG channel processing, the cross-correlation was likely to fail in these channels. It seemed reasonable that the timing of artefacts was constant across channels, so that use of this timing data might be expected to yield good results for all channels. In contrast, individual template scaling might have been expected to produce better results, but, in the event did not. This was probably because scaling would have yielded inaccurate results in the presence of concurrent EEG for artefact with low amplitude.

2.4.4 Clinical acceptability

The EIT artefact subtraction reduced the occurrence of the artefact spikes, suggesting that the average artefact waveform calculated with the method was a good representation of the waveform population. However, there were still occasional residual artefacts after subtraction; these were presumably due to differences between the averaged and each single artefact waveforms because of intraindividual artefact variations. The two EEG readers did not consider this spurious signal as a significant problem, and considered the quality of the cleaned files suitable for EEG reporting.

2.4.5 Comparison with fMRI

The application of our best method gave positive results in cleaning EEG traces contaminated by artefact due to simultaneous EIT recording. These were comparable with the results obtained by applying a similar technique for the removal of artefacts in the EEG recorded during spike-triggered and continuous fMRI.

Although they have different origins, EIT and fMRI artefacts can be both separated from the underlying EEG through artefact time alignment and averaging. In fMRI, the artefact time alignment was achieved by time-locking EEG segments to an external signal that represented the cause of the artefacts. This can be:

- the ECG, in case of artefacts related to the blood flow effects in the static field of the MR scanner (Pulse Artefact, PA) (Allen et al. 1998) or
- the commands that control the beginning of the MRI image acquisition sequence, in case of artefacts related to the changing field applied during fMRI image acquisition (Sijbers et al. 1999; Allen et al. 2000; Garreffa et al. 2003).

In our best method, instead, the reference signal was a channel of the EEG itself automatically selected by the software as the one with most recognisable artefact.

The amplitude of the artefacts was different for EIT and for fMRI. In the former case it has been shown that the averaged artefact can have peak-to-peak (pk-pk) amplitude between 70 and 280 μV. The artefacts due to the fMRI considered for artefact average subtraction have two different amplitudes, depending on the cause. The Pulse Artefact has an averaged pk-pk amplitude of 36 μV (Allen et al. 1998), while the magnetic field gradient related artefact has a median value of 4.0 mV pk-pk, that was reduced to 571 μV after software down-sampling and low-pass filtering (Allen et al. 2000). Due to this high amplitude, EEG recording systems with high dynamic range have to be used in fMRI so that the EEG amplifiers do not saturate. In the EIT case, standard EEG systems can be used.

Both fMRI artefacts and EIT artefacts have unpredictable intra-individual amplitude variation and large inter-individual difference in amplitude and shape. This results in a small divergence between the averaged artefact and each current artefact, leading to a residual spurious signal in the correct trace. Our two experienced EEG readers did not consider this a significant problem and the same conclusion has been drawn in the fMRI studies; actually both processing techniques retain typical EEG characteristics.

At present, our method works only off-line, while on-line processing for fMRI has been developed (Garreffa et al. 2003), but it is fully automated as other EEG-fMRI processing tools (Sijbers et al. 1999). The fMRI technique takes less than 1/5 of the length of the EEG recording to process it, being less computationally expensive than the presented algorithm. However, only 4 EEG channels were processed for this timing, whereas 21 were processed with this EIT algorithm. The optimization of the processing code had not been considered in this study, as this was written in the high level language MATLAB. If this method proves to be clinically useful, then it is likely that the procedure can be optimised to run in real time with a more powerful processor and lower level processing language.

2.4.6 Future work

Further improvement may be possible by using the clock signal of the EIT system, which marks the beginning of the EIT frame collection to time lock the templates to each artefact waveform, so avoiding the cross-correlation. Placement of the EEG and EIT electrodes, to keep them further apart, keeping a broad coverage of the scalp, and a proper skin abrasion to decrease the electrode-skin contact impedance, could decrease the amplitude of the artefact seen in the EEG. The problem could also be tackled in the frequency domain or with techniques such as principal or

independent component analysis or blind sources separation. The artefact generated while sharing the same electrodes between the EEG and the EIT could also be investigated, but will require the use of EEG amplifiers with a high dynamic range. In this study, we only explored the use of separate electrodes.

Although more sophisticated methods may reduce further the residual artefacts, we have demonstrated that the method described here has clinical utility in its present form. This will enable preliminary studies of EIT to be conducted in parallel with EEG in a clinical environment, without interfering with routine EEG.

Chapter 3 – Pilot study on identification of regional conductivity changes using scalp electrodes during epileptic seizures in humans

3.1 Introduction

The local impedance change may be expected to be of about 10% during epilepsy when recorded with an applied current of some tens of kHz (Section 1.2.5.2). It is not exactly know what is the magnitude when this is recorded with scalp electrodes. However this may expected to be attenuated due to partial volume effects, the shunting of the current by CSF and scalp, and resistance of the skull. This has been modelled in my group for the specific case of visual evoked potentials recorded near DC and local changes were attenuated by 3 orders of magnitude (Gilad et al. 2005b). I epilepsy it may be expected that larger volumes of cortex would be activated and, at least in some stages, would be in superficial cortex. A reasonable estimate, therefore, would be that an upper bound for the expected impedance changes in this study would be 0.1%. The study presented in this chapter was the first attempt to build on the previous development work and collect EIT data and images under the challenging conditions of recording over days in epileptic patients observed on the ward.

3.1.1 Purpose

The purpose of the present study was to assess, for the first time, if large-scale changes in conductivity due to epileptic activity could reproducibly be measured with EIT from scalp electrodes in human subjects. These would be measured in the form of boundary voltage variation and localised in reconstructed tomographic images. Measuring impedance changes related to spontaneous seizures from scalp electrodes may be predicted to suffer from several technical problems. First, using scalp electrodes, the current that will flow through the brain will be considerably reduced with respect to that in the scalp, owing to the high skull resistivity, and the voltage changes at the boundary due to impedance changes in the brain will be small. Secondly, seizures are an unpredictable event, which prevent the possibility of controlled experiment and often involves dramatic movement of the subject, which were inhibited in animal studies with anesthetization or brain stem transection. Therefore large motion artefacts in the baseline might obscure the signal due to seizures. In addition, the EIT procedure injects a large artefact into the EEG signal, which must be recorded simultaneously for clinical purposes (Chapter 2).

3.1.2 Experimental design

EIT was set to run continuously together with the EEG on 7 patients undergoing pre-surgical assessment for Neurosurgery at King's College Hospital London. EIT was recorded using the UCLH-EIT Mark 1b (Yerworth et al. 2002) which utilized a single impedance 4 terminal measuring circuit multiplexed up to 31 electrodes. Segments of the two recordings close to seizures were considered together. The boundary voltage measurements were normalized to a period preceeding the epilepsy onset chosen as baseline, which represented their value during normal brain activity. The conductivity changes characteristic of a seizure would then translate in a significant deviation of the boundary voltages from the baseline of some fractions of percent in the period immediately before the seizure onset (pre-onset period; figure 1). A delay of up to 60 seconds between the impedance change and the scalp EEG onset could be expected due to the time the epileptic activity takes to build up and propagate from the deep focus to the brain surface (Section 1.2.5.3). After being normalized and filtered, measurement combinations, which were likely to be corrupted, were eliminated and the significance and size of the remaining voltage changes were assessed. A set of other EIT segments not related to any seizure was analysed with the same method to determine whether these changes occurred in concurrence with epilepsy. Image reconstruction of the data obtained at the seizure onset was done using a linear algorithm based on truncated singular value decomposition (tSVD), with the sensitivity matrix constrained to the brain. The results were then visually inspected and compared to the EEG, video and MRI findings.

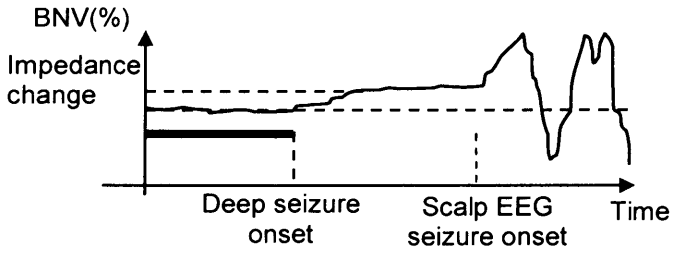

Figure 3-1 Example of a boundary voltage measurement (BNV). In most of the cases in this study, seizure onset was in the deep mesial temporal lobe. Activity would commence here and then only spread to the surface cortex after several seconds. The scalp EEG only detects activity in superficial cortex so, in the ideal case, EIT would detect impedance changes due to the deep onset several seconds before the scalp EEG changed or clinical activity could be seen. The period between the end of the baseline (black bar) and therefore deep seizure onset, and the scalp EEG onset, was termed the pre-onset period (grey bar) and was the period during which we expect to see the boundary voltage changes.

In the study, impedance was recorded using the UCLH Mark 1b system, in which constant current was injected, and the in-phase component of the resulting voltages were recorded and used to calculate the transfer impedance. The terms "impedance" or "voltage" below were used interchangeably and refer to this in-phase component which strictly was the real component of the transfer impedance.

3.2 Methods

3.2.1 Trial set-up

Seven patients undergoing pre-surgical assessment for Neurosurgery at the King's College Hospital, London were voluntarily recruited for this study (Table 3-1). Each subject gave informed consent for the study, which was approved by the local committee on the Ethics of Human Research. EIT and video-EEG ran continuously with two separated sets of electrodes for periods of 2 to 10 days in order to collect data during spontaneous epileptic seizures.

Table 3-1 Patients characteristics, including MRI and EEG findings and doctor diagnosis. (MTS = mesio-temporal sclerosis; DNET = dysembryoblastic neuroepithelial tumour; CPS = complex partial seizure).

Subject	Gender	Age	MRI	EEG	Diagnosis
1	male	20	No definite abnormalities	Rt posterior temporal/ mid-temporal	CPS, Rt temporal onset
2	female	37	Rt MTS	Rt fronto-temporal, some Lt involvement. Not conclusive	CPS, Rt superior frontal/ pre-frontal on-set with gradual spreading
3	male	30	Lt DNET at parahippocampal gyrus	Rt fronto-temporal onset, some Lt temporal involvement	CPS, onset on the Lt parahippocampal gyrus with rapid spread to the Rt
4	male	32	No definite abnormalities	No clear lateralization	Lt occipital onset
5	female	26	Lt MTS and abnormalities in inferior part	No clear lateralization, possibly Rt predominance	Inferior Lt temporal onset
6	male	39	Lt frontal convexity cavernous haemangioma	No clear lateralization, possibly Lt onset	Lt frontal onset
7	male	20	Lt hippocampal atrophy	Lt fronto-temporal onset	CPS, Lt temporal onset

The EEG was recorded with 21 electrodes in a modified Maudsley electrode placement system (Binnie et al. 1982) and 32 similar additional EIT electrodes were applied in a

modified 10-20 electrode placement system (Figure 3-2). Standard 10 mm diameter silver/silver-chloride EEG cup electrodes were used for both systems and electrode paste was applied every morning to enhance the contact impedance.

The filter described in Chapter 2 was required to remove the EIT artefact on the EEG. The EIT measuring current injected was of 2.2mA at 38.4kHz from diametrically opposed electrodes. Time difference images of conductivity were reconstructed from boundary voltage variations with respect to a period preceding the seizures (baseline), using a linear algorithm based on truncated singular value decomposition. Each image was obtained starting from sets of 258 boundary voltage measurements collected with a sampling rate of 2-2.5 Hz (one full image data set collection every 0.4-0.5 seconds).

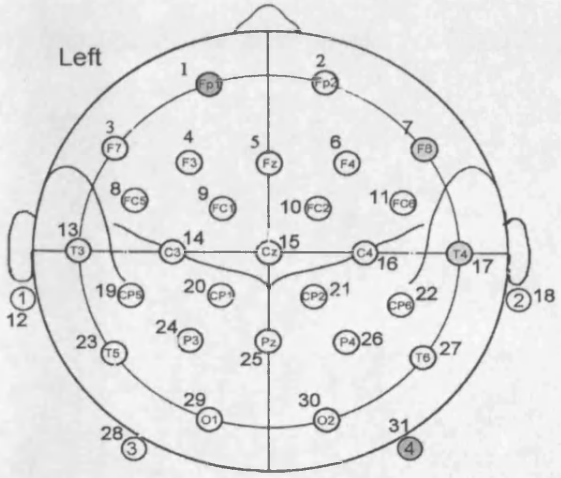

Figure 3-2 EIT electrodes positions. Electrode positions 12-18-28-31 were added to the International 10-20 system and the electrodes of the mid-line (Fz, Cz and Pz) were placed 1 cm behind the normal positions (modified from Tidswell el al. 2001).

3.2.2 Raw data processing

EIT impedance measurement segments of 50-190 seconds were analyzed in relation to the onset of the EEG (EEG onset) and the one observed on the video (Clinical onset).

Preliminary impedance measurement elimination. Each segment included measurements from 258 drive-receive electrode combinations (EC), which were median filtered with a window 5 data samples long. EC have been discarded if the absolute value of the voltage measured was exceeding 4.8 V or going below 0.2 V for more than 70% of the length of the segment.

Baseline selection. The baseline was chosen, after visual inspection of all the remaining EC (ECR), as a period of 20 seconds with no significant voltage variations starting no more than 90 seconds before the scalp seizure onset. The baseline had to satisfy the following criteria:

(i) less than 10% of ECR had to have a standard deviation during the baseline greater than 2% of the baseline, after linear baseline correction (see below);

(ii) without considering this additional ECR subset, the absolute slope of the linear fit to the 20 seconds following the baseline had to be larger than the absolute slope of the linear fit to the baseline in more than 50% of the recording combinations (Figure 3-3).

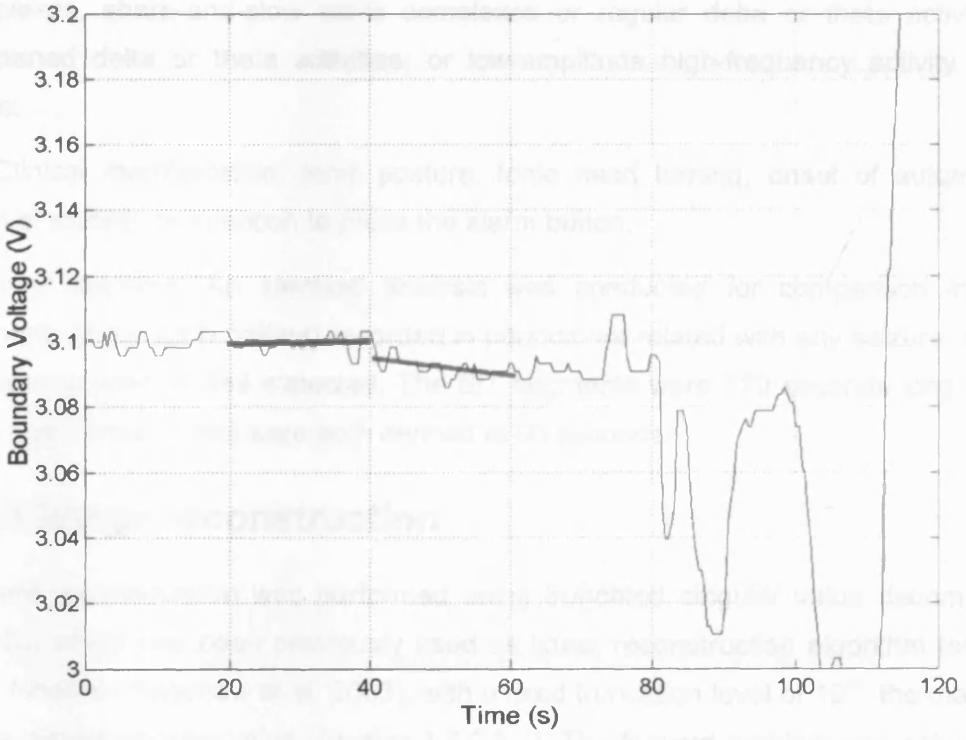

Figure 3-3 The trend of the linear fit to the 20 seconds following the baseline (green) was larger than the trend of the linear fit to the baseline (red) in this example of a boundary voltage measurement from subject 1, seizure 1 (EEG onset at 80 sec; Clinical onset at 76 sec).

Baseline correction and outlier elimination. ECR were low-pass filtered (35th order FIR filter, -6dB point at 0.2 Hz) and for each ECR a least-squares procedure was employed to find the best linear fit to the baseline period (Boone et al. 1994). The slope and intercept of this line were then used to correct all the traces, which were expressed as a percentage change respect to the mean value of the baseline. If the standard deviation during the baseline period was exceeding 2% or changes larger than +/- 10% were

seen for more than 50 % of the period between the end of the baseline and the seizure onset, the ECR was discarded. For clarity we will refer to the remaining normalized boundary voltage as NBV.

Scalp pre-onset period. The scalp pre-onset period was defined as the period between the end of the baseline and the first of the following events:

(i) Movement artefact on the boundary voltage recordings: sudden change within 3 data points of more than 1% occurring in the trace obtained as the average of the absolute value of the NBV;

(ii) EEG onset: clear ictal patterns, such as rhythmic sharp waves, spike-and-slow wave complexes, sharp-and-slow wave complexes or regular delta or theta activities, or sharpened delta or theta activities, or low-amplitude high-frequency activity in beta range;

(iii) Clinical manifestation: tonic posture, tonic head turning, onset of automatisms, onset of staring, or intention to press the alarm button.

'Dummy' seizures. An identical analysis was conducted for comparison in 7 EIT segments (1 for each patient) recorded in periods not related with any seizure. Here no impedance change was expected. The EIT segments were 120 seconds long and the EEG and Clinical onset were both defined at 90 seconds.

3.2.3 Image reconstruction

A linear reconstruction was performed using truncated singular value decomposition (TSVD), which has been previously used as linear reconstruction algorithm for EIT of brain function (Bagshaw et al. 2003), with a fixed truncation level of 10^{-3} the magnitude of the largest singular value (Section 1.2.2.2.1). The forward problem was solved using a UCL group modified version of EIDORS-3D Toolkit (Polydorides N and Lionheart W.R.B. 2002) and a realistic head shaped 4 layer model (scalp, skull, CSF, brain) of 136000 elements generated with I-DEAS software (Tizzard et al. 2005). The conductivity values given to each compartment were: 0.15 S/m for the scalp, 0.015 S/m for the skull, 1.79 S/m for the CSF, 0.37 S/m for the brain. The sensitivity matrix was calculated for the whole head and then constrained to the brain region. This was done only once since the used head mesh and measuring protocol were standard for all the patients. The rows of the sensitivity matrix corresponding to the measurement

combinations discarded in the raw data processing were removed before the pseudo-inversion. The data used to reconstruct the images were the average of 3 individual data sets. This was done to reduce the high frequency noise in the data and to look for significant changes occurring over a time-scale of a few seconds (Fox et al. 2004).

This approach alters the relation between the reconstructed change within the image and the boundary voltages. In order to correct for this, the conductivity value of each voxel of the reconstructed image was multiplied by a scaling factor of 3.5. This factor was determined according to an empirical calibration based on simulations of spherical conductivity increases of 5%, 10% and 15% of 20mm radius in 3 different positions of the brain. Those represented the range of impedance changes expected during epilepsy (Section 1.2.5.2).

3.3 Results

A total of 22 seizures in 7 patients were collected with simultaneous EIT and EEG, ranging from 1 seizure to 6 seizures per subject. In 3 seizures, it was not possible to find a baseline period that satisfied the criteria described above and were not considered further.

3.3.1 Technical issues

All the necessary electrodes (31+1 for the EIT and 19+1 for the EEG) were successfully positioned on the patients' head. The level of current was insensible in all subjects and they were all willing in carry on with the experiments. The EEG was recovered accurately with the filtering and allowed the clinical diagnosis of the epileptic conditions.

3.3.2 Raw voltage changes

No reproducible changes were observed during seizures and the changes were substantially larger than the estimated magnitude of 0.1%.

The baseline periods ended between 80 to 5 seconds before the EEG onset and the absolute trend of the linear fit after the baseline was larger than that of the baseline in between 55.3% and 97.8% of the electrode combinations considered in each seizure. The total amount of electrode combinations eliminated per seizure according to the criteria described in Section 3.2.2 ranged from 3.5 to 43.4%. In 15 seizures, the

normalized boundary voltage (NBV) diverged at the EEG onset, or at the clinical onset if it occurred earlier, with a standard deviation between 1.1 and 7.6 %; the remaining 4 seizures had a standard deviation exceeding 13% (Table 3-2).

Table 3-2 Parameters calculated for each seizure: percentage of electrode combinations with an increase of the trend of the linear fit after the baseline (I.T.); total amount of electrodes combinations eliminated (EC.E.); standard deviation of the boundary voltage samples at the first onset (EEG or Clinical) (S.C.).

Subject	1						2	3			4		5
Seizure	1	2	3	4	5	6	1	1	2	3	1	2	1
I.T.	66.9	95.4	96.5	82.7	88.9	75.6	57.7	90.5	81.1	88	92.1	55.3	80.7
EC.E.	7.4	20.5	34.9	21.3	43.4	3.5	3.9	17	19.4	18.6	6.6	15.1	7.4
S.C.	2.1	4.8	15	4.1	53	1.2	1.7	3	3.1	1.1	13.3	2.6	4.9

Subject	6			7		
Seizure	1	2	3	1	2	3
I.T.	94.7	74.6	70.2	97.1	74.5	97.8
EC.E.	5.4	3.9	6.2	40.3	5.4	30.6
S.C.	2.2	3.8	5.6	4.8	7.6	14.3

Similar results were obtained for the EIT segments not related with any seizure (Table 3-3). The absolute trend of the linear fit after the baseline was larger than that of the baseline in 64%-92% of the electrode combinations. The total amount of electrode combinations eliminated ranged from 3.5% to 18.2% and the NBV had a standard deviation at the 'EEG onset' between 1 and 5.4%.

Table 3-3 Parameter calculated for each 'dummy'seizure.

Subject	1	2	3	4	5	6	7
I.T.	92.1	83.7	70.7	67.6	78.4	79.9	64.5
EC.E.	12.4	10.8	18.2	8.9	4.6	3.5	4.6
S.C.	3.7	5.4	4.4	3	1	1.3	1.4

Images have been reconstructed using the remaining electrode combinations (NBV) for all the real seizures (Figure 3-4) and the 'dummy' (Figure 3-5) and no consistent changes between or within subjects could be recognised in them . In 6 out of 19 seizures, localized conductivity decreases could be recognised together with other broader changes before seizure onset and only two seizures of subject 1 had similar location and time course. All the localized conductivity changes reconstructed were of 60% up to 450% in regions of the brain not concordant with the EEG and MRI findings (Figure 3-6; Table 3-4).

Subject 1

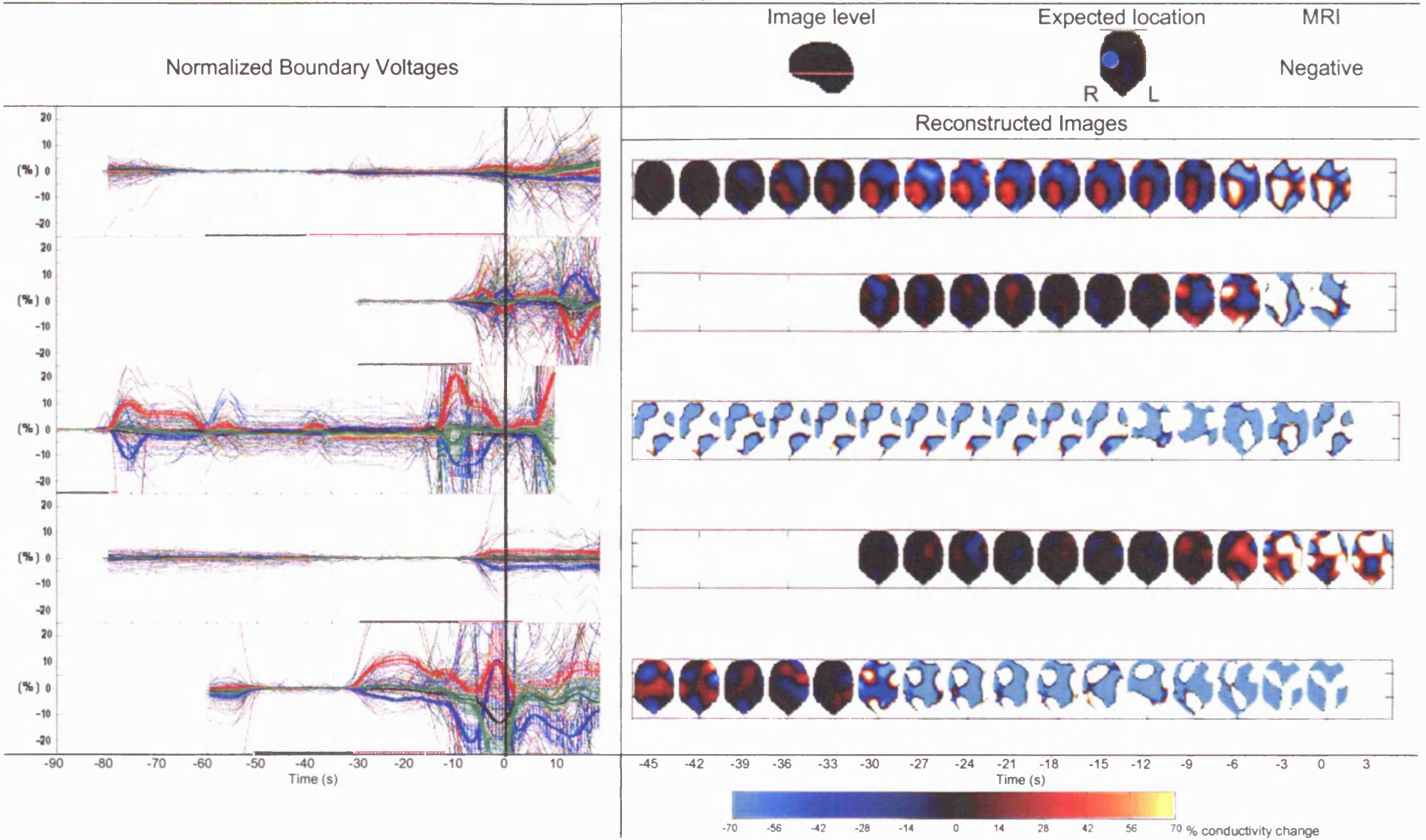
Normalized Boundary Voltages
Image level
Expected location
MRI
R
L
Negative
Reconstructed Images
20
10
(%) 0
-10
-20
-90 -80 -70 -60 -50 -40 -30 -20 -10 0 10
Time (s)
-45 -42 -39 -36 -33 -30 -27 -24 -21 -18 -15 -12 -9 -6 -3 0 3
Time (s)
-70 -56 -42 -28 -14 0 14 28 42 56 70 % conductivity change

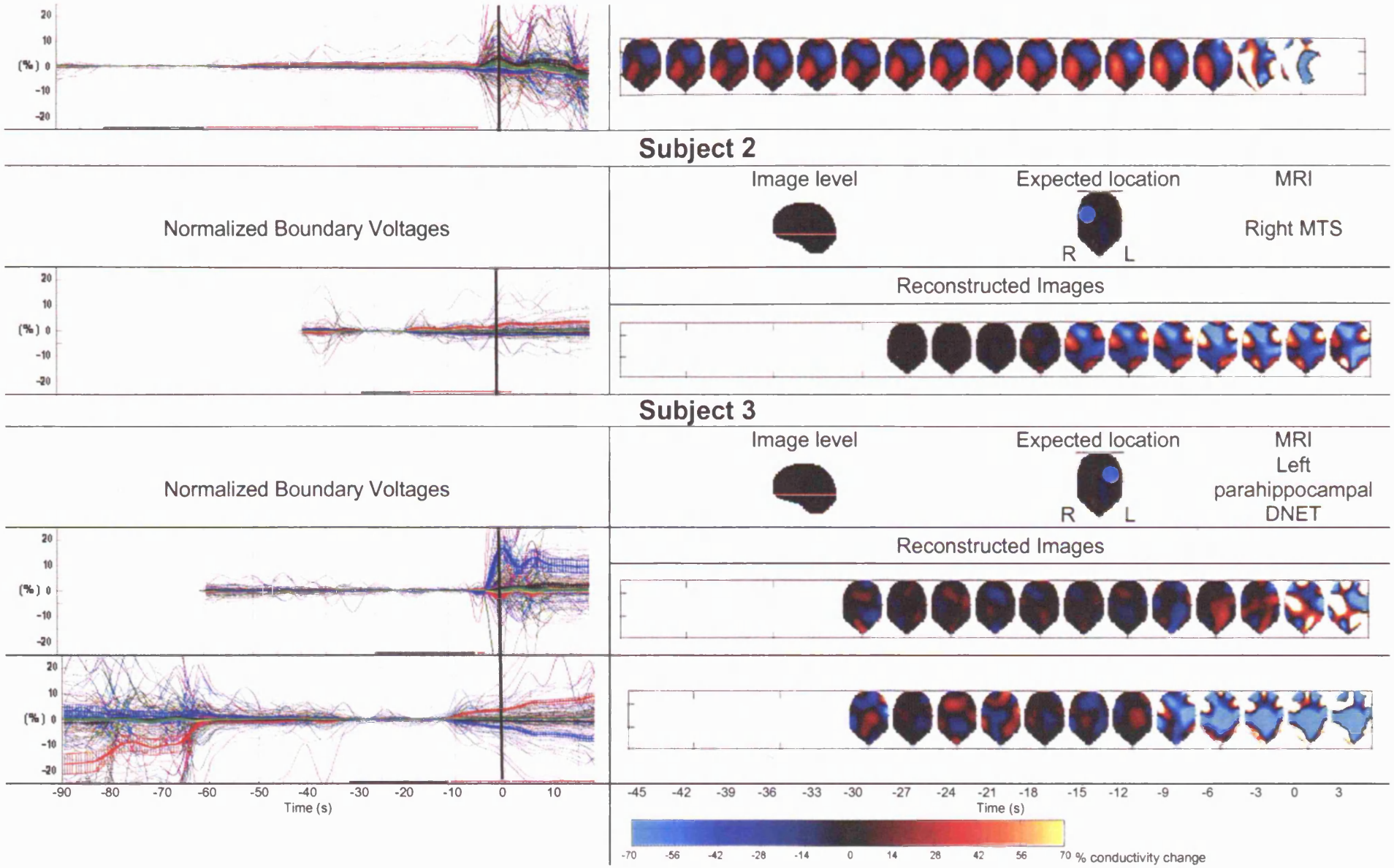
Subject 2
Image level
Expected location
MRI
Right MTS
R
L
Normalized Boundary Voltages
Reconstructed Images
Subject 3
Image level
Expected location
MRI
Left
parahippocampal
DNET
R
L
Normalized Boundary Voltages
Reconstructed Images
20
10
(%) 0
-10
-20
-90 -80 -70 -60 -50 -40 -30 -20 -10 0 10
Time (s)
-45 -42 -39 -36 -33 -30 -27 -24 -21 -18 -15 -12 -9 -6 -3 0 3
Time (s)
-70 -56 -42 -28 -14 0 14 28 42 56 70 % conductivity change

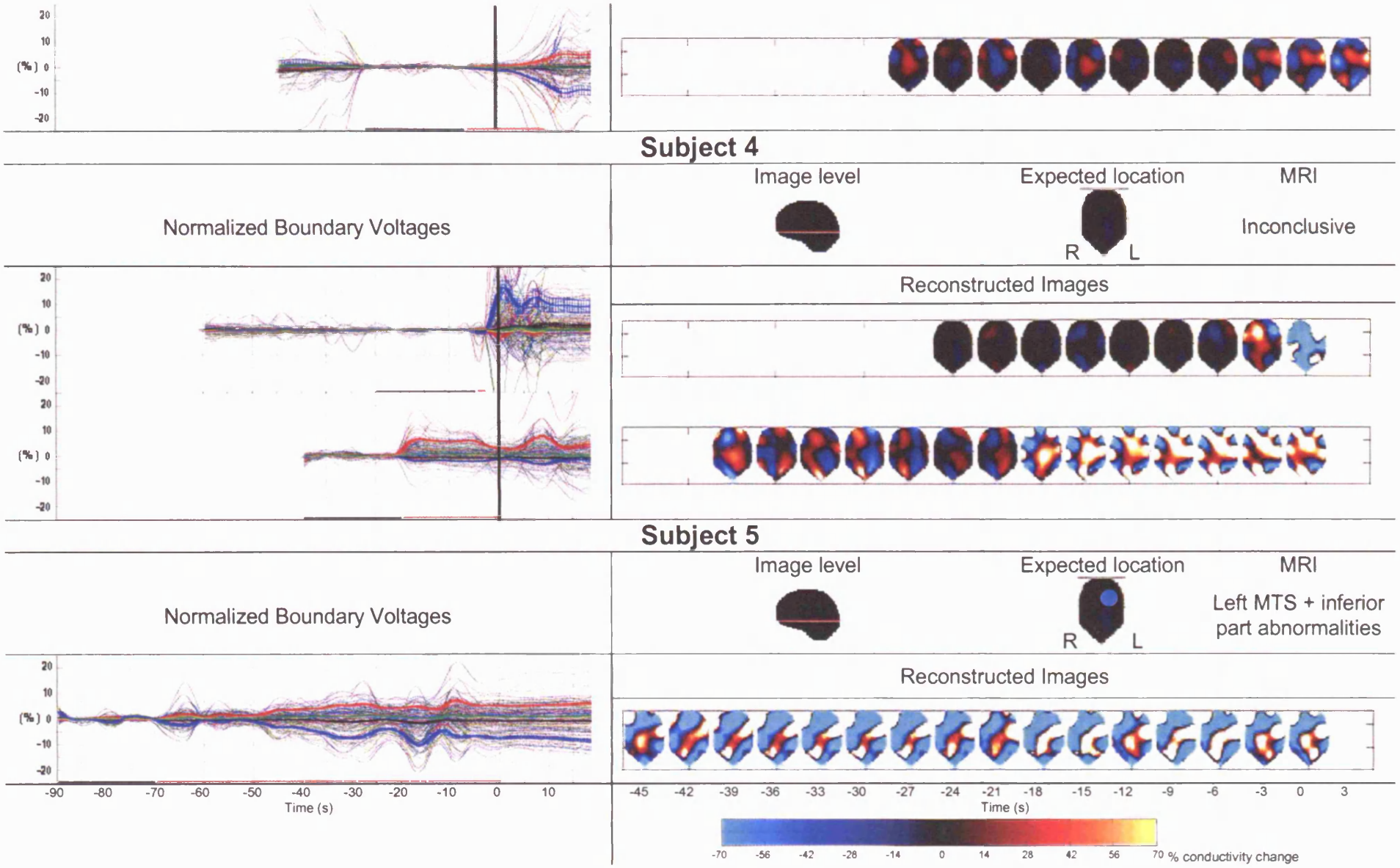
20
10
(%) 0
-10
-20
Subject 4
Image level
Expected location
MRI
Normalized Boundary Voltages
R
L
Inconclusive
Reconstructed Images
Subject 5
Image level
Expected location
MRI
Normalized Boundary Voltages
R
L
Left MTS + inferior part abnormalities
Reconstructed Images
-90 -80 -70 -60 -50 -40 -30 -20 -10 0 10
Time (s)
-45 -42 -39 -36 -33 -30 -27 -24 -21 -18 -15 -12 -9 -6 -3 0 3
Time (s)
-70 -56 -42 -28 -14 0 14 28 42 56 70 % conductivity change

Subject 6

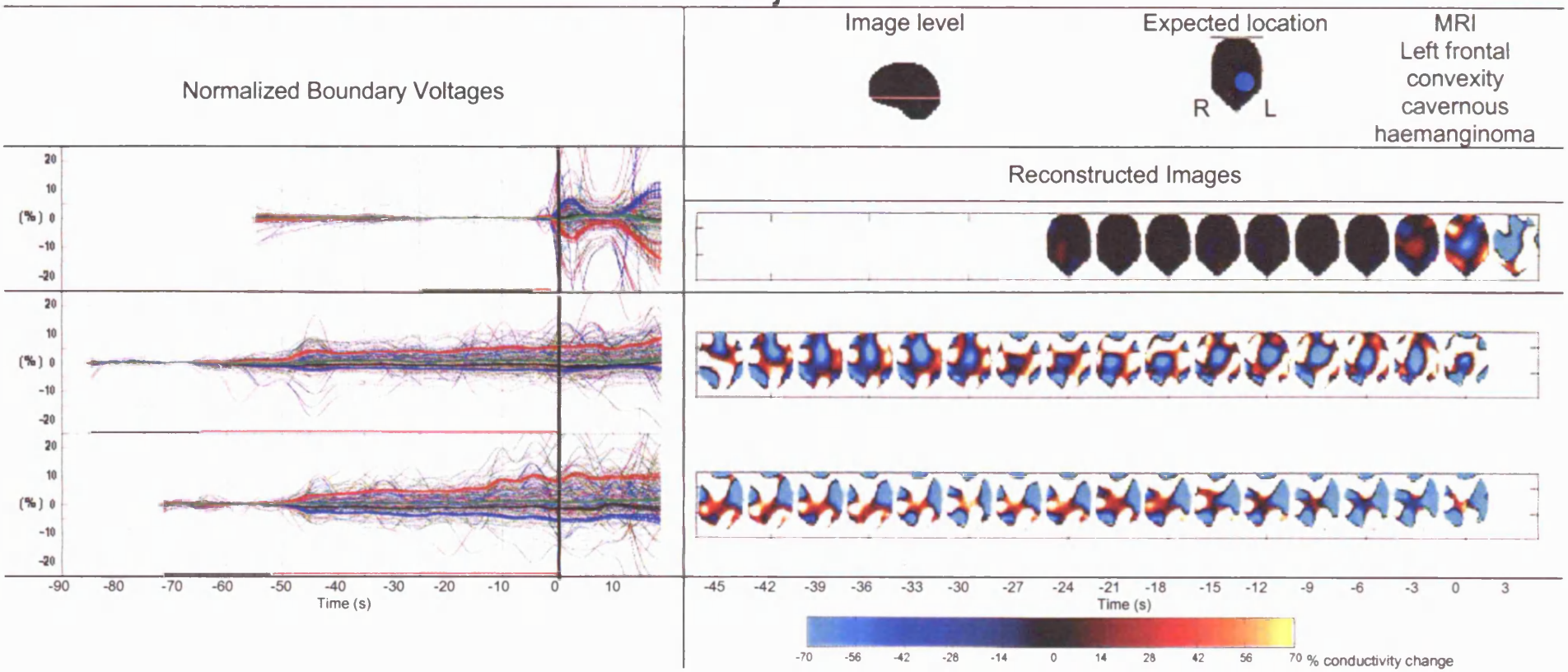
Normalized Boundary Voltages
Image level
Expected location
R
L
MRI
Left frontal convexity cavernous haemanginoma
Reconstructed Images
20
10
(%) 0
-10
-20
-90 -80 -70 -60 -50 -40 -30 -20 -10 0 10
Time (s)
-45 -42 -39 -36 -33 -30 -27 -24 -21 -18 -15 -12 -9 -6 -3 0 3
Time (s)
-70 -56 -42 -28 -14 0 14 28 42 56 70 % conductivity change

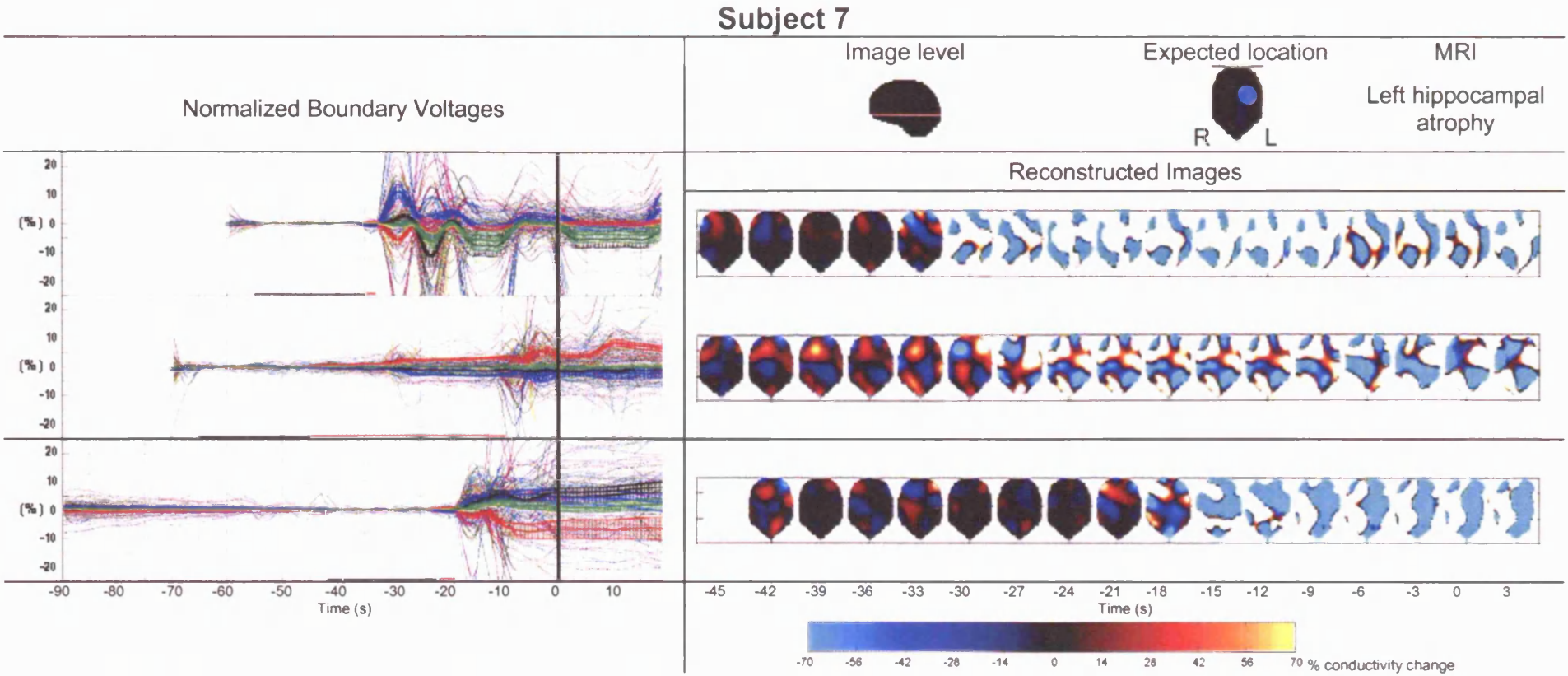

Figure 3-4 : Boundary voltages normalized to the mean baseline value (expressed in % changes) are represented and lined up respect to the EEG onset marked by the bold black vertical line. The black horizontal line marks the baseline period while the red line marks the pre-onset period. The average (± SE) of the 20% NBV with largest increase (red), of the 20% with the smallest increase (green), of the 20% with the smallest decrease (black) and of the 20% with the largest decrease (red) during the pre-onset period are displayed. The images are reconstructed from the average of 3 data sets every 3 seconds, starting from 45 seconds before the EEG onset. The level of the transverse tomographic slice is shown at the top of the table. The colours scale representing conductivity changes was calibrated with a simulation of a conductivity change in a spherical volume of 20mm radius in different brain position. The diagram at the top shows the location of the expected change as suggested by the video-EEG and MRI findings.

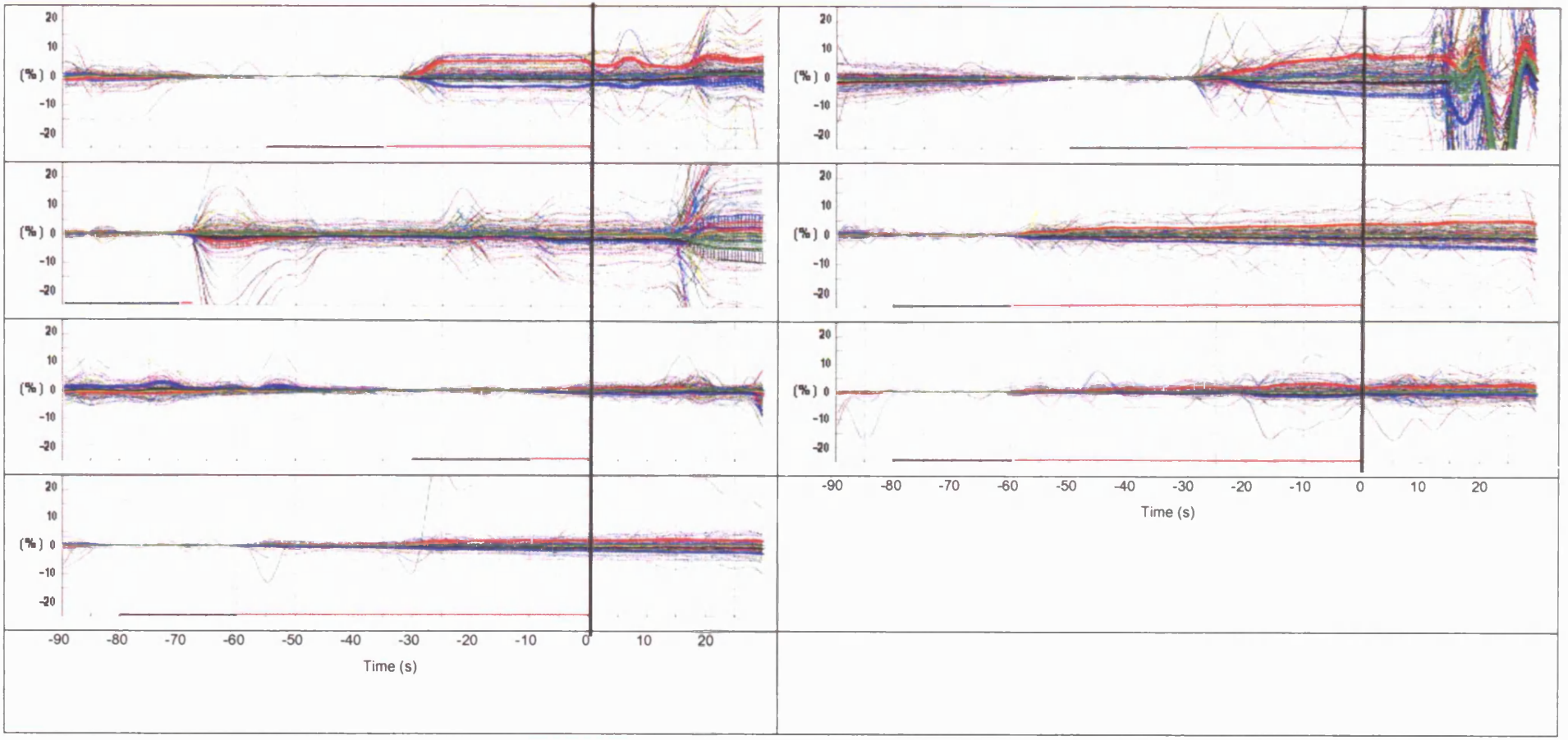

Figure 3-5 Boundary voltages normalized to the mean baseline value (expressed in % changes) measured in non-seizure periods are represented and lined up respect to the 'EEG onset' marked by the bold black vertical line. The black horizontal line marks the baseline period while the red line marks the pre-onset period. The average (± SE) of the 20% NBV with largest increase (red), of the 20% with the smallest increase (green), of the 20% with the smallest decrease (black) and of the 20% with the largest decrease (red) during the pre-onset period are displayed.

(a) Patient 1: seizure 1

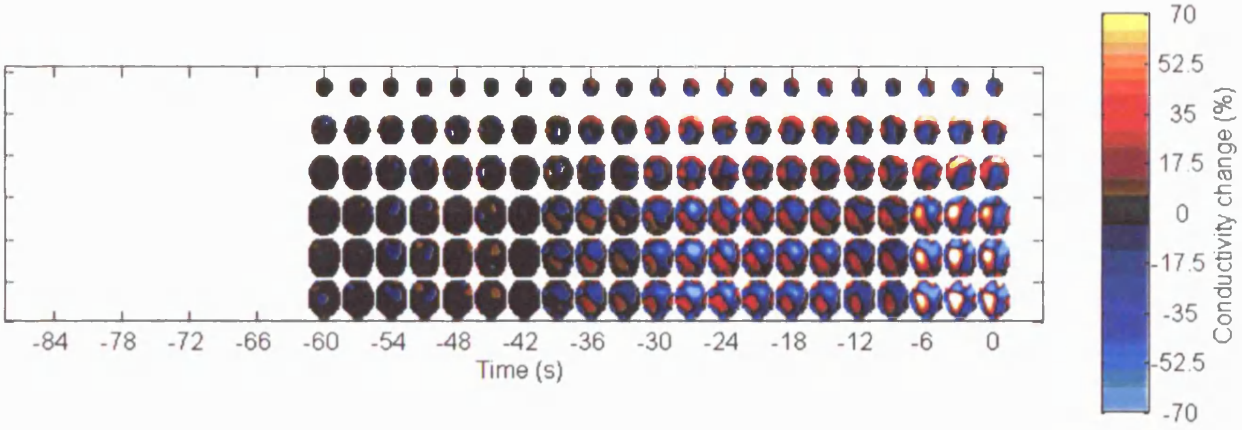

(b) Patient 1: seizure 6

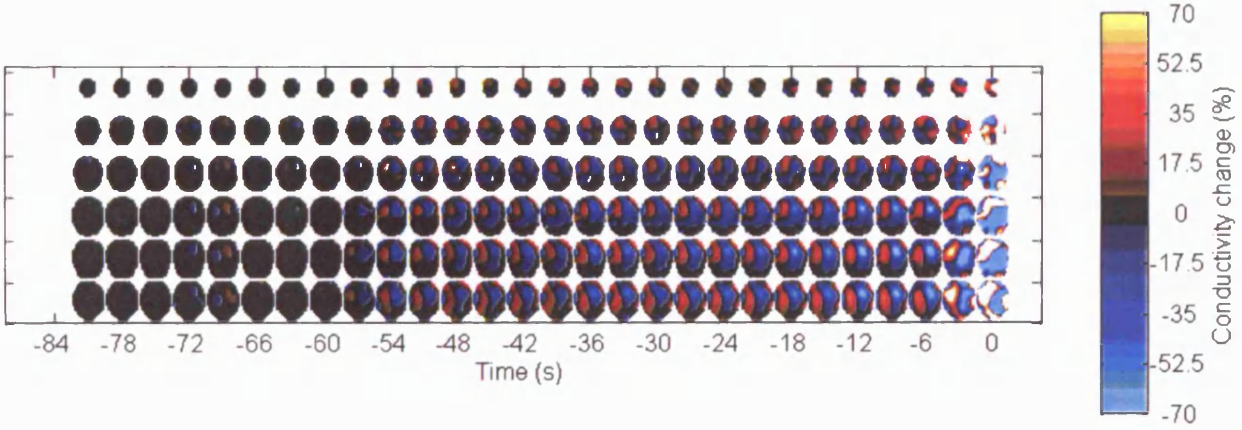

(c) Patient 2: seizure 1

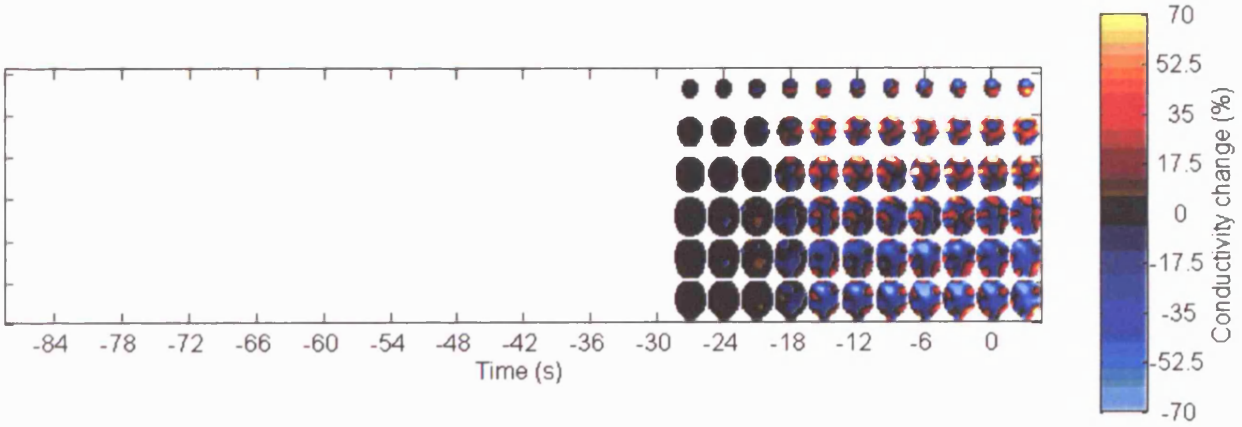

(d) Patient 5: seizure 1

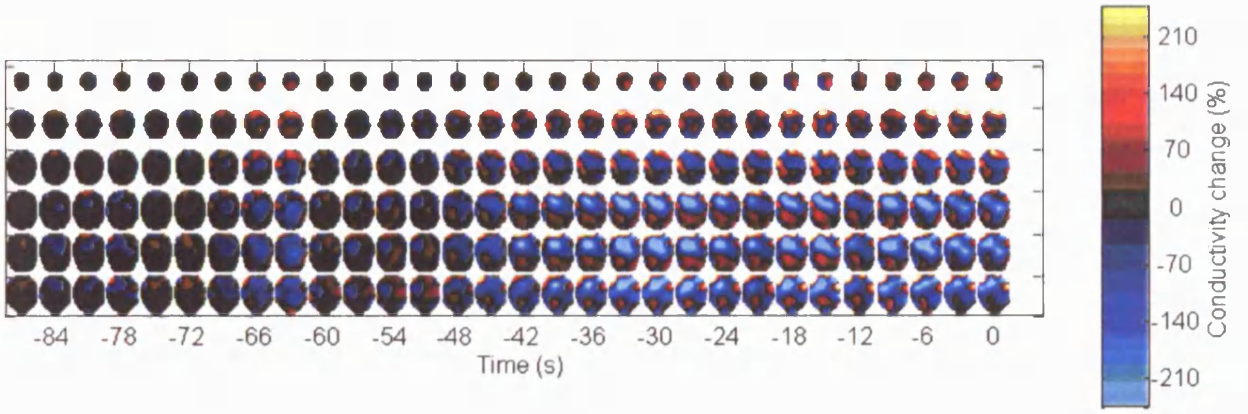

(e) Patient 6: seizure 2

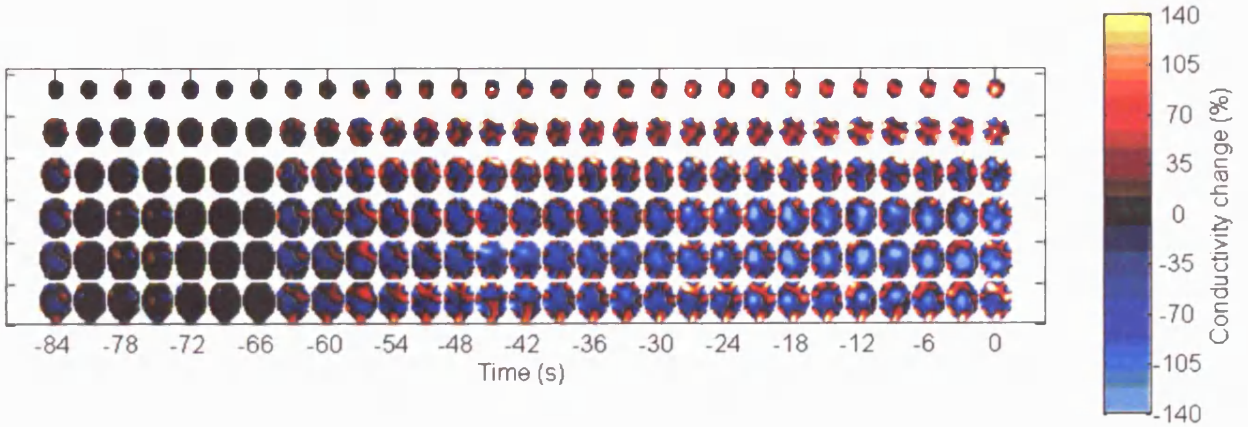

(f) Patient 6: seizure 3

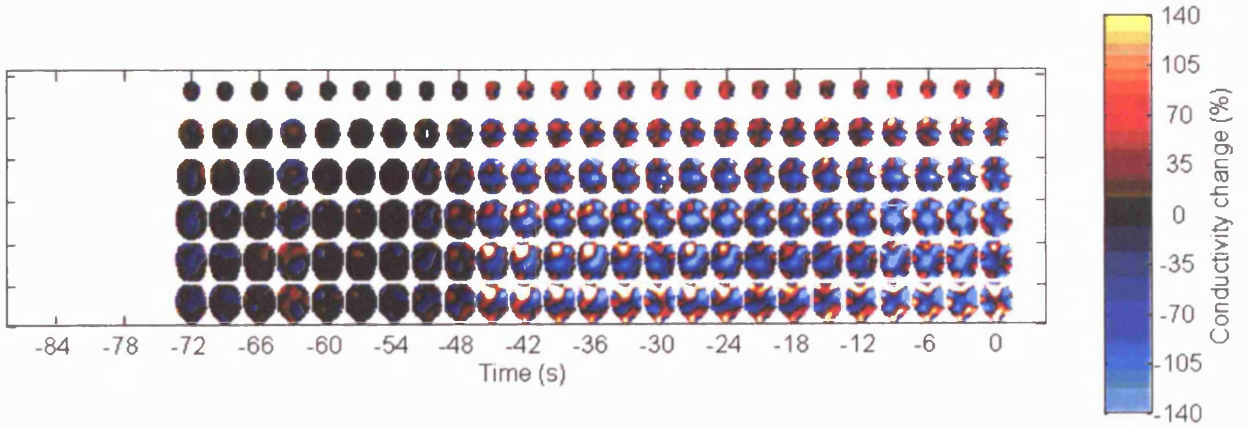

(g)

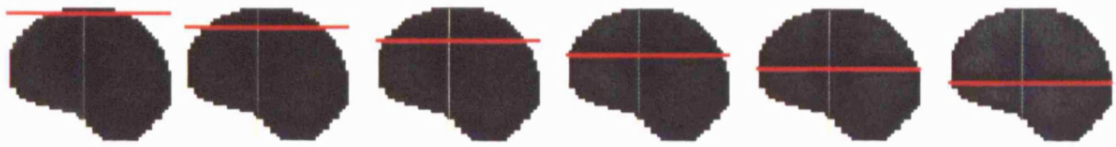

Figure 3-6 In seizure 1 and 6 of patient 1 (a, b), seizure 1 of patient 2 (c), seizure 1 of patient 5 (d), seizure 2 and 3 of patient 6 (e, f) localized conductivity decreases are recognisable, but they are not concordant with MRI and video-EEG findings (Figure 3-5). The colour scale has been changed for different seizure to avoid saturation. The slices are transverse section of the brain from the top towards the bottom (left to right in (g)) and the time was referred to the EEG onset.

Table 3-4 Summary of conductivity changes expected from traditional diagnosis techniques (video-EEG and MRI) and reconstructed with EIT for different seizures.

Subject	Expected conductivity changes	Reconstructed conductivity change
1	Right temporal decrease	1. Left posterior focal decrease + right temporal increase 2. No recognisable changes 3. Scattered changes
2	Right superior frontal/ pre-frontal decrease with gradual spreading	Occipital decrease spreading to the middle
3	Left parahippocampal gyrus decrease with rapid spread to the right	1. No recognisable changes 2. Decrease involving the whole brain
4	Left occipital decrease	1. No recognisable changes 2. Mesial structure increase surrounded by decreases
5	Inferior left temporal decrease	Large occipital decrease spreading to the right + large left increase spreading to the front
6	Left frontal decrease	1. Mesial region decrease + increases in the lateral regions 2. Occipital increase + left temporal decrease
7	Left temporal decrease	Scattered changes

The conductivity changes reconstructed in seizures 1 and 6 of subject 1 (a, b in Figure 3-6) have similar location and time course as shown by the trend of the mean conductivity change in the brain region represented in Figure 3-7.

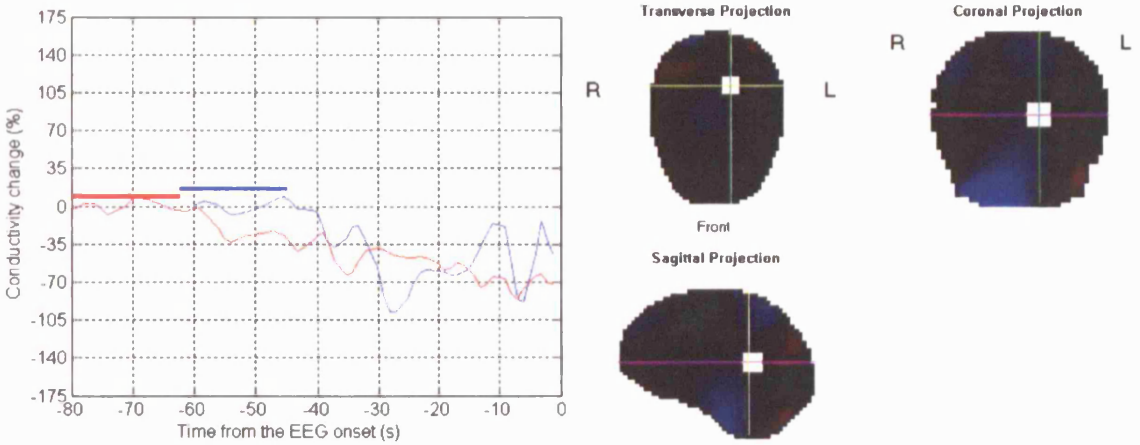

Figure 3-7 Mean conductivity changes reconstructed in seizure 1 (blue) and 6 (red) of subject 1 in the brain region shown on the right, where localized conductivity decreases have been identified. In the left graph the thick horizontal lines mark the baseline periods of each seizure.

The relation between a simulated conductivity change in the brain and the averaged reconstructed conductivity change in a cube (15x15x15 mm) centred on the peak reconstructed conductivity change was linear for the considered range of changes (Figure 3-8). The ratio between the two values slightly depends on the position of the perturbation and is 4.05 if it is in the centre of the brain, 3.26 if it is on the back and 3.4 if it is on the right. A scaling factor of 3.5 was chosen to scale the reconstructed conductivity changes in the above results.

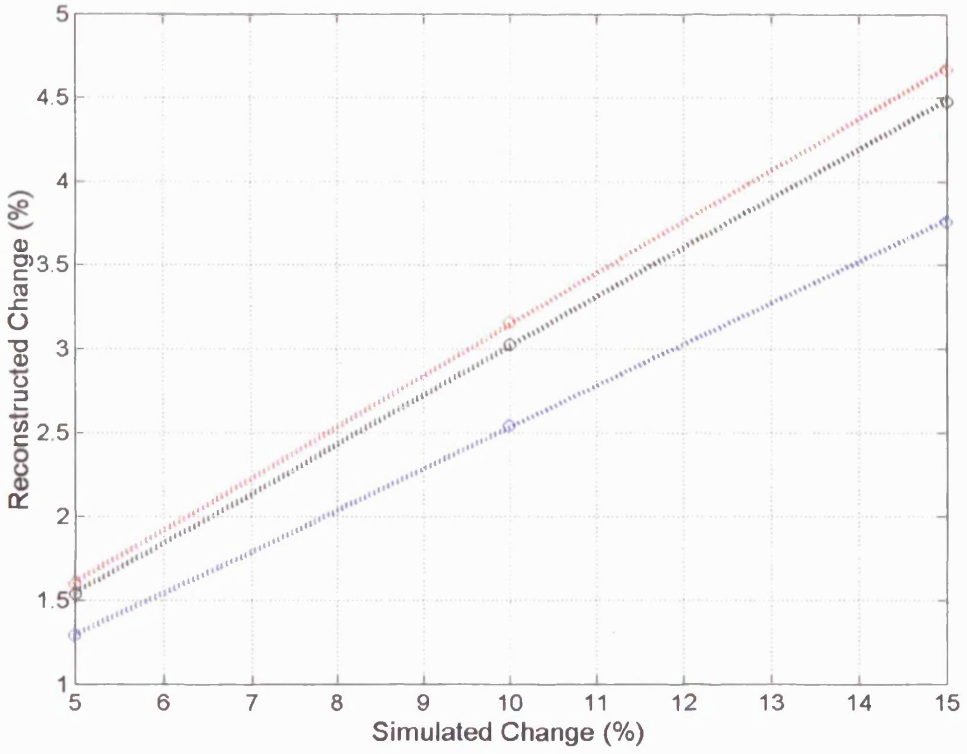

Figure 3-8 Average conductivity changes reconstructed in a cubic volume (15x15x15 mm) centred on the voxel with the peak reconstructed conductivity for each simulated change (5%, 10%, and 15%) in each position: centre (blue), back (red), right (black).

3.4 Discussion

3.4.1 Summary of results

Experiments were performed to develop for the first time a method to record and analyse EIT during natural epileptic activity in concurrence with video-EEG from standard scalp electrodes in humans. Seizures are unpredictable events, preventing the possibility of conducting controlled experiments, so we proposed long term EIT during presurgical video-EEG monitoring in a Telemetry ward as a feasible solution. Hours of EIT were available at the end of the experiments and only relevant segments were considered in a similar method to that of standard EEG analysis. There were significant boundary voltage changes in the majority of the electrode combinations after the baselines, before seizure onset, and led to voltages that diverged at seizure onset with standard deviations between 1.1% and 53% after elimination of the noisiest combinations (3.5-43.4% of the 258 combinations used). A Finite Element Model developed in our group validated with tank experiment (Gilad O. et al. 2005) predicts maximum changes in the boundary voltages of

0.001% measured at near DC frequency (current 100-200 μA) for a change of 1% in the conductivity of the primary visual cortex. Considering that the maximum conductivity decrease obtained from animal exposed cortex was no more than 15%, according to the model we would expect changes of around 0.1% in the scalp voltage measurements if considering that epilepsy may involve larger area of the cortex. Therefore our results exceeded this predictions by about one or two orders of magnitude. Similar results were obtained in EIT segments not related with any seizure occurrence. The conductivity reconstructions did not display consistent reproducible changes and showed decreases far larger than that measured locally with cortical and implanted electrodes during induced epilepsy in animals.

3.4.2 Robustness of the data collection and analysis method

We have shown that simultaneous measurement can be done using two separated sets of electrodes for EIT and EEG and that EEG can be recovered for clinical diagnosis through hardware and software filtration. The EIT electrodes can easily be positioned by a technician of the ward in between the EEG electrodes and the signals can be successfully synchronized by using the EIT artefact in the EEG recordings as reference.

3.4.3 Boundary voltage changes

UCLH Mark 1b has shown the potentiality of imaging 12% conductivity decreases in tank experiment using a sponge in saline solution in the presence of the skull (Yerworth et al. 2002). Reproducible boundary voltage changes related to visual evoked potentials (VEP) were possibly recorded with an HP 4284A impedance analyser from scalp electrodes (Tidswell et al. 2001b). This suggests that when acquired in controlled situation with a fixed protocol, without subject movements, boundary voltage changes can be reliably measured. In this study most of the seizures occurred when the subjects were moving, chatting or doing other activities reflecting in poor quality of the EIT recordings that were mostly corrupted. Nevertheless two seizures occurred when the patients were sleeping and still not convincing data sets were obtained (Figure 3-4; Subject 1 - Seizure 1; Subject 3 - Seizure 1). The raw impedance changes are therefore unlikely to be related to seizure activity; these were probably artefact caused by unstable electrode contact, as similar changes were measured during periods not seizure related.

The major sources of error were possibly random, as predicted by Boone et al. (Boone et al. 1994), the signal-to-noise ratio being inadequate for the following reasons. (i) The amount of current passing trough the brain was probably too small compared to that shunted by the scalp and then the sensitivity to impedance changes in the brain insufficient; (ii) the boundary voltage measurements were probably corrupted by subject movements, which changed the electrodes contact with the scalp, giving rise to apparent voltage variations; (iii) the baseline itself was difficult to identify and its variability was often larger than the signal we intended to measure.

3.4.4 Reconstructed conductivity

The artefacts in the boundary voltage probably hid any genuine change due to impedance variation inside the brain, and then the reconstructed images did not display reproducible features. In two seizures similar conductivity alterations were reconstructed, but they were far too large to be genuine.

Systematic errors due to various simplifications of the reconstruction algorithm could be present. Factors that might be expected to influence the precision of the forward problem solution include the following: (i) assuming a standard geometry for the head shape and the electrodes position for all the patients; (ii) assuming anisotropic tissues (neuronal tissue and skull for example) isotropic; (iii) using a fixed truncation level for the tSVD, disregarding the noise level of the data. Furthermore the calibration of the reconstructed conductivity did not take into account some factor on which it depends such as: the number of singular values used for the decomposition or the number of electrodes combinations eliminated.

3.4.5 Is the method we used optimal?

The trial set up has integrated well with standard EEG practice and has shown that it does not interfere with patient clinical evaluation. On the EIT side, considering that conductivity changes are likely to be due to cell swelling, a lower frequency for the measuring current might be expected to produce larger changes and less errors due to stray capacitance. Most in vivo impedance measurements inevitably include baseline fluctuation (Boone et al. 1994) and can be corrupted by subject movement or electrode misplacement. These issues might be ameliorated by the baseline linear correction and voltage measurement outlier elimination we employed: (i) The linear drift correction of the baseline would compensate for slow baseline fluctuation. (ii) The threshold on the baseline noise would eliminate electrode combinations with

unstable electrode contact. (iii) The threshold on the changes occurring before the EEG onset would eliminate electrode combinations most influenced by movement. (iv) The low pass filtering would allow detection of voltage changes occurring in a physiological time scale. Ideally the threshold settings should be stricter than those used in our study to detect changes of the order of 0.1%.

3.4.6 Future work

The principal source of error appears to be movement artefact. The design of conventional EEG electrodes – a cup which contains a semi-liquid gel – is already well designed to reduce movement artefact, but hydro-gel electrodes may be superior. We have examined different electrode designs for scalp EIT recording (Tidswell et al. 2003b) and future work will include a re-examination of these in relation to recording under epilepsy telemetry conditions. Signal processing tools already implemented in EEG analysis could be used to separate the feature of interest from major noise in our boundary voltage measurements.

Improvements to the forward and inverse problem may also help, if data quality can be improved. Individual head shape geometry could be obtained from patient MRI (Tizzard et al. 2005) and accurate electrodes positions could be detected using 3-dimensional electrode localization methods, such as photogrammetry (Russell et al. 2005). The forward model could be also improved and include the anisotropy of the head tissues. Finally, a truncation level prediction method could be implemented to take into account the noise level of the data and to optimize the solution to the inverse problem (Handersen 1992; Perez-Juste Abascal et al. 2005).

Chapter 4 – A feasibility study for imaging epileptic seizures by EIT using a realistic FEM of the head

4.1 Introduction

It has already been shown that impedance increases locally in the brain by 3-12% at 1kHz up to 22% using square pulses of 200ms at 50 Hz during induced epileptic seizures (VAN HARREVELD and Shade 1962; Elazar et al. 1966; Fox et al. 2004). Resistance changes of 5.5-7.1% associated with focal and generalized seizures have been imaged with EIT using a ring of electrodes placed on the exposed cortex of rabbits with a current of 5mA at 51 kHz (Rao 2000). It therefore seems plausible that these changes are large enough to enable EIT to produce images of conductivity variations of clinical interest. Nevertheless, in the pilot study described in Chapter 4, using scalp electrodes in humans, we were unable to measure reproducible boundary voltage changes during seizures. In 22 seizures from 7 subjects, no reproducible changes in images or scalp impedance data could be observed as they were diverging with a standard deviation of 1-54% (Fabrizi et al. 2006b). The most probable explanation for the observed changes was that true scalp voltage changes due to cerebral seizure activity were obscured by movement artefact.

4.1.1 Purpose

This work arose after the previous unsuccessful experimental study; we set out to re-engineer our EIT hardware and recording system in order to maximise the chance of detecting reliable changes. The purpose of this study was therefore to use computer modelling of the problem to suggest the best recording parameters and arrangement, set a specification for accuracy for hardware, and, finally, estimate if EIT imaging of seizures appeared feasible with the suggested optimal arrangement.

The modelling included estimation of the expected changes during seizures with applied current from 5 Hz to 4 MHz, in order to suggest an optimum frequency for recording, as this is the available range in current EIT systems (Oh et al. 2005; McEwan et al. 2006). Values for the conductivity of the tissues of the head (scalp, skull, grey and white matter and eyes), either at rest or during epileptic seizures, were taken from the literature. As studies did not completely cover this frequency range, a secondary purpose of the study was to review the literature and extrapolate a best estimate for these parameters where needed.

4.1.2 Experimental design

The complex boundary voltages on the scalp were calculated by solving the forward problem for a realistic 3D Finite Element Model (FEM) of the human head under normal conditions and during focal epileptic seizures. The FEM comprised regions of grey and white matter, cerebrospinal fluid (CSF), skull, scalp and eyes. The frequency spectrum of the complex conductivity under normal conditions and of its changes due to focal epilepsy were extrapolated from the literature at 7 frequencies between 5Hz and 4MHz. Four brain regions, which are common sources of epileptic activity, were chosen as the epileptic onset areas. The detection from scalp measurements was of increasing difficulty, as they decreased in volume and increased in depth. For simplicity, the tissues were all assumed to be isotropic.

Two different current level patterns with respect to frequency were considered. First, a uniform level of 100μA across frequency. Secondly, an increasing pattern with frequency, as the International Electrotechnical Commission IEC601 standard specifies a 'patient auxiliary current' limit of 100μA from 0.1 Hz to 1 kHz; then 100*f μA from 1 kHz to 100 kHz where f is the frequency in kHz; then 10 mA above 100 kHz (IEC601-1 1988). The complex boundary voltages were recalculated with these current levels, in order to estimate the best single frequency to adopt to detect boundary voltage changes related to epilepsy.

To assess whether the voltage changes obtained in the simulation were large enough to provide clinically useful EIT images, we produced reconstructed images from projected scalp voltage changes after the addition of random noise of 0.3-0.4% up to 100 kHz. For this purpose, 50 kHz was selected for the frequency of applied current as findings from the previous section predicted that it would give the highest signal-to-noise ratio. The degree to which noise could be reduced by averaging was included in the estimate for different systems, on the basis that a temporal resolution of 1 second is needed to record epileptic seizures.

EIT systems may broadly be categorized according to the number of parallel current sources and recording circuits. For the purpose of estimating how much averaging is possible, we have defined three systems – a) Serial – a single impedance measuring circuit with a multiplexer, such as the UCH Mk2.5 system (McEwan et al. 2006); b) Semi-parallel – multiple parallel recording but a single current source which is multiplexed between different electrode pairs, for example the Kyung Hee Univesity Mk1 (Oh et al. 2007) or c) Fully parallel – multiple simultaneous current injection and record, such as the ACT-3 (Cook et al. 1994). The degree of averaging

was estimated as follows: for 31 electrodes, the reconstruction algorithm usually employed in our group has 258 electrode combinations, with 21 different injection pairs. If one period of waveform is sufficient for each measurement and 1 μs is need for the combination switching, the number of frames n which can be averaged in 1 second is 1/(258*(1/f+1e-6)) for a serial system, 1/(21*(1/f+1e-6)) for a semi-parallel system and f for a fully-parallel system, where f is the measuring frequency (Table 4-1). The noise reduction respect to averaging 2 periods is given by √(n/2).

Table 4-1 Waveform periods that can be averaged in 1 frame/sec (resulting noise reduction factor).

System	50 Hz	50 kHz
Serial	no (no)	185 (10x)
Semi \\	2.4 (no)	2268 (34x)
Fully \\	50 (5x)	50k (158x)

4.2 Conductivity properties of tissue in the head

4.2.1 Conductivity values for resting conditions

The conductivity values assigned to the mesh for each frequency were obtained with a cubic interpolation between data points taken from the literature. The studies considered were those which reported data which corresponded most closely to living human tissue in the frequency range 5Hz-4MHz. If the frequency range was only partially covered, then data were interpolated from different studies. Data obtained at a temperature closest to that of the body were used when available and if not a linear correction of +2 %/°C was applied (Foster and Schwan 1989). Four-terminal measurements were preferred over two-terminal measurements.

The model used in this study was isotropic and homogeneous, so average representative conductivity values for anisotropic tissues such as scalp, skull and white matter were adopted.

4.2.1.1 Scalp

The scalp is the soft tissue that envelops the skull. It is composed primarily by: the skin, connective tissue (superficial fascia), epicranial aponeurosis and epicranius.

The latter is a wide, musculofibrous layer, which covers a large part of the head, from the occipital bone to the eyebrow. It consists of two parts of muscle fibres parallel to the skull, the Occipitalis and the Frontalis, connected by a large tendinous aponeurosis, the galea aponeurotica, which covers the superior aspect of the cranium. During EIT experiments, the stratum corneum of the skin is often removed by abrasion. As we are not aware of any validated direct measurements of scalp conductivity, we have approximated it as a homogenous layer of skeletal muscle. Conductivity was therefore estimated from values of excised bovine paravertebral muscle at body temperature, taking into account muscle anisotropy at 10 Hz-10 MHz (Gabriel et al. 1996a). Considering that muscle fibres in the scalp are parallel to the head surface and to the skull, the final representative scalp conductivity was considered as 2/3 transverse and 1/3 longitudinal that of the muscle, as the current may cross the fibres in the longitudinal or transverse direction (Horesh 2006).

4.2.1.2 Skull

The skull is made of 28 bones, mainly flat, joined by sutures. These comprise a trabecular layer embedded in two cortical layers. The representative skull conductivity was considered as 2/3 that of cortical bone and 1/3 that of trabecular to represent this composition. Cortical and trabecular bone are anisotropic; unfortunately, no studies which account for this appear to have been performed over the frequency range of interest. Cortical bone admittivity has been measured on rat femur freshly excised over a frequency range of 10 Hz-100 MHz at body temperature without considering anisotropy (Kosterich et al. 1983). Trabecular bone was represented using measurements on frozen cancellous bovine femur samples (Sierpowska et al. 2003) defrosted at room temperature just before the measurements, which were conducted between 20 Hz and 5 MHz. Human trabecular bone was found to be about twice more conductive than bovine under similar experiment conditions (Sierpowska et al. 2005), so the real part of the conductivity was doubled and increased by 30% to adjust a recording temperature of 22 to 37 °C.

4.2.1.3 Cerebrospinal fluid (CSF)

CSF is an ionic fluid with high conductivity and null permittivity. The former was almost constant between 10 Hz and 10 kHz for human CSF at body temperature (Baumann et al. 1997). As CSF is a purely resistive medium, the mean of the values below 10 kHz was taken to be constant up to 4 MHz.

4.2.1.4 Grey matter

Grey matter mainly comprises nerve cell bodies and their branches, a small proportion of myelinated axons and glial cells; its structure is essentially isotropic. In-vivo measurement in humans have been conducted at 50 kHz (Latikka et al. 2001), but the admittivity of bovine tissue in-vitro was measured between 10 Hz and 20 MHz (Gabriel et al. 1996a). These data were translated according to the Lattika recordings at 50 kHz.

4.2.1.5 White matter

White matter mainly comprises myelinated nerve axons, which have different longitudinal and transverse conductivity, and is anisotropic. Since the nerve fibres are randomly oriented, the white matter has been considered to have an equivalent volume of 1/3 of fibres longitudinal to the current path and 2/3 transverse (Ranck, Jr. 1963a). The conductivity of a bundle of parallel axons was measured in the two directions in-vivo in the dorsal column of cats between 5 Hz and 50 kHz (Ranck, Jr. and BEMENT 1965). An averaged conductivity (1/3 longitudinal + 2/3 transverse) was calculated as representative of the white matter. The conductivity of in-vitro bovine tissue has been measured between 10 Hz and 20 MHz (Gabriel et al. 1996a). These data were translated according to the mean difference from the spectrum obtained from Ranck and Bement recordings for the overlapping frequency range and employed in the model.

4.2.1.6 Eyes

The eye is a complex ensemble of structures, whose admittivities have been measured separately. Only the cornea, lens, retina, sclera, vitreous and aqueous humours compartments were considered; the other parts of the eye are physically small and their contribution was discounted. The volume of each compartment was estimated from the images on http://www.discoveryfund.org/anatomyoftheeye.html. Due to lack of information through our frequency range, the admittivities extrapolated between 10 Hz and 100 GHz with a model simulating four Cole-Cole type dispersions were employed in the model (Gabriel et al. 1996b). The admittivity of retina was assumed to be equal to that of cornea, since they were similar between 1 MHz and 10 MHz (Gabriel et al. 1996a) and that of aqueous humour was assumed equal to that of vitreous humour, since they were similar between 5 Hz and 2 kHz (Lindenblatt and Silny 2001).

4.2.1.7 Values employed in the model

The real part of the conductivities of the tissues is about 1 order of magnitude larger than the imaginary part (Figure 4-1; Table 4-2), it will then dominate the overall conductivity of the head. The derived spectra present α-dispersion at about 100 Hz and β-dispersion around 10 kHz-100 kHz, confirming the reliability of the chosen data.

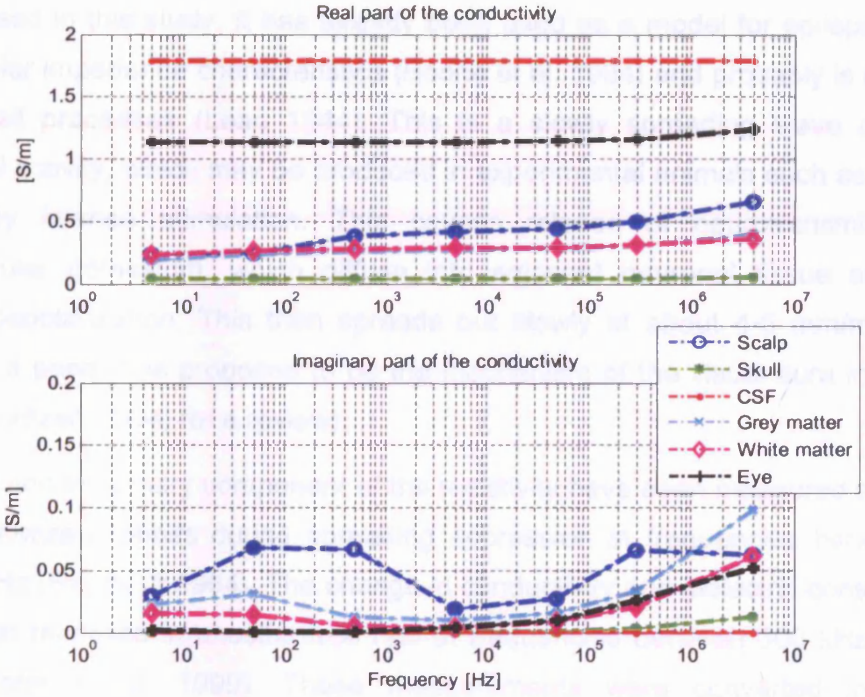

Figure 4-1 Estimated conductivity of normal tissues in the adult human head employed in this study.

Table 4-2 Estimated values of the real (Re) and imaginary (Im) conductivity of normal tissues in the adult human head employed in this study in the frequency range 5Hz-4MHz.

Tissue		Frequency						
		5Hz	50Hz	500Hz	5kHz	50kHz	300kHz	4MHz
Scalp	Re (S/m)	0.235	0.247	0.382	0.419	0.437	0.503	0.653
	Im (S/m)	0.029	0.067	0.067	0.019	0.027	0.066	0.062
Skull	Re (S/m)	0.037	0.037	0.038	0.038	0.039	0.041	0.047
	Im (S/m)	5e-4	4e-4	1e-4	2e-4	0.001	0.002	0.012
CSF	Re (S/m)	1.793	1.793	1.793	1.793	1.793	1.793	1.793
	Im (S/m)	0	0	0	0	0	0	0
Grey matter	Re (S/m)	0.185	0.232	0.259	0.270	0.285	0.306	0.391
	Im (S/m)	0.023	0.030	0.012	0.009	0.016	0.033	0.098

White matter	Re (S/m)	0.238	0.273	0.283	0.288	0.296	0.309	0.361
	Im (S/m)	0.016	0.014	0.005	0.004	0.009	0.019	0.062
Eyes	Re (S/m)	1.136	1.139	1.139	1.142	1.150	1.163	1.238
	Im (S/m)	0.002	0.001	0.001	0.004	0.009	0.026	0.052

4.2.2 Conductivity changes due to focal epilepsy

Published data for impedance changes during seizures is discontinuous over our frequency range, so we have used more continuous recordings made during the similar phenomenon of spreading depression (SD) to extrapolate over the frequency range used in this study. It has already been used as a model for epilepsy since it has similar impedance characteristics (Boone et al. 1994) and probably is due to the same cell processes (Leao 1944). This is a slowly spreading wave of intense neuronal activity, which may be produced in experimental animals such as the rat or rabbit by intense stimulation. This causes release of neurotransmitters and extracellular potassium, which diffuse into adjacent neuronal tissue and cause further depolarization. This then spreads out slowly at about 4-5 mm/min, like a ripple in a pond. It is proposed to be the mechanism of the visual aura in migraine (see (Lauritzen 1994) for a review).

The real and imaginary component of the resistivity have been measured separately in anesthetized rabbits during spreading depression at frequencies between 5Hz and 50kHz (Ranck Jr 1964). The change in conductivity and dielectric constant have also been recorded in anesthetized rats at frequencies between 300 kHz and 100 MHz (Yoon et al. 1999). These measurements were converted in specific conductivity and scaled to take into account differences between epilepsy and spreading depression, such as lower extracellular space shrinkage (Lux et al. 1986).

Resistance changes of 9.5±1.4% during focal epileptic seizures at 47 kHz were measured locally in anesthetized rabbits (Rao 2000). The ratio between this change and the change in the real part of the resistivity in spreading depression at 50 kHz (Ranck's measurement closer to 47 kHz) was used to transform changes due to spreading depression to changes due to epilepsy (Appendix A). Since the basic mechanisms underlying both spreading depression and epilepsy are likely to be identical (VAN HARREVELD and Shade 1962) we considered that the changes in cell membrane were the same in both conditions. The main difference between them is then the different extent of cell swelling. When the extracellular space shrinks, more current is likely to go through the cells (Ranck Jr 1964). Since cell swelling is less in epilepsy, we assumed that the variation in the real and imaginary

component of the resistivity would be reduced to the same extent in epilepsy with respect to spreading depression; the same conversion was used also at frequencies different from 50 kHz. The predictions from these assumptions were similar to those found experimentally by Elazar et al. (Elazar et al. 1966) and Fox et al. (Fox et al. 2004) and coherent with physiological processes (Appendix A).

The imaginary part of the conductivity of the grey matter has a larger proportional change than the real part (Figure 4-2), but its absolute change is smaller (Figure 4-3).

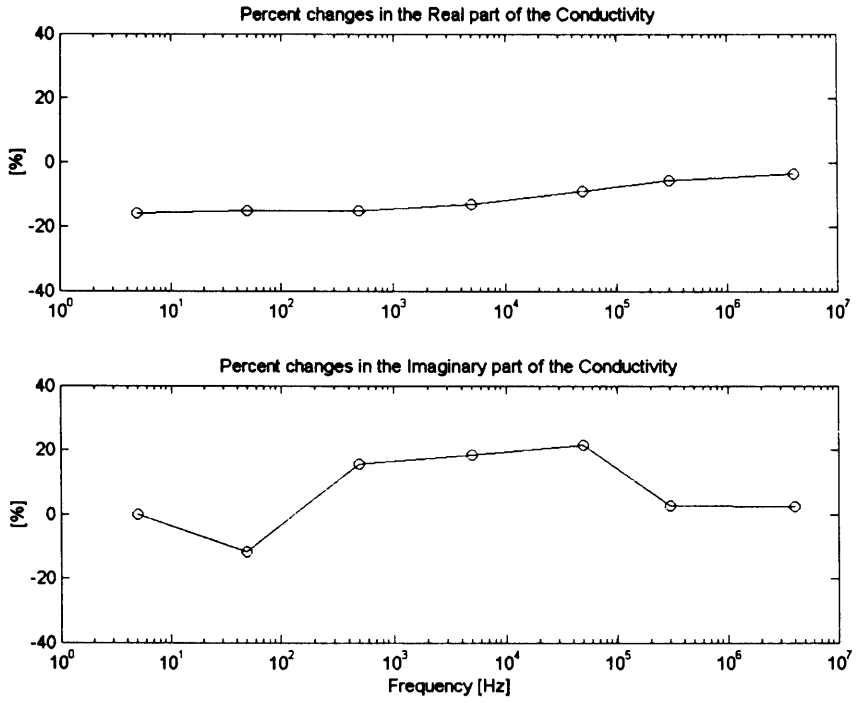

Figure 4-2 Estimated conductivity proportional change due to focal epilepsy.

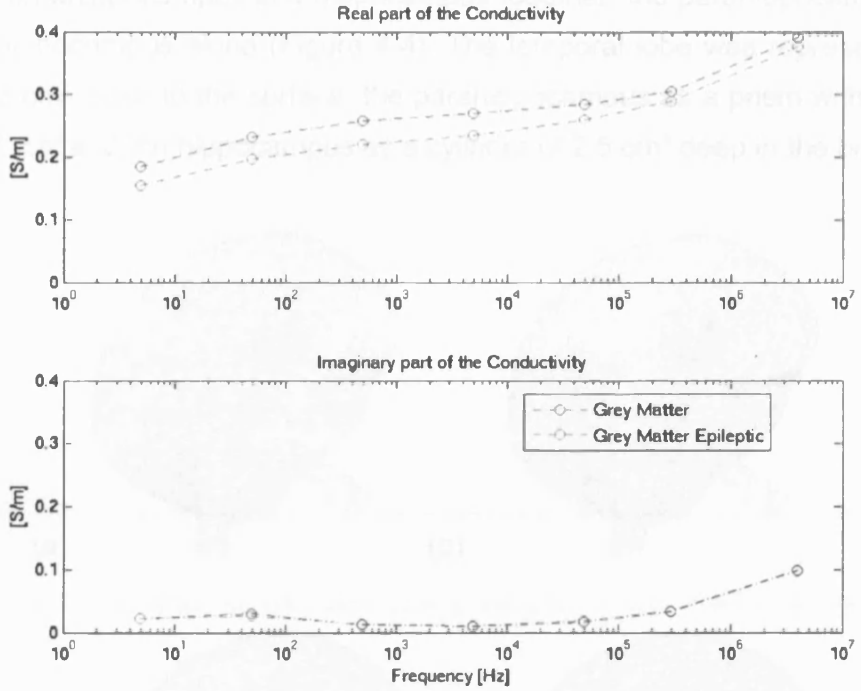

Figure 4-3 Estimated conductivity absolute change due to focal epilepsy.

4.3 Methods

4.3.1 Forward problem and 3D Finite Element Model

In order to determine the magnitude of the boundary voltage complex changes before and during seizures, the complex forward problem was solved for a realistic 3D Finite Element Model of the human head. The model was obtained using a UCL group modified version of EIDORS-3D Toolkit, which includes a finite element field solver, (Polydorides and Lionheart 2002) and a realistic head shaped multi-compartment mesh of 53000 elements generated with I-DEAS software (Tizzard et al. 2005). The compartments included scalp, skull, CSF, white and grey matter and eyes. Thirty-one electrodes and one ground, 10 mm in diameter, were placed in a modified 10-20 system on the surface of the scalp. A frequency-dependent contact resistance, obtained experimentally, was included in the model; it decreased from 3 kΩ at 5 Hz to 250 Ω at 4 MHz.

The forward problem was solved at 5 Hz, 50 Hz, 500 Hz, 5 kHz, 50 kHz, 300 kHz, and 4 MHz. In each case, the value of the complex conductivity at that frequency was assigned to each compartment. The forward problem was first solved for brain under normal conditions. Then it was solved using the same mesh with modification of the grey matter conductivity for four possible epileptic regions: the lateral temporal

lobe, the parahippocampus and hippocampus together, the parahippocampus alone and the hippocampus alone (Figure 4-4). The temporal lobe was represented as a disc of 18 cm^3 close to the surface, the parahippocampus as a prism with triangular base of 6 cm^3 and the hippocampus as a cylinder of 2.5 cm^3 deep in the brain.

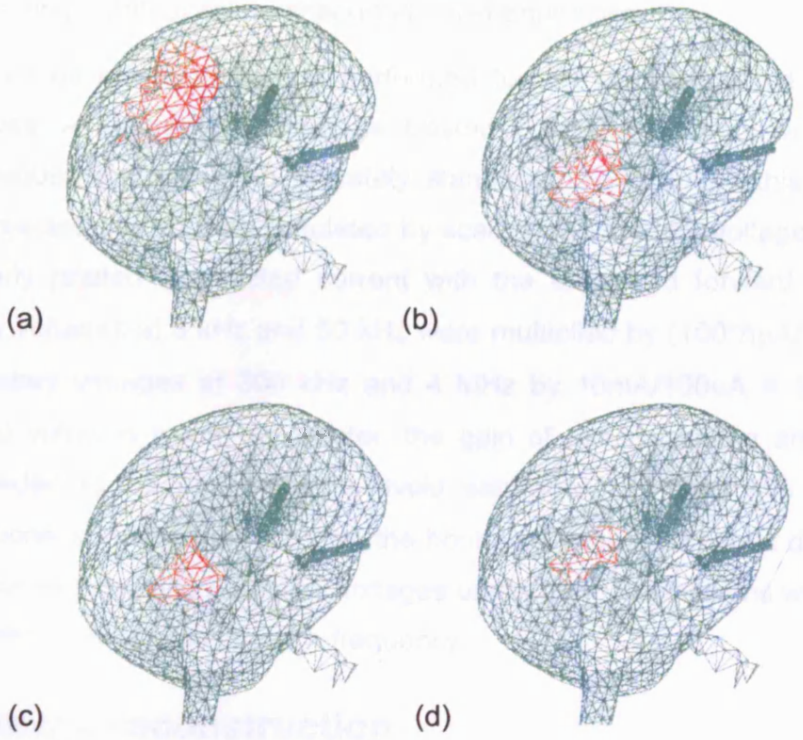

Figure 4-4 Focal seizure areas: (a) right lateral temporal lobe; (b) right hippocampus and parahippocampus; (c) right parahippocampus; (d) right hippocampus.

Data from the simulations were obtained from all 94395 possible non-equivalent electrode combinations, according to symmetry and reciprocity principles. No potential differences were calculated from electrode pairs containing current carrying electrodes, as in the experimental case. Calculation of the forward solution with this method was previously validated by comparing the potentials estimated using this method with those obtained by analytical solutions for a homogeneous sphere (Bagshaw et al. 2003) and by comparing the predicted boundary voltages with experimental measurements in spherical tank and humans at frequency below 100 Hz (Gilad et al. 2005b).

4.3.2 Boundary voltage analysis method

The complex boundary voltages obtained from all the possible 4 terminal electrode combinations with a current of 100 μA were considered and the same analysis was conducted separately on the real and imaginary part. Combinations with a low

amplitude which could not be accurately measured or likely to be obscured by noise – less than 0.1 μV for changes during seizures or 100 μV for standing boundary voltages under normal conditions – were eliminated from further investigation for each frequency. The average of the highest 1% of the proportional changes in the boundary voltages was taken as a representative index together with the corresponding mean absolute change across frequencies.

The above estimates were first performed for the same injected current at all frequencies. A theoretical advantage existed if greater currents were injected at higher frequencies according to safety standards. To examine this, the effect of greater injected current was simulated by scaling of boundary voltages, since these are linearly related to injected current with the employed forward problem. The boundary voltages at 5 kHz and 50 kHz were multiplied by (100**f*)μA/100μA = *f* and the boundary voltages at 300 kHz and 4 MHz by 10mA/100μA = 100. Since the measured voltages would be greater, the gain of the measuring amplifiers would have needed to be decreased to avoid saturation. To take this into account, combinations with less than 1 μV on the boundary voltage changes during seizures or 1 mV on the standing boundary voltages under normal conditions were eliminated from further investigation for each frequency.

4.3.3 Image reconstruction

In order to examine whether the predicted changes would translate into clinically useful images, images of the above perturbations were reconstructed using the potential changes obtained from the simulation of a polar injection protocol of 258 electrode combinations with a current of 5 mA at 50 kHz, as allowed by the IEC601 safety regulations (IEC601-1 1988). Random noise with RMS of 0.35% and of 20% was added respectively to the real and imaginary part of the boundary voltages before reconstruction. This noise level was that present on the boundary voltages measured on a 2 litres cylindrical saline tank (0.15 m diameter, 100 mm high), filled with saline of decreasing concentration (0.2% to 0.00125% NaCl), employing a polar injection protocol on 32 equally spaced stainless steel electrodes on a single ring (McEwan et al. 2006). To simulate the possibility of noise reduction with averaging, the noise was decreased 10, 34 or 158 times for serial, semi-parallel or fully parallel systems respectively (Table 4-1). The linear inverse problem was solved using a complex sensitivity matrix pseudo-inverted by truncated singular value decomposition (Bagshaw et al. 2003), with a fixed truncation level of 10^{-3} for the

magnitude of the largest singular value, employing the same mesh of the forward problem.

4.4 Results

4.4.1 Boundary voltages changes with 100μA applied at all frequencies

4.4.1.1 Real part

The top 1% of changes was 0.77%(1.45μV) at 5-50 Hz falling to 0.12%(0.2μV) at 4 MHz for a seizure in the temporal lobe. It decreased with depth of seizure site to 0.05%(0.13μV) at 5 Hz for a seizure in the hippocampus falling to 0%(0μV) at 4 MHz (Figure 4-5; Table 4-5).

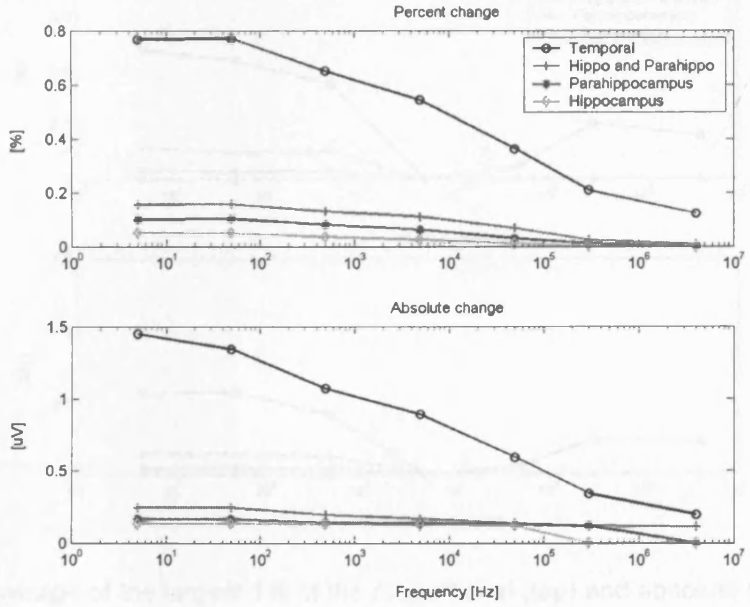

Figure 4-5 Average of the largest 1% of the proportional (top) and absolute (bottom) changes in the real part of the boundary voltages due to seizures, injecting 100 μV at all frequencies.

The proportion of electrode combinations with measurable signal increased with the increase of the size of the epileptic region and its proximity to the surface (Table 4-3).

Table 4-3 Percentage of electrode combinations with a standing voltage more than 100 μV for normal conditions and 0.1 μV for changes during seizures.

	5 Hz	*50 Hz*	*500 Hz*	*5 kHz*	*50 kHz*	*300 kHz*	*4 MHz*
Temporal	79.00	78.70	76.66	74.00	66.75	53.19	35.16
Para+Hippo	56.37	56.34	51.28	45.47	31.61	13.15	1.37
Parahippocampus	41.63	41.68	35.55	29.36	16.18	3.60	0.00
Hippocampus	23.84	23.59	17.90	12.79	4.03	0.02	0.00

4.4.1.2 Imaginary part

The top 1% of changes was 0.48-0.44%(0.56-0.54μV) at 5-50 Hz falling to 0%(0μV) at 5 kHz for a seizure in the temporal lobe. It fell to 0%(0μV) at all frequencies for a seizure in the hippocampus (Figure 4-6; Table 4-5).

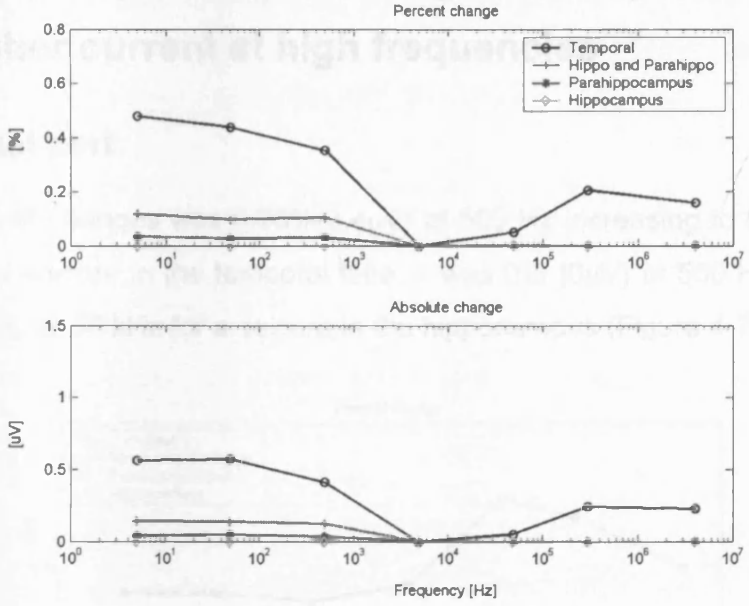

Figure 4-6 Average of the largest 1% of the proportional (top) and absolute (bottom) changes in the imaginary part of the boundary voltages due to seizures, injecting 100 μV at all frequencies.

The proportion of electrode combinations with measurable signal was lower than in the real part (Table 4-4).

Table 4-4 Percentage of electrode combinations which measure more than 100 μV on the voltage under normal conditions and 0.1 μV on the change.

	5 Hz	*50 Hz*	*500 Hz*	*5 kHz*	*50 kHz*	*300 kHz*	*4 MHz*
Temporal	2.36	3.63	1.50	0.00	0.19	4.22	11.40
Para+Hippo	1.03	1.45	0.91	0.00	0.01	0.00	0.00

Parahippocampus	0.39	0.45	0.32	0.00	0.00	0.00	0.00
Hippocampus	0.00	0.00	0.00	0.00	0.00	0.00	0.00

Table 4-5 Averages of the highest 1% changes at 5Hz - 50Hz when the current level is kept constant across frequency.

	Real	Imaginary
Temporal	0.77%(1.45μV) - 0.77%(1.35μV)	0.48%(0.56μV) - 0.44%(0.57μV)
Para+Hippo	0.15%(0.25μV) - 0.16%(0.24μV)	0.12%(0.15μV) - 0.1%(0.14μV)
Parahippocampus	0.1%(0.16μV) - 0.1%(0.16μV)	0.03%(0.05μV) - 0.03%(0.05μV)
Hippocampus	0.05%(0.13μV) - 0.05%(0.13μV)	0% - 0%

4.4.2 Boundary voltages changes during seizures using higher current at high frequencies

4.4.2.1 Real part

The top 1% of changes was 0.26%(3.4μV) at 500 Hz increasing to 0.97%(21μV) at 50 kHz for a seizure in the temporal lobe. It was 0% (0μV) at 500 Hz increasing to 0.06%(1.8μV) at 50 kHz for a seizure in the hippocampus (Figure 4-7; Table 4-8).

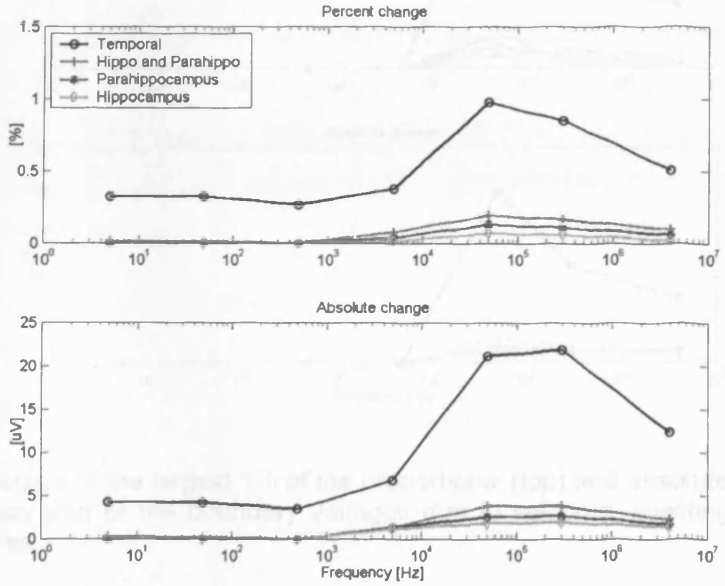

Figure 4-7 Average of the largest 1% of the proportional (top) and absolute (bottom) changes in the real part of the boundary voltages due to seizures, injecting higher current at high frequencies.

The proportion of electrode combinations with measurable signal increased with the increase of the size of the epileptic region, its proximity to the surface and the increase of the measuring frequency (Table 4-6).

Table 4-6 Percentage of electrode combinations which measure more than 1 mV on the voltage under normal conditions and 1 μV on the change.

	5 Hz	*50 Hz*	*500 Hz*	*5 kHz*	*50 kHz*	*300 kHz*	*4 MHz*
Temporal	15.74	15.08	12.89	55.65	92.31	93.94	89.50
Para+Hippo	0.26	0.19	0.00	21.60	79.30	82.12	68.75
Parahippocampus	0.00	0.00	0.00	8.57	69.39	72.88	54.38
Hippocampus	0.00	0.00	0.00	1.09	53.75	58.42	36.02

4.4.2.2 Imaginary part

The top 1% of changes was 0%(0μV) up to 500 Hz and increased to 1.39%(20μV) at 50 kHz for a seizure in the temporal lobe. It was 0% (0μV) up to 500 Hz and increased to 0.08%(1.2μV) at 50 kHz for a seizure in the hippocampus (Figure 4-8; Table 4-8).

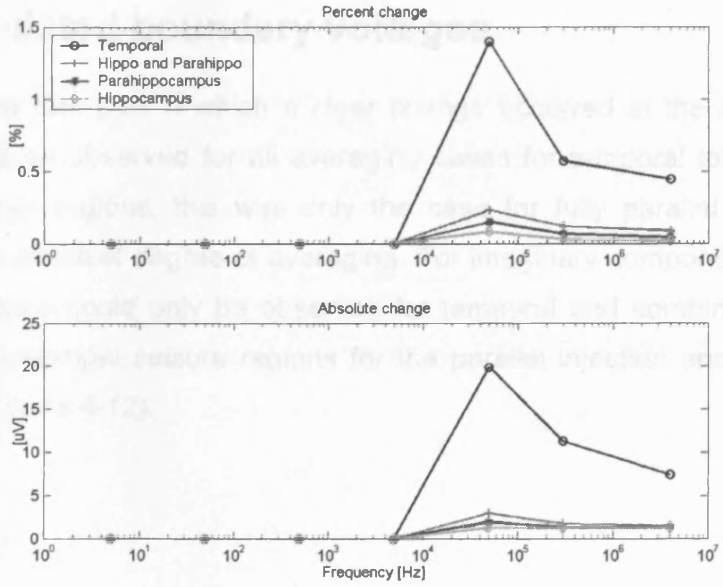

Figure 4-8 Average of the largest 1% of the proportional (top) and absolute (bottom) changes in the imaginary part of the boundary voltages due to seizures, injecting higher current at high frequencies.

At low frequencies, no electrode combinations had a measurable signal and the overall amount increases with the increase of the frequency (Table 4-7).

Table 4-7 Percentage of electrode combinations which measure more than 1 mV on the voltage under normal conditions and 1 μV on the change

	5 Hz	*50 Hz*	*500 Hz*	*5 kHz*	*50 kHz*	*300 kHz*	*4 MHz*
Temporal	0.00	0.00	0.00	0.00	35.52	64.93	74.20
Para+Hippo	0.00	0.00	0.00	0.00	23.61	37.72	43.28
Parahippocampus	0.00	0.00	.0.00	0.00	15.46	22.22	26.27
Hippocampus	0.00	0.00	0.00	0.00	5.56	8.14	10.42

Table 4-8 Averages of the highest 1% changes at 50kHz when the current level is conformed to the IEC601 standard

	Real	Imaginary
Temporal	0.97%(21.1μV)	1.4%(19.8μV)
Para+Hippo	0.19%(3.75μV)	0.23%(2.9μV)
Parahippocampus	0.12%(2.5μV)	0.15%(1.9μV)
Hippocampus	0.06%(1.75μV)	0.08%(1.2μV)

4.4.3 Images reconstructed after addition of noise to simulated boundary voltages

Images of the real part in which a clear change occurred at the site of simulated seizure could be observed for all averaging cases for temporal lobe seizures. For the other three regions, this was only the case for fully parallel systems, which permitted the greatest degree of averaging. For imaginary component images, such accurate images could only be observed for temporal and combined hippocampal and parahippocampal seizure regions for the parallel injection and recording case (Figure 4-9-Figure 4-12).

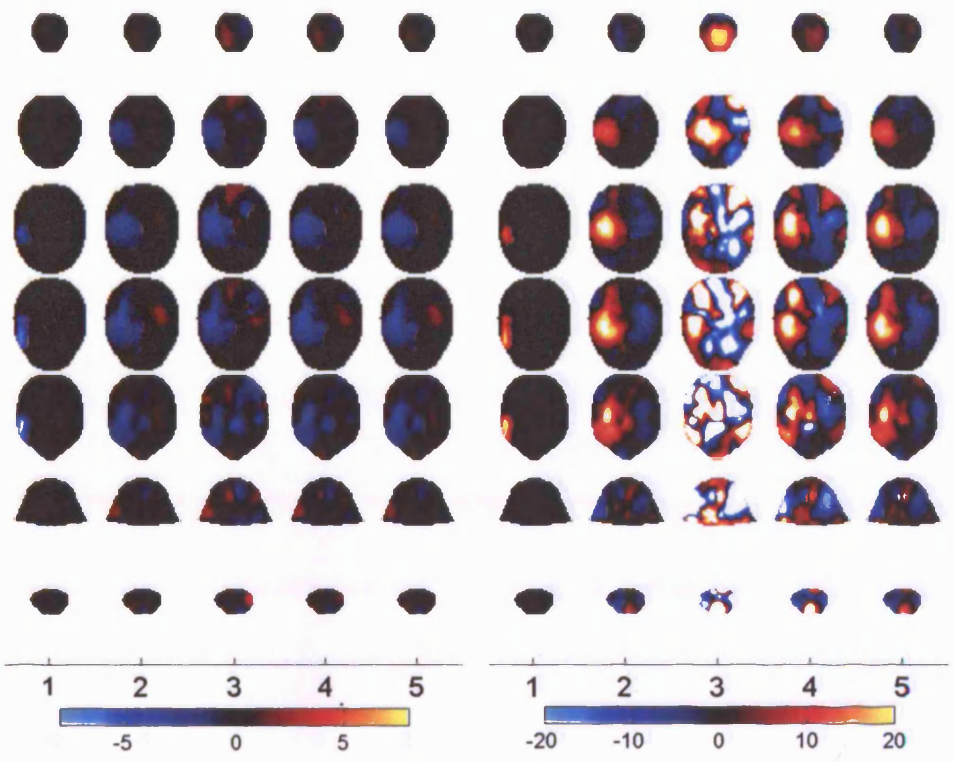

Figure 4-9. Temporal lobe seizure. In this and the following figures, columns indicate simulated seizure region (1), reconstruction without noise (2), reconstruction with noise for EIT systems with serial current injections and voltage measurements (3), with serial current injections, but parallel voltage measurements (4) and with parallel current injections and voltage measurements (5). Slices are shown from top of the head (top) to bottom (bottom). The colour bar indicates percentage impedance change. Real and imaginary changes are shown on the left and right respectively.

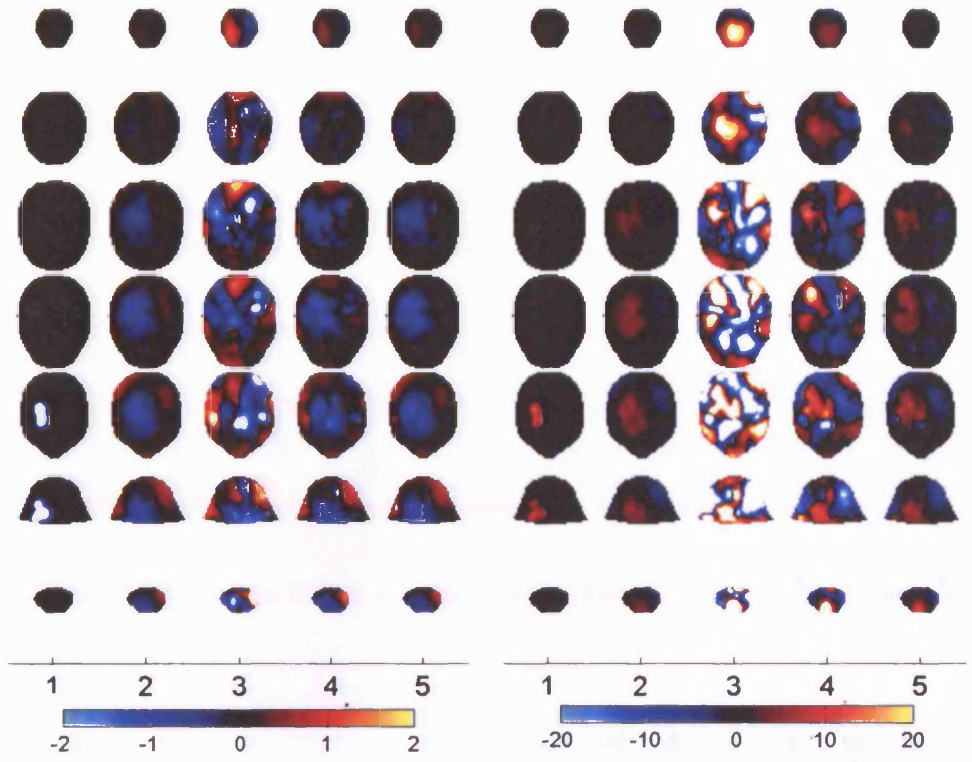

Figure 4-10 Parahippocampus and hippocampus together.

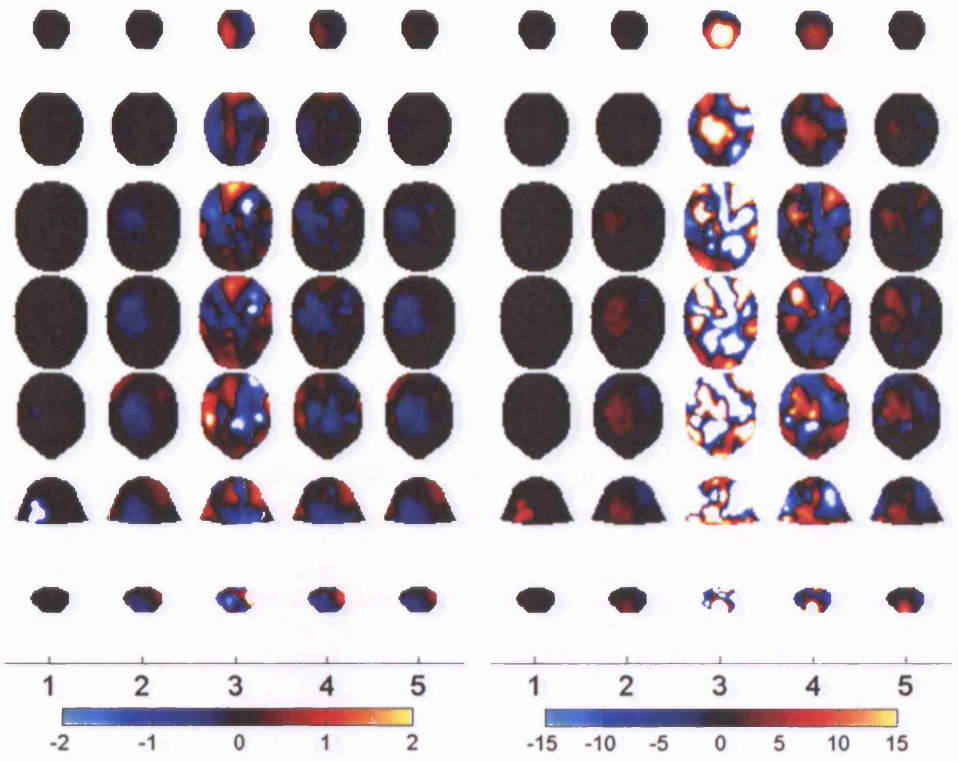

Figure 4-11 Parahippocampus.

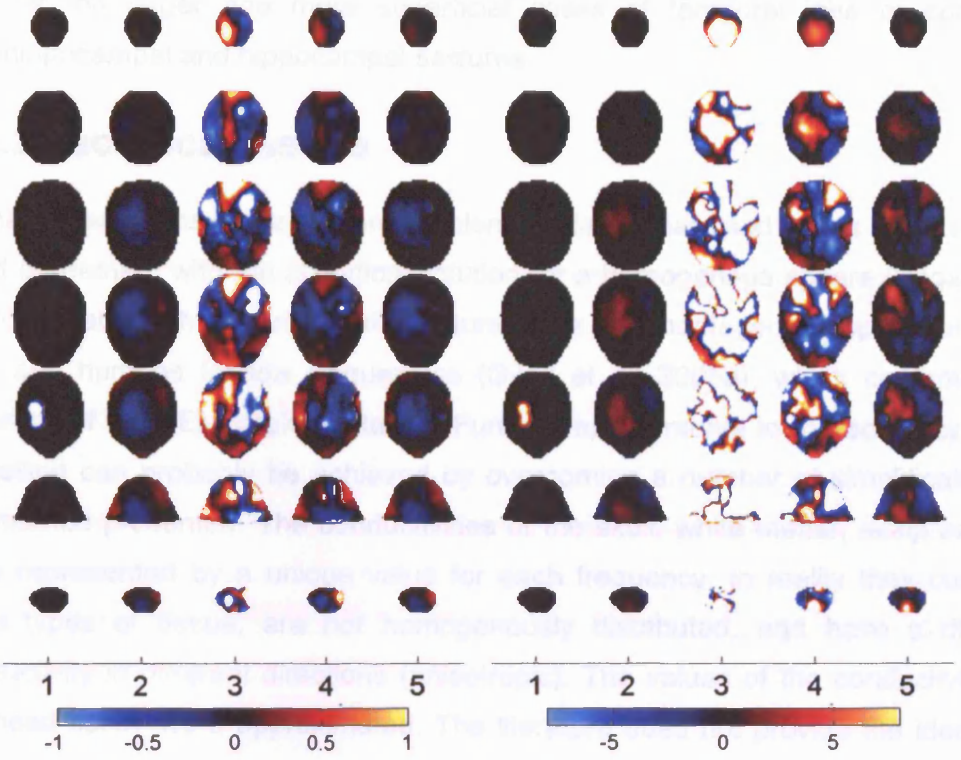

Figure 4-12 Hippocampus.

4.5 Discussion

4.5.1 Summary of results

For a current level of 100 μA at all frequencies, the top 1% of the changes of the boundary voltage was almost 0.8% (1.5 μV) and 0.5% (0.6 μV) for the real and imaginary part respectively for lateral temporal lobe perturbation at 5-50 Hz. The same changes for seizures in parahippocampus and hippocampus together or separate were up to 10 times smaller. With higher current for high frequency, the top 1% of the changes of the boundary voltages was almost 1% (21 μV) and 1.4% (20 μV) for the real and imaginary part respectively for lateral temporal lobe perturbation at 50 kHz. The same changes were still up to 10 times smaller for seizures in smaller and deeper regions of the grey matter. In comparison, noise was estimated as 0.035, 0.01 or 0.002% for serial, semi-parallel or fully parallel systems respectively. With these settings, reasonably accurate images of the real component could be obtained during temporal lobe seizure for all averaging cases, and for the other three regions only for imaging with a parallel recording and injection system which permitted the most averaging. Images of the imaginary component were

noisier but appeared reasonably accurate for parallel injection and recording only, and for the larger and more superficial cases of temporal lobe or combined parahippocampal and hippocampal seizures.

4.5.2 Technical issues

Numerical solutions of the forward problem similar to that used in this study showed good agreement with the analytical solution for a homogenous sphere (Bagshaw et al. 2003), and with experimental measurements in a homogenous spherical saline tank and humans for low frequencies (Gilad et al. 2005a), which confirmed the accuracy of the FEM implementation. Further improvements to the accuracy of the modelling can probably be achieved by overcoming a number of simplifications in the method presented. The conductivities of the skull, white matter, scalp and eye were represented by a unique value for each frequency. In reality they comprise more types of tissue, are not homogenously distributed, and have a different conductivity in different directions (anisotropic). The values of the conductivities of the head tissue were approximated. The literature does not provide the ideal data for our model, which would be given by human in-vivo 4 terminal measurements on the considered frequency range. We selected studies that were as close as possible to this standard and did reasonable corrections and integrations between information, therefore the conductivity spectra finally adopted can be considered the best approximation of the real ones with our current knowledge. The forward problem was solved using Laplace's equation, which assumes the frequency of the measuring current low enough to consider the quasi-steady Maxwell's equations. The solution of the full Maxwell's equations is essentially indistinguishable from that of Laplace's equation up to 1 MHz, but for higher frequency the solution of the first set would have been preferable (Soni et al. 2006).

The noise included in the simulated data before reconstruction was given by preliminary results on a tank and was assumed to be random. This may be worse in the case of real measurement on patients on the ward (Meeson et al. 1996) and it may not be random, and therefore not possible to reduce with averaging. Our estimate assessed the level of signal-to-noise ratio necessary to obtain a clinically useful EIT image, but a rigorous noise characterisation is necessary.

4.5.3 Best measuring frequencies

Using the same current of 100 μA at all frequencies, as in a measuring set-up where all the frequencies are injected together recordings at the lower frequencies of 5 and

50 Hz have the highest changes in percent and absolute values. This appears physiologically reasonable, as the greatest change in conductivity during seizures occurs at these frequencies. This is because the greatest distinction between extra- and intra-cellular space occurs at these low frequencies, being the current mostly confined outside the cell membrane.

Increasing the current according to the IEC601, the frequency with the highest changes is 50 kHz. This is because the benefit from injection of increased current appears to outweigh the larger intrinsic changes at low frequencies. This is self-evident for the criterion of absolute voltages, which may be expected to be higher as a result of the larger current injected. However, the explanation for proportional cases is not immediately apparent, as these might be expected to be independent of injected current – the standing and changed voltages during seizures might be expected to scale proportionately. The explanation is presumably because fewer voltages were above the exclusion threshold for voltages too low to be significant, and these include those with the larger changes.

The RMS noise in the boundary voltages is about 0.3-0.4% for the real part in frequencies up to 100 kHz and it varies between 100-350% at 50 Hz and 15-25% at 50 kHz for the imaginary component. For a seizure in the temporal lobe, this translates to a signal-to-noise ratio of 2:1-3:1 for the real part measurement at 5-50 Hz with a current of 100 μA and at 50 kHz with a current of 5 mA; while for the imaginary part would be below 1:1.

Reducing the noise with averaging, it is likely that the signal-to-noise ratio could be increased 10 times at 50 kHz for a system like our UCH Mark 2.5 which collects data with serial current injection and voltage measurement.

4.5.4 Noise influence on the image reconstruction

With the level of noise which is likely to be present in our measurement with the UCH Mark 2.5 after averaging, only changes in the real part of the conductivity of the temporal lobe can be recognised in the reconstructed images. When the changes happen in deeper parts of the brain, the signal-to-noise ratio is too low to give a clinically useful image. The noise is too large in the imaginary part and obscures the signal in any situation. This also suggests that if movement artefacts, which are of the order of few percent, are present it would be not feasible to reconstruct any image.

The SNR may be enhanced averaging more frames, but with a penalty in temporal resolution, using other signal processing tools or a different EIT system. A semi-parallel system seems to be able to image the real part of the perturbation in an area as small as the parahippocampus, but only the imaginary part of a perturbation in the temporal lobe. A fully-parallel system seems to be able to image everything, but the imaginary part for a perturbation in the hippocampus.

4.5.5 Future work

Performance improvements rely on the possibility of reducing the baseline noise and on the intrinsic EIT instrumentation sensitivity. It may also be possible to average across different seizures in the same subject, assuming that those arising from the same onset zone can be identified clinically. Now that figures for the boundary voltage changes expected during seizures have been estimated, we have to ascertain that baseline noise can be kept well below the signal under controlled and clinical conditions.

The baseline variability in previous experiments was of the order of a few percent using standard EEG electrodes and it was mostly related to movement, and was presumably due changes in contact impedance (Fabrizi et al. 2006b). Alternative electrode designs have been explored (Tidswell et al. 2003a) and will be reconsidered for reducing movement artefacts under ambulatory condition. Future work may include the use of signal processing tools, such as principal component analysis, already implemented in EEG, to enhance EIT sensitivity, which may separate the voltage changes of interest from the noise (Perez-Juste Abascal 2007).

It seems possible that baseline variability can be reduced below the signal we expect, especially when the seizure occurs in the temporal lobe. The first experiment we may carry out in the telemetry ward would be similar to that conducted by Gilad (Gilad et al. 2005a). Employing patients with known epileptic conditions, we could place an array of electrodes on the side of the head where the epilepsy onset area is expected, inject current from the best current injection pair and record potential from all the other electrodes combinations without involving current injection switching. This would be the optimal set-up to measure seizure-related boundary voltage changes, whose detection would lead to a future application of EIT as new method for neuroimaging in epilepsy.

An additional possibility is to use an EIT system with parallel recording or current injection. In addition to the UCH Mk 2.5 and the UCH Mk 1b, we have also been

developing one with parallel recording capabilities, the KHU Mk 1 system, in collaboration with Kyung Hee University (Oh et al. 2007). We plan to conduct clinical studies with this and one of the UCH systems. On the basis of these predictions, it seems plausible that neocortical seizures could be imaged if movement artefact could be kept to a minimum. This could be achieved by recording in the quiet interval of a few seconds before clonic or tonic movement occurs. It may also be possible to improve signal-to-noise by averaging across seizures and by recording at different frequencies and employing signal processing tools which separate the signal of interest from background activities. With these manoeuvres, it may also be possible to image deeper seizures from the mesial temporal lobe or deeper sources from other regions of the brain.

Chapter 5 – Analysis of resting noise characteristics of three EIT system in order to compare suitability for time difference imaging with scalp electrodes during epileptic seizures

5.1 Introduction

In practice, clinical images acquired with biomedical Electrical Impedance Tomography appear noisy and usually suffer from limited spatial resolution. This is due to the underdetermined nature of the image reconstruction, systematic instrumentation errors, and random noise. The bottleneck is not usually clear and will depend on the practical circumstances of the clinical application. For example, one of the most successful applications of EIT has been in imaging lung ventilation (Woo et al. 1992; Frerichs 2000); in this case, the physiological parameter of interest changes by many tens of per cent as air passes into the lungs, and image quality is probably degraded by uncertainties in electrode position and inaccuracies in the model used to reconstruct images. In contrast the amplitude of the changes due to epileptic seizures is far smaller. The feasibility study in Chapter 4 showed that images of epileptic conductivity changes in the temporal lobe could be reconstructed when the random noise level was 0.04%, while, in deeper regions, a noise level of 0.002% was required.

The UCH Mk1b, the UCH Mk2.5 and the KHU Mk1 are three EIT systems potentially suitable for imaging these small changes. As shown in Chapter 3 in the intended clinical application, recordings were made over several days. Sources of noise included physiological drift, fluctuation and movement artefacts. These changes were approximately 1-54%. However, these are unavoidable and outside the scope of this study.

This work is an examination of the characteristics of baseline noise from these systems, with the intention that this could suggest the system likely to yield the best signal quality, and any modifications which could be employed to optimise the signal-to-noise ratio.

5.1.1 Background

5.1.2 Three EIT systems suitable for imaging epileptic seizures

5.1.2.1 UCH Mk 1b

This utilizes a single four electrode impedance-measuring circuit with an analogue demodulator which is multiplexed to up to 32 electrodes (Yerworth et al. 2002). It serially addresses software selectable electrode combinations. The current source and cross point switches are included in a small head box separated from the main base box by a ribbon cable of 5m, which was intended to enable continuous monitoring over days in ambulatory subjects. The in-phase component of the impedance is measured with an analogue phase-sensitive demodulator. A programmable gain amplifier is used to minimize the digitization noise for each electrode combination. It operates at a single selectable frequency between 225 Hz and 65.5 kHz and can apply a current of up to 5mA peak to peak at 50 kHz. Leads to the patient are unscreened and so kept as short as possible – in this study about 30 cm.

5.1.2.2 UCH Mk 2.5

This utilizes one module of the Sheffield Mk 3.5 multifrequency EIT system (Wilson et al. 2001), which comprises a four electrode impedance measuring circuit, multiplexed up to 32 electrodes (McEwan et al. 2006). The in-phase voltage is calculated with synchronized digital demodulation and has a single gain which was optimized for the range of the transfer impedance of the head of up to 70Ω (McEwan et al. 2006). It can operate at frequencies between 20 Hz and 1.6 MHz. It employs a multifrequency composite waveform and records a total of 30 frequencies, divided into 3 sequential packets of 10 frequencies (Romsauerova et al. 2006a). The current is fixed at 0.28 mA peak-to-peak for each frequency. Leads to the patient are unscreened.

5.1.2.3 KHU Mk1 16-Channels

This comprises a single current source which may address any electrode pair using a multiplexer and 16 parallel voltmeters in a novel radially symmetric architecture (Oh et al. 2005). It employs a digital phase-sensitive demodulator and current waveform

generator. In principle, multiple frequencies may be synthesized and injected but, in this study, 3 single frequencies picked from the available range, 39 Hz to 500 kHz, were applied and recording was at fixed gain. The system employs General Impedance Converters which are individually calibrated for each electrode recording pair to optimize the output impedance at each frequency and the electrode leads were 1.2m long with an outer shield and inner driven screen.

The three systems were provided with DC blocking capacitors on each electrode line. The study was approved by the UCH ethics committee and the systems were certified for safety by the UCH Department of Medical Physics.

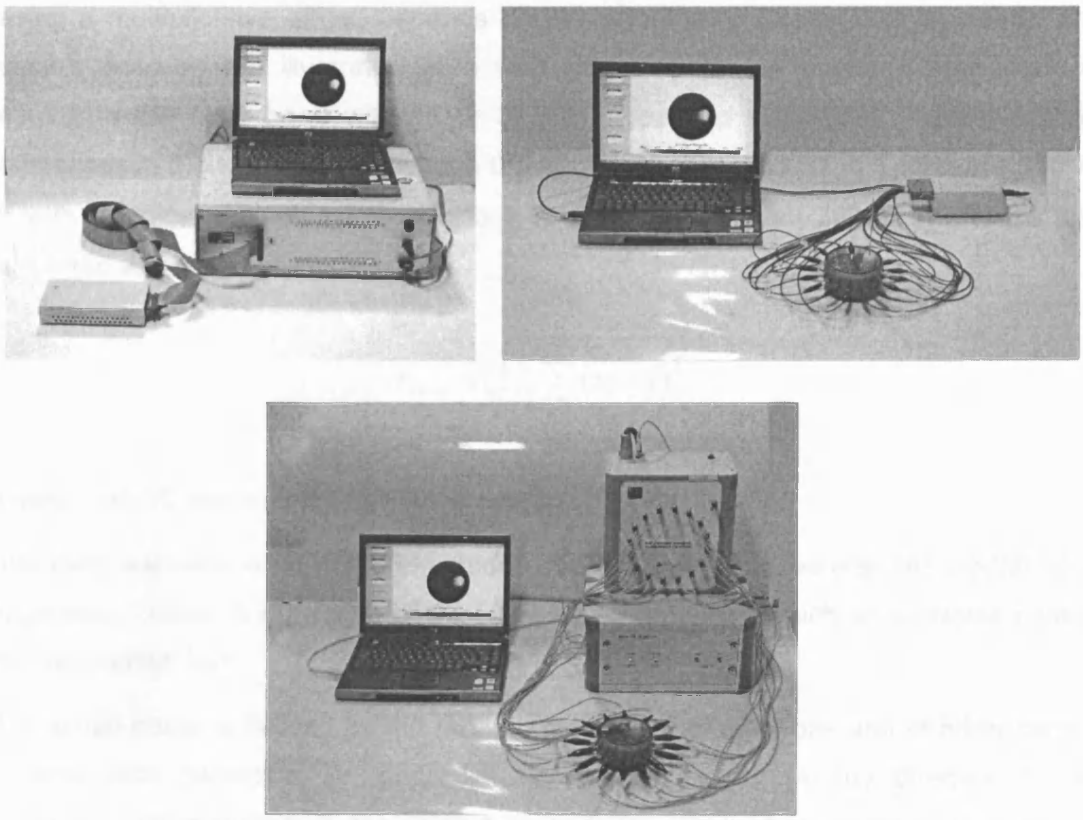

Figure 5-1 EIT systems used in this study. Top left – UCH Mk1b; top right – UCH Mk2.5; lower – KHU Mk1 16 channel. The two latter are shown connected to the cylindrical tank.

5.1.3 Noise

The noise in the voltage measurements has been modelled to predict its propagation through the reconstruction algorithm to the images (Frangi et al. 2002) and attempts have been done to equalize it in different channels so as to have a uniformly distributed

noise in the images (Wang et al. 1994). The SNR can be 3 times larger in the same saline tank for voltages measured close to injecting electrodes with respect to that measured from distant electrodes (Wang et al. 1994). Two main types of equivalent noise sources have been identified in these studies: 1) electronic noise in the current drivers and 2) in the voltage detectors. The first one has a multiplicative effect in that it depends on the signal level, because it propagates through the transimpedance; the second has a signal-independent additive contribution due mainly to thermal noise. Another source of noise intrinsic to the systems is that associated with quantization of the signal (Bennett 1948). In addition to these, the physiological variability of the measured transimpedance has been suggested as a fourth source of noise, which, having a multiplicative effect, depends on the signal level (Meeson et al. 1996). The possible sources are illustrated here with reference to our intended application of imaging in the adult head with 16 or 32 EEG type cup electrodes. Typical transfer resistances in the adult human head in the frequency range 20 Hz to 1 MHz are 8 to 70 Ω, with a typical median value of about 40 Ω (McEwan et al. 2006). The noise was calculated as:

$$V_{RMS} = \sqrt{\frac{1}{N}\sum_{i=1}^{N}\left(x_i - \hat{x}\right)^2} \tag{5-1}$$

Where x_i are N data points and $\hat{x}$ their average.

The noise was estimated at the electrodes, therefore the sources after the amplification stage were divided by the gain of the UCH Mk2.5 amplifier, which is 30. Noise causes may be divided into:

1) Thermal noise is caused by the random movement of electrons and of other current carriers. This generates an unpredictable instant current in any direction in the electronics of the system, in the contact impedances and load impedance. The spectral density of the RMS thermal noise can be calculated with the Nyquist equation:

$$\frac{V_{th}}{\sqrt{B}} = \sqrt{4kTR} \tag{5-2}$$

Where k is the Boltzmann constant (1.38×10^{-23} J/K), T is the temperature in Kelvin, B is the bandwidth in Hz and R is the resistance in Ω. For example, for a resistive load of

40Ω (R_L) and contact impedances of 1kΩ (R_C) at 20°C, the spectral density of the thermal noise is $\sqrt{4kT(2R_C + R_L)}$ ≈ 5 nV/√Hz, assuming that the dissipation of the resistor is large enough to not increase its temperature, and it is dominated by the contact impedance.

2) The Analogue to Digital Converter (ADC) of the system introduces quantization noise, due to the bit resolution. In most cases it results in an addition of random noise to the signal, which is related to bandwidth of measurement and so the sampling rate. The quantization error is uniformly distributed between ±½ LSB with zero mean and RMS of LSB/√12 (Bennett 1948). For example the ADC of each of the 3 systems has 12 bit resolution and ±1V full scale deflection (FSD) for the UCH Mk2.5 and KHU Mk1. Therefore they have a RMS quantization error of $(2V/2^{12})/\sqrt{12} \approx 141\mu V$, which corresponds to 5μV for a system with gain 30. This noise is white and its spectral density is dependent on the sampling frequency f_s of the ADC according to:

$$\frac{LSB/\sqrt{12}}{\sqrt{f_s/2}} \tag{5-3}$$

In the UCH Mk2.5, 2048 samples are taken for each cycle of the slowest frequency carrier of each époque. For example we assume f_s 2.52*2048 kHz ≈ 5 MHz. The quantization noise spectral density is then 3 nV/√Hz.

3) The voltage receive amplifiers do not have ideal behaviour and introduce a white noise that can influence measurements on a single resistor. A typical high input impedance FET based OP-AMP, the OPA 655, has a noise of 6-8 nV/√Hz between 1kHz and 100 kHz (http://focus.ti.com), being higher at low frequency.

These three noise sources are well defined and an estimate of their total effect may be made. If we assume the noise is random and uncorrelated (Frangi et al. 2002), the RMS values of these noise components can be added together as:

$$V_{rms} = \sqrt{V_{rms1}^2 + V_{rms2}^2 + V_{rms3}^2} \tag{5-4}$$

This results in a total RMS noise spectral density of 9 nV/√Hz. This is the noise on the spectrum of the carrier frequencies. After demodulation, the spectral noise density will still be the same, but the bandwidth will be reduced according to low-pass filter (or

equivalent) stage of the demodulator, so the total noise will be reduced with respect to that on the carrier (Frangi et al. 2002). For example, in the UCH Mk2.5 the demodulation is performed with a Digital Fourier Transform (DFT) which is computed using 4096 samples over one waveform of the slowest frequency, so the Fourier spectrum will have a resolution of 2049 frequency bins. Considering a sampling frequency of f_s = 2.52*2048 kHz ≈ 5 MHz, the bandwidth of each sample is Nyquist frequency/number of samples of the spectrum =(f_s/2)/2048 ≈ 1.22 kHz, so the total RMS noise on the modulated signal is 9 nV/√Hz x √1.22kHz ≈ 0.31 μV, which correspond to 0.44 μV in amplitude.

There are other noise sources which are difficult to estimate as they depend on particular experimental conditions and so can only be estimated empirically. These include:

4) Electromagnetic interference results from coupling to the system, cables and subject from surrounding sources of electromagnetic radiations (Grimnes and Martinsen 2000). If the coupling between these sources and the electrodes is different, then a differential signal can be generated and, if the coupling fluctuates, it can result in noise. Furthermore, since the ground electrode is in a specific point of the body, the leakage current will flow through it and will generate a potential across the recording electrodes, which fluctuates with the coupling. Multiplexing can cause a charge injection during switching and so a transient effect in charging and discharging the stray capacitance, the capacitance of the switches and the DC blocking capacitance (see (Saulnier 2005) for a recent review). Even if these components remain constant (i.e. no subject or cable movement), the continuous change of the recording pairs can cause the parasitic capacitance to discharge during the voltage measurements. If the level of charge fluctuates, this phenomenon can produce noise. Furthermore it is possible that the parasitic capacitances change because of environmental factors, not involving the EIT hardware.

5) On a saline tank, or between the electrode and conductive gel, the metal-electrolyte interface can contribute to the noise with spontaneous voltage fluctuations, which tend to decrease when the contact potential between metal and electrolyte have had time to stabilize (Huigen et al. 2002). In human subjects, the skin-electrolyte interface introduces a contact impedance which is responsible for further thermal noise and possible potential oscillations (Huigen et al. 2002).

6) Electronic noise of the current source which is signal dependent (Frangi et al. 2002).

7) Finally, physiological noise is also present and probably depends on the autonomic activity of muscle and blood vessels, on the variations in skin property, on the oscillations of the body temperature and on other impedance changes not related with the phenomenon of interests (Meeson et al. 1996).

5.2 Purpose

The purpose of the present chapter was to investigate the possible sources of noise in the UCH Mk1b, UCH Mk2.5 and KHU Mk1 16 channel in order to suggest ways to improve the signal-to-noise ratio and then select the most suitable system for conducting clinical experiments. Where possible, we attempted to divide the noise in its components due to electronics and thermal noise, to metal-ion interaction and environment and to ion-skin interaction and physiological processes, by recording in resistors, saline filled tanks and human subjects. We also explored the noise dependence on measuring frequency and on load impedance and the difference between 4-terminal and multiplexed measurements.

5.3 Design

The measurements were collected at the maximal acquisition rate and current injection allowed by each frequency, safety standard and system performance. Three representative frequencies were selected for each system. The range was limited downward by the acquisition speed of the UCH Mk2.5 at about 1 kHz and upward by the maximal operating frequency of the UCH Mk1b at about 100 kHz. The UCH Mk2.5 and KHU Mk1 could function at higher frequencies, but the image rate limited the acquisition speed and the clinical signal may be expected to decrease at high frequency (Fabrizi et al. 2006a), so the frequencies recorded were between 1kHz and 100 kHz. Measurements were made at the slightly differing frequencies of 100 kHz and 65 kHz, because of the design of the different system. An analysis of tissue properties in this range in the head indicates that differences in conductivity are less than 8 mS/m (0.7 %) and so negligible (Fabrizi et al. 2006a). Noise recorded in a saline tank (Brown and Seagar 1987; McEwan et al. 2005) was similar in this range, so the measurements have been treated as comparable. Only the real part of the voltages was considered in this study as in the widely used Sheffield Mk 1 (Brown and Seagar 1987). The reason is

that in EIT, measurement of the in-phase and quadrature component may be made, but all successful clinical studies have only recorded the in-phase component, as the quadrature component is contaminated by errors due to stray capacitance.

In order to ascertain the sources of noise, experiments of increasing complexity were performed. The simplest measurement comprised single channel 4-terminal measurements on resistors of increasing values. It was used to examine the effect of increasing load over the whole range of transfer impedances likely to be encountered in different subjects in the human head of 8-70 Ω (McEwan et al. 2006). This characterized the noise due to the electronics and the influence of increasing load on the thermal noise of a purely resistive object. This was then repeated on a resistor network with use of the multiplexer in order to assess if additional noise was introduced by the series resistance and stray capacitance of the multiplexer. Similar tests were conducted on a saline phantom to assess the noise derived from the metal-electrolyte interaction and from electromagnetic and mechanical effects, such as saline movement and temperature fluctuations. In both of these, the effect of load was assessed, but to a lesser extent than with the single channel 4 terminal recording. Measurements were made in three selected channels, which had serially increasing distance from the polar current injection electrode. This closely simulates the situation in in-vivo recordings in the head, where different channels in any one recording will encounter a range of transfer impedances. The range with this method was 10 – 18 Ω in three steps for the resistor phantom. Finally, recordings were made in a resting human subject with scalp electrodes in order to determine the effects of the electrode-skin contact impedance variations and physiological noise, such as autonomic activity of muscle and blood vessels and body temperature variations.

5.4 Methods

5.4.1 Recording arrangement

Each system was connected to the test objects with cables which were 30 cm-long unscreened cables for the Mk 1b, 55cm-long 37-way unscreened ribbon cable for the Mk 2.5 and 1.2m-long triaxial cable with driven and shielded screens for the KHU Mk1. Each acquisition was executed at three frequencies, representing the low, medium and

high frequency ranges for each system, that were chosen to be as similar as possible between the 3 systems to allow comparison (Table 5-1).

All measurements except for the single electrode combination on one resistor were made in a ring with 16 electrodes. Single channel measurements were made with current injected into electrodes 4 and 12 and recording from 13-14, 14-15 or 15-16, so that three different transfer impedances were addressed. The same set-up was used for all the systems; therefore the same loads were measured. Multiplexed measurements were made with a protocol with which current was injected through diametrically opposed electrodes in turn and voltage recordings were made serially from remaining adjacent pairs in each case. Noise was calculated from 1024 consecutive measurements from each of the three above combinations in turn; the remaining data were discarded.

Table 5-1 Settings of the systems for single and multiple channel measurement.

System	Frequency	Acquisition rate		Current
		Single channel	Multiple ch.	
UCH Mk1b	1.2 kHz	32 ms/meas	1250 ms/meas	0.14 mA
	9.6 kHz	23 ms/meas	246 ms/meas	1 mA
	65.5 kHz	21 ms/meas	123 ms/meas	2.6 mA
UCH Mk2.5	2 kHz	22.5 ms/meas	2200 ms/meas	0.138 mA
	10.08 kHz	22.5 ms/meas	2200 ms/meas	0.138 mA
	101.6 kHz	22.5 ms/meas	2200 ms/meas	0.138 mA
KHU Mk1 16 channel	1 kHz	65 ms/meas	118 ms/meas	0.14 mA
	10 kHz	60 ms/meas	84 ms/meas	1 mA
	100 kHz	60 ms/meas	84 ms/meas	1.12 mA

5.4.2 Resistor recordings

A 4-terminal measurement was performed on 3 loads (14, 44 and 77 Ω, Figure 5-2), with 1 kΩ as contact impedance.

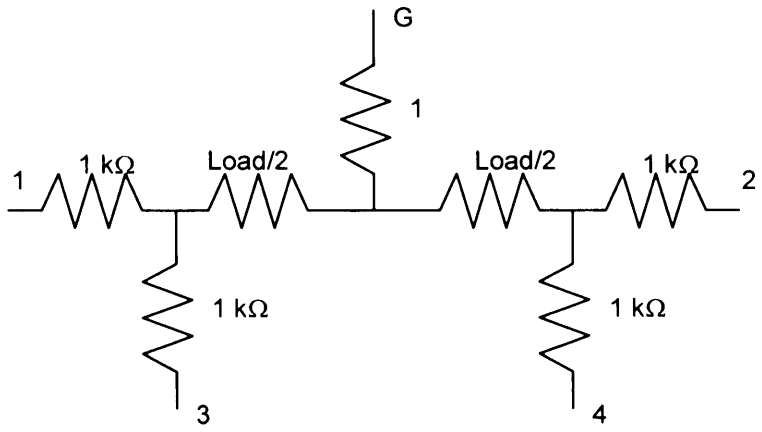

Figure 5-2 Four terminal measurement set-up. The injecting pair was connected to terminal 1 and 2 and the measuring pair to terminal 3 and 4. The ground (G) was connected in the middle of the load. Load = 14, 44 or 77Ω.

The multiplexed recording was performed on a symmetrical resistor network with 16 terminals (Figure 5-3) (Griffiths 1988; Griffiths 1995; Meeson et al. 1996; Hahn et al. 2000; Hahn et al. 2001). This was chosen for simplicity against more complete and accurate phantoms which simulate the impedance of the body and give the possibility of local impedance changes to test the reconstruction algorithms (Griffiths 1995; Schneider et al. 2000; Hahn et al. 2001) because we were interested in testing the performance in the measurement only of the real component of the voltages and we were not directly addressing image reconstruction. The KHU Mk1 was connected to the network using an extension of 30cm-long unscreened cables; the other systems were connected directly. The choice of the resistance in the development of the phantom were that the load to the current source and the transimpedance were similar to that on the head (Hahn et al. 2000). The transfer resistances from the three selected channels were calculated independently with a circuit simulation (5Spice, www.5spice.com) at DC and were 18, 13 and 10 Ω, while the input impedance for the current source was 740 Ω, therefore in the range of that likely to be encountered on the head.

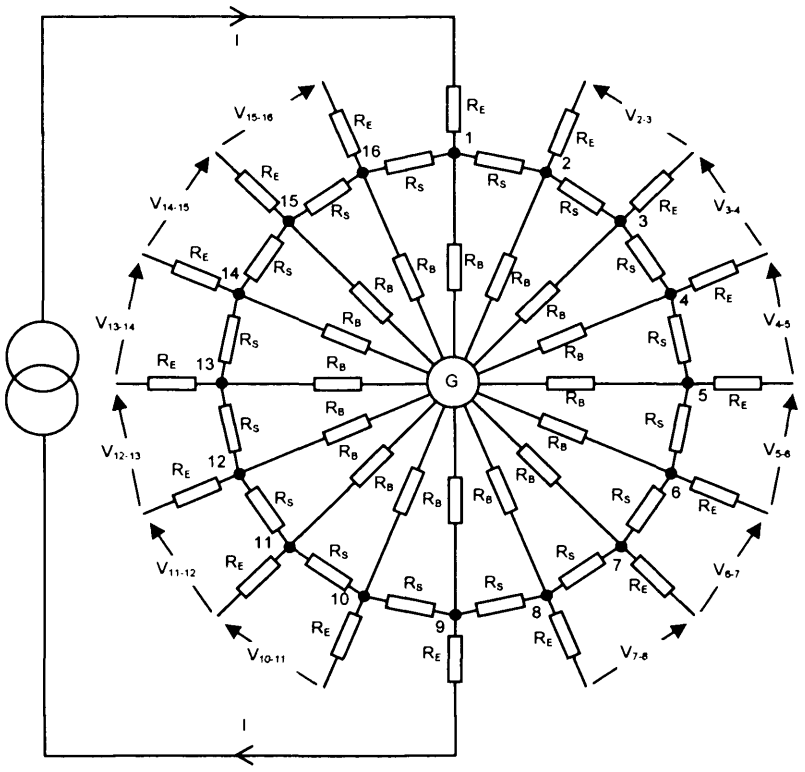

Figure 5-3 Resistor network experiment. Rb=Re=300 Ω, Rs=75 Ω. The current was injected from diametrically opposed electrodes and measurements done on the other adjacent electrodes pairs. For the analysis the electrode combinations with drive on 4-12 and measurements on 13-14, 14-15 and 15-16 were chosen.

5.4.3 Saline tank

A cylindrical tank (9cm diameter, 5cm deep) with 16 equally spaced, recessed stainless steel electrodes, 5mm in diameter, in a single ring (Figure 5-1), was filled with 200 ml of 0.3% NaCl solution at room temperature of 20 °C (Holder et al. 1996a). The ratio of recorded voltages for the three channels selected to represent different loads at the middle carrier frequency was 1, 1.18 and 2.05. For the 4-terminal measurement the current was injected between electrodes 4-12 and voltage recorded between 13-14, 14-15, 15-16. The receive electrodes measure decreasing loads, the further they are from the drive electrodes.

5.4.4 Human

A single ring of 16 Ag-AgCl standard EEG cup electrodes of 10 mm diameter was placed just above the level of the ears of a healthy 27 year-old male volunteer, and recordings were made with the subject reclining in a chair in a comfortable position. The

skin was previously abraded with abrasive gel and the electrodes applied with 10-20 conductive paste (D.O. Weaver&Co., Aurora, CO 80011, USA) to improve the contact impedance. Each electrode had an unscreened wire of 5 cm onto which the cables of the systems were clipped. The ratio of recorded voltages for the three channels selected to represent different loads at the middle carrier frequency was 1, 1.24 and 5.46.

5.4.5 Data analysis

1024 boundary voltage measurements were collected during each recording, irrespective of the time taken. These were divided in 4 segments of 256 each and multiplied by a Hanning window. The DC component was subtracted from each segment and four 256-points spectra of the amplitude of the real part of the voltages (R) were analyzed with FFT (MATLAB function) and then averaged together. This averaging does not reduce the noise of the signal but that of the spectrum, so it improves the estimation of each frequency content.

The spectra appeared to be white but there were occasional outlying values, presumably due to instrumentation non-idealities (Figure 5-4). For ease of analysis, each spectrum was reduced to the mean noise frequency content after exclusion of data from any outlying frequency with noise content 2 standard deviations (SD) greater than the mean. This was justified on the basis that those values were above 7 Hz, while impedance changes in epilepsy do not exceed 2 Hz (Elazar et al. 1966; Fox et al. 2004). These were then assessed for statistical significance by five way analysis of variance using the statistical Toolbox of Matlab v 6.5 (www.mathworks.com); the variables were experimental preparation, carrier frequency, load, multiplexer presence and EIT system. The residuals from the linear model, not including interactions, were normally distributed, so it appeared that the assumptions for using ANOVA were satisfied.

Unless stated otherwise, all noise below is expressed as percentage proportion of the adjusted mean frequency content relative to the standing voltage (DC component), this is termed *proportional noise*. In figures and results below, noise is shown as mean ± 1SE.

5.5 Results

5.5.1 Difference across variables

There was a significant difference between all the variables except for the presence of the multiplexer for proportional noise (Table 5-2). All spectra are shown in (Figure 5-4).

Table 5-2 Significance of the difference in noise with respect to experimental variables (5-way ANOVA). The marked p values show the variables which are significantly different ($p<0.05$) as indicated in Figure 5-5, Figure 5-6, Figure 5-9 and Figure 5-10.

Variable	Proportional noise (%)		Absolute noise (μV)	
	F value	p	F value	p
Preparation (resistor, tank, human)	7.42	0.0008*	4.12	0.018*
EIT system (UCH Mk1b, Mk2.5, KHU Mk1)	7.39	0.0009*	16.4	0*
Multiplexing	0.29	0.59	7.94	0.006*
Carrier frequency (low, medium, high)	4.43	0.01*	8.34	0.0004*
Load (low, medium, high)	7.02	0.001*	3.98	0.02*

Figure 5-4 Spectra of the proportional noise amplitude. For each test object, the top rows (a - c) refer to 4-terminal measurements and bottom rows (d - f) refer to multiplexed ones. In each plot, the different traces are for three loads. For each test object, the rows "high" "medium" and "low" refer to the carrier frequency used (Table 5-1).

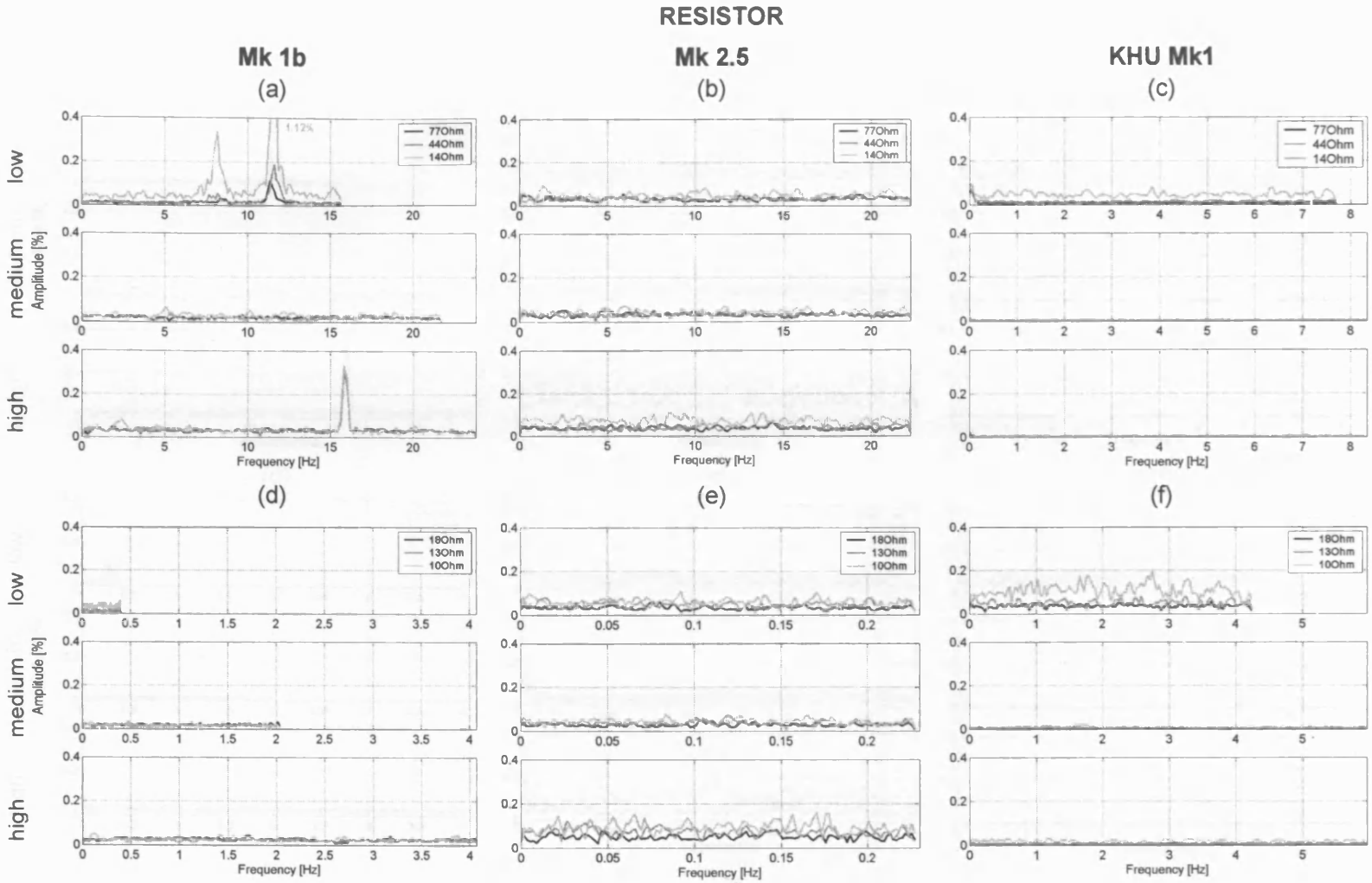
RESISTOR
Mk 1b
Mk 2.5
KHU Mk1
(a)
(b)
(c)
(d)
(e)
(f)
low
medium
high
Amplitude [%]
Frequency [Hz]
77Ohm
44Ohm
14Ohm
18Ohm
13Ohm
10Ohm
1.12%

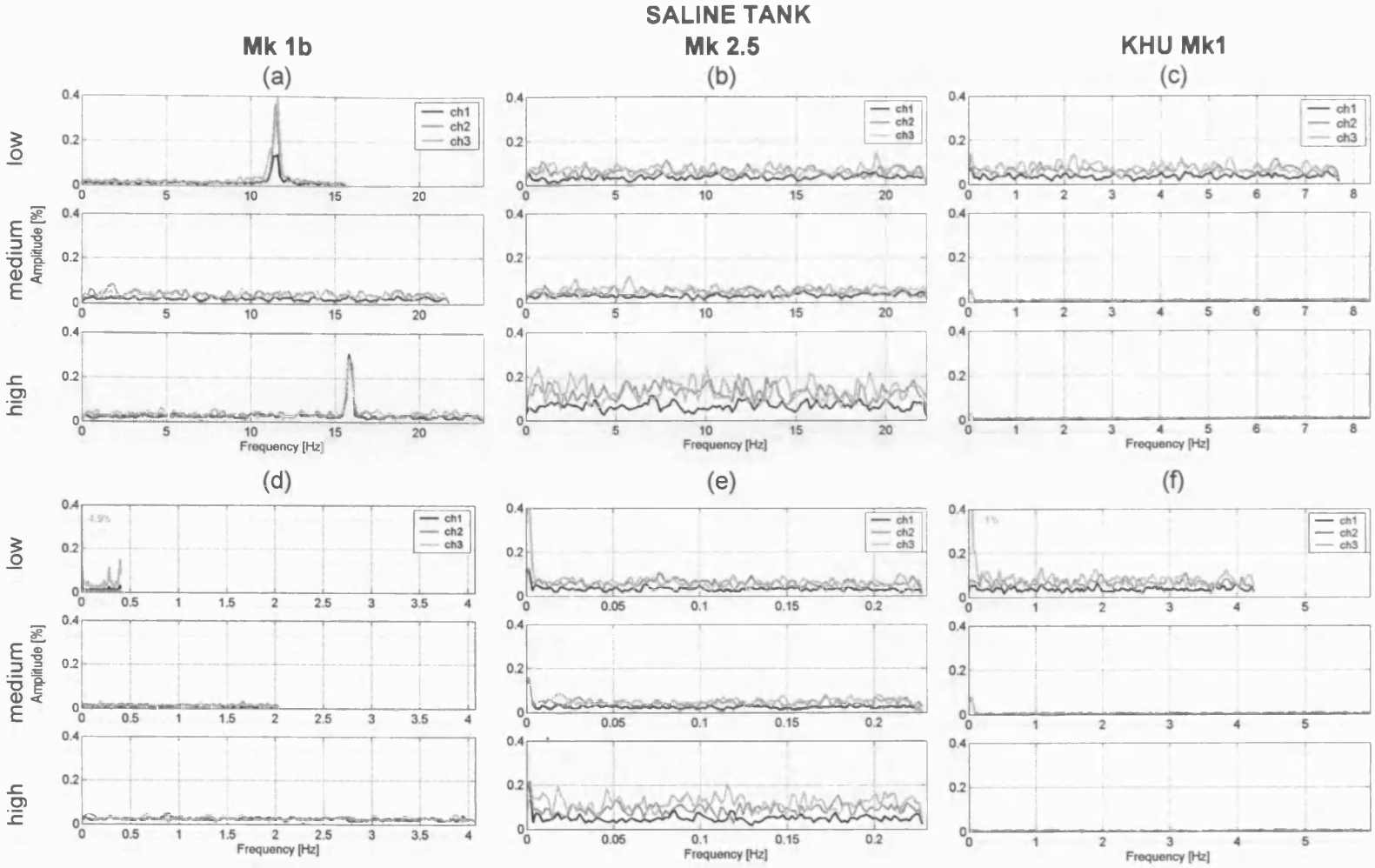
SALINE TANK
Mk 1b
Mk 2.5
KHU Mk1
(a)
(b)
(c)
(d)
(e)
(f)
low
medium
high
Amplitude [%]
Frequency [Hz]
ch1
ch2
ch3

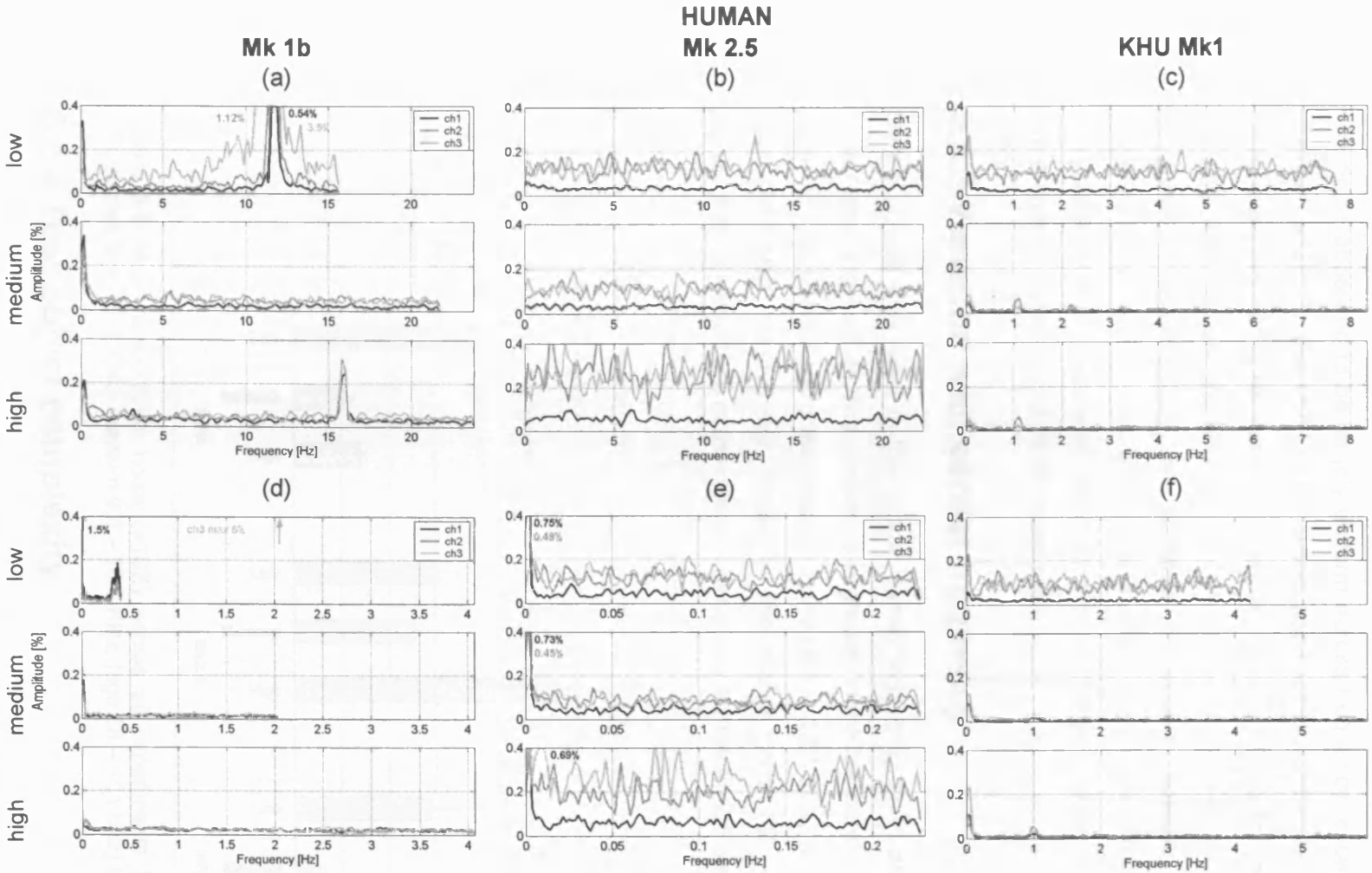
HUMAN
Mk 1b
Mk 2.5
KHU Mk1
(a)
(b)
(c)
(d)
(e)
(f)
low
medium
high
Amplitude [%]
Frequency [Hz]
ch1
ch2
ch3
1.12%
0.54%
3.5%
1.5%
0.75%
0.48%
0.73%
0.45%
0.69%

5.5.2 Variation with frequency

The noise appeared to be largely uniform across frequency, except for two system specific cases: (i) the UCH Mk1b when used without multiplexing had a higher content around 12 Hz for the low carrier and around 16 Hz for the high carrier; (ii) the KHU Mk1 showed harmonics of about 1 Hz when applied on a human subject. As these changes could be ascribed to system specific non-idealities in instrumentation, rather than a consistent effect, they were excluded from further analysis by the procedure of elimination of any noise values across frequencies which were at more than 2 SD from the mean.

5.5.3 Variation with carrier frequency

Overall, noise was least in the middle carrier frequency band and greatest in the lower band (Figure 5-5). Mean noise was greater in the low band (1 – 2 kHz) by 251, 71 or 771 % compared to the medium band (9.6 – 10.1 kHz) for the Mk1b, Mk2.5 and KHU Mk1 respectively. Noise in the higher band (65 – 101 kHz) was significantly greater than in the medium band only for the Mk2.5 system – by 121%.

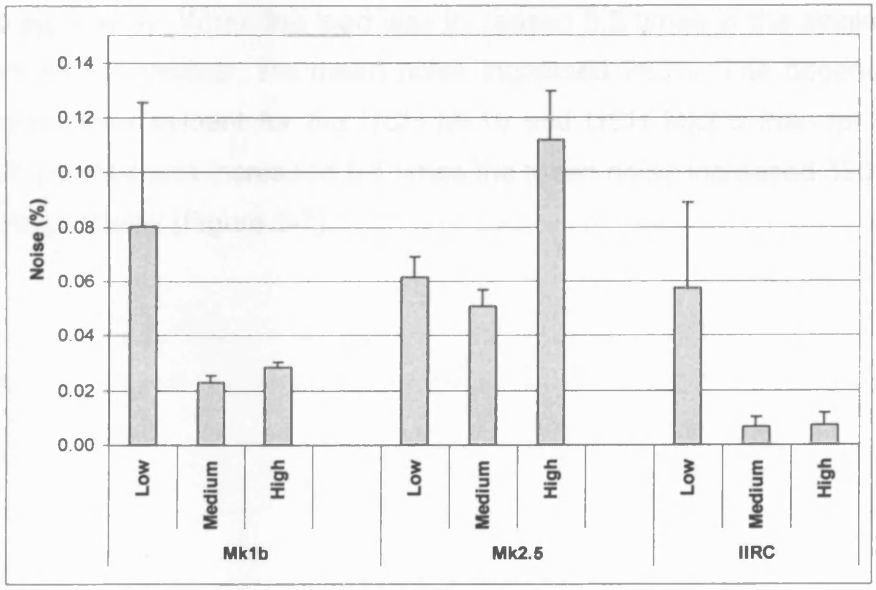

Figure 5-5 Mean proportional noise (+1SE) across all experiments for different carrier frequencies (low 1 – 2 KHz, medium 9.6 – 10.1 KHz, high 65 – 101 kHz) (n=18, $p < 0.05$).

5.5.4 Test object complexity

Noise increased with recording on the saline filled tank and human by 27 and 167% compared to the resistor measurements (Figure 5-6).

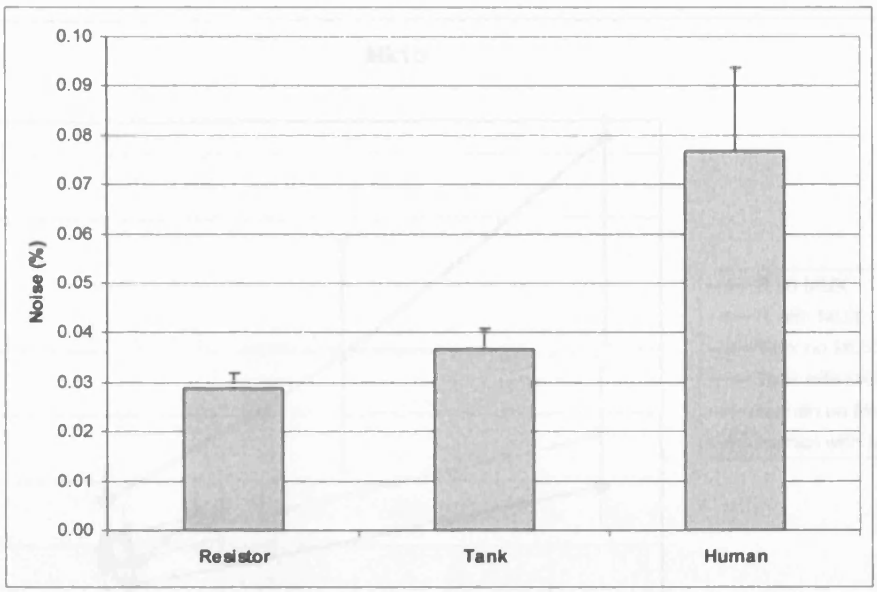

Figure 5-6 Mean proportional noise (+1SE) across all experiments for different experimental preparations (Resistor/saline filled tank/human) (n=54, $p < 0.05$).

5.5.5 Load

Overall, the noise increased with load. The precise loads varied between experiments with or without multiplexing and different test objects and so data are presented separately. When the load was increased 5.5 times in the single channel experiment on the resistor, the mean noise increased 263%. The dependence on the load was more evident for the UCH Mk1b and UCH Mk2.5 than for the KHU Mk1; when the load was increased 5.5 times the mean noise increased 326%, 242% and 12% respectively (Figure 5-7).

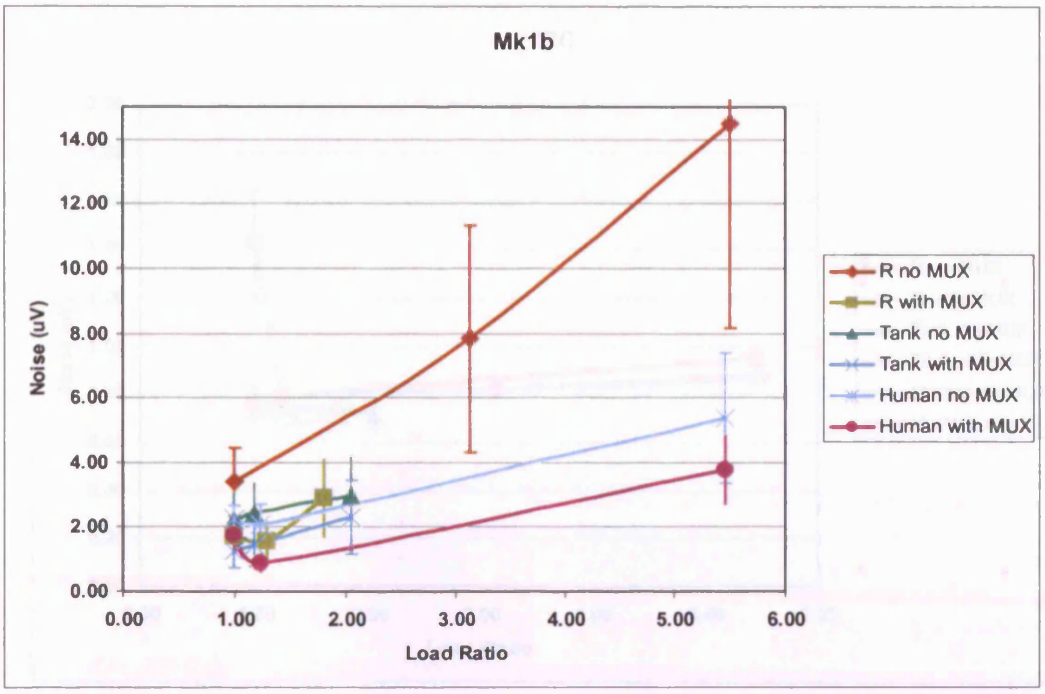
Mk1b
Noise (uV)
14.00
12.00
10.00
8.00
6.00
4.00
2.00
0.00
0.00
1.00
2.00
3.00
4.00
5.00
6.00
Load Ratio
R no MUX
R with MUX
Tank no MUX
Tank with MUX
Human no MUX
Human with MUX

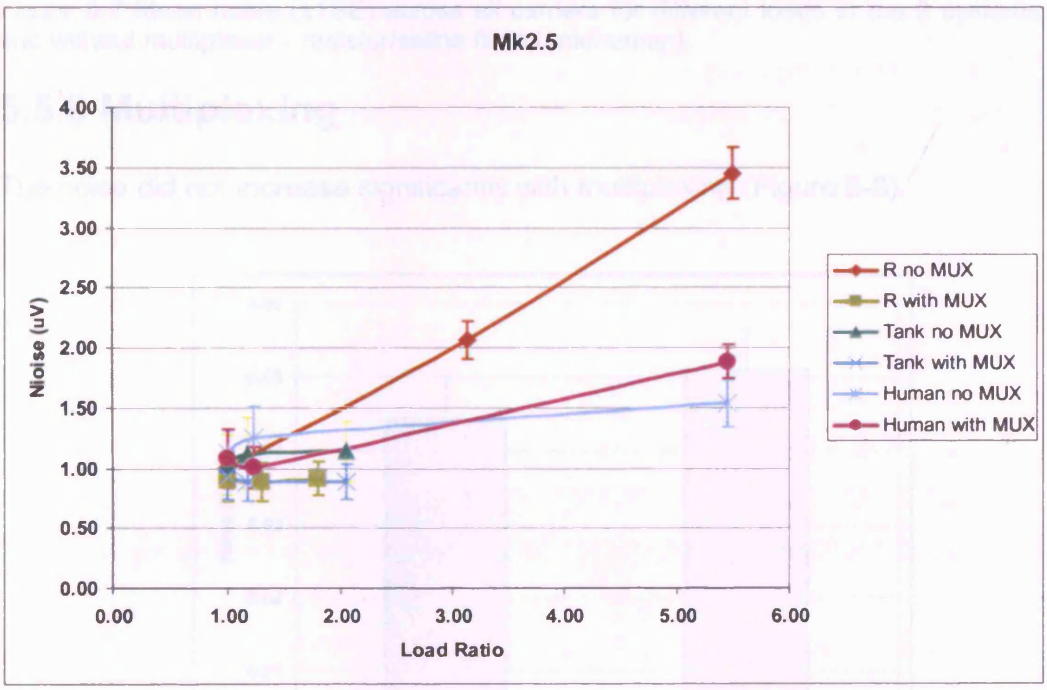
Mk2.5
Noise (uV)
4.00
3.50
3.00
2.50
2.00
1.50
1.00
0.50
0.00
0.00
1.00
2.00
3.00
4.00
5.00
6.00
Load Ratio
R no MUX
R with MUX
Tank no MUX
Tank with MUX
Human no MUX
Human with MUX

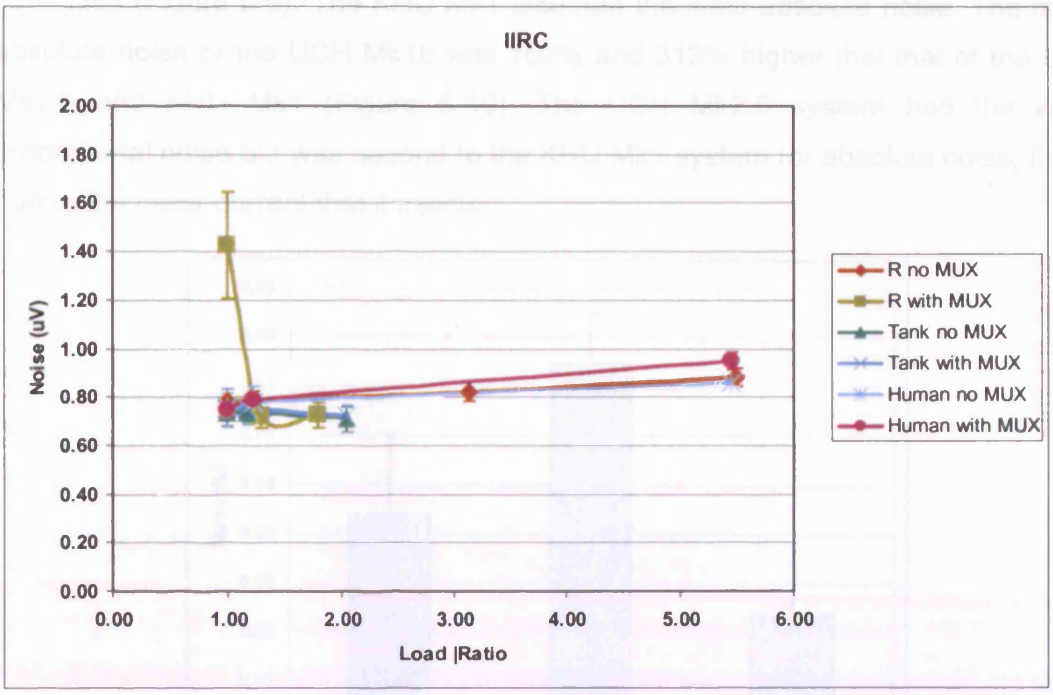

Figure 5-7 Mean noise (±1SE) across all carriers for different loads in the 3 systems (with and without multiplexer - resistor/saline filled tank/human).

5.5.6 Multiplexing

The noise did not increase significantly with multiplexing (Figure 5-8).

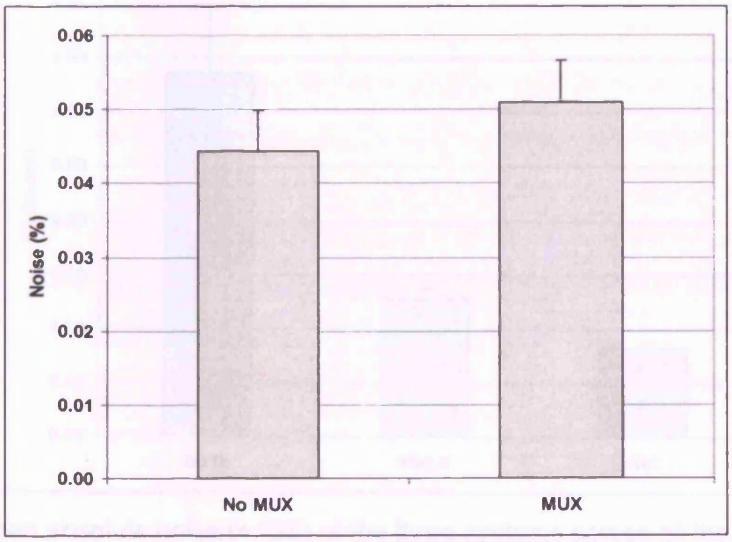

Figure 5-8 Mean proportional noise (+1SE) across experiments with and without multiplexing.

5.5.7 EIT system

The KHU Mk1 had the lowest noise of the three systems. The mean proportional noise of the UCH Mk2.5 was 70% and 216% higher than that of the UCH Mk1b and

KHU Mk1 (Figure 5-9). The KHU Mk1 also had the least absolute noise. The mean absolute noise of the UCH Mk1b was 162% and 313% higher that that of the UCH Mk2.5 and KHU Mk1 (Figure 5-10). The UCH Mk2.5 system had the worst proportional noise but was second to the KHU Mk1 system for absolute noise; this is due to the lower current that it injects.

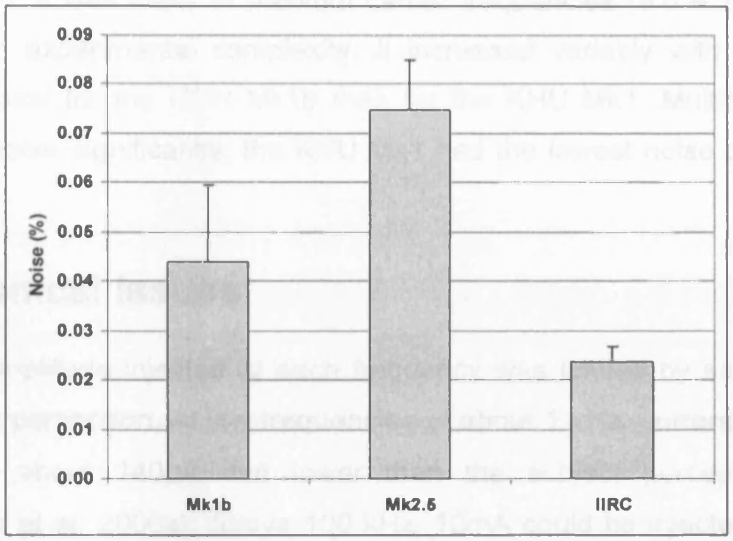

Figure 5-9 Mean proportional noise (+1SE) of the three systems across all the experiments (n=54, $p < 0.05$).

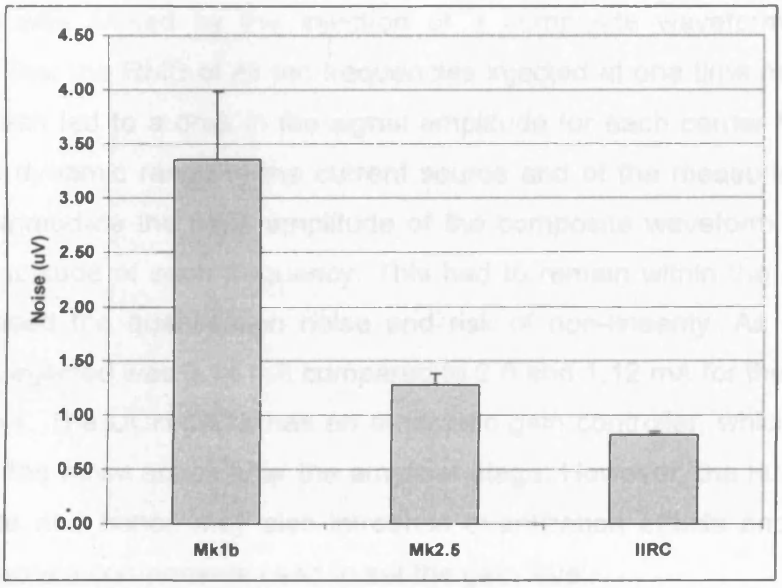

Figure 5-10 Mean absolute noise (+1SE) of the three systems across all the experiments (n=54, $p < 0.05$).

5.6 Discussion

5.6.1 Summary of results

The noise for all the three systems was generally uniform over frequency, except for the UCH Mk1b. It was lower at medium carrier frequencies (9.6 – 10.08 kHz) and increased with experimental complexity. It increased variably with load and was more proportional for the UCH Mk1b than for the KHU Mk1. Multiplexing did not increase the noise significantly; the KHU Mk1 had the lowest noise overall (0.02%, 0.8 μV).

5.6.2 Technical issues

The current amplitude injected at each frequency was limited by safety standards and by patient perception. At low frequencies of about 1 kHz, current injected by all systems was about 140μA and lower than the subject perception threshold (Romsauerova et al. 2006a). Above 100 kHz, 10mA could be injected according to safety limits, but none of the systems had this capability, so the current was the highest attainable by the instrumentation. The current that could be injected with the UCH Mk2.5 was limited by the injection of a composite waveform which was designed so that the RMS of all ten frequencies injected at one time met the safety standard, which led to a drop in the signal amplitude for each carrier frequency. In addition, the dynamic range of the current source and of the measuring amplifiers had to accommodate the peak amplitude of the composite waveform, which is 10 times the amplitude of each frequency. This had to remain within the linear range, which increased the quantisation noise and risk of non-linearity. As a result, the peak current injected was 0.14 mA compared to 2.6 and 1.12 mA for the UCH Mk 1b and KHU Mk1. The UCH Mk1b has an automatic gain controller, which may be an advantage if the noise arises after the amplifier stage. However, the number of gain levels is finite and hence may also introduce quantization effects and uncertainty due to the discrete components used to set the gain level.

In order to keep the experiment as similar as possible between systems and practically feasible, we had to use 30cm-long extensions of unscreened wires to test the KHU Mk1 on the resistor network and electrodes on human had 5cm-long unscreened wires, on which the system cables were clipped. This may have introduced extra stray capacitance.

All measurements except for the single electrode combination on one resistor were made in a ring of 16 electrodes and the transfer impedances with and without multiplexing were equivalent and changed only by selecting different combinations. The single channel measurements on the resistor were done using 3 physically different loads of 14, 44 and 77 Ω, while the transfer impedance when multiplexing was of 10, 13 and 18 Ω so the load multiples were not directly comparable. However, this appears not to have affected the conclusion that there was not a significant effect of multiplexing on the noise and that there is a significant difference across loads.

5.6.3 Possible explanations for the observed noise

The estimated noise due to thermal noise, quantization noise and amplifier noise was about 0.54 μV when integrating the noise at all frequencies. The noise measured from the KHU Mk1 was white and of mean amplitude of 0.8 μV at each frequency sample, which has a bandwidth of 0.046 Hz. If we consider 6 Hz as the entire signal bandwidth, the overall noise is 9 μV, 20 times larger than the estimated noise. It therefore appears that thermal, quantization and amplifier noise are too small to explain the observed noise.

The sources of noise are not clear; it is probably due to a combination of other factors, such as electromagnetic interferences, stray capacitance and noise deriving from other system components, such as the current source. Nevertheless, it is possible to analyze the noise empirically in relation to the different measurement variables. The increase in noise with test object complexity was as expected and is probably due to voltage fluctuations at the electrodes, present in the saline filled tanks and human subjects, and the additional noise in the latter because of physiological variability (Meeson et al. 1996). On top of a component independent from the signal, the increase in noise with load suggests the presence of a multiplicative contribution, such as noise coming from the current drive or transimpedance fluctuations (Wang et al. 1994; Meeson et al. 1996; Frangi et al. 2002), further test could be designed to test this hypothesis, switching off the current source. The SNR was 3.3 times larger on average for high-signal measurement in the same experiment, therefore in agreement with Wang et al. results (Wang et al. 1994). This and reduction with recording in the middle carrier bands suggests that clinical recording should take place in the middle frequency bands for which the systems are optimised, and electrode impedance should be reduced as much as

possible. Unexpectedly, multiplexing did not introduce any additional noise; so, serial recording does not appear to introduce a disadvantage in this respect, although parallel recording would permit more averaging.

5.6.4 Implications for clinical experiments

The purpose of this study was to determine if it appeared that a radical re-design was needed, or whether these noise levels appeared compatible to EIT imaging of the small boundary voltage changes expected during seizures. Overall, the best noise was observed with the KHU Mk1, and was about 0.02% at each frequency and 0.16% (RMS) in total. A precise analysis of whether this might be expected to yield robust clinical images is outside the scope of this study, but the largest boundary voltage changes predicted during seizures were about 1% for peripheral lateral temporal lobe seizures, and 0.1% for deeper mesial temporal ones (Fabrizi et al. 2006a). Although these figures represent just the largest changes, there will be an averaging effect in image production, as signals from many channels will be used in reconstruction. Overall, the noise is therefore of the same or one order of magnitude less than the expected signal, and it seems plausible that it might be possible to reconstruct images with the existing systems.

Without undertaking a major system re-design, the next issue is whether these findings suggest any simple modifications to the recording protocol which might improve the signal to noise ratio. The UCH Mk1b would benefit from signal post-processing tools like time averaging and band-pass filtering, which could reduce the noise by about a factor of 2 as it collects about 4 frames per second and the bandwidth of changes during epileptic seizures is near DC to 1 Hz. At the middle frequencies, this would reduce noise to about 0.02%. For the UCH Mk2.5, use of screened cables may reduce the noise at 101 kHz to that at 10.08 kHz, from 0.11% to 0.05%. Injection of current at a single frequency would allow injection of 750 μA at 10 and 101 kHz (Romsauerova et al. 2006a). This could reduce the proportional noise independent from the current level by 5 times. Noise of the KHU Mk1 could be reduced by $\sqrt{12} \approx 70\%$ by averaging the 12 frames it can collect each second, as it has parallel recording. Overall, therefore, the KHU Mk1 has the lowest noise but it suffers from the practical disadvantage that all the leads will need to be connected to the subject's head. Moreover this system has only 16 channels available, while the UCH systems have 32, and can only measure voltages from adjacent electrodes. It was not sure if a system with such limitations could provide useful clinical images of the head. This issue was addressed in the following chapters.

Chapter 6 – Protocol selection for the KHU Mk1 16 channel system

6.1 Introduction

The multi-frequency 16 channel KHU Mk1 system has been designed for data collection with a fixed protocol similar to the Sheffield Mark 1 system with a set hardwired protocol of parallel recording from pairs of adjacent electrodes and flexible serial current injection, which is also usually performed from adjacent electrodes (Brown and Seagar 1987). This is sufficient for a complete set of independent measurement in a 2D geometry, because the entire voltage field can be sampled and all non-adjacent combinations obtained by linear correlation of the others. Unfortunately, this may be unsuitable for 3D imaging of the human head because adjacent current injection does not permit enough current to enter the cranium (Bayford et al. 1996). A workaround is possible by designing a protocol for electrode placement on the head without changes internally to the system; the limitation is that it is not possible to address any recording electrode pair in software, as in the UCH Mk 1b or Mk2.5 (Yerworth et al. 2002; McEwan et al. 2006), but the system addresses pairs in the original fixed sequence. In this study, an empirical approach has been used to select such an electrode protocol which produces EIT images of reasonable quality with the limitation of 16 channels and fixed pair selection.

6.1.1 Background

6.1.1.1 Obstruction to current flow into the brain by the resistive skull

The current applied with scalp electrodes is attenuated before reaching the brain because of the high contrasts in conductivity of the compartments of the head. The high resistivity of the skull pushes the current through the less resistive scalp, and the highly conductive cerebrospinal fluid (CSF) shunts the current before it reaches the cortex (Liston et al. 2002). The resulting current density was estimated to be at most 1-10% of that injected at any possible electrode combinations, using computer simulation with an anatomically accurate Finite Element Model of the head (Gilad et al. 2007). A similar value of 15% was estimated with current MRI imaging of rabbit cortex when injecting through electrodes placed diametrically opposite across the head (Joy et al. 1999). The current tends to penetrate the skull through sutures and natural foramina, such has the optic foraminae or foramen magnum, and the current

density on the cortex may be higher in correspondence of these portals (Gamba and Delpy 1998).

6.1.1.2 Comparison between systems with current injection through pairs of or multiple electrodes

The measurement protocol of most EIT systems is based on the original configuration of the Sheffield Mk1 (Brown and Seagar 1987). This employs 16 electrodes with fixed hard-wired adjacent current injection and measurement, and was designed for 2D geometries and reconstruction algorithms. The electrodes are equally spaced on a single ring around the object. Current is injected sequentially through each adjacent pair of electrodes and voltage is measured for each injection between the remaining 13 adjacent pairs. Measurements have tetrapolar arrangement, therefore voltage measurements on pairs which include one or both drive electrodes are not used. This protocol is easily obtained by connecting the channels of the system sequentially around the object and provided clinically successful images in gastric empting and lung ventilation (see (Brown 2003) for a review).

On the other hand, EIT systems with multiple current sources are usually driven with an optimal current synthesized with *trigonometric current patterns* (Gisser et al. 1988). A set of currents, termed *pattern*, is applied simultaneously to a multiplicity of electrodes and voltage is measured serially (Gisser et al. 1988) or in parallel (Cook et al. 1994) on these same electrodes. Since the currents delivered from the electrodes are all at the same frequency and in phase with each other, the pattern refers to the function that describe their amplitudes, which are adjusted according to the desired current. Those are regulated so that the net total current through all the electrodes is close to zero, which means that the sum of all positive injections is almost equal to that of all injections of reverse polarity. An optimal current may be obtained by the sequential application of more current patterns, whose magnitude functions are *orthogonal* to each other. Consider a 2D symmetrical object with a ring of L electrodes on its surface. A typical example of optimal current is synthesized with a sequence of *L-1 spatial cosines* $T^k = [T_1, T_2, \ldots, T_L]^k$, which are orthogonal current (i.e. amplitude) patterns, with $k=1,2\ldots,L-1$. The current injected from electrode l for the current pattern k is:

$$T_l^k = M \sin k\theta_l$$

Where M is the maximal amplitude, $\theta_l = 2\pi l/L$ is the angular position of the electrode l and k is the spatial frequency. This means that, for example, the first current pattern is obtained by injecting a set of currents whose magnitudes is distributed in a sinusoidal fashion: 0 at electrode 1, M at electrode $L/4$, 0 again at electrode $L/2$ and M at electrode $3L/2$. For k = 2, the currents are changed to new values, so as to have two sinusoidal variations of the amplitude around all the L electrodes. This process continues until $L-1$ trigonometric current patterns have been applied to retrieve the chosen optimal current. The optimal current depends on the position of the perturbation and can be selected with an iterative adaptive method, which maximise the difference between voltages at the boundary without and with a contrast object in a tank test (Gisser et al. 1988). The cosine patterns are the best for concentric targets and gave clearer images of a 2D centred object in a saline bath than adjacent pattern (Cheng et al. 1990). However, the influence of the contact impedance was underestimated as it was represented by small, purely resistive and balanced components. In reality, errors in the model of the contact impedance, the electrode size, the electrode location and the boundary shape may dramatically affect images reconstructed with trigonometric patterns, as the voltage is measured from the same electrodes that inject the current (Kolehmainen et al. 1997). For this reason, and because parallel systems are more complex in design and calibration and less flexible than those based on tetrapolar measurements, it is not yet clear if the theoretical advantages of parallel systems will provide more clinically useful images than suboptimal but more practically robust systems in which current is inject through electrode pairs in a serial fashion (McEwan et al. 2007).

6.1.1.3 Electrode configurations for 3D EIT imaging

EIT systems were originally designed for 2D impedance imaging; however, the conductivity reconstruction problem is intrinsically 3D as the current cannot be confined in a single plane. For this reason, 3D reconstruction algorithms and systems with 32-64 channels have been developed to more accurately reconstruct impedance distributions using adjacent data collection (Metherall et al. 1996) or trigonometric patterns (Dehghani et al. 2005; Halter et al. 2007). These used multi-plane electrode arrangements and demonstrated improved localization and resolution in simulation and tank experiments. In all these studies, different electrode configuration were tested to find the optimal arrangement for the intended application. Electrode configurations, for lung imaging, have also been experimentally designed to produce 3D images of cylindrical geometries adopting a

16 channel EIT system designed for 2D adjacent stimulation (Graham and Adler 2007). There were seven combinations of physical position of the electrodes and current injection patterns, obtained by varying the mapping of the 16 channels of the system to the electrodes. The best appeared to be placing the electrodes in 2 rings which were vertically aligned with the channels connected sequentially in each ring.

6.1.1.4 Use of widely spaced current injection pairs in order to increase penetration of current into the cranial cavity

The current that reaches the brain depends on the relative position of the injecting electrodes, so improved penetration can be achieved with appropriate configurations (Rush and Driscoll 1968; Joy et al. 1999). In tank measurements made with a human half-skull suspended in a head-shaped container filled with electrolytic fluid, it was observed that the current density in the middle of the brain was estimated to be maximal when the driving electrodes were 180° apart and was 1.3 times that at the farthest point from the electrodes on the surface of the brain (Rush and Driscoll 1968). The current density on the surface was instead maximal just underneath electrodes at 30° and was 12 times higher than that at the centre. If the electrodes were closer, the shunting effect of the scalp predominated (Rush and Driscoll 1968). Therefore, because of the presence of the skull in the head, adjacent excitation may not have sufficient sensitivity to reconstruct deep internal impedance changes. For this reason, for EIT studies in the adult head, a diametric excitation pattern was designed, in which current is injected between two diametrically opposed electrodes and voltage is measured between adjacent pairs not including the driving pair. This protocol provided a 10 times higher sensitivity and better localization than adjacent excitation for a perturbation in the centre of a 2D Finite Element Model which included scalp, skull, CSF and brain (Bayford et al. 1996). Based on this study, an electrode configuration for 3D imaging of the head employing a serial 32-channel EIT system was empirically designed (Gibson 2000). This system can flexibly address any electrode pair for current injection and another for voltage measurement, in order to perform one tetrapolar impedance measurement at a time. However, the number of electrode combinations used to produce a single image was limited to less than 300 in order to achieve the required frame rate. A 32 electrode placement based on the 10-20 system (Binnie et al. 1982) was devised to provide an even coverage of the scalp. Current was injected between polar and nearly-polar electrode pairs and voltages measured from almost adjacent electrodes along three lines joining the driving electrodes: two parallel to the equator and one

passing over the apex (Figure 6-1; Figure 6-2). For example the first injection was between electrodes 1 and 30 and measurements between 2-7, 7-17, etc. Moreover, additional measurements were done between four electrodes lower down on the head respect to those of the 10-20 system to increase vertical accuracy (electrode 18, 31, 28, 12 in Figure 6-1). This protocol was termed EEG31, and was tested by imaging a Perspex rod in a saline-filled head-shaped tank with a real human skull. Images of the perturbation were reconstructed with a 3D localization error of 18±5% the coronal dimension of the head using a FEM and truncated singular value reconstruction algorithm (Bagshaw et al. 2003).

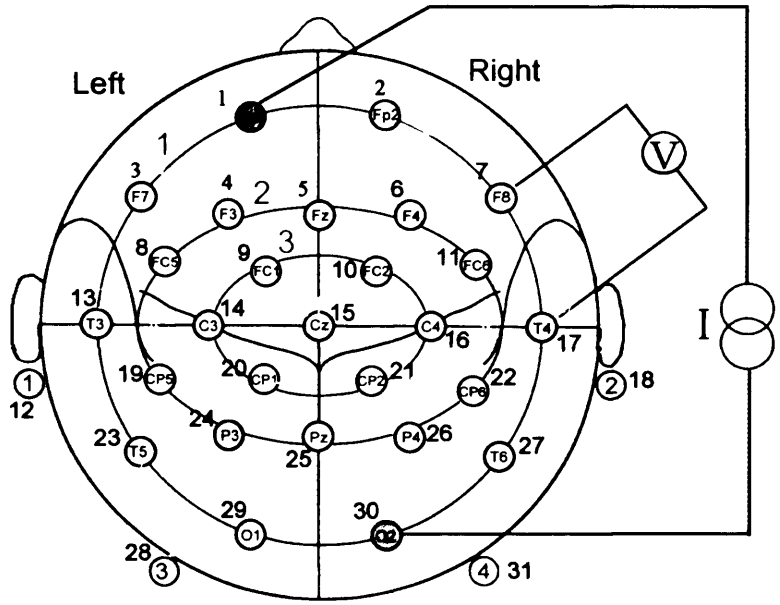

Figure 6-1 Electrode placement for the EEG31 protocol. The electrodes are arranged in approximately in 3 rings. Current is injected between diametrically opposed electrodes on ring 1, ring 2 or between ring 1 and 2. Voltage is measured between approximately adjacent electrodes (modified from (Tidswell et al. 2001b)).

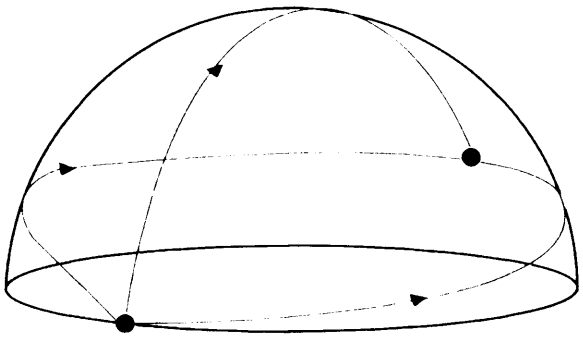

Figure 6-2 In the EEG31 protocol, voltages are measured along three lines (blue) joining the driving electrodes (red dots): two parallel to the equator and one passing over the apex (Gibson 2000).

6.1.1.5 Rationale for this study

The KHU Mk1 is a 16 channel semi-parallel system designed primarily for 2D EIT imaging (Oh et al. 2007). It has a single current source which may be multiplexed to any channel pair and parallel measurement between adjacent channels. It is well engineered and offered the opportunity for improved signal-to-noise in recording during epileptic seizures. It therefore seemed desirable to adapt for this purpose, with the intention that its performance could be compared with the UCH Mk 2.5 system, which records in a serial fashion from 32 electrodes. In order to do this, it was necessary to adapt the KHU Mk1 so that reasonable current penetration into the brain could be obtained, with the limitation of 16 channels and fixed recording in pre-defined pairs.

6.1.2 Purpose

The purpose of this study was to devise a protocol suitable for imaging brain function with the KHU Mk1 system. Its performance was assessed using computer simulation and two numerical models of the head. This was done in comparison with the 31 channel protocol used previously in the UCL group for imaging brain function with the UCH Mk 1 or 2 systems, able to address any electrode pair flexibly with a multiplexer.

6.2 Design

Ten electrode protocols were assessed using two models of increasing complexity. First, EIT images were simulated for a homogeneous model of adult head, with five spherical conductivity perturbations in an axial plane approximately mid-way between the vertex and foramen magnum. Second, the four best protocols from this study were employed in reconstruction of models of epileptic seizures in four brain regions, which are common sources of epileptic activity (Chapter 4), in an anatomically realistic finite element model (FEM) of the head. Conductivity changes for injected current at 10 kHz were simulated; this was chosen because the greatest changes may be estimated to occur at this frequency according to the simulation study for the levels of current allowed by the KHU Mk1, similar to that in Chapter 4.

The protocols were designed according to the following principles. The electrode combinations were designed using 16 electrodes, placed on the scalp in a modified 10-20 electrode placement system, which provided an even head coverage (Gibson 2000). The limitations of the KHU design were such that any current injection pair of

the 16 electrodes could be addressed, but recording was only allowed between pairs of sequential channels. Voltage measurements are collected between the electrodes of the drive pair and the adjacent ones and are subsequently removed off-line as they are saturated. These known saturated drive-record pairs were omitted in the following stated protocols.

6.2.1 Protocol design

6.2.1.1 Recording arrangements

Recording was arranged in one of three modes. All of them were necessarily from adjacent electrode pairs.

1. spiral (Figure 6-3) – recording commenced from the inferior ring of electrodes and continued towards superior electrodes up to the vertex;
2. zigzag (Figure 6-3) – commenced from anterior electrodes and then approached the posterior ones;
3. spiral_2 (Figure 6-4) – commenced from the inferior ring of electrodes and continued towards electrodes in the in the intermediate ring between the most superior and inferior.

The two electrodes over the occiput were moved inferiorly in an attempt to improve the resolution in the vertical direction; those are termed "s-o" (sub-occipital). All the measurements from adjacent electrodes were considered, as they are recorded in parallel by the system, but those near isopotential lines were removed from the reconstruction.

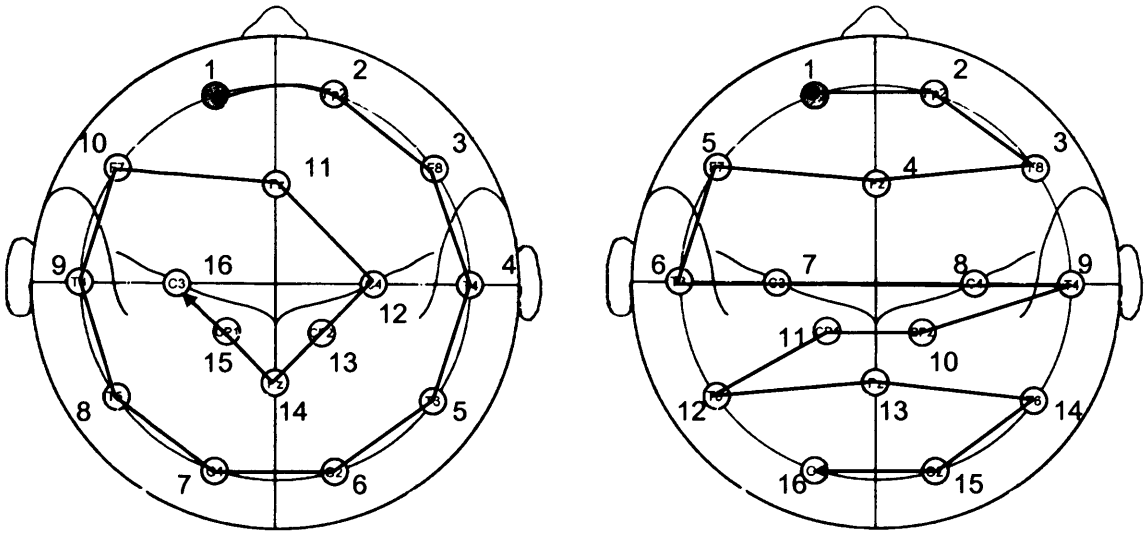

Figure 6-3 Spiral numbering (left); zigzag numbering (right).

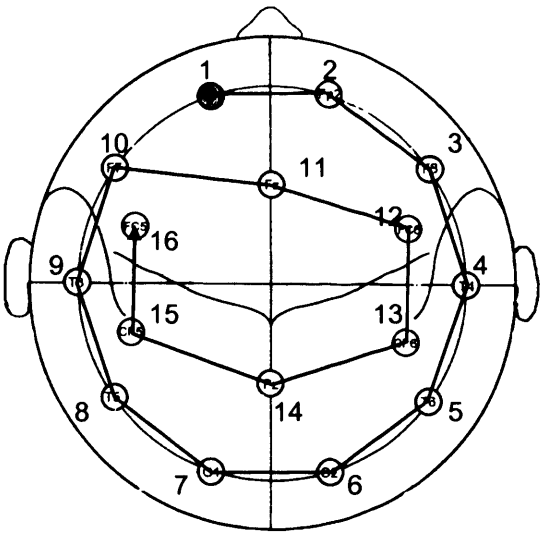

Figure 6-4 Spiral numbering 2, with two rings.

6.2.1.2 Current drive arrangements

There were 3 different configurations for current injection. These were selected from injection with electrode pairs at 180°, 120° or 60° separation. 1) 180°, 120°, and 60° (zigzag_180+120+60, zigzag_s-o, spiral_180+120+60, spiral_s-o, spiral_2_180+120+60, spiral_2_s-o); 2) 180° and 120° only (spiral_180+120, spiral_2_180+120) and 3) 180° and 60° only (spiral _180+60, spiral_2_180+60).

6.2.1.3 Final tested protocols

The ten tested combinations were arrived at as follows. Each of the spiral and spiral_2 voltage recording methods were combined with the 3 current drive arrangements (spiral_180+120+60, spiral_180+120, spiral_180+60, spiral_2_180+120+60, spiral_2_180+120, spiral_2_180+60). For the zigzag voltage record, only the injection at all separations was employed because it provided poor reconstructions. Three more combinations were obtained by placing the occipital electrodes inferiorly – these were only combined with the current drive at all separations (zigzag_s-o_180+120+60, spiral_s-o_180+120+60, spiral_2_s-o_180+120+60). Each was compared with the EEG31 protocol.

6.2.2 Methods of evaluation

The accuracy of the 10 different protocols was evaluated using computer simulation with 1) a homogeneous FEM of a head shaped-tank and 2) a realistic FEM of the head with scalp, skull, CSF, white and grey matter and eyes. In addition, for comparison, the EEG31 protocol used previously in our group (Gibson 2000;

Tidswell et al. 2001b) was evaluated. Boundary voltage data were simulated for the protocols and then noise was added, before reconstruction into images. The quality of the images was evaluated quantitatively according to the localization error of the reconstructed perturbation, presence of unwanted conductivity changes, deformation of the perturbation and sensitivity to the changes. In addition, a singular value decomposition analysis was conducted to evaluate the amount of independent information provided by each protocol (Dehghani et al. 2005). A qualitative evaluation of the selected main perturbations and of the images at the plane of the simulated target was also conducted, as there could be a reconstructed perturbation in the correct place, but not being the main one, and to assess the presence of other features not corresponding with the simulated object.

6.3 Methods

6.3.1 Generation of simulated data

Boundary voltage data were created employing:

1) a mesh of 52000 elements of a head shaped tank filled with 0.1% saline (Tidswell et al. 2001a) and with placement of 10mm-radius spherical conductivity perturbations of 8% decrease in 5 positions on a plane approximately half way between the apex and the foramen magnum. These were at distances of 45, 20 from the centre of the head along a line from the side to the centre, in the centre and at distances of 45 and 70 mm along a line from the centre to the back of the head.

2) a mesh of 53000 elements of a realistic head with simulation of epileptic seizures with a uniform conductivity decrease of 12%, in the temporal lobe, in the parahippocampus, in the hippocampus and in the combined parahippocampus and hippocampus. The temporal lobe was represented as a disc of 18 cm^3 close to the surface, the parahippocampus as a prism with triangular base of 6 cm^3 and the hippocampus as a cylinder of 2.5 cm^3 deep in the brain. The conductivity values employed for each tissue were those at 10 kHz:

    - grey matter: 0.285 S/m;
    - white matter: 0.291 S/m;
    - CSF: 1.79 S/m;

- skull: 0.039 S/m;
- scalp: 0.425 S/m;
- eyes: 1.144 S/m.

Noise was added to the boundary voltages as normally distributed random data n, with mean 0 and standard deviation 0.03%, equivalent to the noise measured on a saline tank, according to:

$$\tilde{x} = x + nx \tag{6-1}$$

Where $\tilde{x}$ are the noisy data and x are the noise free data.

The tested protocols for the homogenous case were:

1) EEG31;
2) injection: 180°+120°+60°; measurement: zigzag;
3) injection: 180°+120°+60°; measurement: zigzag_s-o;
4) injection: 180°+120°+60°; measurement: spiral;
5) injection: 180°+120°+60°; measurement: spiral_s-o;
6) injection: 180°+120°; measurement: spiral;
7) injection: 180°+60°; measurement: spiral;
8) injection: 180°+120°+60°; measurement: spiral_2;
9) injection: 180°+120°+60°; measurement: spiral_2_s-o;
10) injection: 180°+120°; measurement: spiral_2;
11) injection: 180°+60°; measurement: spiral_2.

Than only the EEG31 and the best four 16 channel protocols were used with the realistic head mesh.

6.3.2 Image reconstruction

A sensitivity matrix linear reconstruction algorithm was employed and inversion was performed with truncated singular value decomposition (Zadehkoochak et al. 1991; Bagshaw et al. 2003) (Section 1.2.2.2.1). In regularizing the Jacobian, the same truncation level of 0.1% of the largest singular value was used for all the protocols (Tidswell 2004). The sensitivity matrix was set to be the brain region only, where the perturbations were confined, and its rank and singular values above truncation

level calculated as an indication of the amount of independent measurements and of the useful singular values, which is proportional to the amount of useful information (Dehghani et al. 2005). A coarser mesh with 25000 elements of the same tank was used to reconstruct the simulated data from the tank, while the same mesh was used to reconstruct the data from the anatomical model.

6.3.3 Evaluation of images

A 3D representation of the reconstructed main perturbation and the axial slice of the head passing through the centre of the simulated perturbation were displayed for qualitative image evaluation. These were compared with the simulations themselves and the images obtained with the EEG31 258 combination protocol used for 3D imaging of the head (Tidswell et al. 2001a). The reconstruction involves a spatial averaging and loss of information due to the singular value truncation and images were smoothed with an averaging filter in MayVi (Ramachandran 2003). As a result, the reconstructed values of the conductivity change do not correspond with those of the simulation; for this reason the scale of the displayed images was chosen in order to show the features of interest.

The following four *figures of merit* were combined into one single *general error* index to evaluate the quality of the reconstructed images. This was obtained by summing the single errors weighted according to their importance and averaging across perturbations.

1. *localization error (weight 1.5)*: displacement of the centre of mass of the reconstructed perturbation respect to its real position as percent of side-to-side dimension of the mesh, which represent the 'diameter' of the object;
2. *occurrence of significant artefacts (weight 0.75)*: proportion of volume with conductivity changes above the half maximum conductivity change not belonging to the reconstructed perturbation;
3. *error in matching the shape of the original perturbation (weight 0.50)*: mean deformation of the reconstructed perturbation in each direction as percentage of the object 'diameter';
4. *error in reconstructed value (weight 0.25)*: proportional difference between the originally simulated perturbation and the mean reconstructed perturbation;

"Reconstructed perturbation" refers to the main perturbation in the reconstructed image. This is the bulk of at least 10 *adjacent* voxels with conductivity changes above the half maximum closest to the centre of mass of *all* the voxels with conductivity changes above the half maximum (Figure 6-5). If the maximum reconstructed change did not belong to a bulk of at least 10 voxels, it was considered an artefact, set to null and the new maximum used to calculate the new half maximum threshold. The *centre of mass* was calculated as a weighted average:

$$X = \frac{\sum_i w_i x_i}{\sum_i w_i} \quad Y = \frac{\sum_i w_i y_i}{\sum_i w_i} \quad Z = \frac{\sum_i w_i z_i}{\sum_i w_i} \tag{6-2}$$

Where X, Y, Z are the coordinate of the center of mass, x_i, y_i, z_i are the coordinate of the center of each voxel and w_i is its *weight* defined as:

$$w_i = v_i \Delta\sigma_i \tag{6-3}$$

Where $\Delta\sigma_i$ is the conductivity change in that voxel and v_i its volume. The value of the reconstructed perturbation $\Delta\sigma_{pert}$ was taken to be the average of the conductivity changes inside the reconstructed perturbation, weighted for the volume of the voxels:

$$\Delta\sigma_{pert} = \frac{1}{V}\sum_i v_i \Delta\sigma_i \tag{6-4}$$

Where V is the total volume of the main reconstructed perturbation.

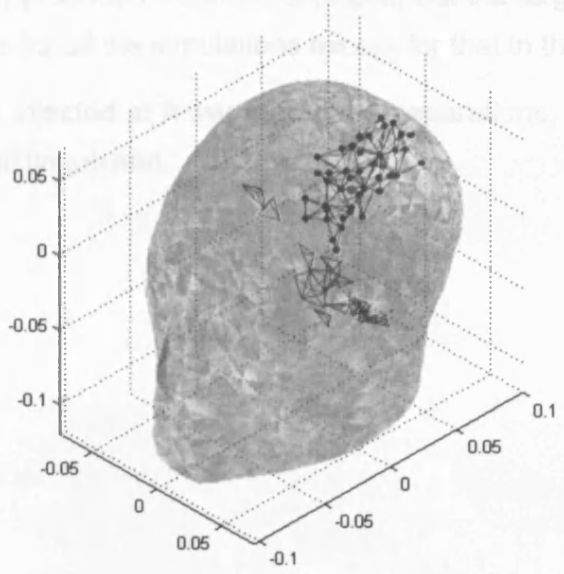

Figure 6-5 Method for selection of the main perturbation in reconstructed images in order to permit objective analysis. The centre of mass (shown in red) of all the voxels with conductivity changes above half of the maximum in the image (shown as green) was first calculated. The main perturbation was then selected as all the voxels with a change greater than half the maximum directly connected to each other and closest to the centre of mass (blue).The scale on the axis is in meters.

6.4 Results

6.4.1 Simulated head-shaped tank

6.4.1.1 Qualitative assessment

Image quality with the 10 protocols appeared to fall into three groups :

1) The best images were obtained with the five protocols with current injection at all three separations except for the zigzag (zigzag_s-o_180+120+60, spiral_180+120+60, spiral_s-o_180+120+60, spiral_2_180+120+60 and spiral_2_s-o_180+120+60). These protocols produced similar good images in which the largest changes were localized and in the correct position with little artefacts elsewhere. These were similar to those obtained with the EEG31 protocol. Even for these highest quality images, all the main reconstructed perturbations were broader than the real target (Figure 6-6). Some images presented reconstruction artefacts in the opposite direction of the expected change. Perturbations near the surface are reconstructed more accurately and with less artefacts.

2) The zigzag recording protocol with all three current separations (zigzag_180+120+60) produced localized changes, but the largest changes were in the incorrect positions for all the simulations except for that in the back of the head.

3) When current was injected at fewer than three separations, more central objects could not be clearly distinguished.

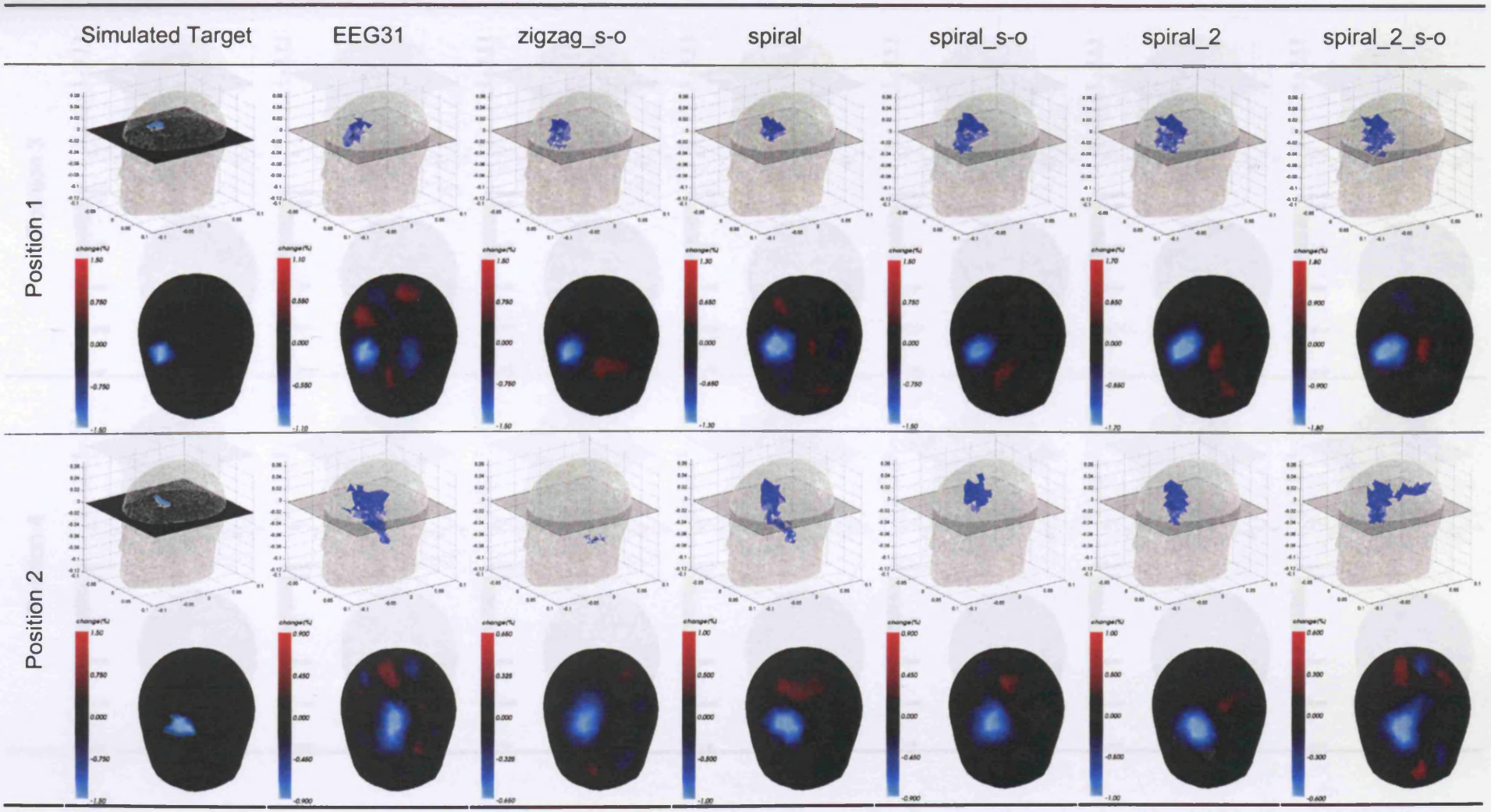
Simulated Target
EEG31
zigzag_s-o
spiral
spiral_s-o
spiral_2
spiral_2_s-o
Position 1
Position 2

Position 4
Position 3

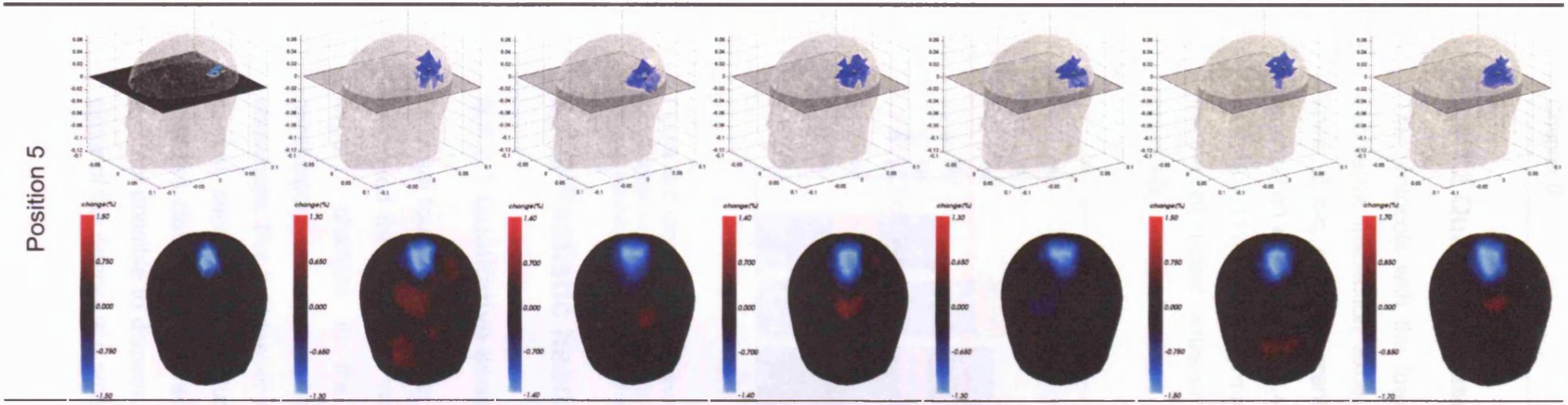

Figure 6-6 Reconstructed images from simulation for a homogeneous head – the best 5 protocols only are shown. Images are displayed as a transparent 3D model with the main reconstructed perturbation (blue volume). Below each, is a 2D slice through the centre of the simulated perturbation.

6.4.1.2 Quantitative assessment

The protocols with the lowest general error corresponded to those apparent on qualitative inspection except for the zigzag_s-o (spiral, spiral_2, spiral_s-o and spiral_2_s-o, all with current injection at all separations. These also had the lowest localization error (6.68%-8.46%) (Figure 6-7). The occurrence of significant artefact (3.94%-7.11%), the deformation of the reconstructed image (19.57%-24.07%), and the reconstructed value error (79.68%-84.21%) were similar for these four best protocols.

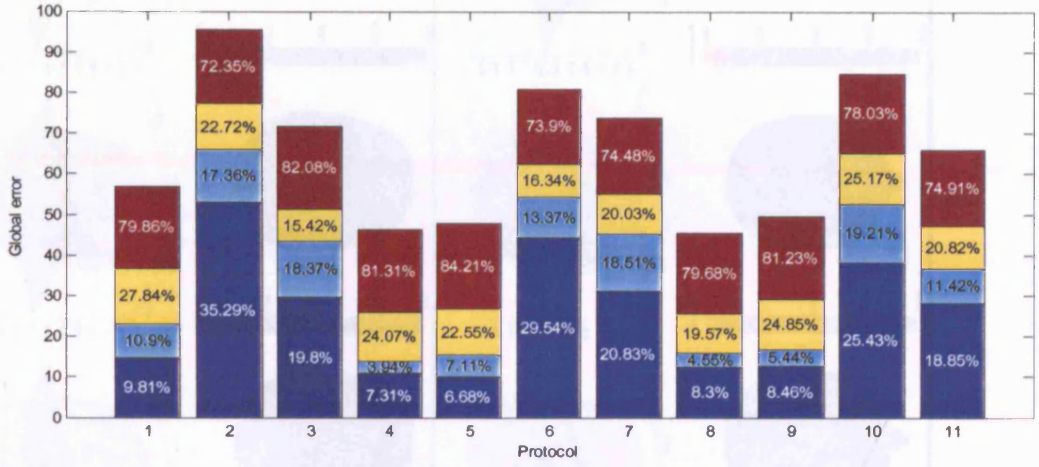

Figure 6-7 Global error of each protocol and mean contribution of each parameter: blue – localization error; cyan – occurrence of significant artefact; yellow – deformation; maroon – error in reconstructed value. The protocol numbers refer to the list in section 6.3.1.

6.4.2 Realistic head model

6.4.2.1 Qualitative assessment

Only the four best protocols, from the previous evaluation, as well as EEG31, were employed for this study. With these, all appeared to permit reconstruction of the larger changes in the temporal lobe and combined hippocampus and parahippocampus with changes in the correct location and with little noise elsewhere. For the deeper and smaller perturbations, the spiral_s-o (with all three current separations) produced the best images, as it was able to reconstruct changes close to the correct locations in both cases. With the EEG31 protocol, it was not possible to discern accurate changes corresponding to the true change for either of the deeper and smaller abnormalities.

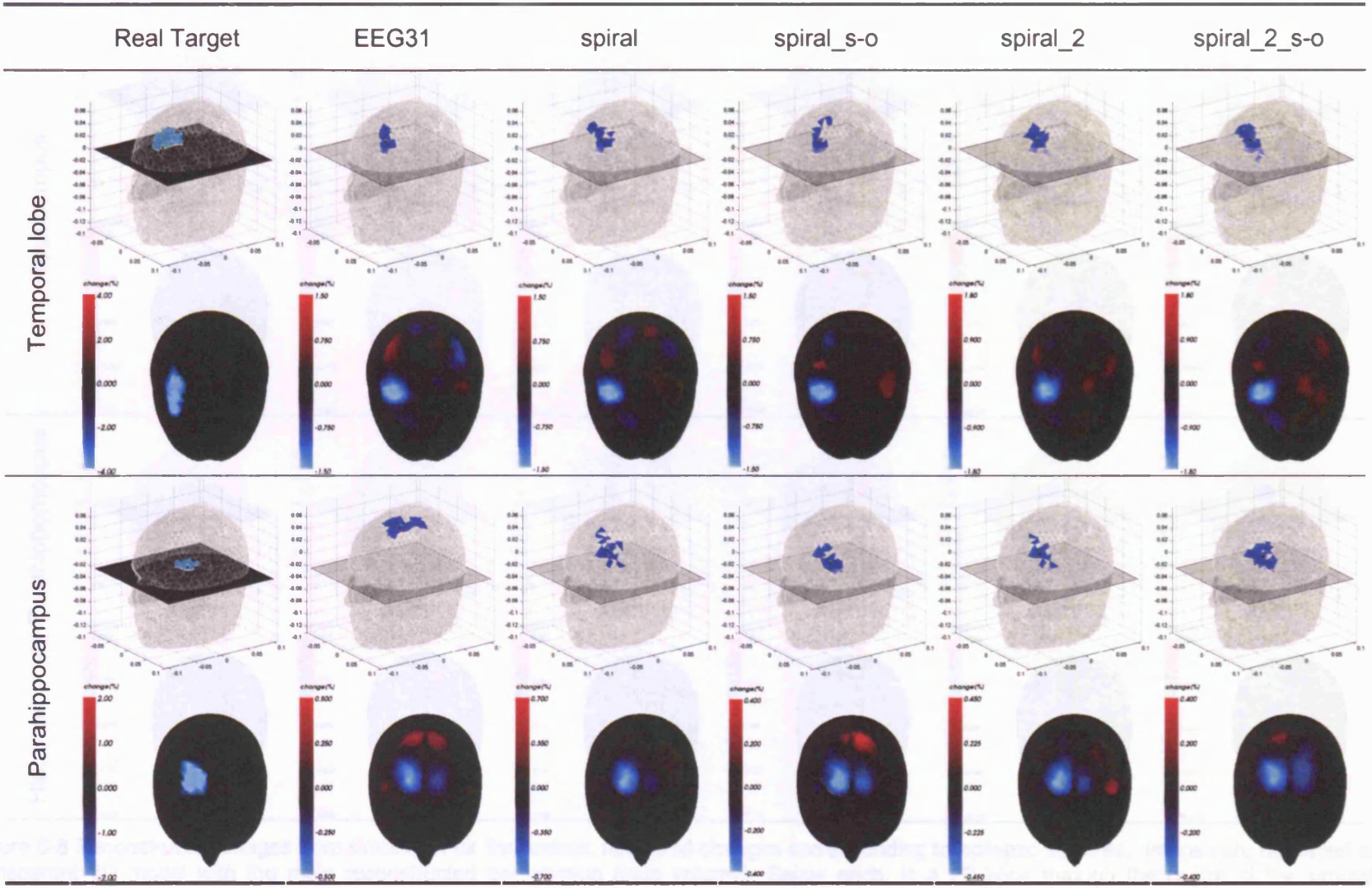
Real Target
EEG31
spiral
spiral_s-o
spiral_2
spiral_2_s-o
Temporal lobe
Parahippocampus

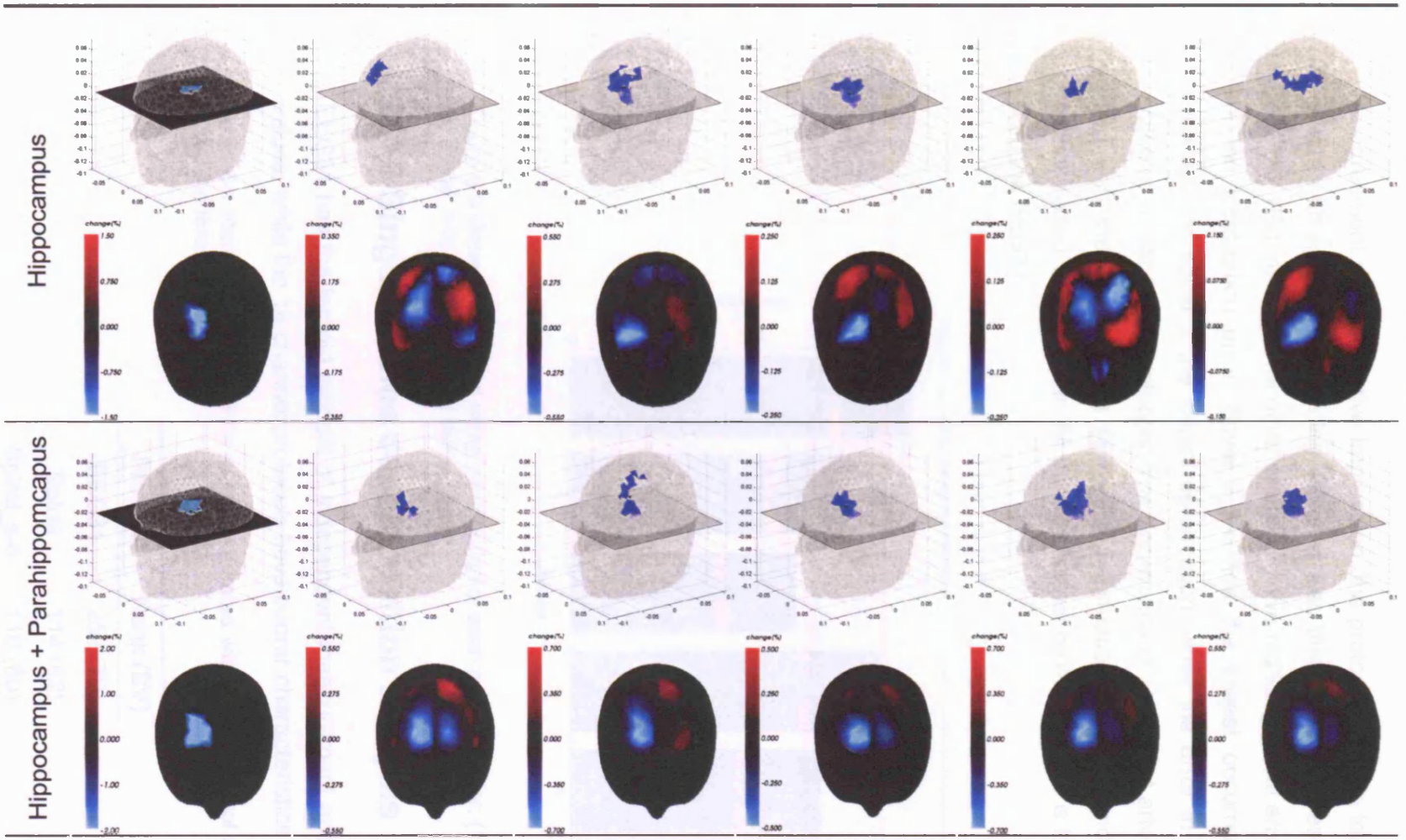

Figure 6-8 Reconstructed images from simulation for the realistic head and changes corresponding to epileptic seizures. Images are displayed as a transparent 3D model with the main reconstructed perturbation (blue volume). Below each, is a 2D slice through the centre of the simulated perturbation.

6.4.2.2 Quantitative assessment

In agreement with qualitative impression, the protocol with the lowest general error is that with spiral_s-o recording, which is also that with the lowest localization error (9.22%) (Figure 6-9). The other protocols have higher general error mostly because of the localization error. Spiral_2_s-o has the lowest occurrence of significant artefact and spiral_2 the lowest deformation, while the error in the reconstructed value is similar for all protocols. The occurrence of significant artefact is higher than that with the head-shaped tank, the deformation is lower and the error in the reconstructed value similar. All the 16 channel protocols have a lower general error than the EEG31.

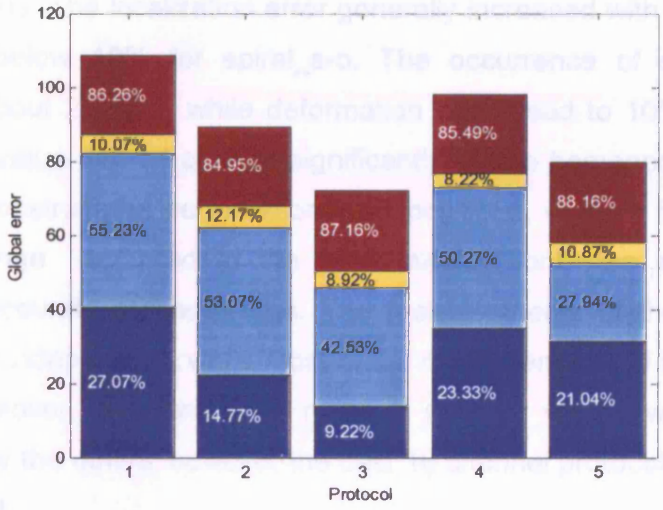

Figure 6-9 General error and mean contribution of each parameter for: (1) EEG31; (2) Spiral; (3) Spiral_s-o; (4) Spiral_2; (5) Spiral_2_s-o.

6.4.3 Singular value decomposition analysis

EEG31 has the largest amount of independent measurement and relevant singular values, while the 16 channel protocols have poorer characteristics (Table 6-1).

Table 6-1 Rank of the sensitivity matrix generated with each protocol and singular values above the threshold of 0.1%.

Protocol	Rank (SV)
EEG31	252 (79)
Spiral	114 (62)
Spiral_s-o	110 (60)
Spiral_2	108 (58)
Spiral_2_s-o	111 (60)

6.5 Discussion

6.5.1 Summary of results

This study demonstrated that it is possible to obtain reliable and localized 3D images of conductivity changes of a few percent in the head employing 16 channels and adjacent voltage measurements in presence of realistic noise. The images obtained were comparable or superior to those obtained with a protocol which employs 31 electrodes.

The best protocols were spiral, spiral_s-o, spiral_2 and spiral_2_s-o in the homogenous case, and spiral_s-o in the realistic case, all with current injection with three separations. The localization error generally increased with the realistic mesh, but was still below 10% for spiral_s-o. The occurrence of significant artefact increased to about 28-55%, while deformation decreased to 10% and error in the reconstruction value did not change significantly. In the homogeneous case, it was possible to reconstruct the perturbation in all positions, while in the simulated case when the change occurred in the hippocampus, only the spiral_s-o protocol produced an accurate reconstruction. The measurements of the EEG31 protocol were almost all independent, while most of the measurements of the other protocols were not. Moreover, the number of relevant singular values was higher for this protocol than for the others, however the best 16 channel protocols performed better than the EEG31.

6.5.2 Technical issues

When regularizing the sensitivity matrices, the same truncation level of 0.1% of the largest singular value was adopted for all protocols. This threshold may have not been optimal for some of the protocols, which may benefit from a different regularization selection.

The images demonstrated an appropriately localized conductivity change that corresponded to the position of the simulated target. However in the reconstructed images there were some smaller artefactual changes elsewhere which were of opposite polarity. These were probably introduced by the reconstruction algorithm and the simulated noise (Tidswell et al. 2001b). This could partially explain the artefactual changes seen in patients (Chapter 3).

For the homogeneous tank, a different mesh was employed for production of the simulated data and its reconstruction. In the realistic case, it was technically difficult

to achieve this, and the same mesh was therefore employed for both simulation and reconstruction. This meant to assume the ideal model in the inverse problem as there was no difference between the model used to generate the data, which had added white noise, and that used to reconstruct the images. This was justified because the purpose of this work was to compare different electrode protocols, rather than assess the accuracy of a reconstruction algorithm for use in an in vivo situation.

As the protocols were selected experimentally, not all the possible combinations were considered in this study. In fact, a colleague attempted to undertake this early on in the work and had to abandon the attempt as the computational complexity was enormous with the number of possible permutations. This was therefore a limited practical study based on sound physical principles. It may well be that a more comprehensive approach in the future may yield better results but it was encouraging that the best protocols proved to be adequate in reconstructing impedance changes due to epilepsy in a realistic finite element model. This provides justification for this empirical approach.

6.5.3 Best protocol

The best protocol needs to be selected with respect to its intended application, which is the localization of epileptic foci. The most important factor is therefore the ability to locate correctly the conductivity change. Once the epileptic focus is located correctly, the presence of other significant conductivity changes in other regions of the brain could be misleading for surgery, so it is preferable that all the significant changes belong to the main reconstructed perturbation. If all the significant changes belong to the main perturbation it is important to define its boundary for resection of the pathological area only. Moreover, protocols which have the highest sensitivity in the brain will have the biggest chance to pick up boundary voltage changes related to an internal conductivity variation.

From the simulation of the head-shaped tank it appeared that the best protocols were the ones with spiral, spiral_s-o, spiral_2 and spiral_2_s-o and injection at all angles. These had the lowest general error, the lowest localization error and occurrence of significant artefacts, as confirmed by the quality of the produced images. Within these protocols, spiral_s-o appears to have the lowest general error and localization error, when considering a realistic head model and it seems to be the only protocol with the possibility of reconstructing a conductivity change in the hippocampus alone.

6.5.4 Explanation of findings

The 16 channel spiral_s-o protocol performed better than the traditional EEG31 probably because current was injected at 180°, 120° and 60° whereas the EEG31 protocol only employs current injection at 180° . This provided a more even sensitivity coverage of the brain region, as different areas are reached better with current injected at different angles (Rush and Driscoll 1968; Joy et al. 1999), while the EEG31 was designed to maximise the current density in the centre of the brain as the injections were at 180° only. For the 16 channel protocols, all the injection angles were necessary to properly reconstruct the perturbation in any position and two electrodes moved inferiorly helped in improving the image quality, possibly because they improved the vertical resolution.

However EEG31 provides more independent measurement and relevant singular values than the 16 channel protocols and employing more channels is expected to give images with a better resolution. Probably the resolution obtainable with 16 channels is sufficient to identify the perturbations which were simulated and the basis images associated with the relevant singular values contained more significant information.

Moreover, there may be the possibility that reducing the number of electrodes reduces the error in the model, as there are less electrodes which can be misplaced or with wrong diameter, even though it can not be the case in the real head simulation as the same mesh was adopted for the forward and inverse problem.

Finally the potential measured adopting 16 channels is larger than that measured adopting 31 channels as the electrodes are more far apart on the head. This may be helpful in real experiments as large voltages can be measured more accurately than smaller ones. However in this experiment this should not make a difference as the added noise was proportional to the voltage.

6.5.5 Implications of this study

The goal of this study was to design a measuring configuration for the KHU Mk1 with 16 electrodes, serial current injection and adjacent parallel voltage measurement. The results encourage the view that it may be possible to obtain satisfactory images of the human head during epilepsy employing only 16 channels.

On the basis of these findings, it is recommended that the spiral_s-o protocol is used in clinical practice. Somewhat surprisingly, this appeared to produce better

results than the EEG31 protocol which employed double the number of electrodes. An assessment of any advantages of using more electrodes with the optimal spiral_s-o protocol was outside the scope of this work, but the current conclusion suggests that reasonable images could be obtained with only 16 additional electrodes for EIT to the EEG ones. This would be practically less demanding; and it may reduce the possibility of committing errors in electrode placement and of discrepancy between the model used for reconstruction and the real electrodes position and diameter. Further work requires the assessment of this protocol in a tank first and then on patients in comparison with the EEG31.

Chapter 7 – Comparison of two EIT systems suitable for imaging in epilepsy

7.1 Introduction

The noise study demonstrated that boundary voltage changes due to epilepsy are at the limit of detectability for the present EIT systems. However, it was also clear that the UCH Mk2.5 and the KHU Mk1 could benefit from technical and practical improvement for long term impedance monitoring. It is not clear which of the two systems is the most likely to yield to clinical useful functional images of epileptic seizures as the former has more electrodes and therefore is expected to have better spatial resolution, but also has higher baseline noise which might obscure the small changes on the scalp.

This chapter compares the performance of these two systems for reconstruction of 3D time difference images. Both systems incorporated modifications to optimise the signal-to-noise ratio and to enable long term monitoring.

7.1.1 Background

7.1.1.1 Comparison of design of the two systems

7.1.1.1.1 UCH Mk2.5

This system comprises a four electrode impedance measuring circuit, multiplexed up to 32 electrodes (McEwan et al. 2006). It has a single gain which was optimized for the range of the transfer impedance of the head of up to 70Ω (McEwan et al. 2006). It can measure at frequencies between 20 Hz and 1.6 MHz and employs a multifrequency composite waveform of 30 frequencies, divided into 3 sequential packets of 10 frequencies each (Romsauerova et al. 2006a). The current is fixed at 140 μA for each frequency. Leads to the patient are unscreened and kept as short as possible. However it suffered from the practical limitation of a relatively slow acquisition rate of 2.2 sec/frame for 3D imaging the head, while a time resolution of 1 sec or less would be preferable for epilepsy monitoring as the related changes happen on this time scale. Moreover, the relative noise of the UCH Mark2.5 would be decreased if there were an increase in the current level (Chapter 5). For this purpose, some technical changes were undertaken: the current level was increased to 400 μA at each frequency in the range between 2kHz and 128kHz, the gain of the recording circuit was decreased by 3 times to avoid saturation, and the timing was adjusted so that one complete data set could be recorded in under 1 second (Appendix C).

7.1.1.1.2 KHU Mk1

The KHU Mk1 comprises a single current source which may address any electrode pair using a multiplexer and 16 parallel voltmeters, which measure voltages from adjacent channels (Oh et al. 2007). It measures at a single frequency between 39 Hz and 500 kHz and recording is at fixed gain, selected before the experiment between 14 available steps. The system employs General Impedance Converters which are individually calibrated for each electrode recording pair to optimize the output impedance at each frequency and the electrode leads were 1m long with an outer shield and inner driven screen. However this system was not suitable for long term monitoring in a telemetry ward as it is not wearable, the leads of the electrodes were only 1m long to limit stray capacitance and load and it did not have a protocol appropriate for 3D head imaging because of the 16 channels and adjacent measurements limitation. The protocol has now being designed (Chapter 6) and the system has been provided with 5m long leads which can be separated into 4+1m through a connector box which can be easily unplugged by the subject under test.

The main differences between the two systems are summarized in Table 7-1.

Table 7-1 Main differences between the UCH Mk2.5 and the KHU Mk1.

UCH Mk2.5	KHU Mk1
32 channels	16 channels
Multi frequency (20Hz-1.6MHz)	Single frequency (39Hz – 500kHz)
Serial (flexible injection and measurement)	Semi-parallel (serial/flexible current injection, parallel/adjacent measurement)
Unscreened 50cm leads	Screened 5m leads

7.1.1.2 Previous tank experiments

Saline tank experiments have been traditionally conducted in our group in order to test new systems or new reconstruction algorithms for 3D imaging of the brain. The 3D localization error and resolution, which can be obtained in the head shaped tank without and with skull, can be estimated from previous studies. The first type of phantom was of simplified geometry and represented the head as a Perspex sphere of 19 cm of diameter with 31 chlorided silver electrodes 1 mm in diameter in positions based on a modified 10-20 system of EEG electrode placement, in which the skull was simulated with an hollow shell of plaster of Paris (Tidswell et al. 2001a;

Liston et al. 2004). Images of a Perspex rod (20mm diameter x 20mm length), representing a 100% conductivity decrease, in different positions inside this tank were reconstructed with a linear algorithm employing an analytical model of a 3-shelled sphere (Liston et al. 2004) and a FEM of the same kind (Bagshaw et al. 2003). The localization error was defined as the distance between the peak change of the reconstruction and the real position of the object and it was 14.0±5.8mm (7.4±3% of the tank diameter) and 15±5mm (7.9±2.6%) respectively.

To test the influence of the geometry, a latex head-shaped tank was then manufactured (Tidswell et al. 2001a) with 31 chlorided silver electrodes in the modified 10-20 disposition with the option of insertion of a real human skull. The internal dimensions of the tank were about 19.5cm in the anterior-posterior midline plane and 14.6cm in the coronal plane passing through the centre of it. The localization error of the same Perspex rod in the head-tank without the skull was 13±7mm (8.9±4.8% of the coronal dimension) (Bagshaw et al. 2003). A 12% impedance increase was then generated by a polyurethane sponge (density 5% w/v, 2.5 cm diameter and 2.8 cm length. Vitafoam, UK) (Tidswell et al. 2001a). The localization error obtained with an analytical homogeneous sphere model was about 13.4mm (9.2%) and 28.3mm (19.4%) without and with skull respectively, but z-localization was not considered, so the reported error was effectively 2D and therefore an underestimation of the localization error.

There are no results about the resolution of the reconstruction of images of a sponge, therefore the resolution of the images of the Perspex rod will be considered. In (Liston et al. 2004), the resolution was defined as the full-width at half-maximum (FWHM) in the axial plane (xy-plane) containing the peak change and also in the direction perpendicular to it (z axis) and was 57.7±8.9mm (39.5±6.1%) and 81.6±17.2mm (55.9±11.8%) respectively in the spherical tank with a skull simulated by a spherical shell of Plaster of Paris. In (Bagshaw et al. 2003) the resolution was defined only along the anterior-posterior axis (y axis) and was 44±10mm (30.1±6.8%) in the same tank. The FWHM for a Perspex rod in the head shaped tank in the anterior-posterior direction only was 50±16mm (34.2±11%) without skull and 34±8mm (23.3±5.5%) with skull (Bagshaw et al. 2003).

In summary, the localization error as defined in Section 6.3.3 for a sponge is approximately 10% for a homogeneous tank and 20% with a skull without considering the vertical direction; the expected FWHM for a Perspex rod may be expected to be approximately 34% without the skull or 23% with the skull in the anterior-posterior direction, but higher in the vertical direction.

7.2 Purpose

The purpose of this chapter was to compare the performance of the optimised UCH Mk2.5 and of the KHU Mk1 EIT systems in imaging a test object with similar contrast to the changes in the brain during a seizure, in a head-shaped tank. Questions to be addressed were:

1) What resolution can be expected in a tank without and with the skull ?
2) Which system performs better and should be selected for clinical studies ?
3) How does the new electrode protocol for the KHU system perform ?

7.3 Design

7.3.1 Experiment set-up

The UCH Mk2.5 and KHU Mk1 were used to collect data from a saline filled tank without and with the presence of a real human skull. The test object was produced by a sponge, yielding a conductivity change of 30%, intended to be similar to that during a seizure (Tidswell et al. 2001a). The dimensions of the sponge were those of the temporal lobe (50mm diameter, 15mm thickness) for the experiment without the skull and were smaller for the experiment with the skull (30mm diameter, 20mm thickness) to allow the sponge to pass through the foramen magnum.

7.3.2 Settings of the systems

16 electrodes and two optimal measuring protocols specified in Chapter 6 were used for the KHU Mk1 (spiral_180+10+60 and spiral_s-o_180+120+60). For the UCH Mk 2.5 system, two protocols were tested : 1) 31 electrodes and a measuring protocol with diametrically opposed current injection pairs (EEG31) (Gibson 2000) and 2) the best 16 channel protocol as employed for the KHU Mk 1. Data were collected with the highest current level allowed by the systems and the safety standard regulation (IEC601-1 1988). With the UCH Mk2.5, all images were reconstructed for 4kHz only, although a multifrequency combined waveform was injected. Recording for the KHU Mk 1 was only undertaken at 10 kHz. These were the frequencies with the highest boundary voltage changes associated with epilepsy at the current level employed according to a computer simulation similar to that in Chapter 4.

7.3.3 Boundary voltage preprocessing

The real part of the boundary voltage measurements was considered and expressed as a percentage of the mean value of the baseline. Boundary voltages with more than 1% or 0.5% baseline noise for the case without and with the skull respectively, and with outlying changes were discarded. The outlying changes were taken to be those exceeding 0.1% (i.e. 3%) of the local conductivity change, and those which exceed 6 times the standard deviation of the remaining changes in order to include data which may have had a greater amplitude when the disturbance was near the edge of the tank.

The data were then processed using principal component analysis (PCA) in time and only the first principal component (PC) was used for image reconstruction (Perez-Juste Abascal 2007). This represents the most relevant time response occurring in all channels at the same time. Each channel can be represented as one point in the time base, where each "coordinate" is one frame, or in the PC base, where each "coordinate" is one PC (Figure 7-1). Each channel will have a different projection on each PC. If only one PC is taken, it is like approximating all the channels using vectors with different magnitude but same direction, that of the 1^{st} PC. At this point they have to be projected back onto the time basis. The "angles" between the 1^{st} PC and the vectors of the time base are the same for all the channels. This means that the value at a given frame is given for each channel by the magnitude of its 1^{st} PC multiplied by the scalar product between the 1^{st} PC base and the time base representing that frame. These products are the same for all the channels, which means that the frames of each channel are fixed values (the "angles") multiplied by a factor depending on the channel (the 1^{st} PC). All the channels represent then the same pattern in time with different magnitude. For this reason the SNR after PCA is the same for all the channels as the scaling operation does not influence it.

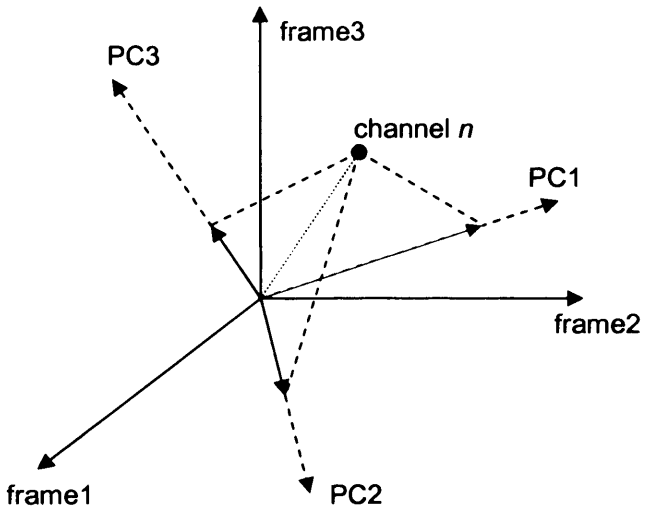

Figure 7-1 Intuitive explanation of the PCA. Let assume an acquisition of 3 frames only. Each channel *n* can be represented as one point in the time (frame) base, where each "coordinate" represents one frame, or in the PC base, where each "coordinate" represents one PC. If only the 1st PC is considered (red) and projected back onto the time base, the only thing which distinguishes the channels is the size of this vector as the "angles" between this direction and the time basis are constant.

7.3.4 Image reconstruction

Time difference images were obtained with a sensitivity matrix linear reconstruction algorithm and inversion was performed with truncated singular value decomposition (Zadehkoochak et al. 1991; Bagshaw et al. 2003). The singular value truncation threshold for a successful image reconstruction depends on the noise level of the data and on the difference between the tank and its model. Since this last parameter is difficult to estimate (Tidswell 2004), images were reconstructed with three different levels – the commonly used truncation level of 0.1% of the largest singular value (Gibson 2000; Liston et al. 2004), and two other levels, above and below this.

As the position, dimensions and size of the perturbation were known, errors could be calculated from the difference between these expected values and those of the reconstructed image to evaluate the adequacy of the systems in reconstructing 3D images of the head. Images were assessed qualitatively and quantitatively as in Chapter 6.

7.4 Methods

7.4.1 Tank

The head-shaped tank was that described in (Tidswell et al. 2001a). This was formed from a silicone-rubber cast of a head-shaped model, made from a human

skull covered with clay, to simulate the extra-cranial tissues of the scalp, head and neck. The thickness of the simulated scalp was 3–4 mm. The other tissues of the face and neck were modelled to give an approximation of the surface of the human head. 31 silver electrodes, 1 cm in diameter, were placed in a modified 10-20 system. The electrodes were embedded into the inner walls of the tank during the casting process.

When data were collected without the skull, the tank was filled with 0.1% saline and a decrease of 30% in conductivity was generated by a cylinder of polyurethane sponge (density 2% w/v, 50mm diameter and 15mm thickness, which simulated the shape of the temporal lobe), inserted inside the tank. The sponge was suspended by a porous wooden support, 3mm in diameter, which was also present in the baseline, and placed successively in 3 positions along the coronal plane of the tank: centre, half way between centre and surface, surface. All air was removed from the sponge by repeated compression in the saline. 40 data sets (frames) were collected for each experiment: 20 as baseline and 20 after insertion of the sponge.

When data were collected with the skull present, the tank was filled with 0.2% saline, to a level 30mm lower than the previous, enough to submerge the skull. The decrease in conductivity was obtained with a smaller cylinder of the same material (30mm diameter and 20mm thickness). The sponge was placed again in 3 positions along the coronal plane of the tank: centre, half way between centre and surface, surface. The distance between consecutive positions were between 15 and 30 mm.

7.4.2 Settings of the systems

Boundary voltages were collected with the KHU Mk1 with 16 electrodes in the tank with a current of 930 μA at 10 kHz. The protocols used were spiral and spiral_s-o, which included 33 injection pairs and took about 1 second to acquire 1 frame (Chapter 6).

Boundary voltages were collected with the UCH Mk2.5 employing all the 31 channels and the EEG31 protocol (0.9 sec/frame) and then employing only the first 16 channels and the spiral_s-o protocol (1.2 sec/frame). The current injected was a composite waveform including 2, 4, 8, 16, 32, 64, 128 kHz. The current level was 400 μA at each frequency in all the experiments except when recording with the EEG31 and the skull in place, in which case the level was reduced to 320 μA.

7.4.3 Boundary voltage preprocessing

The data were expressed as percent of the mean baseline value, the noise calculated as the standard deviation of the baseline, the signal as the mean value after sponge insertion and the signal-to-noise ratio (SNR) as the ratio between these last two values.

Boundary voltages with noise larger than 1% and signal exceeding 6 times the standard deviation of all channels were discarded for the case with no skull. Boundary voltages with noise larger than 0.5%, signal exceeding 3% or 6 times the standard deviation of all changes lower than 3% were discarded for the case with skull.

The difference in SNR of the highest 5% signals, which differed slightly for the protocols and after exclusion of outliers, was assessed for statistical significance for different systems, protocols, positions of test object, presence of the skull. Results were pooled and analyzed with student's t test and were all presented as mean±SD.

7.4.4 Image reconstruction

Time difference images were reconstructed with a sensitivity matrix linear reconstruction algorithm and inversion was performed with truncated singular value decomposition (Zadehkoochak et al. 1991; Bagshaw et al. 2003). A mesh of 52000 elements of the head tank was used. When the skull was present, this was inserted in the model with a conductivity of 0.0048 S/m (Tidswell et al. 2001a) and the mesh was cut according to the saline level. The rows of the Jacobian corresponding to outlier or noisy combinations were eliminated before inversion and 3 truncation levels were tested: 0.2%, 0.1% and 0.05% of the largest singular value. The reconstructed images were quantitatively evaluated according to localization error, occurrence of significant artifacts, error in matching the shape of the original perturbation, error in reconstructed value (Chapter 6). The truncation level with the best general error was chosen for comparison between EIT systems and protocols. Selected levels were as in Table 7-2.

Table 7-2 Truncation level as percent of the highest singular value for each system/protocol combination in the experiments without and with the skull.

System	Protocol	Experiment	
		No skull	Skull
KHU Mk1	Spiral	0.2%	0.05%
	Spiral_s-o	0.1%	0.1%
UCH Mk2.5	EEG31	0.1%	0.2%
	Spiral_s-o	0.1%	0.05%

For these, the errors in each position were reported. A 3D representation of the main reconstructed perturbation and the axial slices of the head passing through the centre of the simulated perturbation and 1cm above and below, was also displayed for qualitative image evaluation.

7.5 Results

7.5.1 Boundary voltages

The baseline noise in the boundary voltages of the KHU Mk1 was 0.019±0.023% (mean±SD, n=3584), compared to that of the UCH Mk2.5, which was 0.193±0.168 (n=3129).

7.5.1.1 Comparison between protocols and systems

There was no significant difference between the protocols for each system (Figure 7-2). However, there was a significant difference between the KHU Mk1 and the UCH Mk 2.5 – SNR 45 vs 4 ($p<0.001$).

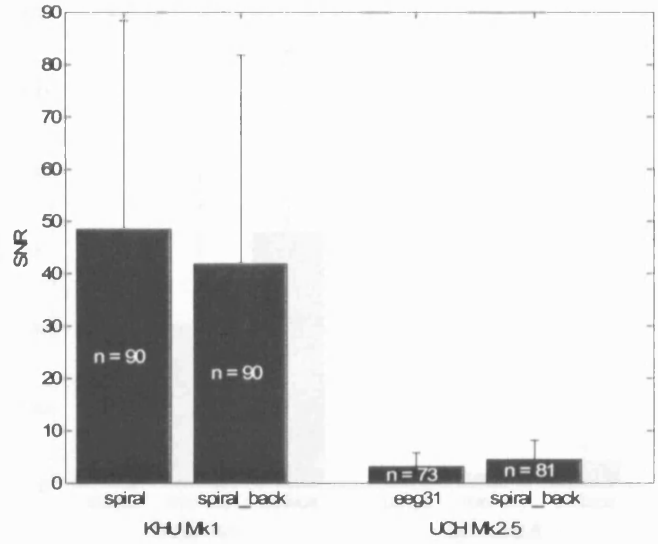

Figure 7-2 SNR for different protocols and systems (n = number of observations).

7.5.1.2 Effect of the skull

The presence of the skull decreased the SNR by 42.7% for the KHU Mk1 and by 42% for the UCH Mk2.5 (Figure 7-3) ($p < 0.001$ in both cases).

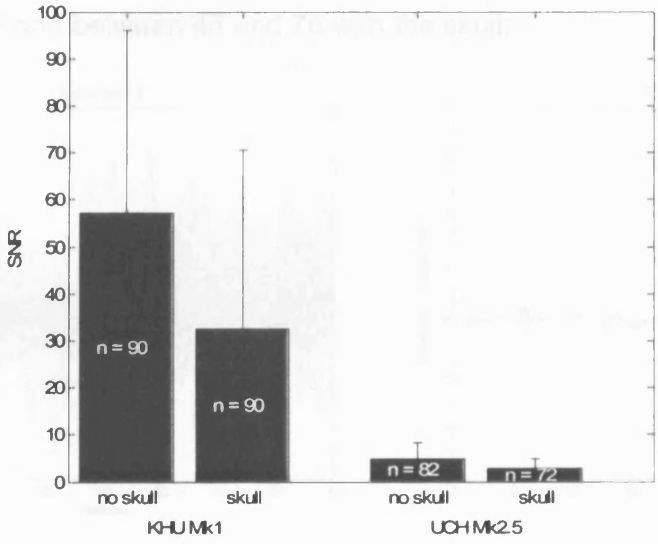

Figure 7-3 SNR without and with skull for the two systems.

7.5.1.3 Effect of the position

The SNR increased by 38% and 117% with respect to the central position when the sponge was moved towards the edge of the head for the KHU Mk1, while it increases by 71% and 242% for the UCH Mk2.5 (Figure 7-4) ($p<0.001$ in all positions for UCH Mk2.5 and between centre and surface for KHU Mk1).

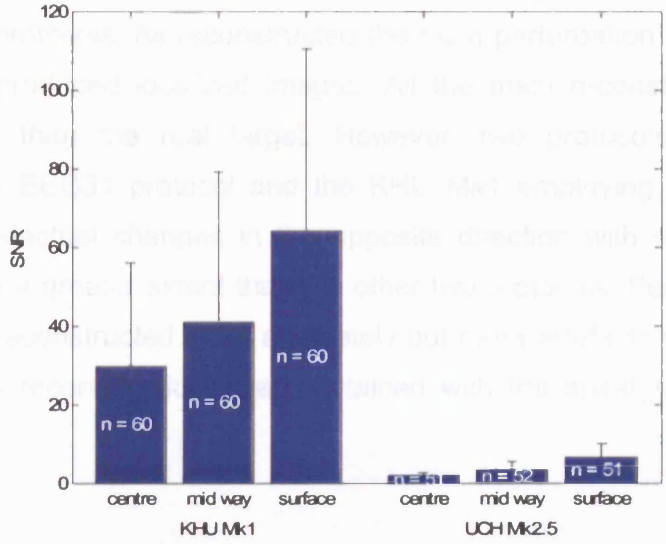

Figure 7-4 SNR for different positions and systems.

7.5.1.4 Effect of PCA

After PCA, the SNR improved between 1.02 and 4.16 times (Figure 7-5). The highest SNR after PCA was using the spiral_s-o protocol with the KHU Mk1 and it increased from 81 to 249 as the test object moved from the centre to the edge without the skull and between 46 and 76 with the skull.

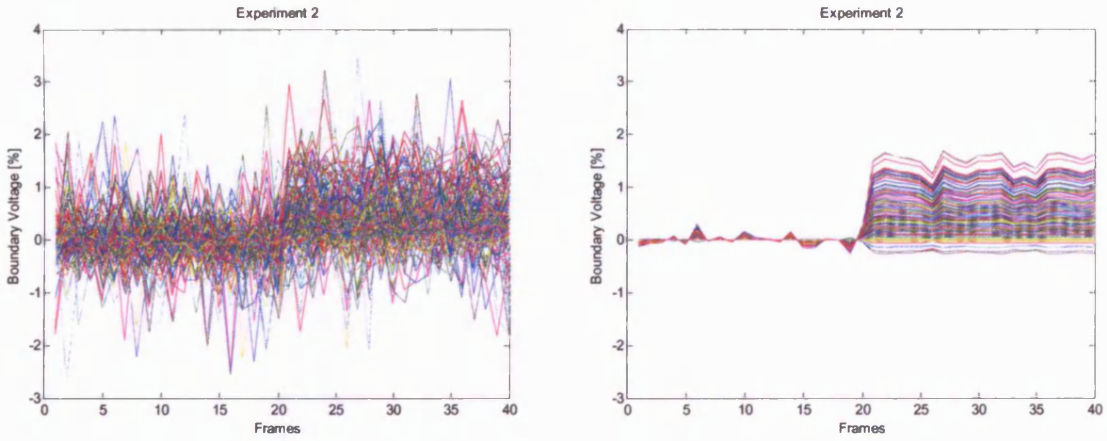

Figure 7-5 Maximal SNR improvement with PCA. Raw boundary voltage data (left) and projected on the 1st PC (right) for the 2nd position collected with the UCH Mk2.5 with EEG31 protocol. Each trace is a tetrapolar measurement of 40 frames, and the perturbation is inserted at frame 20.

7.5.2 Image reconstruction

7.5.2.1 Without skull

7.5.2.1.1 Qualitative assessment

Overall, there was no substantial difference in image quality between the four systems and protocols. All reconstructed the main perturbation close to the correct position and produced localized images. All the main reconstructed perturbation were broader than the real target. However, two protocols, the UCH Mk2.5 employing the EEG31 protocol and the KHU Mk1 employing the spiral protocol, presented artefactual changes in the opposite direction with respect to the main perturbation to a greater extent than the other two protocols. Perturbations near the surface were reconstructed more accurately but more artefacts were apparent. The most accurate reconstructions were obtained with the spiral_s-o protocol in both systems.

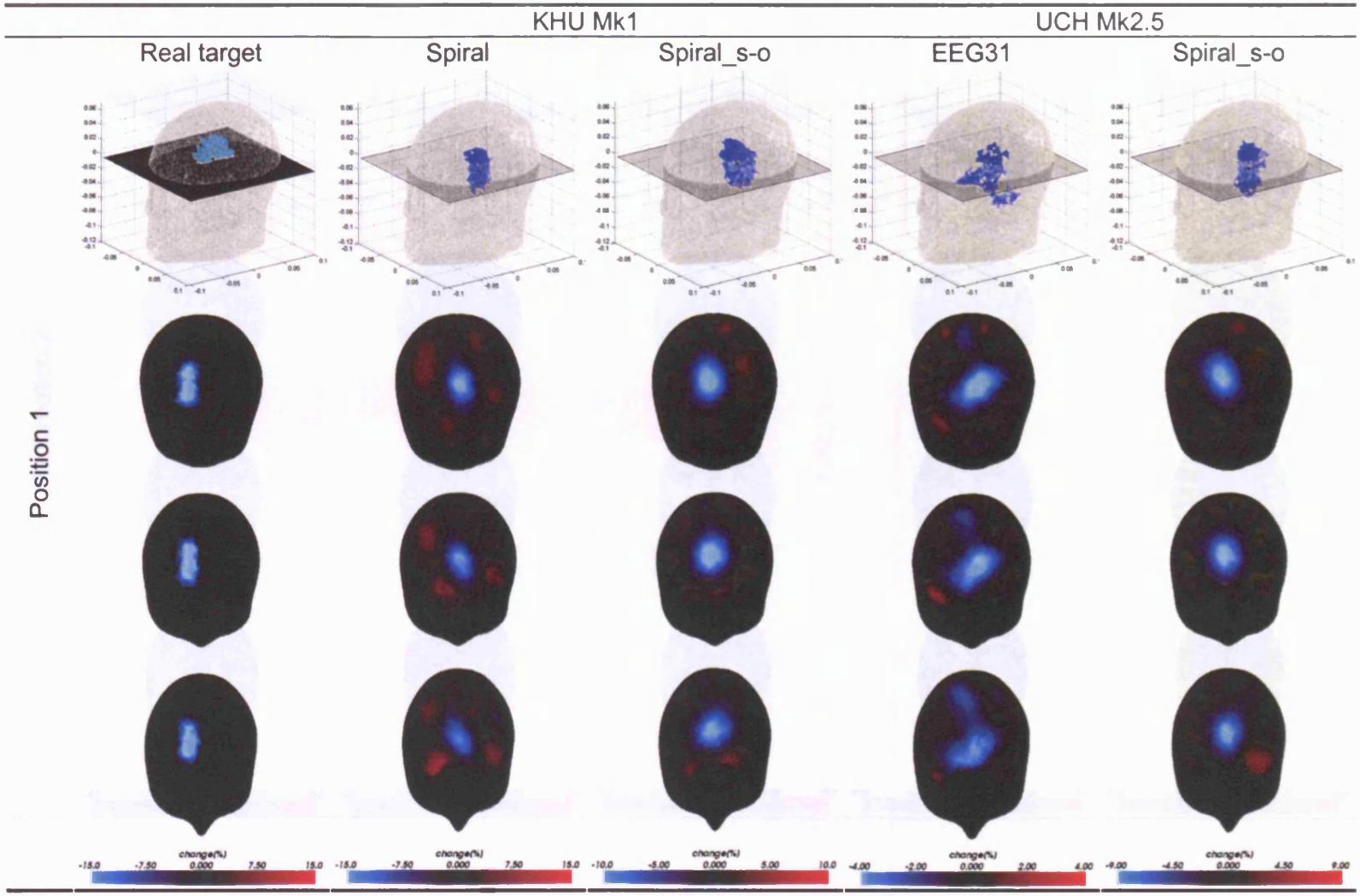
KHU Mk1
UCH Mk2.5
Real target
Spiral
Spiral_s-o
EEG31
Spiral_s-o
Position 1
change(%)
-15.0 -7.50 0.000 7.50 15.0
change(%)
-15.0 -7.50 0.000 7.50 15.0
change(%)
-10.0 -5.00 0.000 5.00 10.0
change(%)
-4.00 -2.00 0.000 2.00 4.00
change(%)
-9.00 -4.50 0.000 4.50 9.00

Perturbation 2

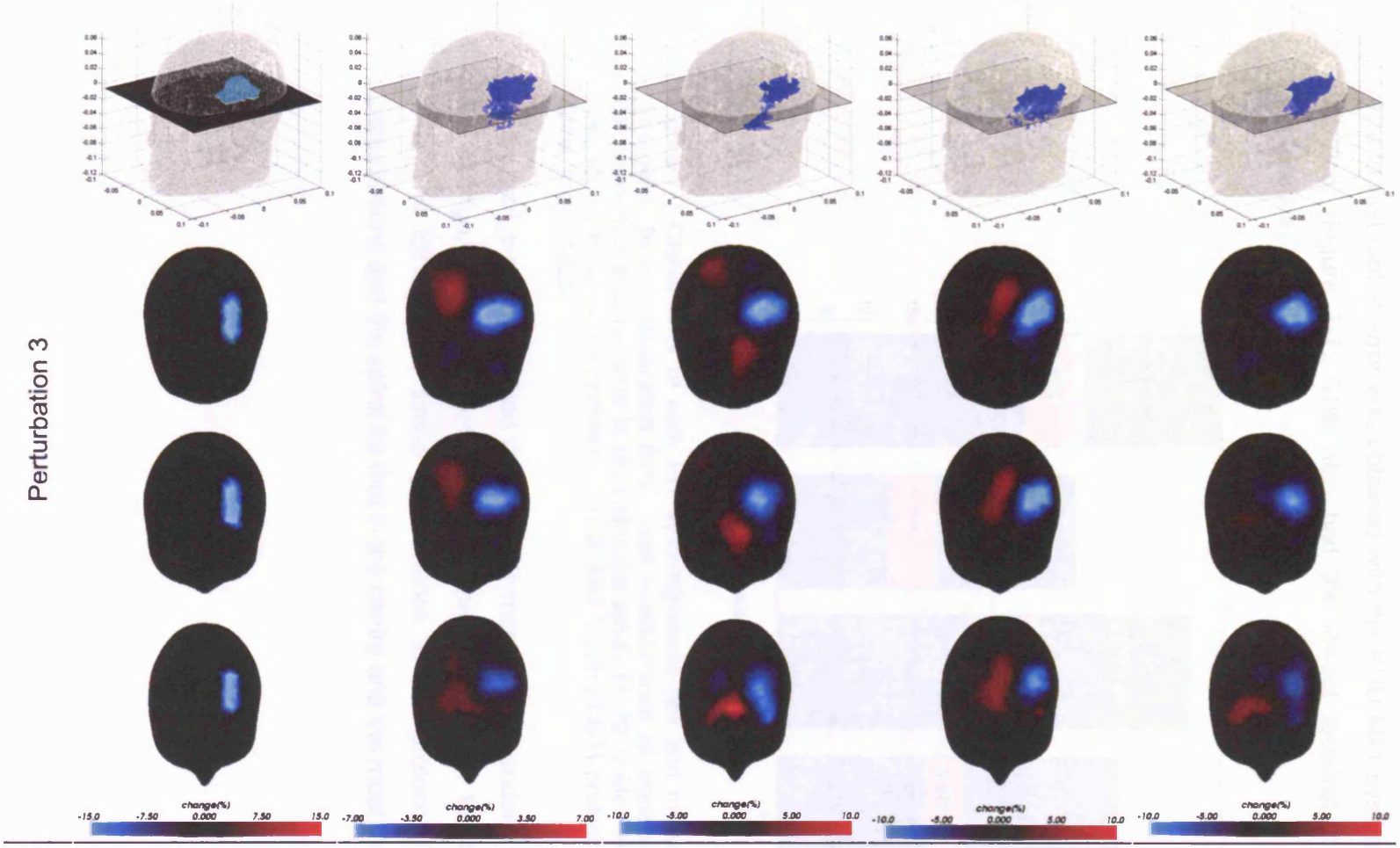

Figure 7-6 Reconstructed images from a single frame for the three perturbation positions without the skull. Images are displayed as a transparent 3D model with the main reconstructed perturbation (blue volume). Below each, are three 2D slices: the middle one is that through the centre of the real perturbation (shown in the 3D model) the top one is that 1cm above and the bottom one is that 1cm below. In the first column the real position of the sponge is shown.

7.5.2.1.2 Quantitative assessment

The lowest global error was obtained with the KHU Mk1 system with the spiral_s-o protocol (Figure 7-7). This also had the lowest localization error and artefact occurrence.

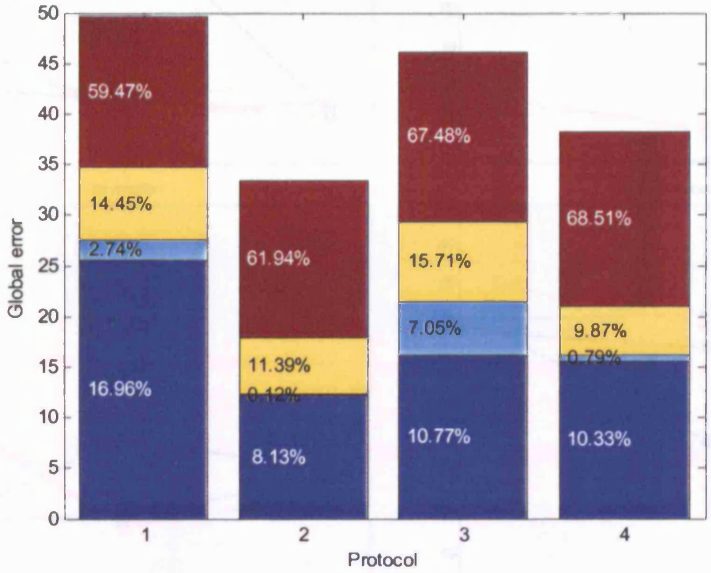

Figure 7-7 Global error of each EIT system/protocol pair and mean contribution of each parameter: blue – localization error; cyan – occurrence of significant artefact; yellow – deformation; maroon – error in reconstructed value. (1) KHU Mk1 with spiral protocol; (2) KHU Mk1 with spiral_s-o protocol; (3) UCH Mk2.5 with EEG31 protocol; (4) UCH Mk2.5 with spiral_s-o protocol.

The spiral_s-o protocol had similar performance, independent from the position of the sponge, whether implemented with the KHU Mk1 or the UCH Mk2.5 (Figure 7-8). The EEG31 had similar performance to this protocol for the most lateral perturbations and the spiral for that in the centre and the most external.

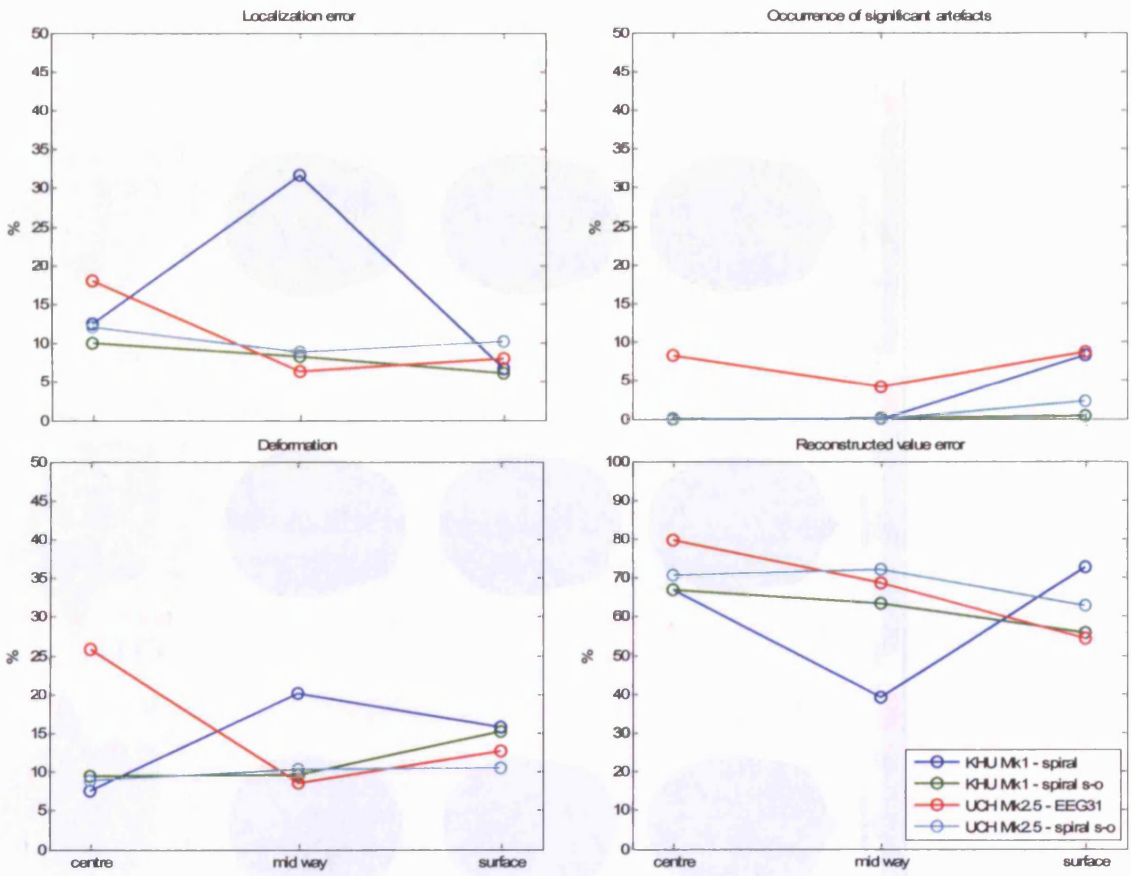

Figure 7-8 Localization error, occurrence of significant artefact, deformation and error in reconstructed value of each EIT system/protocol pair for the three positions of the sponge without skull.

7.5.2.2 With skull

7.5.2.2.1 Qualitative assessment

All the protocols except the spiral produced the main perturbation close to the correct position and with localized changes corresponding to the test objects. All the reconstructions were broader than the real target and presented some artefactual changes in the opposite direction with respect to the main perturbation, especially with the sponge in more lateral positions. The KHU Mk1 with the spiral protocol performed clearly worse than the others in all situations.

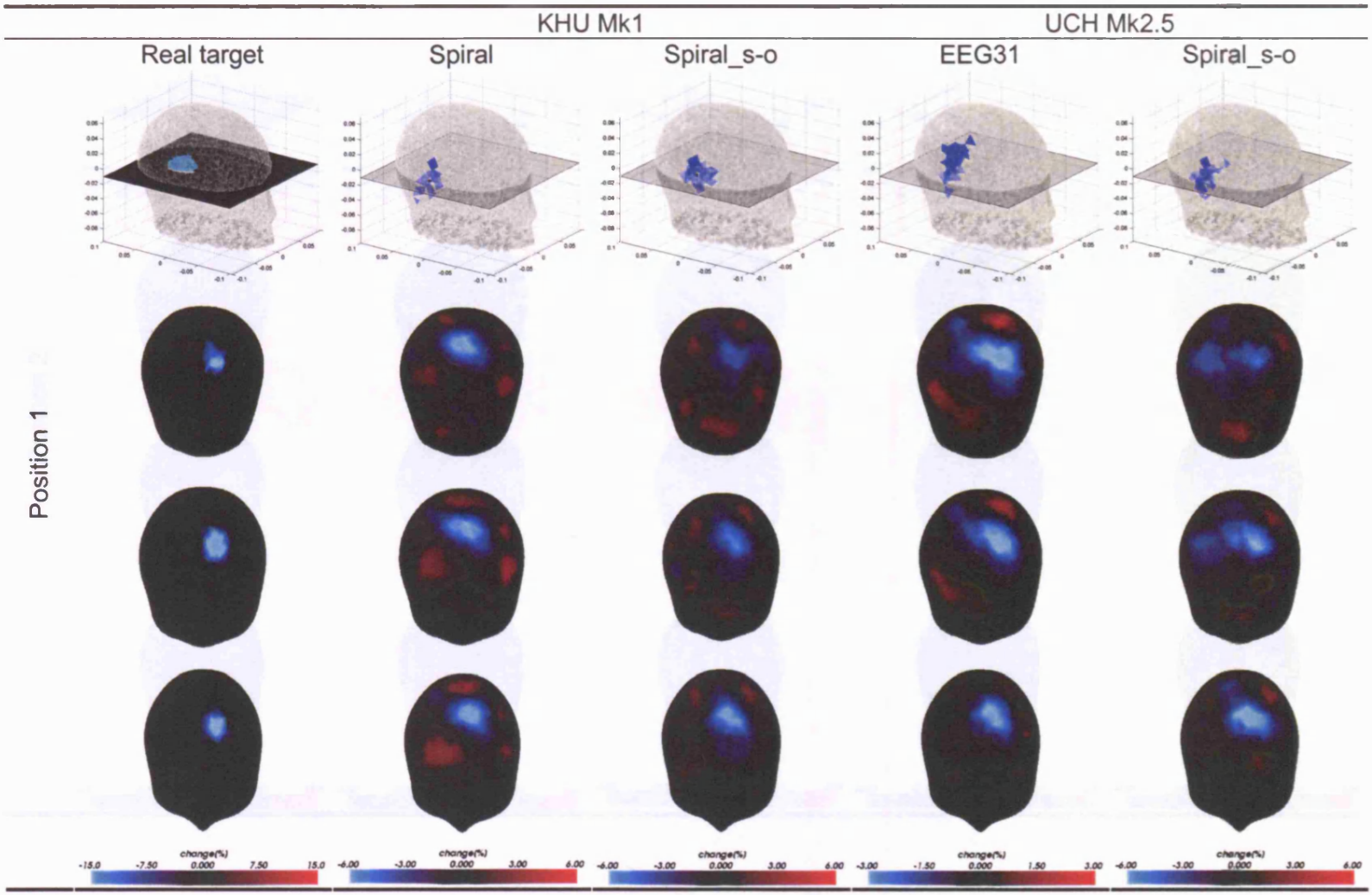
KHU Mk1
UCH Mk2.5
Real target
Spiral
Spiral_s-o
EEG31
Spiral_s-o
Position 1
change(%)
-15.0 -7.50 0.000 7.50 15.0
change(%)
-6.00 -3.00 0.000 3.00 6.00
change(%)
-6.00 -3.00 0.000 3.00 6.00
change(%)
-3.00 -1.50 0.000 1.50 3.00
change(%)
-6.00 -3.00 0.000 3.00 6.00

Position 2

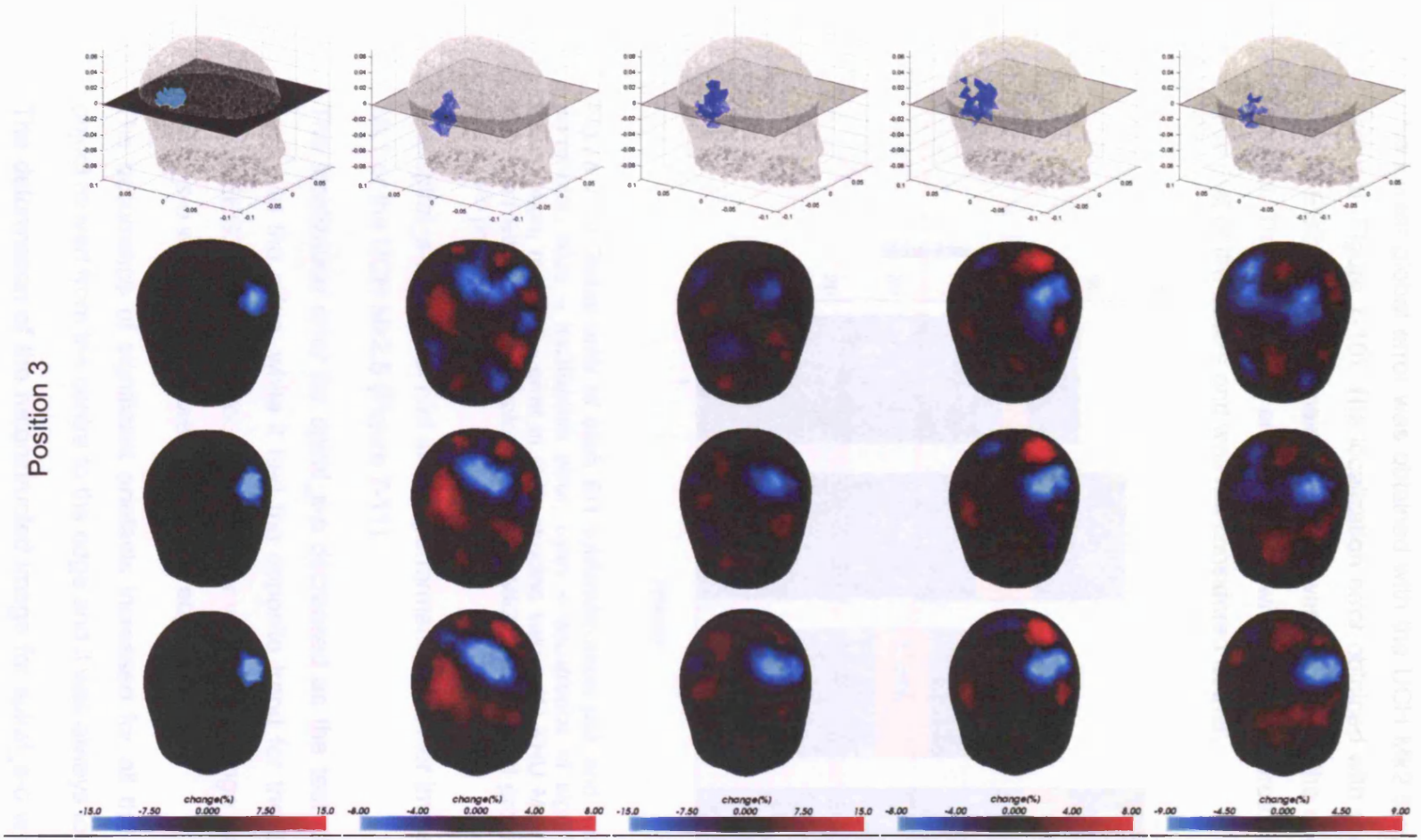

Figure 7-9 Reconstructed images from a single frame for the three perturbation positions with the skull. Images are displayed as a transparent 3D model with the main reconstructed perturbation (blue volume). Below each, are three 2D slices: the middle one is that through the centre of the real perturbation (shown in the 3D model) the top one is that 1cm above and the bottom one is that 1cm below. In the first column the real position of the sponge is shown.

7.5.2.2.2 Quantitative assessment

The lowest global error was obtained with the UCH Mk2.5 system and the EEG31 protocol (Figure 7-10). The localization error obtained with spiral_s-o was similar to that of EEG31 and the main difference was caused by the occurrence of significant artefact. The localization error obtained with the spiral protocol was at least double than that of the others and was not considered further.

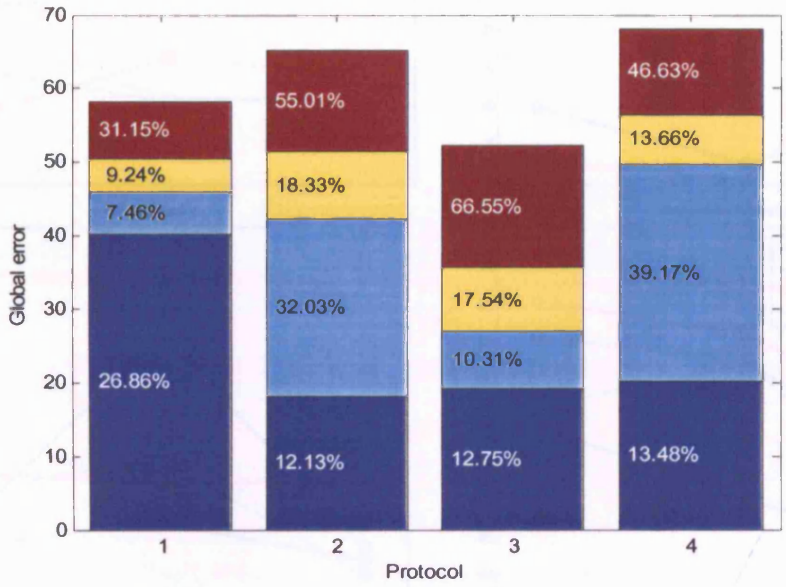

Figure 7-10 Global error of each EIT system/protocol pair and mean contribution of each parameter: blue – localization error; cyan – occurrence of significant artefact; yellow – deformation; maroon – error in reconstructed value. (1) KHU Mk1 with spiral protocol; (2) KHU Mk1 with spiral_s-o protocol; (3) UCH Mk2.5 with EEG31 protocol; (4) UCH Mk2.5 with spiral_s-o protocol.

The spiral_s-o protocol had similar performance whether implemented with the KHU Mk1 or the UCH Mk2.5 (Figure 7-11).

The localization error for spiral_s-o decreased as the test object moved from the centre to the edge, while it had the opposite trend for the EEG31 protocol. As a result EEG31 had lower localization error when the sponge was in the centre, while spiral_s-o when it was more towards the edge.

The occurrence of significant artefacts increased for all the protocols as the test object moved from the centre to the edge and it was always lower for EEG31.

The deformation of the reconstructed image for spiral_s-o was worse with the test object mid way between the centre and the edge, while it was independent from the position for EEG31.

The error in the reconstructed value decreased as the test object moved from the centre to the edge and it was generally lower for spiral_s-o.

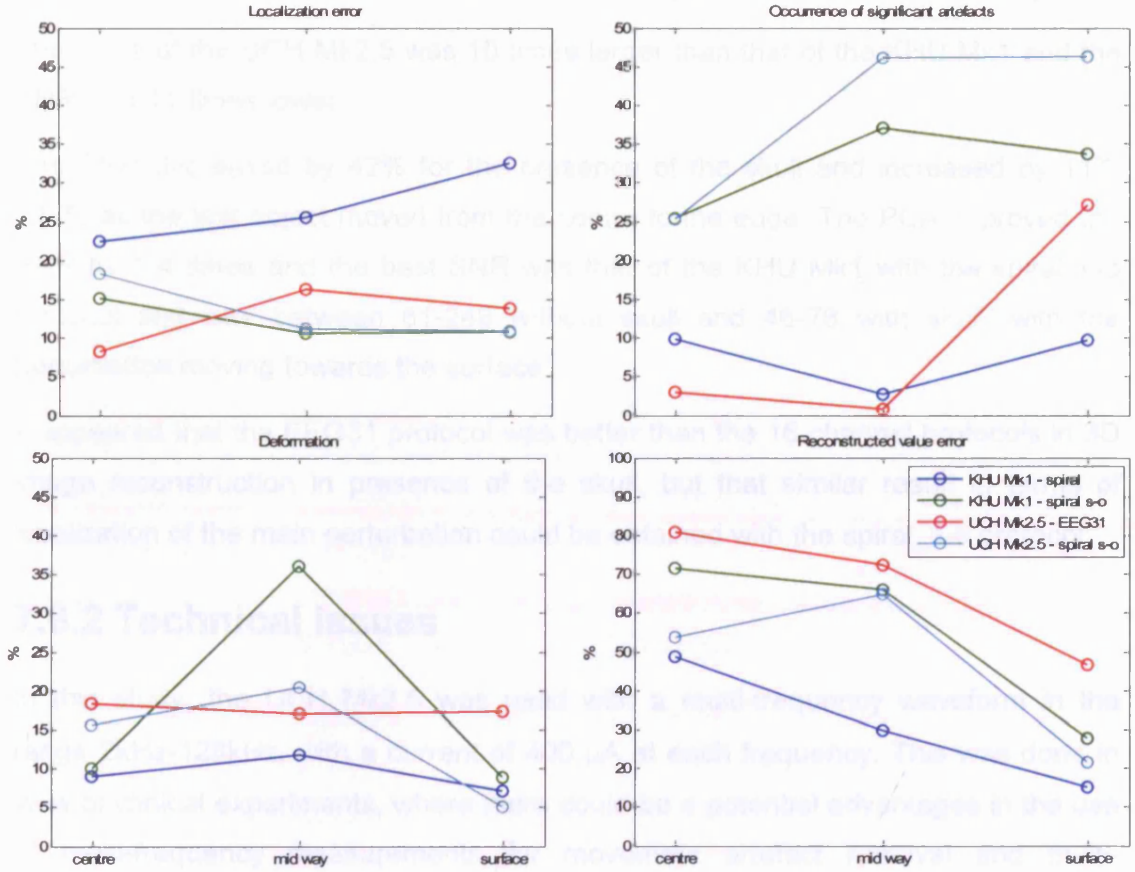

Figure 7-11 Localization error, occurrence of significant artefact, deformation and error in reconstructed value of each EIT system/protocol pair for the three positions of the sponge in the presence of the skull.

7.6 Discussion

7.6.1 Summary of results

In a homogeneous medium focal perturbations can be reconstructed within 8.1-10.8% of the image diameter, with an occurrence of significant artefact of 0.1-7% and with a deformation of 9.9-15.7%, while the presence of the skull may increase these errors to 12.1-13.5%, 10.3-39.2% and 13.7-18.3% respectively.

Without the skull the spiral_s-o protocol had the lowest general error, localization error of 8-10% and produced focused and almost artefact free images.

With the skull in place EEG31 had lower general error than spiral_s-o, however had similar localization error (12-13.5%) and performed better when the perturbation was in the centre, but became more similar when this was moved towards the surface.

The main difference between the EEG31 and the spiral_s-o protocol was in the smaller occurrence of significant artefacts. KHU Mk1 with spiral protocol did not reconstruct the main changes close to the real target (localization error = 26%).

The noise of the UCH Mk2.5 was 10 times larger than that of the KHU Mk1 and the SNR was 11 times lower.

The SNR decreased by 42% for the presence of the skull and increased by 117-242% as the test object moved from the centre to the edge. The PCA improved the SNR by 1-4 times and the best SNR was that of the KHU Mk1 with the spiral_s-o protocol and was between 81-249 without skull and 46-76 with skull, with the perturbation moving towards the surface.

It appeared that the EEG31 protocol was better than the 16 channel protocols in 3D image reconstruction in presence of the skull, but that similar result in terms of localization of the main perturbation could be obtained with the spiral_s-o protocol.

7.6.2 Technical issues

In this study, the UCH Mk2.5 was used with a multi-frequency waveform in the range 2kHz-128kHz, with a current of 400 μA at each frequency. This was done in view of clinical experiments, where there could be a potential advantages in the use of multi-frequency measurements for movement artefact removal and multi-frequency analysis of impedance changes due to epilepsy. However, in this study, time difference images were obtained with measurement only at 4 kHz. In case the use of multi-frequency measurement transpires not to confer an advantage in clinical application, then the current level could be increased to 1.65 mA at a single frequency above 11.67 kHz. With this change, computer simulation suggests that the mean of the highest 1% boundary voltage changes would increase from about 0.35% (measured at 4 kHz) to 0.54% (measured at 128 kHz) in temporal lobe epilepsy.

The KHU Mk1 acquired at 1 frame/sec because the controlling software was not optimized for a protocol with more than 16 injecting pairs. This could be improved to obtain a frame rate 3x faster. In this eventuality, the possibility of averaging 3 frames to reduce random noise in the data or in the images by 40% would be available.

The purpose of this work was to investigate for the first time the capability of the modified UCH Mk2.5 and of the KHU Mk1 16-channel systems to reconstruct 3D images of a conductivity perturbation in the human head. However this was an approximation of the real problem of reconstructing impedance changes related to

epilepsy. The conductivity decrease of 30% was an overestimation of the conductivity changes that may be measured at 4 kHz and 10 kHz during seizures, which are about 13% and 12% respectively, however the volume of the sponge used with the skull in place was about ½ of that of the temporal lobe. It may be possible that in real experiments these two approximations would cancel each other. Nevertheless the decrease of 42% in the SNR obtained in this study between the case without skull and with skull included also the change in the volume of the perturbation. So the skull is only partially responsible of this decrease.

The SNR may be expected to be 50% lower in human experiments as the noise is double, because of electrode-skin interface variability and physiological noise (Fabrizi et al. 2007). Moreover the signal may be reduced because of the difference in conductivity between the CSF and the brain (6:1), which may shunt the current around the region of interest, but this is probably negligible in respect to the reduction due to the skull presence.

7.6.3 Possible explanation of findings

Images reconstructed with the UCH Mk2.5 and the KHU Mk1 adopting spiral_s-o or EEG31 protocol produced images of better quality than in the previous tank experiments conducted in our group in terms of localization error and deformation. This is probably due mostly to superior instrumentation, implementation of PCA, which improved the SNR, and use of the correct conductivity guess to solve the forward problem (Bagshaw et al. 2003) since the experimental settings were similar.

The KHU Mk1 has 10 times lower noise than the UCH Mk2.5 and therefore 9 times higher SNR when considering the spiral_s-o in both systems. Nevertheless the reconstructed images with the two systems and this protocol appear only slightly better for the KHU Mk1. This suggests that a 3 fold SNR difference is not crucial in deciding the quality of the image, because systematic errors may dominate in these conditions. This is probably because of the use of PCA which separates the signal from the noise, even though after this analysis the SNR for the KHU Mk1 is still higher than for UCH Mk2.5, and of the spatial averaging effect in reconstructing the images. However the SNR may become more relevant in clinical applications where the noise is higher because of electrode-skin interface variability and physiological noise and may be partly correlated in all channels, which may cause PCA to fail in discriminating the relevant signal.

When the skull was absent the 16 channel spiral_s-o protocol performed better than the traditional EEG31 probably because current was injected at 180°, 120° and 60° whereas the EEG31 protocol only employs current injection at 180° . This provided a more even sensitivity coverage of the brain region, as different areas were reached better with current injected at different angles.

When the skull was present, EEG31 performed slightly better than the spiral_s-o protocol. The advantage in using EEG31 was evident only for more central positions of the test object and it was mainly a lower occurrence of significant artefacts. This was probably because polar injection maximized the amount of current passing through the centre of the brain, and therefore the sensitivity in this region (Bayford et al. 1996). Moreover the advantage given by current injected from closer electrodes may have been reduced by the skull as it may have shorten it across the scalp. Besides spiral_s-o has a lower sampling of the volume as it employs 16 channels, while the EEG31 31 channels, which may impair the sensitivity in some regions of the brain when the skull is present.

However it is not clear the reason why this was not seen in the simulation study in Chapter 6 for the real head. In this case the general error estimated for the spiral_s-o protocol was only 14% higher than that found in the tank study, while that for the EEG31 was 108% higher, in particular the localization error and the occurrence of significant artefact were 2.1 and 5.3 times respectively. This may suggest that the electrodes used in the EEG31 which are not included in the subset of the spiral_s-o are above the sutures of the skull which are not included into the simulation. This may allow more current into the cranial cavity, increasing the sensitivity in this region (Gamba and Delpy 1998) respect to the simulation. Another explanation may be that the spiral_s-o protocol is more feasible to reconstruct images of conductivity changes in the epileptic foci than the EEG31 and its performance are more independent from the position and size of the perturbation. It may also be that the EEG31 benefits from the choice of an optimal truncation level more than the spiral_s-o, whose performance did not vary notably if this was optimized.

7.6.4 Recommendations for future work

The UCH Mk2.5 employing the EEG31 protocol has better 3D imaging performances than the KHU Mk1 employing the 16 channels protocol spiral_s-o. Besides, the UCH Mk2.5 is more portable and has the possibility of multi-frequency analysis and movement artefact removal, while the KHU Mk1 can be faster and has a higher SNR. As the SNR does not seem to influence the reconstructed images in

this study, it is advisable to employ the UCH Mk2.5 with the EEG31 protocol for clinical experiments in first instance. However, in the eventuality that the SNR is too low for discerning the relevant signal from the noise, the use of the KHU Mk1 system may be considered. Moreover spiral_s-o should be tested, as it has a similar localization error to EEG31, it may have the potential to reconstruct deep and small impedance changes and there may be the possibility that reducing the number of channels will reduce the error in the model, as there are less electrodes which can be misplaced or with wrong diameter.

Chapter 8 – Discussion

8.1 Progress made during this work

In this thesis, a design and implementation of a method for Electrical Impedance Tomography of epileptic seizures is presented, showing the feasibility of this application.

The work presented in Chapter 2 demonstrates the feasibility of simultaneous recording of EIT and EEG with recovering of the latter from artefacts introduced by EIT current injection. These were reduced to less than 10 μV making the EEG traces acceptable for routine reporting in about ¼ of the length of the recording.

Chapter 3 presents the development of a new method to record and analyse EIT during natural epileptic activity in concurrence with video-EEG from standard scalp electrodes in humans. However in the event of reanalysing data collected during 22 seizures of 7 patients genuine changes related to seizure activity were obscured by movement artefact and large baseline drift.

The work in Chapter 4 shows on a Finite Element Model that the highest proportional boundary voltage changes related to epileptic seizures are of 1% at 50 kHz when injecting a current meeting the safety standard. It also shows that reasonably accurate images of the real component could be obtained during temporal lobe seizure with proportional noise of about 0.035% (RMS) which is expected to be achievable with serial systems.

The possible sources of baseline noise are reviewed and investigated for the UCH Mk1b, UCH Mk2.5 and KHU Mk1 in Chapter 5. It is shown that thermal noise, quantization noise and amplifier noise are only responsible of 0.5% of the recorded noise and that it mostly depends on other factors such as electromagnetic interferences, stray capacitance and noise deriving from other system components. However the lowest proportional noise was for the KHU Mk1 and of about 0.16% (RMS) in humans.

Chapter 6 describes the development of a 3D protocol to image the human head for the KHU Mk1, which has only 16 channels and adjacent measurements. This protocol employed a spiral arrangement of the electrodes covering the head homogeneously and provides a localization error within 10% of the coronal size of the head.

Finally, the work in Chapter 7 shows that the protocol developed in Chapter 6 for the UCH Mk2.5 and KHU Mk1, optimized for epilepsy recordings, produces images of a head-shaped saline tank with a localization error of 8.1% of the head diameter

without skull and 12.1% with skull. However it appeared that a 31 channel protocol still provides better general performance in the presence of the skull.

8.2 Discussion

8.2.1 Possibility of employing EIT as presurgical assessment method in epilepsy

The work in this thesis showed that EIT has the chance of being successfully employed as presurgical imaging method in the diagnosis of intractable epilepsy. EIT could be used to produce functional images of epileptic seizures, which is not practical with the traditional scans. It was demonstrated that conductivity changes related to epilepsy can be reconstructed with the noise level of available EIT systems in a realistic computer simulation. It has also been shown that EIT can be recorded in concurrence with EEG in a Telemetry ward over days and that the latter can be recovered from induced artefacts and used for routine clinical reporting employing separated sets of electrodes for the 2 systems. Finally impedance changes of similar value of those expected during epilepsy were effectively imaged in a head-shaped phantom including a real skull within a localization error of 12%, which would be sufficient for lateralization of the seizure occurrence, with a frame rate of 1 sec.

This was achieved in the absence of physiological noise and movement artefacts and employing a custom Finite Element Model with known electrode positions to solve the forward and inverse problem. The former issues may be solved employing PCA and multi-frequency recordings, while the latter employing custom made meshes and techniques to define the coordinate of the electrodes. Overall, it seems plausible that it will be possible to image impedance changes occurring in onset areas of the size of the temporal lobe anywhere in the brain. However it also seems that it may be possible to image deeper and smaller foci using the KHU Mk1 which has lower noise, therefore higher SNR, and the newly developed 16 channels protocol spiral_s-o, but probably the images would include unwanted artefacts.

8.2.2 Bottleneck of EIT in epilepsy

The bottleneck for feasible recording seems in first instance the possibility of separating the signal correlated with the epilepsy onset from the other components, which can be regarded as noise. This may be partially achieved by reduction of

noise sources such as variation of contact impedance, stray capacitances and external electromagnetic interferences and applying analysis technique such as PCA. However the presence of movement artefacts is the most restrictive limitation, which it may be possible to solve by employing multi-frequency measurements. Other restraints, which can be addressed, are to employ more accurate models for the solution of the forward and inverse problem; a procedure for this has been developed in our group so that it is now possible to segment and mesh a subject's MRI in a few hours.

8.2.3 Optimal arrangement for clinical studies

The Telemetry ward is a feasible environment for EIT recording of epileptic seizures as EIT can be recorded in concurrence with EEG without influencing the routine clinical assessment for Neurosurgery. EEG can be recovered to a level acceptable for diagnosis and a method for impedance data analysis in concurrence with EEG and video has been developed. It is advisable to employ the UCH Mk2.5 with the EEG31 protocol for clinical experiments in the first instance, as this has been shown to have the best performance in terms of 3D image reconstruction, is more portable and has the possibility of multi-frequency analysis and maybe movement artefact removal. However, in the eventuality that the SNR is too low for discerning the relevant signal from the noise in case of smaller seizure onset, the use of the KHU Mk1 system may be considered. Moreover spiral_s-o should be tested, as it has similar localization error to EEG31, it may have the potential to reconstruct deep and small impedance changes and there may be the possibility that reducing the number of channels reduces the error in the model, as there are less electrodes which can be misplaced or with wrong diameter.

8.3 Future work

The most important work, which the author wished he had the time to conduct, is now to collect impedance data on human patients. At the time of writing our group is running collaboration with the King's College Hospital Telemetry Unit and has received safety approval for the employment of the UCH Mk2.5 in this hospital. The development of the new protocol which employs only 16 channels will help in making EIT recording more feasible since the practical procedure of placing the electrodes on the head will be reduced by half. These data will be collected with the optimized UCH Mk2.5 and the low noise KHU Mk1 and analysed as explained in Chapter 3. It would be of great advantage if the KHU Mk1 could be miniaturized for

clinical trials as screen leads could be shorten and its size less concerning for the hospital staff.

The data pre-processing could be enhanced by implementing principal component analysis across time as shown in Chapter 7 (Perez-Juste Abascal 2007) or in the case of the UCH Mk2.5 across frequency to separate the movement artefacts from the signal itself.

The work in Chapter 6 and 7 demonstrated that a further, improved protocol for 3D images could be designed, which only employs 16 channels and may be better than the traditionally adopted EEG31 (Gibson 2000). This protocol was limited by the speed of the EIT system which was then employed. Availability of new semi-parallel systems such as the KHU Mk1 may open new possibility for reconsidering more optimal experimental design (i.e. determining optimal sets of injection-measurements).

Since the noise appeared to derive from stray capacitance variation an effort should be made to use unscreened leads as short as possible, feasibly with the UCH Mk2.5. Additionally, the fluctuation of the voltage at the electrode-electrolyte and electrolyte-skin interfaces, and movement artefact may be reduced considering new electrodes as those employed in headnets for EEG recordings (Tidswell et al. 2003a), provided these headnets are carefully designed to minimise the contact impedance.

The reconstruction algorithm may also be improved by minimizing the difference between the forward model and the real object. This could be achieved:

1. by developing custom meshes for each of the patients derived from their MRI scans which are usually taken during presurgical evaluation;
2. adopting 3D localization techniques to identify the exact position of the electrodes, such as photogrammetry, where pictures of the head are taken from different angles and identifying the electrodes in each of them it is possible to retrieve their 3D location respect to defined fiducial points (Russell et al. 2005).

Finally improvement on the inverse problem can be achieved by implementing other regularization techniques instead of the truncated singular values decomposition. Tikhonov regularization method has been suggested as an alternative; in this case the singular values, and therefore the base images, are not just truncated but smoothly filtered (Borsic et al. 2002). This could be also enhanced with an optimal and automatic regularization parameter selection, instead of looking at the images

outcome for deciding upon the singular value truncation level (Perez-Juste Abascal et al. 2005).

Recording boundary voltage changes related to epilepsy has been made feasible for human experiment in the hospital and the possibility to record them has improved after this study. Moreover this work could be used as a guideline for design of new EIT systems intended for this purpose. If successful, EIT will be a breakthrough in low-cost and portable brain imaging and many clinicians and patients will benefit from it. I am honestly looking forward for the outcome of the soon to come clinical study in detection of conductivity changes related to epilepsy.

Appendix A – Derivation and physiological explanation of the conductivity change due to epilepsy

In this appendix it is explained how data from different sources in the literature were integrated to generate the spectrum of the conductivity changes of the grey matter during epilepsy in the frequency range 5Hz-4MHz. A physiological explanation of the resulting spectrum is also given.

A.1 Derivation of the conductivity changes

In the following procedure to derive the complex conductivity changes:

- ρ^{*r}_{n} (= ρ'^{r}_{n} +j ρ''^{r}_{n}) is the resistivity before the beginning of the spreading depression at frequencies between 5 Hz and 50 kHz, where the superscript *r* stays for Ranck;
- ρ^{*r}_{sd} (= ρ'^{r}_{sd} +j ρ''^{r}_{sd}) is the average of the resistivity over the 30 sec with the highest changes at frequencies between 5 Hz and 50 kHz, where the superscript *r* stays for Ranck (Ranck, Jr. 1963a);
- $\Delta\sigma'^{y}_{sd}$ is the percent change in conductivity at frequencies between 300 kHz and 100 MHz, where the superscript *y* represents Yoon measurements;
- $\Delta\varepsilon^{y}_{sd}$ is the percent change in dielectric constant at frequencies between 300 kHz and 100 MHz, where the superscript *y* represents Yoon measurements;
- $\Delta\rho_{ep}$ is the resistivity change due to epilepsy measured at 47 kHz by Rao (Rao 2000).

The correction factor to account for the differences between SD and epilepsy is calculated as:

$$R_{\rho} = \frac{\Delta\rho_{ep}}{\Delta\rho'^{r}_{sd}} \qquad \text{(A-1)}$$

where:

$$\Delta\rho_{sd}^{\prime r} = \frac{\rho_{sd}^{\prime r}(50kHz) - \rho_{n}^{\prime r}(50kHz)}{\rho_{n}^{\prime r}(50kHz)} \tag{A-2}$$

We can estimate the resistivity during epilepsy at frequencies between 5 Hz and 50 kHz as:

$$\begin{aligned} \rho_{ep}^{\prime r} &= \left(\rho_{sd}^{\prime r} - \rho_{n}^{\prime r}\right) R_{\rho} + \rho_{n}^{\prime r} \\ \rho_{ep}^{\prime\prime r} &= \left(\rho_{sd}^{\prime\prime r} - \rho_{n}^{\prime\prime r}\right) R_{\rho} + \rho_{n}^{\prime\prime r} \end{aligned} \tag{A-3}$$

And the conductivity for normal, spreading depression and epileptic conditions as:

$$\begin{aligned} \sigma^{\prime r} &= \rho^{\prime r} / \left(\rho^{\prime r 2} + \rho^{\prime\prime r 2}\right) \\ \sigma^{\prime\prime r} &= \rho^{\prime\prime r} / \left(\rho^{\prime r 2} + \rho^{\prime\prime r 2}\right) \end{aligned} \tag{A-4}$$

The percentage changes in conductivity at frequencies between 5 Hz and 50 kHz are then:

$$\begin{aligned} \Delta\sigma_{ep}^{\prime r} &= \frac{\sigma_{ep}^{\prime r} - \sigma_{n}^{\prime r}}{\sigma_{n}^{\prime r}} \\ \Delta\sigma_{ep}^{\prime\prime r} &= \frac{\sigma_{ep}^{\prime\prime r} - \sigma_{n}^{\prime\prime r}}{\sigma_{n}^{\prime\prime r}} \end{aligned} \tag{A-5}$$

To translate the percent change of the conductivity at frequencies between 300 kHz and 100 MHz due to SD in percent change due to epilepsy, another conversion factor was calculated:

$$R_{\sigma} = \frac{\Delta\sigma_{ep}^{\prime r}(50kHz)}{\Delta\sigma_{sd}^{\prime r}(50kHz)} \tag{A-6}$$

Therefore the conductivity changes due to epilepsy at frequencies between 300 kHz and 100 MHz are:

$$\Delta\sigma_{ep}^{\prime y} = R_{\sigma}\Delta\sigma_{sd}^{\prime y} \tag{A-7}$$

A percent change in the dielectric constant corresponds with a percent change in the quadrature component of the conductivity, therefore:

$$\Delta\sigma''^{y}_{ep} = R_{\sigma}\Delta\varepsilon^{y}_{sd} \quad \text{(A-8)}$$

The overall spectrum of the percent conductivity change was obtained by joining $\Delta\sigma'^{r}_{ep}$ with $\Delta\sigma'^{y}_{ep}$ and $\Delta\sigma''^{r}_{ep}$ with $\Delta\sigma''^{y}_{ep}$ and used to modify the grey matter conductivity to include in the forward model to simulate epileptic conditions.

A.2 Physiological explanation

The model proposed by Ranck (Ranck, Jr. 1963a) will help to explain the spectrum of the conductivity changes due to epilepsy. The current flowing through the brain has two main components: extracellular and intracellular. The latter can flow in the direction of the axis of the fibre (longitudinal) or normally to the axis and across a spherical cell body (transverse). The importance of each component of the current through the cells depends on the orientation of the fibre respect to the current flow, but when the fibres are randomly oriented, as in the cerebral cortex, the effective volume contributing to longitudinal conductivity will be 1/3 and the that contributing to transverse 2/3.

The real part of the conductivity (σ') in general decreases at all frequencies during epilepsy because the extracellular space shrinks and more current is pushed through the cells. $|\Delta\sigma'|$ decreases with frequency increase because the current through the cells tends to effective infinite frequency, which means that the cell membrane is seen as a 'short circuit' between the extracellular and intracellular resistive fluids. In these conditions if the cells are swollen or not does not influence the conductivity. At frequencies below 5 kHz, the current is mostly extracellular and the longitudinal current through the glia is equivalent to that at infinite frequency, since their membrane resistance is low. The longitudinal current can not flow freely in the neurons yet, but their swelling has less influence on $|\Delta\sigma'|$ with frequency increase because also their longitudinal current tends to effective infinite frequency. At frequencies greater than 5 kHz, longitudinal current flows freely through glia and neurons so the $|\Delta\sigma'|$ decreases faster because now 1/3 of the cell volume can be considered interstitial space. Between 20 kHz and 50 kHz, transverse current starts to flow, then the remaining 2/3 of equivalent cell volume begins to be crossed by the current, and its swell loses influence on σ'. Because the volume is greater, the decrease in $|\Delta\sigma'|$ is steeper.

σ'' is one order of magnitude smaller than σ', so its changes are more difficult to measure and more sensitive to errors and variations. For this reason, while $\Delta\sigma'$

calculated across the 30 seconds of maximal SD activity (Ranck Jr 1964) is consistent and then well represented by the mean, $\Delta\sigma''$ has a much higher variability (Figure A.1).

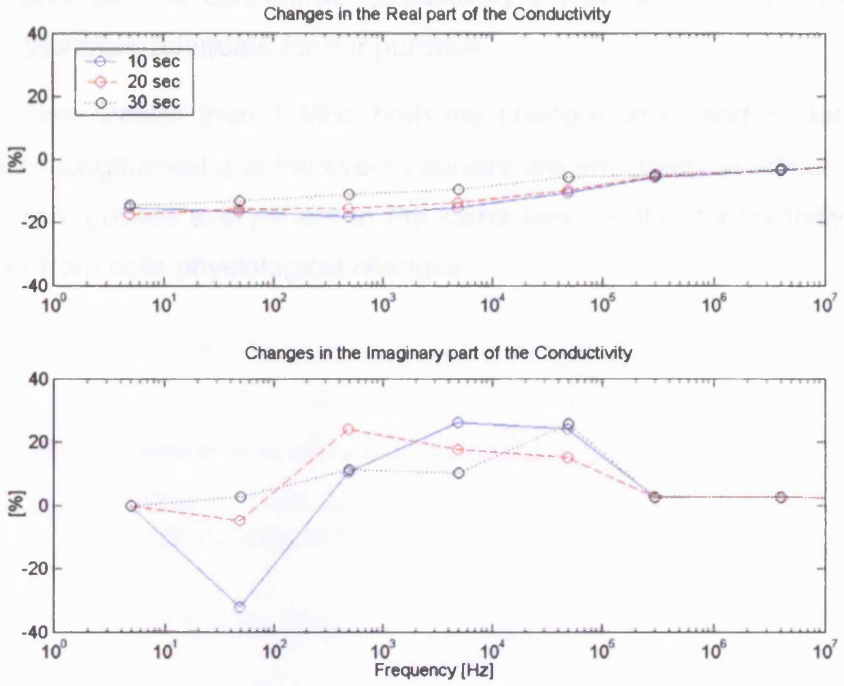

Figure A.1 Real and imaginary part of conductivity change across the 30 seconds of maximal SD activity

Nevertheless the spectrum of $\Delta\sigma''$ in Chapter 4 can be qualitatively explained. We would expect an increase in σ'' at all frequencies, because the cell swelling forces more current to go through the cells. We would also expect a mild increase at low frequencies until 5 kHz when the phase change is due only to the longitudinal current flowing through the neurons, then a steeper increase when the transverse current kicks-in between 20kHz-50kHz then a decrease when also the transverse current is effectively at infinite frequency, tending to 0 when all the current can go everywhere.

In the spectrum of the observed changes, σ'' decreases at 50 Hz ($\Delta\sigma''<0$). At these frequencies, variations in σ are given by the longitudinal current in the neuronal cells: a decrease in the conductivity can be due to a decrease in the membrane resistance of these cells, which is likely to happen in epilepsy due to ion channels opening. At higher frequencies, σ'' becomes more independent from changes in neuronal membrane resistance because the current through the neurons tends to effective infinite frequency. Nevertheless the extracellular space shrinks, so the current is pushed through the cells and $\Delta\sigma''$ is positive.

The large decrease between 50 kHz and 300 kHz could be due to the difference in Ranck's and Yoon's experiments, but a decrease in $\Delta\sigma''$ was expected when also the transverse current becomes effectively at infinite frequency.

The $\Delta\sigma''$ curve can be considered qualitatively correct and in the right order of magnitude, therefore adequate for our purpose.

At frequencies greater than 1 MHz both the changes in σ' and σ'' tend to zero because both longitudinal and transverse current are effectively at infinite frequency and the current passes everywhere in the same way, so the conductivity becomes independent from cells physiological changes.

Appendix B – Graphical User Interface for UCH Mk2.5 data collection

B.1 Introduction

The newly developed UCH Mark2.5 will be used in clinical settings by technicians or physicians with no previous knowledge about programming or impedance data collection. For this reason a graphical user interface (GUI) to allow easy EIT data collection was designed and written using MATLAB v.7. This consists of 4 main stages:

1) Experiment information input
2) Contact impedance check
3) Reciprocity check
4) Data collection

The following sections cover each GUI window in order of appearance.

B.2 Start

In this window (Figure B.2) the user select the kind of experiment is about to perform, whether human or tank, the difference will be clear later.

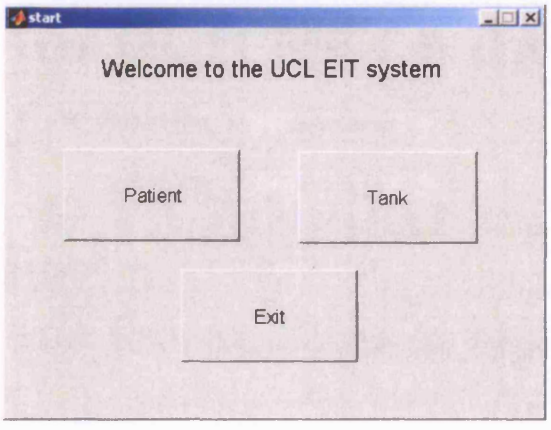

Figure B.2 Start window.

B.3 Experiment information

In this window the user introduces information regarding the experiment he is about to perform, which will be used to save the data with significant names. This is different in case a tank study or a human study is performed.

If the experiment is a tank study (Figure B.3), the information to provide is:

- *tank type*: resistor, 2D tank, head tank, etc.;
- *system type*: the user may wan to keep note of which mk2.5 was used;
- *test type*: saline 0.1%, blood etc.

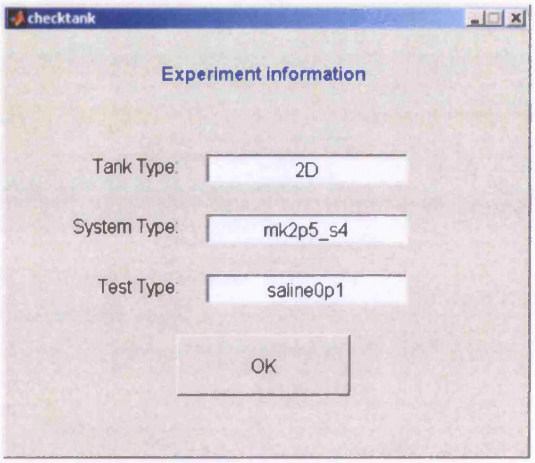

Figure B.3 Tank experiment information window.

If the experiment is a human study, the information to provide is (Figure B.4):

- *patient name*
- *system type*

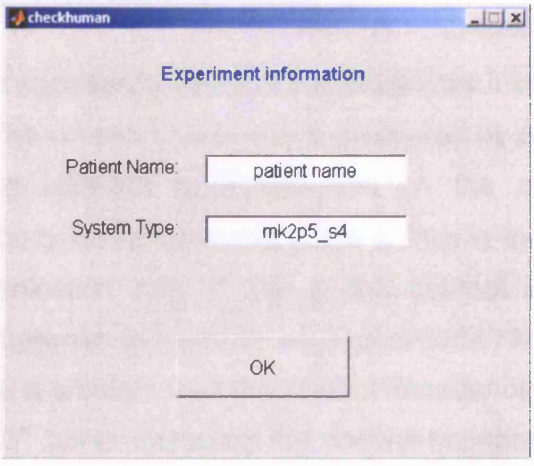

Figure B.4 Human experiment information window.

B.4 Protocol selection

In this window the user can select one of the available boundary voltage collection protocols (Figure B.5). The section appears at the bottom of the window. Other protocol could be added, but they must be compiled and tested first. Each protocol has an explanatory description of its features. After this is done the user can decide whether to proceed with impedance and reciprocity check, pressing *calibration*, or to go straight to the acquisition, pressing *skip calibration*.

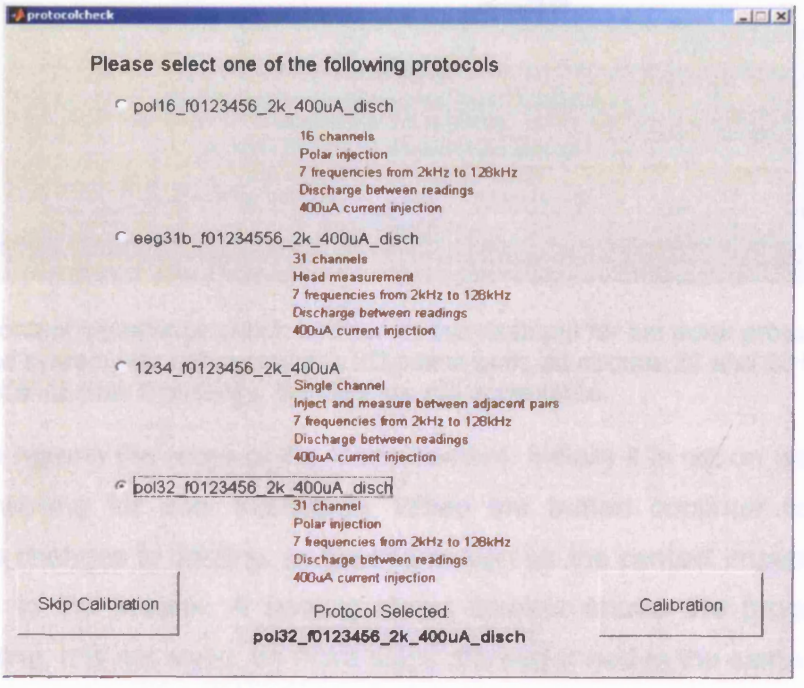

Figure B.5 Protocol selection window.

B.5 Contact impedance check

In this window a contact impedance check of the electrodes involved in the selected protocol is performed. The contact impedance is measured by performing 2-terminal measurements between adjacent electrodes and on the assumption that the transimpedance of the body is negligible respect to it. This is then displayed in Ω as one bar for each combination (the 1st bar is the contact impedance between electrodes 1-2, the 2nd between 2-3 and so on, Figure B.6). One expects that if for example electrode 3 has a problem then the contact impedance between 2-3 and 3-4 will be high (2nd and 3rd bars). Generally the contact impedance should be lower than 2kΩ. For simplicity the average value across frequency is displayed, but the lower frequencies have higher contact impedance than the higher.

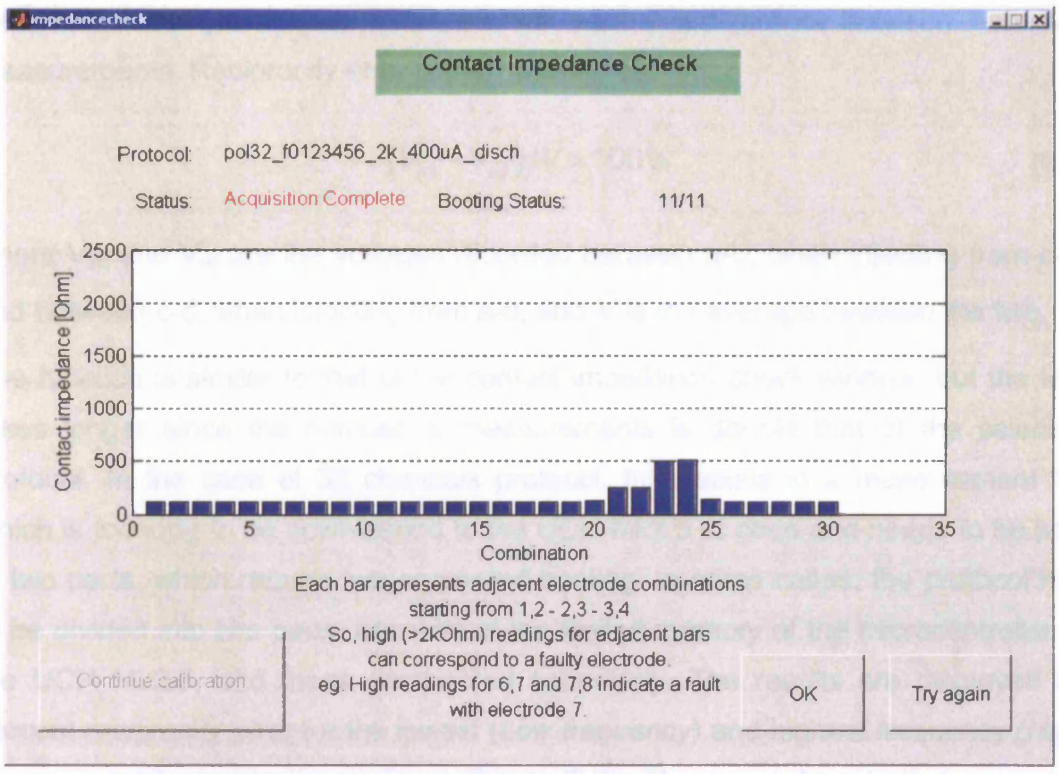

Figure B.6 Contact impedance check window. In this example for the polar protocol with 32 channels. The system was connected to a 2D saline tank, electrodes 22 and 23 have worse contact impedance than the others, but they are still acceptable.

A *status* tab reports the stage of the measurement. Initially it is set on *waiting* as the system is waiting for user instruction. When the button *continue calibration* is pressed this changes to *booting*, as the information for the contact impedance check are passed to the system. A *booting status* counter shows the progress of the booting routine, it is not serial, as more steps are performed in the same instruction. Then it goes to *acquiring* and at the end to *acquisition complete*.

If the user is happy with the contact impedance measurement, they can proceed to the reciprocity check by pressing *OK*, otherwise they can perform the impedance check again. In this case the booting is not needed as it is clear from the booting status tab.

B.6 Reciprocity check

In this window, a reciprocity check on the combinations used in the selected protocol is performed. This test is based on the reciprocity theorem (Chapter 1); in a perfect system, the voltage measured from a pair of electrodes c-d, while injecting current from another pair a-b, is identical to the voltage measured between a-b, when injecting from c-d. In reality imbalance in the current injection and voltage measuring paths, such as the resistance and capacitance of the different electrode leads,

electrode/electrolyte/skin interfaces, etc. will result in a difference between these two measurements. Reciprocity error is then defined as:

$$(V_{ab} - V_{cd})/\bar{V} \times 100\% \quad \text{(0-1)}$$

where V_{ab} and V_{cd} are the voltages recorded between a-b, when injecting from c-d, and between c-d, when injecting from a-b, and $\bar{V}$ is the average between the two.

The function is similar to that of the contact impedance check window, but the test takes longer since the number of measurements is double that of the selected protocol. In the case of 32 channels protocol, this results in a measurement list which is too long to be downloaded to the UCH Mk2.5 at once and needs to be split in two parts, which require two separated booting. In some cases, the protocol has to be divided into two parts, because of the limited memory of the microcontroller of the UCH Mk2.5, and these are booted separately. The results are displayed as percent reciprocity error for the lowest (*Low frequency*) and highest frequency (*High frequency*) adopted in the protocol (Figure B.7). These can be scrolled using the buttons *next* and *prev*(ious) in the bottom right of the graph. As low frequencies are less influenced by the stray capacitance imbalance the reciprocity error for these is expected to be lower than for the high frequencies. So the error should be below 10% for frequencies of about 100 kHz and lower for frequencies of about 2 kHz on a tank; this figure may be worse on human subjects (Yerworth et al. 2002). Since the test is long, depending on the number of electrodes employed (for example 2'30" for 258 combination protocol), the user can skip it by pressing *OK* directly.

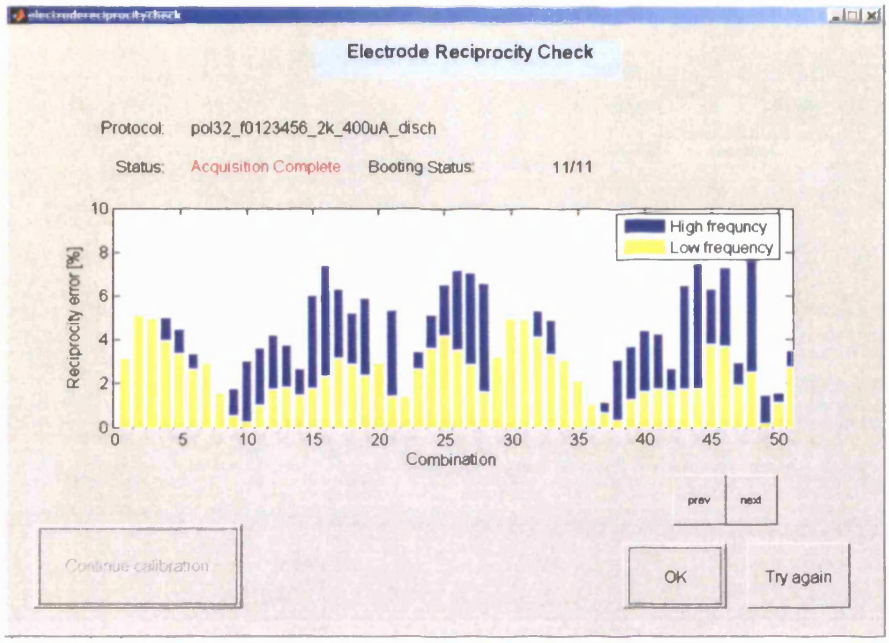

Figure B.7 Electrode reciprocity check window.

B.7 Data collection

This part of the GUI is different according to the kind of test the user is about to perform. This can be on a tank, on a human with predetermined time of acquisition or on a human with continuous acquisition.

B.7.1 Tank data collection

This window is designed to easily allow successive data set collections with user defined length and name, which are input in the panel on the top right corner of the window. After the acquisition is performed, the mean boundary voltage across time and frequency are displayed for each tetrapolar combination (Figure B.8).

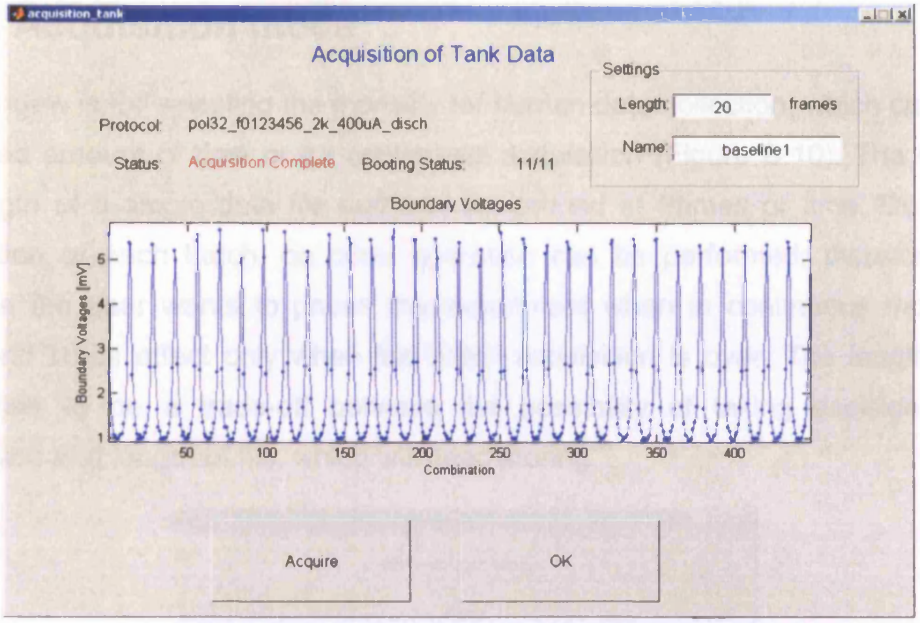

Figure B.8 Tank data acquisition window. In this example the boundary voltages of a 2D polar protocol on a cylindrical phantom are shown.

The data are saved in a 3D matrix as [frequencies x channels x combinations] with the name assigned by the user. This is stored in a directory named *mat files* inside a folder with the general name *protocol system_type tank_type test_type (date)* under *Data Tank* (Figure B.9). Other acquisitions can be run changing the name of the file.

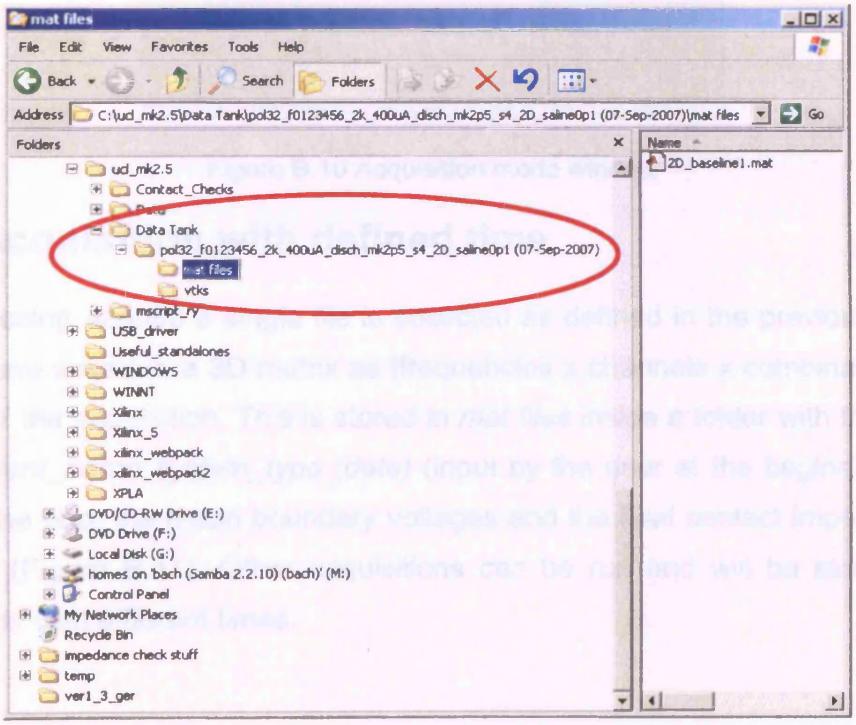

Figure B.9 Saving location of tank data

B.7.2 Acquisition mode

This window is for selecting the modality for human data collection, which can be for a defined amount of time or for continuous acquisition (Figure B.10). The batch is the length of a single data file and can be defined in frames or time. During the acquisition of each batch, no other operation can be performed; therefore if for example the user wants to pause the experiment when in continuous mode, the command takes effect only when the batch acquisition is over. The length of the batch has to be a trade-off between the possibility of taking decision during acquisition and length of file, which will need storing.

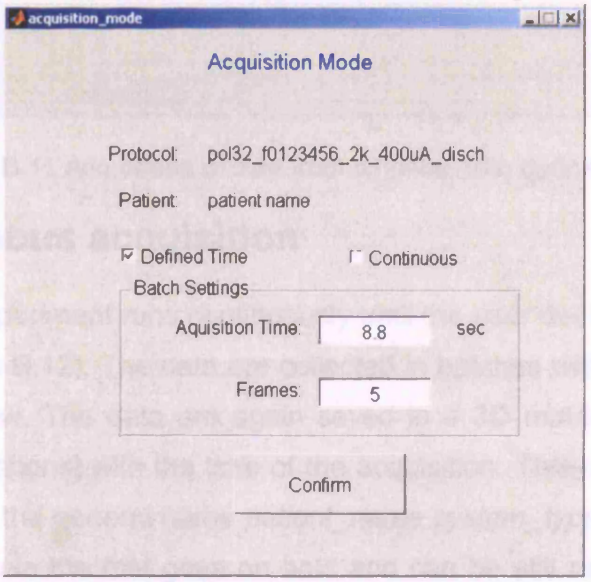

Figure B.10 Acquisition mode window

B.7.3 Acquisition with defined time

When pressing *acquire* a single file is collected as defined in the previous window. The data are saved in a 3D matrix as [frequencies x channels x combinations] with the time of the acquisition. This is stored in *mat files* inside a folder with the general name *patient_name system_type (date)* (input by the user at the beginning) under *Data*. At the end, the mean boundary voltages and the final contact impedance are displayed (Figure B.11). Other acquisitions can be run and will be stored in the same folder with different times.

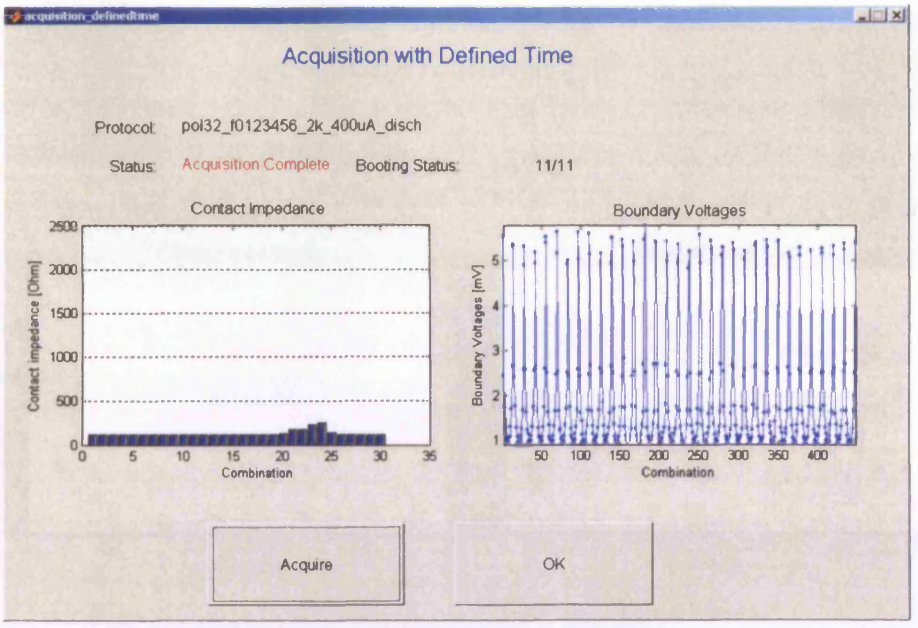

Figure B.11 Acquisition of data from a human with defined time.

B.7.4 Continuous acquisition

In this mode the experiment runs continuously until the user decide to stop or pause the process (Figure B.12). The data are collected in batches with the length input in the previous window. The data are again saved in a 3D matrix as [frequencies x channels x combinations] with the time of the acquisition. This is stored in *mat files* inside a folder with the general name *patient_name system_type (date)* under *Data*. When pressing *pause* the test goes on hold and can be still resumed by pressing *resume*, while when pressing *stop* the system perform one last contact impedance check before resetting the acquisition. These buttons can be pressed at any time, but the system will respond only when either booting is completed or the current batch has been collected. Every 10 batches collected, the mean boundary voltages of the last batch are displayed and contact impedance check is performed. The data stored can then be fetched by the user in a second time and fed into the algorithm for image reconstruction.

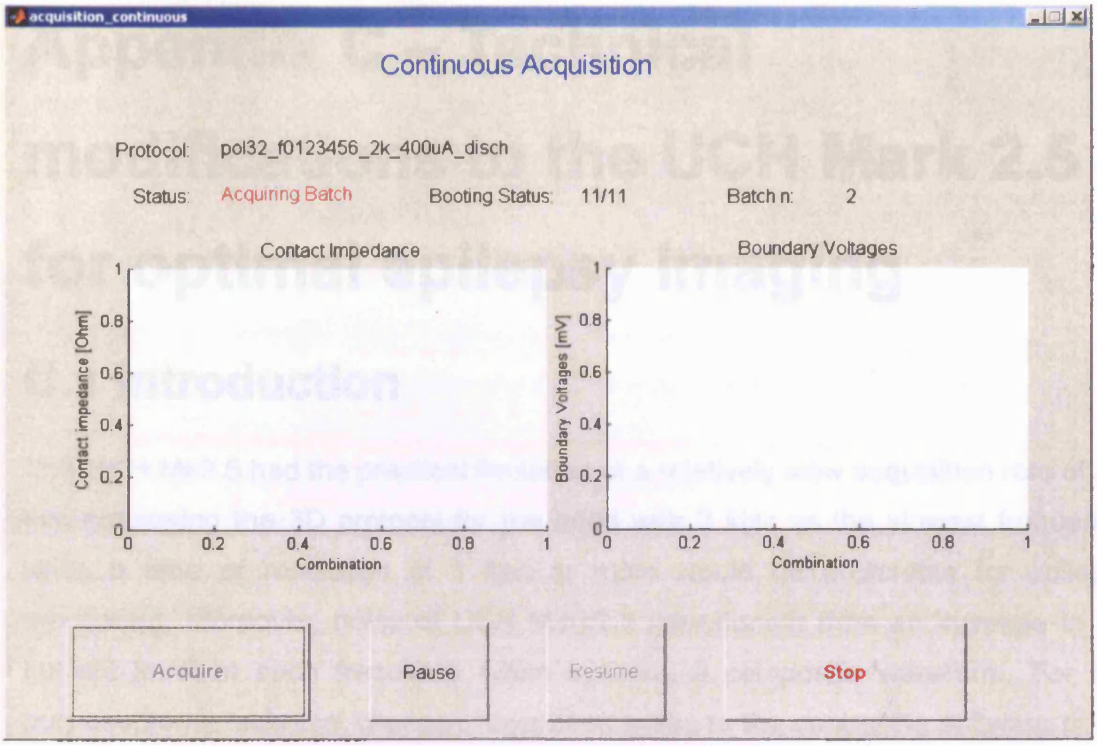

Figure B.12 Continuous acquisition window, while acquiring.

Appendix C – Technical modifications to the UCH Mark 2.5 for optimal epilepsy imaging

C.1 Introduction

The UCH Mk2.5 had the practical limitation of a relatively slow acquisition rate of 2.2 sec employing the 3D protocol for the head with 2 kHz as the slowest frequency, while a time of resolution of 1 sec or more would be preferable for epilepsy monitoring. Moreover, noise of UCH Mark2.5 may benefit from an increase in the current level at each frequency when injecting a composite waveform. For this purpose some technical changes have been made to the controlling software of the UCH Mark2.5 and to the hardware to increase the frame rate to 1 sec and to increase the current level to 400 μA at each frequency. Each section is accompanied by technical details of the code modifications which are intended to be of assistance to any other users who would like to implement additional modifications.

C.2 Software modifications

The UCH Mk2.5 can measure the impedance at 30 frequencies between 20 Hz and 1.6 MHz, driving a current in three sequentially applied packets (époques), which contain ten summed sine waves each (McEwan et al. 2006). This system was designed for acute stroke imaging, as modelling work indicated that sensitivity to the changes in ischemic brain would be maximal over this frequency range (Horesh et al. 2005). This required the design of an optimal applied current pattern over frequency, which exploited the frequency range, but which was not uncomfortable for the patient and met the terms of safety standards (Romsauerova et al. 2006a). With this chosen waveform extending down to 20 Hz, a single frame took about 5 min to collect. However for stroke studies the acquisition time is not a concern as the lesion is not changing over seconds; therefore a slow frame rate was acceptable. On the other hand, in the case of epilepsy study, a faster frame rate is preferable as the impedance changes related to seizures may occur across few seconds, while having a broad frequency spectrum is not crucial, as this EIT

application employs time difference imaging. Besides reducing the number of frequencies per époque would allow to increase the current level at each frequency. An optimized waveform was then generated with the best trade off between frequency spectrum width, speed and current level at each frequency which complied with the safety standard. The factors that were taken into account were that:

1. changes due to epilepsy decrease when frequency increases;
2. higher frequencies are more subject to error due to stray capacitance and are more difficult to calibrate;
3. low frequency have slower acquisition time;
4. the less frequency are used in a composite waveform, the higher is the current level for each frequency, when the peak-to-peak is fixed;
5. contact impedance decreases with frequency (Table C.1).

Table C.1 Impedance (Ω) measured in 2-terminal mode with the Hewlett-Packard 4284A impedance analyser on the head of a human volunteer without and with skin abrasion between distant and close electrodes (Figure C.1).

Frequency	Not abraded		Abraded	
	1-4	*2-3*	*1-4*	*2-3*
1 kHz	3.6 k	2.6 k	939	1.5
5 kHz	1.1 k	0.9 k	759	715
10 kHz	788	703	649	576
20 kHz	644	591	550	495
50 kHz	560	506	476	433
70 kHz	514	484	446	417
100 kHz	493	466	430	304

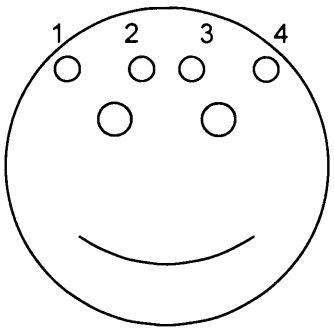

Figure C.1 Electrode positions

C.2.1 Frequency spectrum reduction and software current level increase

Changes due to epilepsy are higher for lower frequencies, but the current that can be injected and acquisition speed are proportional to the frequency. With the hardware and software modifications described in this appendix, a current of 400μA ($283\mu A_{rms}$) could be injected at each frequency above 2.8 kHz, according to the safety regulations (Figure C.2). With these settings the highest changes from standing voltages above 1mV are expected around 3.2 kHz (Figure C.3); therefore it was considered of no use to go below 2 kHz and to go above 128 kHz. This allowed increasing the current at each frequency up to 33% (23% was chosen to avoid saturation problem) via software, maintaining the peak-to-peak within 2^{16}, which is the full scale deflection (FSD) of the 16 bits DAC of the UCH Mk2.5.

> Technical note: The current waveform is defined into two separate functions. The first defines the composite waveform for each époque formed by the sum of a base frequency and up to 9 octave incremented frequencies. The second defines the base frequency of this composite waveform for up to 3 époques.
>
> SINEGEN2_RY_2.CPP is the function that generates the waveform. The *maximal* amplitude at each frequency is defined by the value *scale* at line 118. When using all 10 frequencies *scale* = *5880*, this uses the FSD of the DAC. If the number of frequencies is reduced to 7, then could be *scale* = *7800* (33% larger), as it would give the same peak-to-peak value. However *scale* = *7200* was used (23% larger) to avoid saturation problem. The amplitude of each frequency in each époque is defined in lines 66-75. At each frequency is associate a number which

goes from 0 to 1, where 0 means that the frequency is not used and 1 that the frequency has amplitude = *scale*. For example, this configuration:

```
freqs[0]=1;
freqs[1]=1;
freqs[2]=1;
freqs[3]=1;
freqs[4]=1;
freqs[5]=1;
freqs[6]=1;
freqs[7]=0;
freqs[8]=0;
freqs[9]=0;
```

means that only the first 7 frequencies of the époque are used, and have amplitude = *scale*.

The base frequency of each époque is defined in *mk35main_lf.asm*.

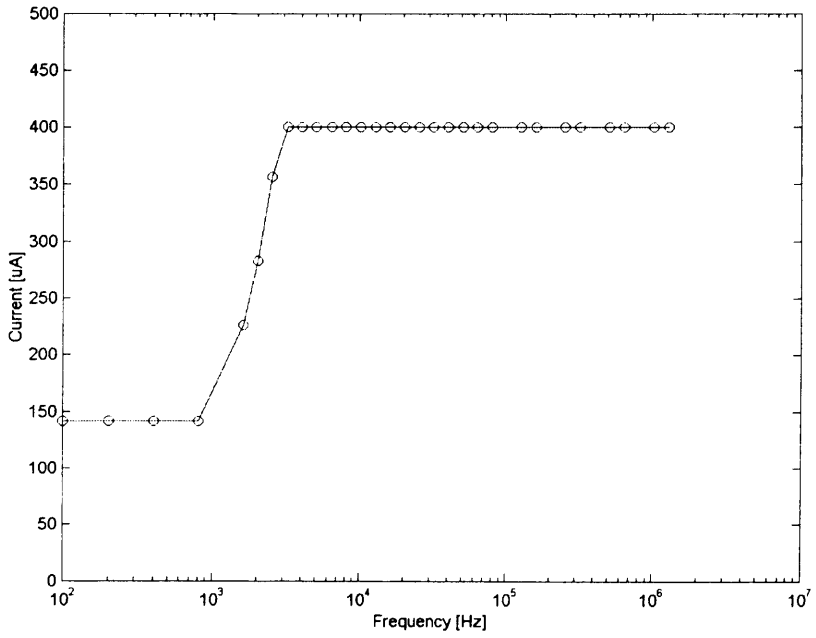

Figure C.2 Current injected in a composed waveform with the modified UCH Mk2.5.

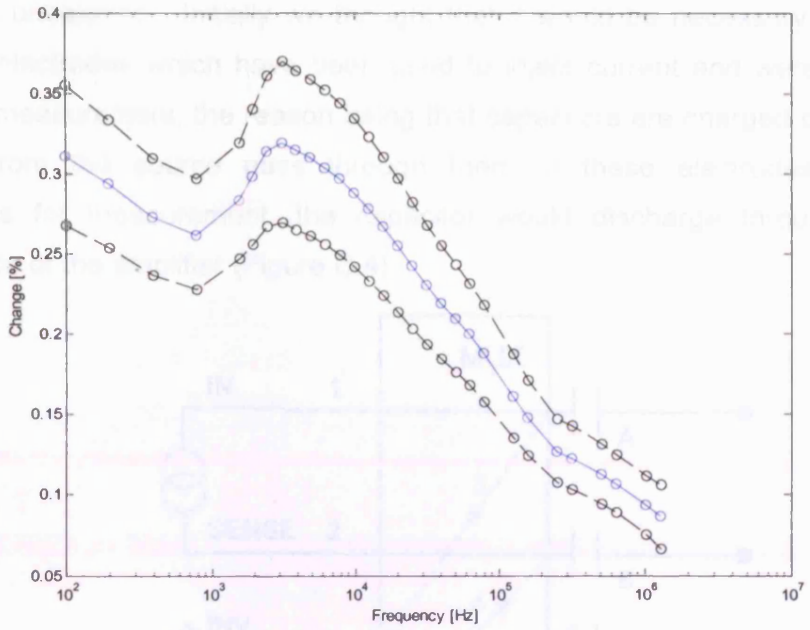

Figure C.3 Mean top 1% (±SD) changes for temporal lobe epilepsy from standing voltages above 1mV.

C.2.2 Acquisition rate increase

To increase the acquisition rate:

1. the number of époques was reduced from 3 to 1, therefore only up to 10 frequencies could be recorded;
2. the number of frequencies per époque was reduced from 10 to 7;
3. the amount of information the computer is expecting to receive was reduced and the latency of the USB connection was speeded-up from 16ms to 5ms;
4. the information transmission to the PC was overlapped with the successive data collection to avoid dead periods.

This resulted in a frame rate of 1.3-1.4frames/sec, but this was slowed down by the introduction of a discharge step (see below) before each transimpedance measurement to 1 frame in 0.9 seconds.

C.2.3 Discharge step

A discharge step was introduced to discharge all the electrodes to be used in a tetrapolar measurement. This was to avoid slow oscillations in the voltage measurement attributed to discharging of the DC blocking capacitor and of the electrode-dielectric interface. These would be charged if a DC offset is present between the beginning and the end of each measurement period or if the current

source is unbalance. Initially we thought that it would be necessary to discharge only the electrodes which have been used to inject current and were going to be used for measurement, the reason being that capacitors are charged only when the current from the source pass through them. If these electrodes were used afterwards for measurement, the capacitor would discharge through the input impedance of the amplifier (Figure C.4).

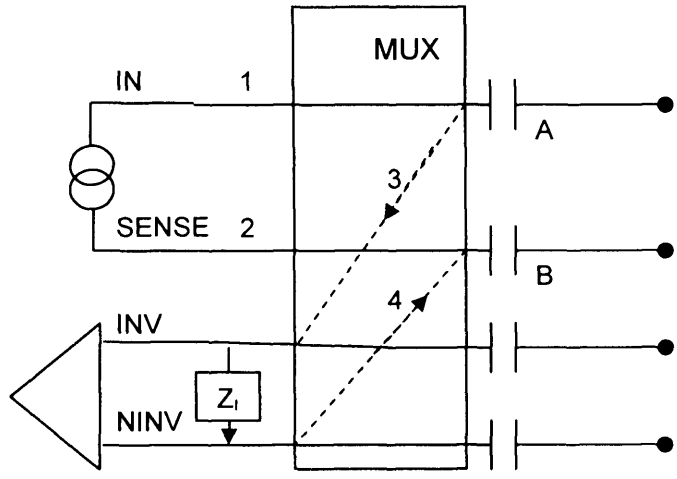

Figure C.4 Discharge problem. After line 1 and 2 have been used for current injection, capacitors A and B may be charged by DC offsets. When line 3 and 4 are created for measurement, this voltage difference drives a current through the input impedance of the amplifier, influencing the real transimpedance measurement.

Nevertheless, experimentally, we found that no matter whether the electrodes used for a recording have been previously used or not for injection, a discharge was present and every time of a different amount. Therefore, since discharging all the electrodes was not requesting extra-time and the code was simpler; all the electrodes were discharged before each measurement (Figure C.5). To avoid excessive slowing of the acquisition, the discharge was not added as an extra measurement, but as 1ms in which all the electrodes that are going to be used for the recording are connected to ground.

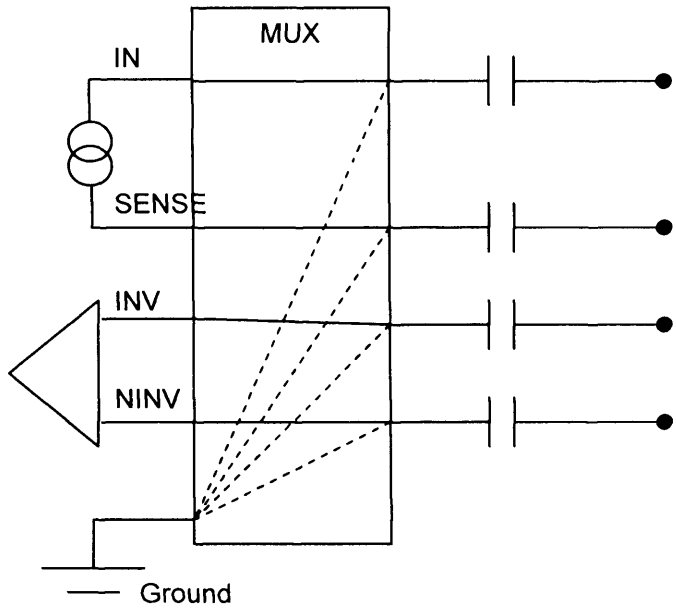

Figure C.5 Discharge process. Before any measurement all the connections in the diagram are created for 1 ms, then the dashed connections are closed and the measurement can start.

Technical note: This is done modifying the C++ function that generates the steps for the DSP code from the list of measurement, splitting each recording into a discharge phase and measuring phase, and the ASSEMBLER main source function which generates the file to be uploaded in the micro-controller and which has to expect the discharging phase.

Protocol Generator Function

---- Addresses of the electrodes (output of the MUX) ----

const int elec_lines[] = {...};

...

/* main function */

void main(int argcnt, char *argptr[])

{...

---- Here starts the main loop which generates the steps of the protocol of the .asm file form the .prt list.

Each measurement from the .prt list generates 2 groups of instructions: one for the discharge and one for the measurement. ----

for (j=0;j<2*leng;j++){

---- Each group of instructions of the protocol for a measurement or discharge conclude the previous group in the first step... ----

---- ... if j is even the previous group of instruction just broke the connection between the measuring amp and the ground and sets a measurement ----

```
if ((j%2) == 0) {
    end_step=0x1000;
}
```

---- ...if j is odd the previous group of instructions set the connection for discharging the measuring electrodes and sets a discharge ----

```
else {
    end_step=0x1800;
}
```

---- NOTE. end_step is set to 0x0000 the first time a break or make function is called ----

```
if ((j%2) == 0) {
```

---- Read in protocol step from the .prt file (excel list) ----

...

---- Connect the electrodes which are about to be used as recording to the ground for discharging ----

```
    xpoint_make_lines(ni_lines, GND1,elecs[4]);
    xpoint_make_lines(i_lines, GND1,elecs[3]);
```

---- Connect the amplifier to the same electrodes, therefore to ground, to not measure anything ----

```
    xpoint_make_lines(ni_lines, NINV, elecs[4]);
    xpoint_make_lines(i_lines, INV, elecs[3]);
```

---- Break the OLD connection of the amplifier if different from the NEW ones ---

```
    if (ni_lines_prev != ni_lines) {
      xpoint_break_lines(ni_lines_prev, NINV, non_inverting);
    }
    if (i_lines_prev != i_lines) {
    xpoint_break_lines(i_lines_prev, INV, inverting);
    }
```

```
        ---- Same thing for the current source ----

      xpoint_make_lines(src_lines, CURIN, elecs[2]);
      xpoint_make_lines(sns_lines, CSENSE,elecs[1]);

      if (src_lines_prev != src_lines) {
      xpoint_break_lines(src_lines_prev, CURIN, source);
      }
      if (sns_lines_prev != sns_lines) {
      xpoint_break_lines(sns_lines_prev, CSENSE, sense);
      }

   }
   else {
        ---- In case a measurement has to be done, just break the connection of the
        measuring amp to the ground ----

      xpoint_break_lines(ni_lines, GND1,elecs[4]);
      xpoint_break_lines(i_lines, GND1,elecs[3]);

        ---- Update simple maps to reflect the new status ----

        ---- Save the NEW line ----
       }
}
```

DSP Code main source function

RunLoop

...Some operations

Initialise the pointer to the buffer which contains the steps of the protocol

```
    STM     #PRTBuff,AR7    ;Load pointer to normal sequence buffer
    STM     #0000,ar6       ;Load 'not low'
    XC      2,BIO           ;if bio low (high) ...compliance
    STM     #ComBuff,AR7    ;Load pointer to copliance sequence
buffer
    XC      2,BIO           ;if bio low (high) ...compliance
    STM     #LowGain,ar6    ;Load 'low gain'
```

RunStep *Loop which runs each measurement*

...Some operations

LoadStep

...Some operations

1000 means that the preparation of the measurement or discharge is finished

```
LD      #1000h,a        ;Prepare to check if loadstep complete
AND     *AR7,a          ;strip loadstep flag
BC      LoadStep,aeq    ;loop back if flag =0 not finding right bit yet
```

...Some operations

Load the value 800 in 'a' which is used as a label to see whether to perform the measurement

```
LD      #800h,a     ;800 means no dishcharge: go measure
AND     *AR7,a      ;Check discharge flag increment ar7
```

If 800 IS NOT in the step, then skip to perform the measurement

```
BC      no_dis,aeq  ; if not discharge, skip to no-dis ;21/02/05
```

If 800 IS in the step then perform the discharge, which is waiting 1ms with the connection created in the previous operations

```
RPT     #50000      ;64000 (.64ms) works, 48000(0.48ms) settles after 1000 frames, 32000 (0.3ms) doesn't work
NOP                 ;need tim_divie=65 for 64000  60 for 48000
RPT     #50000      ;need time_divide=70
NOP                 ;21/02/05
```

After waiting 1ms go unconditionally to the beginning of the loop

```
B       RunStep
```

...Some operations

```
no_dis              ;21/02/05
    RSBX    CPL
    RSBX    OVM     ; A and B accumulators overflow normally
    RSBX    FRCT    ; fractional mode is off
    SSBX    SXM     ;Cause sign extension to occur
```

Obtains ADC samples and generates drive waveform

MK35RecX ADCport, ADCBuf, DACport, DACBuf, nSamples, EpochPad1

Analyse the data with slow FFT on sampled data

MK35SFFT FFT0Res, nSamples

...Some operations in case more than 1 époque

Perform the measurement

```
MK35Qdat    FFT0Res ; ADCBuf;  FFT0Res ;

LD          #2000h,b      ;Prepare to check if RunStep complete
AND         *AR7,b;strip RunStep flag
BC          RunStep,beq   ;loop back if flag =0
NOP
b           RunLoop       ;MainLoop change 7/1/02 to enable reset
```

C.2 Hardware modification

The current and the gain of the amplifiers were optimized for a transimpedance range between 8-70 Ω with a contact impedance of more than 2 kΩ. This was because of the low frequencies planned to use for the stroke application, which ranged from 20 Hz to 1.6 MHz (McEwan et al. 2006).

The voltage rails of the driving amplifier of the Howland current source are ±3.4V (from the data sheet), but to avoid saturation or non-linearities we considered ±3V. The contact impedance at 2 kHz and above is between 1.5 kΩ and 715 Ω (Table C.1). Therefore the current source should be delivering a maximum of I = 6V/1.5kΩ = 4 mA_{p-p}.

The delivered current is linearly related to $1/R_x$ (Figure C.6). Since the current delivered originally was 1.5mA_{p-p}, R_x could be decreased 4/1.5 = 2.7 times, from the original 750 to 280 Ω, we decreased it by 2.5 times adding 499 Ω in parallel to 750 Ω. With these settings the current across 1.5 kΩ and 1 kΩ resistor was 3.6 mA_{p-p}, as expected.

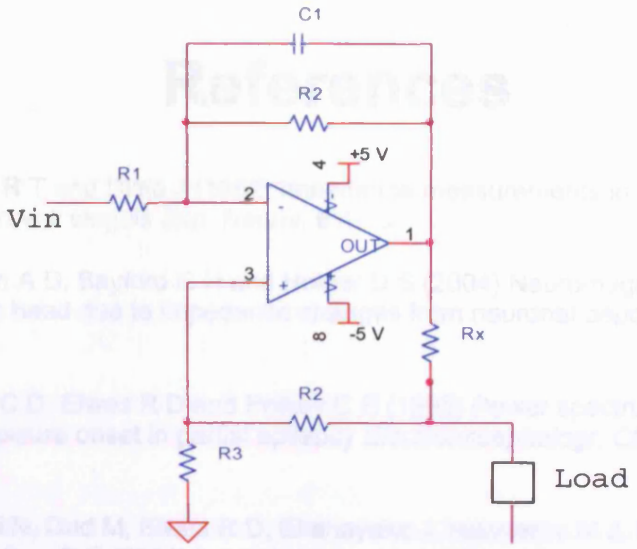

Figure C.6 Howland current source, employed in the UCH Mark2.5.

Consequently the gain of the measuring amplifiers had to be decreased at least by 2.5 times. The gain is given by $1+R_x/R_1$ (Figure C.7). With this configuration the voltage measurements were clipping with a transimpedance of 77 Ω, which was fine with the original components. This was probably due to the fact that in reality the original current was less than the theoretical 1.5 mA_{p-p}, because the higher frequencies were attenuated by the stray capacitance. Decreasing the gain by 3 times and the current to $3.3mA_{p-p}$ (resulting in the 400 μA at each frequency) via software (Section C.1) it was possible to measure transimpedance of 77 Ω, without clipping. This decrease was done adding 2.4 kΩ resistor in parallel to the original 5 kΩ resistor.

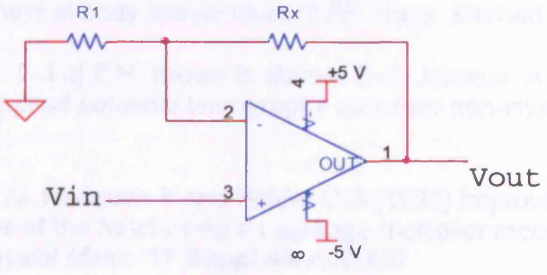

Figure C.7 Measuring amplifiers. The feedback resistors were reduced from 5 kΩ to 1.6 kΩ.

References

Adey W R, KADO R T and Didio J (1962) Impedance measurements in brain tissue of animals using microvolt singals *Exp. Neurol.* **5** 47-66

Ahadzi G M, Liston A D, Bayford R H and Holder D S (2004) Neuromagnetic field strength outside the human head due to impedance changes from neuronal depolarization *Physiol Meas.* **25** 365-78

Alarcon G, Binnie C D, Elwes R D and Polkey C E (1995) Power spectrum and intracranial EEG patterns at seizure onset in partial epilepsy *Electroencephalogr. Clin. Neurophysiol.* **94** 326-37

Alarcon G, Kissani N, Dad M, Elwes R D, Ekanayake J, Hennessy M J, Koutroumanidis M, Binnie C D and Polkey C E (2001) Lateralizing and localizing values of ictal onset recorded on the scalp: evidence from simultaneous recordings with intracranial foramen ovale electrodes *Epilepsia* **42** 1426-37

Allen P J, Josephs O and Turner R (2000) A method for removing imaging artifact from continuous EEG recorded during functional MRI *Neuroimage.* **12** 230-239

Allen P J, Polizzi G, Krakow K, Fish D R and Lemieux L (1998) Identification of EEG events in the MR scanner: the problem of pulse artifact and a method for its subtraction *Neuroimage.* **8** 229-39

Bagshaw A P et al. (2003) Electrical impedance tomography of human brain function using reconstruction algorithms based on the finite element method *Neuroimage.* **20** 752-64

Barber D C and Brown B H (1988) Errors in reconstruction of resistivity images using a linear reconstruction technique *Clin. Phys. Physiol Meas.* **9 Suppl A** 101-4

Barber D C and Brown B H (1989) Applied potential tomography *J. Br. Interplanet. Soc.* **42** 391-93

Baumann S B, Wozny D R, Kelly S K and Meno F M (1997) The electrical conductivity of human cerebrospinal fluid at body temperature *IEEE Trans. Biomed. Eng* **44** 220-223

Baxter A J, Mangnall Y F, Loj E H, Brown B, Barber D C, Johnson A G and Read N W (1988) Evaluation of applied potential tomography as a new non-invasive gastric secretion test *Gut* **29** 1730-1735

Bayford R H, Boone K G, Hanquan Y and Holder D S (1996) Improvement of the positional accuracy of EIT images of the head using a Lagrange multiplier reconstruction algorithm with diametric excitation *Physiol Meas.* **17 Suppl 4A** A49-A57

Bennett W R (1948) Spectra of quantized noise *Bell System Technical Journal* **27** 446-72

Binnie C D, Rowan A, Gutter T (1982) The 10-20 system. In: *A manual of Electroencephalographic Technology*, ed: Cambridge Univ.Press. pp 325-31.

Boone K, Lewis A M and Holder D S (1994) Imaging of cortical spreading depression by EIT: implications for localization of epileptic foci *Physiol Meas.* **15 Suppl 2a** A189-A198

Boone K G (1995) The possible use of applied potential tomography for imaging action potentials in the brain (PhD thesis, University College London)

Boone K G and Holder D S (1995) Design considerations and performance of a prototype system for imaging neuronal depolarization in the brain using 'direct current' electrical resistance tomography *Physiol Meas.* **16** A87-A98

Boone K G and Holder D S (1996) Current approaches to analogue instrumentation design in electrical impedance tomography *Physiol Meas.* **17** 229-47

Borsic A, Lionheart W R and McLeod C N (2002) Generation of anisotropic-smoothness regularization filters for EIT *IEEE Trans. Med. Imaging* **21** 579-87

Brown B H (2003) Electrical impedance tomography (EIT): a review *J. Med. Eng Technol.* **27** 97-108

Brown B H, Barber D C and Seagar A D (1985) Applied potential tomography: possible clinical applications *Clin. Phys. Physiol Meas.* **6** 109-21

Brown B H, Barber D C, Wang W, Lu L, Leathard A D, Smallwood R H, Hampshire A R, Mackay R and Hatzigalanis K (1994) Multi-frequency imaging and modelling of respiratory related electrical impedance changes *Physiol Meas.* **15 Suppl 2a** A1-12

Brown B H and Seagar A D (1987) The Sheffield data collection system *Clin. Phys. Physiol Meas.* **8 Suppl A** 91-97

Cheng K S, Simske S J, Isaacson D, Newell J C and Gisser D G (1990) Errors due to measuring voltage on current-carrying electrodes in electric current computed tomography *IEEE Trans. Biomed. Eng* **37** 60-65

Cole K S and Cole R H (1941) Dispersion and absorpions in dielectrics. I. Alternating current characterisitcs *J. Chem. Phys.* **9** 341-51

Cole K S and Curtis H J (1939) Electrical impedance of the squid giant axon during activity *J. Gen. Physiol.* **22** 649-70

Cook R D, Saulnier G J, Gisser D G, Goble J C, Newell J C and Isaacson D (1994) ACT3: a high-speed, high-precision electrical impedance tomograph *IEEE Trans. Biomed. Eng* **41** 713-22

Dehghani H, Soni N, Halter R, Hartov A and Paulsen K D (2005) Excitation patterns in three-dimensional electrical impedance tomography *Physiol Meas.* **26** S185-S197

Elazar Z, KADO R T and Adey W R (1966) Impedance changes during epileptic seizures *Epilepsia* **7** 291-307

Engel J, Jr. (1993) Update on surgical treatment of the epilepsies. Summary of the Second International Palm Desert Conference on the Surgical Treatment of the Epilepsies (1992) *Neurology* **43** 1612-17

Engel J, Jr., Pedley TA (1998) *Epilepsy: a comprehensive textbook.* Philadelphia: Lippincott-Raven.

Eyuboglu B M, Brown B H and Barber D C (1989) In vivo imaging of cardiac related impedance changes *IEEE EMBS Magazine* **8** 39-45

Eyuboglu B M, Brown B H, Barber D C and Seagar A D (1987) Localisation of cardiac related impedance changes in the thorax *Clin. Phys. Physiol Meas.* **8 Suppl A** 167-73

Fabrizi L, Horesh L, McEwan A, and Holder D S (2006a) A feasibility study for imaging of epileptic seizures by EIT using a realistic FEM of the head *XII Conference on biomedical application of EIT (Seoul, Korea)*

Fabrizi L, McEwan A, Woo E and Holder D S (2007) Analysis of resting noise characteristics of three EIT systems in order to compare suitability for time difference imaging with scalp electrodes during epileptic seizures *Physiol Meas.* **28** S217-S236

Fabrizi L, Sparkes M, Horesh L, Perez-Juste Abascal J F, McEwan A, Bayford R H, Elwes R, Binnie C D and Holder D S (2006b) Factors limiting the application of Electrical Impedance Tomography for identification of regional conductivity changes using scalp electrodes during epileptic seizures in humans *Physiol. Meas.* **27** 163-74

Fitzgerald A J, Holder D S, Eadie L, Hare C and Bayford R H (2002) A comparison of techniques to optimize measurement of voltage changes in electrical impedance tomography by minimizing phase shift errors *IEEE Trans. Med Imaging* **21** 668-75

Foster K R, Schepps J L, Stoy R D and Schwan H P (1979) Dielectric properties of brain tissue between 0.01 and 10 GHz *Phys. Med Biol* **24** 1177-87

Foster K R and Schwan H P (1989) Dielectric properties of tissues and biological materials: a critical review *Crit Rev. Biomed. Eng* **17** 25-104

Fox J E, Bikson M and Jefferys J G (2004) Tissue resistance changes and the profile of synchronized neuronal activity during ictal events in the low-calcium model of epilepsy *J. Neurophysiol.* **92** 181-88

Frangi A F, Riu P J, Rosell J and Viergever M A (2002) Propagation of measurement noise through backprojection reconstruction in electrical impedance tomography *IEEE Trans. Med Imaging* **21** 566-78

Frerichs I (2000) Electrical impedance tomography (EIT) in applications related to lung and ventilation: a review of experimental and clinical activities *Physiol Meas.* **21** R1-21

Frerichs I, Dargaville P A, Dudykevych T and Rimensberger P C (2003) Electrical impedance tomography: a method for monitoring regional lung aeration and tidal volume distribution? *Intensive Care Med.* **29** 2312-16

Frerichs I, Hinz J, Herrmann P, Weisser G, Hahn G, Quintel M and Hellige G (2002) Regional lung perfusion as determined by electrical impedance tomography in comparison with electron beam CT imaging *IEEE Trans. Med. Imaging* **21** 646-52

Freund T F, Buzsaki G, Prohaska O J, Leon A and Somogyi P (1989) Simultaneous recording of local electrical activity, partial oxygen tension and temperature in the rat hippocampus with a chamber-type microelectrode. Effects of anaesthesia, ischemia and epilepsy *Neuroscience* **28** 539-49

FREYGANG W H, Jr. and LANDAU W M (1955) Some relations between resistivity and electrical activity in the cerebral cortex of the cat *J. Cell Physiol* **45** 377-92

Fricke H (1925) The electric capacity od suspensions with special reference to blood *J. Gen. Physiol.* **9** 137-52

Fricke H (1953) The Maxwell-Wagner dispersion in a suspension ellipsoids *J. Phys. Chem.* **57** 934-37

Gabriel S, Lau R W and Gabriel C (1996a) The dielectric properties of biological tissues: II. Measurements in the frequency range 10 Hz to 20 GHz *Phys. Med. Biol.* **41** 2251-69

Gabriel S, Lau R W and Gabriel C (1996b) The dielectric properties of biological tissues: III. Parametric models for the dielectric spectrum of tissues *Phys. Med. Biol.* **41** 2271-93

Gamba H R and Delpy D T (1998) Measurement of electrical current density distribution within the tissues of the head by magnetic resonance imaging *Med. Biol. Eng Comput.* **36** 165-70

Garreffa G et al. (2003) Real-time MR artifacts filtering during continuous EEG/fMRI acquisition *Magn Reson. Imaging* **21** 1175-89

Gibson A P (2000) Electrical impedance tomography of human brain function (PhD, University College London)

Gilad O., Horesh L., Ahadzi G.M., Bayford R.H., and Holder D.S. (2005) Could synchronized neuronal activity be imaged using Low Frequency Electrical Impedance Tomography (LFEIT)?

Gilad O, Ahadzi G M, Bayford R H, and Holder D S (2005a) Near DC conductivity change measurement of fast neuronal activity during human VEP *XI Conf. on Biomedical application of EIT (London, UK)*

Gilad O, Horesh L, Ahadzi G M, Bayford R H, and Holder D S (2005b) Could synchronized neuronal activity be imaged using Low Frequency Electrical Impedance Tomography (LFEIT)? *XI Conf. on Biomedical application of EIT (London, UK)*

Gilad O, Horesh L and Holder D S (2007) Design of electrodes and current limits for low frequency electrical impedance tomography of the brain *Med. Biol. Eng Comput.* **45** 621-33

Giouvanoudi A, Amaee W B, Sutton J A, Horton P, Morton R, Hall W, Morgan L, Freedman M R and Spyrou N M (2003) Physiological interpretation of electrical impedance epigastrography measurements *Physiol Meas.* **24** 45-55

Gisser D G, Isaacson D and Newell J C (1988) Theory and performance of an adaptive current tomography system *Clin. Phys. Physiol Meas.* **9 Suppl A** 35-41

Glickman Y A, Filo O, Nachaliel U, Lenington S, Amin-Spector S and Ginor R (2002) Novel EIS postprocessing algorithm for breast cancer diagnosis *IEEE Trans. Med. Imaging* **21** 710-712

Graham B M and Adler A (2007) Electrode placement configurations for 3D EIT *Physiol Meas.* **28** S29-S44

Griffiths H (1988) A phantom for electrical impedance tomography *Clin. Phys. Physiol Meas.* **9 Suppl A** 15-20

Griffiths H (1995) A Cole phantom for EIT *Physiol Meas.* **16** A29-A38

Griffiths H and Ahmed A (1987) Applied potential tomography for non-invasive temperature mapping in hyperthermia *Clin. Phys. Physiol Meas.* **8 Suppl A** 147-53

Grimnes S, Martinsen OG (2000) *Bioimpedance & Bioelectricity - Basics.* London: Academic Press.

Hahn G, Beer M, Frerichs I, Dudykevych T, Schroder T and Hellige G (2000) A simple method to check the dynamic performance of electrical impedance tomography systems *Physiol Meas.* **21** 53-60

Hahn G, Thiel F, Dudykevych T, Frerichs I, Gersing E, Schroder T, Hartung C and Hellige G (2001) Quantitative evaluation of the performance of different electrical tomography devices *Biomed. Tech. (Berl)* **46** 91-95

Halter R, Hartov A and Paulsen K D (2004) Design and implementation of a high frequency electrical impedance tomography system *Physiol Meas.* **25** 379-90

Halter R J, Hartov A and Paulsen K D (2007) Experimental justification for using 3D conductivity reconstructions in electrical impedance tomography *Physiol Meas.* **28** S115-S127

Handersen P C (1992) Numerical tools for analysis and solution of fredholm integral equations of the first kind *Inv. Problems* **8** 849-72

Harris N D, Suggett A J, Barber D C and Brown B H (1987) Applications of applied potential tomography (APT) in respiratory medicine *Clin. Phys. Physiol Meas.* **8 Suppl A** 155-65

Harris N D, Suggett A J, Barber D C and Brown B H (1988) Applied potential tomography: a new technique for monitoring pulmonary function *Clin. Phys. Physiol Meas.* **9 Suppl A** 79-85

Hinrichs H (1991) EEG data compression with source coding techniques *J. Biomed. Eng* **13** 417-23

Hoffman C J, Clark F J and Ochs S (1973) Intracortical impedance changes during spreading depression *J. Neurobiol.* **4** 471-86

Holder D S (1992a) Detection of cerebral ischaemia in the anaesthetised rat by impedance measurement with scalp electrodes: implications for non-invasive imaging of stroke by electrical impedance tomography *Clin. Phys. Physiol Meas.* **13** 63-75

Holder D S (1992b) Detection of cortical spreading depression in the anaesthetised rat by impedance measurement with scalp electrodes: implications for non-invasive imaging of the brain with electrical impedance tomography *Clin. Phys. Physiol Meas.* **13** 77-86

Holder D S (1992c) Electrical impedance tomography with cortical or scalp electrodes during global cerebral ischaemia in the anaesthetised rat *Clin. Phys. Physiol Meas.* **13** 87-98

Holder DS (2005) *Electrical Impedance Tomography.* Bristol and Philadelphia: Insitute of Physics Publishing.

Holder D S, Hanquan Y and Rao A (1996a) Some practical biological phantoms for calibrating multifrequency electrical impedance tomography *Physiol Meas.* **17 Suppl 4A** A167-A177

Holder D S, Rao A and Hanquan Y (1996b) Imaging of physiologically evoked responses by electrical impedance tomography with cortical electrodes in the anaesthetized rabbit *Physiol Meas.* **17 Suppl 4A** A179-A186

Horesh L (2006) Some novel approaches in modelling and image reconstruction for multi-frequency electrical impedance tomography of the human brain (PhD thesis, University College London, London)

Horesh L, Gilad O, Romsauerova A, Tizzard A, Arridge S, and Holder D S (2005) Stroke type detection by multi-frequency electrical impedance tomography MFEIT - a feasibility study *VI Conference on biomedical application of EIT (London, UK)*

Huigen E, Peper A and Grimbergen C A (2002) Investigation into the origin of the noise of surface electrodes *Med Biol Eng Comput* **40** 332-38

Hurt W D (1985) Multiterm Debye dispersion relations for permittivity of muscle *IEEE Trans. Biomed. Eng* **32** 60-64

IEC601-1 (1988) Medical Electrical Equipment Part I - General Requirements for Safety, International Electrotechnical Commission Committee T62

Ives J R, Warach S, Schmitt F, Edelman R R and Schomer D L (1993) Monitoring the patient's EEG during echo planar MRI *Electroencephalogr. Clin. Neurophysiol.* **87** 417-20

Jaspard F, Nadi M and Rouane A (2003) Dielectric properties of blood: an investigation of haematocrit dependence *Physiol Meas.* **24** 137-47

Jayakar P (1999) Invasive EEG monitoring in children: when, where, and what? *J. Clin. Neurophysiol.* **16** 408-18

Jossinet J (1996) Variability of impedivity in normal and pathological breast tissue *Med. Biol. Eng Comput.* **34** 346-50

Joy M L, Lebedev V P and Gati J S (1999) Imaging of current density and current pathways in rabbit brain during transcranial electrostimulation *IEEE Trans. Biomed. Eng* **46** 1139-49

Kolehmainen V, Vauhkonen M, Karjalainen P A and Kaipio J P (1997) Assessment of errors in static electrical impedance tomography with adjacent and trigonometric current patterns *Physiol Meas.* **18** 289-303

Kosterich J D, Foster K R and Pollack S R (1983) Dielectric permittivity and electrical conductivity of fluid saturated bone *IEEE Trans. Biomed. Eng* **30** 81-86

Kunst P W, de Vries P M, Postmus P E and Bakker J (1999) Evaluation of electrical impedance tomography in the measurement of PEEP-induced changes in lung volume *Chest* **115** 1102-6

Kuzniecky R I and Knowlton R C (2002) Neuroimaging of epilepsy *Semin. Neurol.* **22** 279-88

LaManna J C, McCracken K A, Patil M and Prohaska O J (1989) Stimulus-activated changes in brain tissue temperature in the anesthetized rat *Metab Brain Dis.* **4** 225-37

Lamont G L, Wright J W, Evans D F and Kapila L (1988) An evaluation of applied potential tomography in the diagnosis of infantile hypertrophic pyloric stenosis *Clin. Phys. Physiol Meas.* **9 Suppl A** 65-69

Latikka J, Kuurne T and Eskola H (2001) Conductivity of living intracranial tissues *Phys. Med. Biol.* **46** 1611-16

Lauritzen M (1994) Pathophysiology of the migraine aura. The spreading depression theory *Brain* **117 (Pt 1)** 199-210

Leao A A P (1944) Spreading depression of activity in cerebral cortex *J. Neurophysiol.* **7** 359-90

Lee S K, Yun C H, Oh J B, Nam H W, Jung S W, Paeng J C, Lee D S, Chung C K and Choe G (2003) Intracranial ictal onset zone in nonlesional lateral temporal lobe epilepsy on scalp ictal EEG *Neurology* **61** 757-64

Lindenblatt G and Silny J (2001) A model of the electrical volume conductor in the region of the eye in the ELF range *Phys. Med Biol* **46** 3051-59

Liston A D (2004) Models and image reconstruction in Electrical Impedance Tomography of human brain function (PhD, Middlesex University)

Liston A D, Bayford R H and Holder D S (2004) The effect of layers in imaging brain function using electrical impedance tomograghy *Physiol Meas.* **25** 143-58

Liston A D, Bayford R H, Tidswell A T and Holder D S (2002) A multi-shell algorithm to reconstruct EIT images of brain function *Physiol Meas.* **23** 105-19

Lux H D, Heinemann U and Dietzel I (1986) Ionic changes and alterations in the size of the extracellular space during epileptic activity *Adv. Neurol.* **44** 619-39

Malich A, Fritsch T, Anderson R, Boehm T, Freesmeyer M G, Fleck M and Kaiser W A (2000) Electrical impedance scanning for classifying suspicious breast lesions: first results *Eur. Radiol.* **10** 1555-61

Malonek D, Dirnagl U, Lindauer U, Yamada K, Kanno I and Grinvald A (1997) Vascular imprints of neuronal activity: relationships between the dynamics of cortical blood flow, oxygenation, and volume changes following sensory stimulation *Proc. Natl. Acad. Sci. U. S. A* **94** 14826-31

Mangnall Y F, Baxter A J, Avill R, Bird N C, Brown B H, Barber D C, Seagar A D, Johnson A G and Read N W (1987) Applied potential tomography: a new non-invasive technique for assessing gastric function *Clin. Phys. Physiol Meas.* **8 Suppl A** 119-29

Martin G, Martin R, Brieva M J and Santamaria L (2002) Electrical impedance scanning in breast cancer imaging: correlation with mammographic and histologic diagnosis *Eur. Radiol.* **12** 1471-78

Martinsen O G, Grimnes S and Mirtaheri P (2000) Non-invasive measurements of post-mortem chnages in dielectric properties of haddock muscle - a pilot study *J. Food Eng.* **43** 189-92

McArdle F J, Suggett A J, Brown B H and Barber D C (1988) An assessment of dynamic images by applied potential tomography for monitoring pulmonary perfusion *Clin. Phys. Physiol Meas.* **9 Suppl A** 87-91

McEwan A, Cusick G and Holder D S (2007) A review of errors in multi-frequency EIT instrumentation *Physiol Meas.* **28** S197-S215

McEwan A, Romsauerova A, Yerworth R, Horesh L, Bayford R and Holder D (2006) Design and calibration of a compact multi-frequency EIT system for acute stroke imaging *Physiol Meas.* **27** S199-S210

McEwan A, Yerworth R J, Horesh L, Bayford R H, and Holder D S (2005) Specification and calibration of a multi-frequency MEIT system for stroke *XI Conf. on Biomedical application of EIT (London, UK)*

Meeson S, Blott B H and Killingback A L (1996) EIT data noise evaluation in the clinical environment *Physiol Meas.* **17 Suppl 4A** A33-A38

Meeson S, Killingback A L and Blott B H (1995) The dependence of EIT images on the assumed initial conductivity distribution: a study of pelvic imaging *Phys. Med. Biol.* **40** 643-57

Metherall P (1998) Three dimensional electrical impedance tomography of the human thorax (PhD thesis, University of Sheffield)

Metherall P, Barber D C, Smallwood R H and Brown B H (1996) Three-dimensional electrical impedance tomography *Nature* **380** 509-12

Newton M R, Berkovic S F, Austin M C, Rowe C C, McKay W J and Bladin P F (1994) Ictal postictal and interictal single-photon emission tomography in the lateralization of temporal lobe epilepsy *Eur. J. Nucl. Med.* **21** 1067-71

Newton M R, Berkovic S F, Austin M C, Rowe C C, McKay W J and Bladin P F (1995) SPECT in the localisation of extratemporal and temporal seizure foci *J. Neurol. Neurosurg. Psychiatry* **59** 26-30

Nour S, Mangnall Y F, Dickson J A, Johnson A G and Pearse R G (1995) Applied potential tomography in the measurement of gastric emptying in infants *J. Pediatr. Gastroenterol. Nutr.* **20** 65-72

Oh T I, Lee E J, Woo E J, Kwon O, and Seo J K (2005) Multi-frequency EIT and TAS hardware development *XI Conf. on Biomedical application of EIT (London, UK)*

Oh T I, Woo E J and Holder D (2007) Multi-frequency EIT system with radially symmetric architecture: KHU Mark1 *Physiol Meas.* **28** S183-S196

Osterman K S, Kerner T E, Williams D B, Hartov A, Poplack S P and Paulsen K D (2000) Multifrequency electrical impedance imaging: preliminary in vivo experience in breast *Physiol Meas.* **21** 99-109

Perez-Juste Abascal J F (2007) Improvement in reconstruction algorithms for electrical impedance tomography of brain function (PhD, University College London)

Perez-Juste Abascal J F, Arridge S, Bayford R, and Holder D S (2005) Selecting the regularization parameter for linear Electrical Impedance Tomography of brain function *XI Conf. on Biomedical application of EIT (London, UK)*

Pethig R (1987) Dielectric properties of body tissues *Clin. Phys. Physiol Meas.* **8 Suppl A** 5-12

Piperno G, Frei E H and Moshitzky M (1990) Breast cancer screening by impedance measurements *Front Med. Biol. Eng* **2** 111-17

Polydorides N and Lionheart W.R.B. (2002) Toolkit for three-dimensional Electrical Impedance Tomography: a contribution to the Electrical Impedance Tomography and Diffuse Optical Reconstruction software project. *Mea. Sci. Technol.* **13** 1871-83

Polydorides N and Lionheart W R B (2002) Toolkit for three-dimensional Electrical Impedance Tomography: a contribution to the Electrical Impedance Tomography and Diffuse Optical Reconstruction software project. *Mea. Sci. Technol.* **13** 1871-83

PORTER R, Adey W R and KADO R T (1964) Measurement of electrical impedance in the human brain *Neurology* **14** 1002-12

Porter R J, Sato S (1993) Prolonged EEG and video monitoring in diagnosis of seizure disorders. In: *Electroencephalography - Basic principles, Clinical Application, and Related Fields*, eds: Niedermeyer E., da Silva F.L. Williams & Wilkins, pp 729-38.

Quarato P P et al. (2005) Temporal lobe epilepsy surgery: different surgical strategies after a non-invasive diagnostic protocol *J. Neurol. Neurosurg. Psychiatry* **76** 815-24

Rabbat A (1990) Tissue resistivity., ed: Webster JG. Bristol and New York: Galliard Printers Ltd.

Ramachandran P (2003) Scientific data visualization with MayaVi *Cnf. SciPy: Python for scientific computing (Pasadena, CA)*

Ranck Jr J B (1964) Specific impedance of cerebral cortex during spreading depression, and an analysis of neuronal, neuroglial, and interstitial contributions *Exp. Neurol.* **9** 1-16

Ranck J B, Jr. (1963a) Analysis of specific impedance of rabbit cerebral cortex *Exp. Neurol.* **7** 153-74

Ranck J B, Jr. (1963b) Specific impedance of rabbit cerebral cortex *Exp. Neurol.* **7** 144-52

Ranck J B, Jr. and BEMENT S L (1965) The specific impedance of the dorsal columns of cat: an anisotropic medium *Exp. Neurol.* **11** 451-63

Rao A (2000) Electrical Impedance Tomography of brain activity: studies into its accuracy and physiological mechanisms (PhD thesis, University College London)

Romsauerova A, McEwan A and Holder D S (2006a) Identification of a suitable current waveform for acute stroke imaging *Physiol Meas.* **27** S211-S219

Romsauerova A, McEwan A, Horesh L, Yerworth R, Bayford R H and Holder D S (2006b) Multi-frequency electrical impedance tomography (EIT) of the adult human head: initial findings in brain tumours, arteriovenous malformations and chronic stroke, development of an analysis method and calibration *Physiol Meas.* **27** S147-S161

Rosenow F and Luders H (2001) Presurgical evaluation of epilepsy *Brain* **124** 1683-700

Rush S and Driscoll D A (1968) Current distribution in the brain from surface electrodes *Anesth. Analg.* **47** 717-23

Russell G S, Jeffrey E K, Poolman P, Luu P and Tucker D M (2005) Geodesic photogrammetry for localizing sensor positions in dense-array EEG *Clin. Neurophysiol.* **116** 1130-1140

Saulnier G J (2005) EIT instrumentation. In: *Electrical Impednace Tomography: methods, hystory, and applications*, ed: Holder DS. Bristol: Institute of physics publishing.

Saulnier G J, Ross A S and Liu N (2006) A high-precision voltage source for EIT *Physiol Meas.* **27** S221-S236

Schneider I D, Kleffel R, Jennings D and Courtenay A J (2000) Design of an electrical impedance tomography phantom using active elements *Med Biol Eng Comput* **38** 390-394

Schwan H P (1957) Electrical properties of tissue and cell suspensions *Adv. Biol. Med. Phys.* **5** 147-209

Seagar A D, Barber D C and Brown B H (1987) Theoretical limits to sensitivity and resolution in impedance imaging *Clin. Phys. Physiol Meas.* **8 Suppl A** 13-31

Seagar A D and Brown B H (1987) Limitations in hardware design in impedance imaging *Clin. Phys. Physiol Meas.* **8 Suppl A** 85-90

Seeck M et al. (1998) Non-invasive epileptic focus localization using EEG-triggered functional MRI and electromagnetic tomography *Electroencephalogr. Clin. Neurophysiol.* **106** 508-12

SHALIT M N (1965) The effect of Metrazol on the hemodynamics and impedance of the cat's brain cortex *J. Neuropathol. Exp. Neurol.* **24** 75-84

Sierpowska J, Hakulinen M A, Toyras J, Day J S, Weinans H, Jurvelin J S and Lappalainen R (2005) Prediction of mechanical properties of human trabecular bone by electrical measurements *Physiol Meas.* **26** S119-S131

Sierpowska J, Toyras J, Hakulinen M A, Saarakkala S, Jurvelin J S and Lappalainen R (2003) Electrical and dielectric properties of bovine trabecular bone--relationships with mechanical properties and mineral density *Phys. Med. Biol.* **48** 775-86

Sijbers J, Michiels I, Verhoye M, Van Audekerke J, Van der L A and Van Dyck D (1999) Restoration of MR-induced artifacts in simultaneously recorded MR/EEG data *Magn Reson. Imaging* **17** 1383-91

Sinton A M, Brown B H, Barber D C, McArdle F J and Leathard A D (1992) Noise and spatial resolution of a real-time electrical impedance tomograph *Clin. Phys. Physiol Meas.* **13 Suppl A** 125-30

Smallwood R H, Hampshire A R, Brown B H, Primhak R A, Marven S and Nopp P (1999) A comparison of neonatal and adult lung impedances derived from EIT images *Physiol Meas.* **20** 401-13

Smallwood R H, Mangnall Y F and Leathard A D (1994) Transport of gastric contents *Physiol Meas.* **15 Suppl 2a** A175-A188

Smit H J, Vonk N A, Marcus J T, Boonstra A, de Vries P M and Postmus P E (2004) Determinants of pulmonary perfusion measured by electrical impedance tomography *Eur. J. Appl. Physiol* **92** 45-49

Somjen G G (2001) Mechanisms of spreading depression and hypoxic spreading depression-like depolarization *Physiol Rev.* **81** 1065-96

Somjen GG (2004) *Ions in the brain.* New York: Oxford University Press, Inc.

Soni N K, Paulsen K D, Dehghani H and Hartov A (2006) Finite element implementation of Maxwell's equations for image reconstruction in electrical impedance tomography *IEEE Trans. Med Imaging* **25** 55-61

Tao J X, Baldwin M, Ray A, Hawes-Ebersole S and Ebersole J S (2007) The impact of cerebral source area and synchrony on recording scalp electroencephalography ictal patterns *Epilepsia* **48** 2167-76

Thomas D C, McArdle F J, Rogers V E, Beard R W and Brown B H (1991) Local blood volume changes in women with pelvic congestion measured by applied potential tomography *Clin. Sci. (Lond)* **81** 401-4

Tidswell A T (2004) Functional electrical impedance tomography of adult and neonatal brain function (Phd, University College London)

Tidswell A T, Bagshaw A P, Holder D S, Yerworth R J, Eadie L, Murray S, Morgan L and Bayford R H (2003a) A comparison of headnet electrode arrays for electrical impedance tomography of the human head *Physiol Meas.* **24** 527-44

Tidswell A T, Bagshaw A P, Holder D S, Yerworth R J, Eadie L, Murray S, Morgan L and Bayford R H (2003b) A comparison of headnet electrode arrays for electrical impedance tomography of the human head *Physiol Meas.* **24** 527-44

Tidswell A T, Gibson A, Bayford R H and Holder D S (2001a) Validation of a 3D reconstruction algorithm for EIT of human brain function in a realistic head-shaped tank *Physiol Meas.* **22** 177-85

Tidswell T, Gibson A, Bayford R H and Holder D S (2001b) Three-dimensional electrical impedance tomography of human brain activity *Neuroimage.* **13** 283-94

Tizzard A, Horesh L, Yerworth R J, Holder D S and Bayford R H (2005) Generating accurate finite element meshes for the forward model of the human head in EIT *Physiol Meas.* **26** S251-S261

VAN HARREVELD A and Ochs S (1957) Electrical and vascular concomitants of spreading depression *Am. J. Physiol* **189** 159-66

VAN HARREVELD A and Shade J P (1962) Changes in the electrical conductivity of cerebral cortex during seizure activity *Exp. Neurol.* **5** 383-400

Van Paesschen W (2004) Ictal SPECT *Epilepsia* **45 Suppl 4** 35-40

Van Paesschen W, Dupont P, Van Heerden B, Vanbilloen H, Mesotten L, Maes A, Van Driel G and Mortelmans L (2000) Self-injection ictal SPECT during partial seizures *Neurology* **54** 1994-97

Vollmer-Haase J, Folkerts H W, Haase C G, Deppe M and Ringelstein E B (1998) Cerebral hemodynamics during electrically induced seizures *Neuroreport* **9** 407-10

Vonk Noordegraaf A., Faes T J, Janse A, Marcus J T, Bronzwaer J G, Postmus P E and de Vries P M (1997) Noninvasive assessment of right ventricular diastolic function by electrical impedance tomography *Chest* **111** 1222-28

Vonk Noordegraaf A., Faes T J, Marcus J T, Janse A, Heethaar R M, Postmus P E and de Vries P M (1996) Improvement of cardiac imaging in electrical impedance tomography by means of a new electrode configuration *Physiol Meas.* **17** 179-88

Vonk Noordegraaf A., Kunst P W, Janse A, Marcus J T, Postmus P E, Faes T J and de Vries P M (1998) Pulmonary perfusion measured by means of electrical impedance tomography *Physiol Meas.* **19** 263-73

Vonk-Noordegraaf A, Janse A, Marcus J T, Bronzwaer J G, Postmust P E, Faes T J and de Vries P M (2000) Determination of stroke volume by means of electrical impedance tomography *Physiol Meas.* **21** 285-93

Wang W, Brown B H, Leathard A D and Lu L (1994) Noise equalization within EIT images *Physiol Meas.* **15 Suppl 2a** A211-A216

Wheless J W, Castillo E, Maggio V, Kim H L, Breier J I, Simos P G and Papanicolaou A C (2004) Magnetoencephalography (MEG) and magnetic source imaging (MSI) *Neurologist.* **10** 138-53

Wilson A J, Milnes P, Waterworth A R, Smallwood R H and Brown B H (2001) Mk3.5: a modular, multi-frequency successor to the Mk3a EIS/EIT system *Physiol Meas.* **22** 49-54

Woo E J, Hua P, Webster J G and Tompkins W J (1992) Measuring lung resistivity using electrical impedance tomography *IEEE Trans. Biomed. Eng* **39** 756-60

Yerworth R J, Bayford R H, Cusick G, Conway M and Holder D S (2002) Design and performance of the UCLH mark 1b 64 channel electrical impedance tomography (EIT) system, optimized for imaging brain function *Physiol Meas.* **23** 149-58

Yoon R S, Czaya A, Kwan H C and Joy M L (1999) Changes in the complex permittivity during spreading depression in rat cortex *IEEE Trans. Biomed. Eng* **46** 1330-1338

Zadehkoochak M, Blott B H, George R F and Hames T K (1990) Analysis of the sensitivity method of reconstruction using spectral expansion *Clin. Phys. Physiol Meas.* **11** 351-54

Zadehkoochak M, Blott B H, Hames T K and George R F (1991) The spectral expansion of a head model in electrical impedance tomography *Clin. Phys. Physiol Meas.* **12 Suppl A** 101-5

Zhao T X, Jacobson B and Ribbe T (1993) Triple-frequency method for measuring blood impedance *Physiol Meas.* **14** 145-56